5-24-2012

The Interstellar Transport of Galactic Cosmic Rays

Kelly Lave
Washington University in St. Louis

WASHINGTON UNIVERSITY IN ST. LOUIS

Department of Physics

Dissertation Examination Committee:
Martin H. Israel, Chair
W. Robert Binns
James H. Buckley
Ramanath Cowsik
Bruce Fegley Jr.
Henric Krawczynski
Douglas A. Wiens

The Interstellar Transport of Galactic Cosmic Rays

by

Kelly A. Lave

A dissertation presented to the
Graduate School of Arts and Sciences
of Washington University in
partial fulfillment of the
requirements for the degree
of Doctor of Philosophy

August 2012

Saint Louis, Missouri

Abstract

Using the Cosmic Ray Isotope Spectrometer (CRIS) onboard the Advanced Composition Explorer (ACE) spacecraft, new and improved high-precision measurements of the elemental composition and energy spectra of galactic cosmic rays with energies from ∼50-550 MeV/nucleon and nuclear charge $5 \leq Z \leq 28$ are reported here. These results cover observations during two solar minimum periods of the solar cycle, the most recent of which exhibited very low levels of solar activity and the highest galactic cosmic-ray intensities of the space era. Observations of secondary cosmic-ray species, those produced primarily by spallation interactions of accelerated material with the interstellar medium, and their primary progenitors are used to test the models of the transport of cosmic rays in the Galaxy.

Two principal models were tested: the simple leaky-box model and the nested leaky-box model. In the simple leaky-box model, cosmic rays accelerated at their sources are transported uniformly through the interstellar medium and escape in an energy-dependent fashion from the Galaxy. In the nested leaky-box model, cosmic rays are accelerated at their sources and briefly stored in surrounding cocoon regions before they escape into the Galaxy; escape from the cocoon regions is energy depen-

dent while escape from the Galaxy is independent of energy. Our observed B/C and $(Sc+Ti+V)/Fe$ ratios are compared with the results from these two models, and we find that the simple leaky-box model fits the data very well only when escape from the Galaxy has an unphysical energy dependence below $\sim$1 GeV/nucleon. Though the nested leaky-box model is considered to be more physically reasonable, we could not simultaneously fit the B/C and $(Sc+Ti+V)/Fe$ ratios at all energies. A model that includes a small amount of reacceleration, a process that boosts low-energy cosmic rays up to higher energies, is found to agree well with results from the simple leaky-box model.

Acknowledgements

First and foremost, I want to thank Marty and Bob. You have taught me a great deal about cosmic-ray astrophysics, a subject I knew nothing about before I asked you to support me as your graduate student. I appreciate all your patience and your willingness to sit down with pen and paper to teach me the fundamental concepts I needed to learn (and sometimes re-learn!) for my research. I truly hope that your example has made me a better critical thinker and scientist.

I want to thank my CRIS colleagues at Caltech and Goddard Space Flight Center. You are an inspiring group of people, and I appreciate your encouragement and help over the years. I especially want to thank Mark Wiedenbeck, who helped me produce the results in this thesis by running over 250 models. Though you had your own research, meetings, presentations, and papers to worry about, you somehow found the time to make my work a reality. Also, I never thought I would say this...I have grown fond of programming in IDL!

Thank you to my committee members: Marty, Bob, Jim Buckley, Ram Cowsik, Bruce Fegley, Jr., Henric Krawczynski, and Douglas Wiens. It's never a small commitment to sign on as a thesis examiner, and I appreciate that you set aside time at

the end of the school year to participate in my defense.

Additionally, I'd like to acknowledge that my work was supported not only by funding through the NASA grant NNX08AI11G, but also by the GAANN Fellowship and the NASA Graduate Student Researchers Program (GSRP). I hope these opportunities for graduate students continue to be available for many years to come.

At Washington University, there have been so many people who helped me stay happy, healthy, and sane. To Sarah Hedley and Julia Hamilton – I'm in awe at how deftly you manage the physics department and yet still have time to be the pseudo-moms of the graduate students. Thank you for keeping tabs on us and working miracles when we come to you with problems. To Alison Verbeck – thank you for the library chats (and FB gaming) that helped me blow off steam.

I'd like to give a shout out to the people that made life in the astro department easier/more interesting: Sarah, Brett, Vicky, Qingzhen, Brian (and his trusty dissertation/postdoc scooter), Jerrod, Ryan, Ryan, Richard, Dana, Garry, Paul, Marty, Trey, and Uncle Lauren.

To Joben, Seth, Jenny, Lauren, Michelle, Narelle, Caleb, Alisa, Matt, David, and Bec, my book club friends: I truly love you guys. You are the most honest, considerate, and thoughtful people I know. Getting together with you once a week for dinner and discussion was a joy!

To all my gamer friends through the years: Narelle, Brian, Ken, Brandeis, James, Jarrod, Kyle, Charles, Paul, Karyn, Lydia, Jeremy, Matt, Tiffany, Dave, Lori, Adam, Charles...(did I get everyone?!) Thank you for introducing me to new card and board

games, and for occasionally putting up with my alter-ego Evil Kelly. Here are three things I've learned from you over the years: 1) if Narelle is a cylon and you are not, you have no chance of winning; 2) I still don't like bridge, even when I play with wonderful people like you guys; and 3) no one wants to trade you their precious brick or rock when all you have are flocks of sheep!

To my family at All Saints Church and especially Harry, Mary, and Mary Ann, my "adopted" grandparents: I cherish your love and support. You've been there for me during the good times and the bad, and I have never known a church community that was so welcoming and caring.

To Michelle, the most awesome flat mate ever: I'm so very thankful you put up with my shenanigans these last 8 years because it's been so much fun hanging out, watching the Lord of the Rings movies, and doing puzzles. Wherever I end up next, I will still rely on you to tell me what books to read and movies to watch (except for Mixed Nuts – never again!). And if I ever develop the bad habit of punching and kicking people, I know who to blame.

And finally, I want to thank my family. Some people might call us crazy or weird, but I think we're pretty perfect the way we are. I love you all so very much. This thesis is dedicated to you.

Contents

Abstract **ii**

Acknowledgements **iv**

List of Figures **x**

List of Tables **xiii**

1 Introduction **1**
1.1 Galactic cosmic rays 1
1.2 Sources and acceleration mechanism 4
1.3 Propagation and reacceleration 8
1.4 GCRs in the heliosphere 11
1.4.1 The solar cycle 12
1.4.2 Cosmic ray transport in the heliosphere 13
1.4.3 Solar modulation 14
1.5 Cosmic ray detection 16
1.5.1 The Advanced Composition Explorer 17
1.6 Scope of this work 18

2 The Cosmic Ray Isotope Spectrometer **20**
2.1 The dE/dx versus E' technique 22
2.2 The SOFT hodoscope 25
2.3 Silicon solid-state detector system 26
2.4 CRIS data output 28

3 Data Analysis **30**
3.1 CRIS data selection 31
3.1.1 Data selection using `xpick` 31
3.1.2 Geometrical cuts 34
3.1.3 Instrument performance cuts 36
3.2 Final dataset 40
3.3 Geometry factors 42
3.4 Fragmentation correction 44
3.5 Hodoscope efficiency correction 47

3.6 Intensity and composition 50
3.7 CRIS solar minimum results 53
3.7.1 CRIS energy spectra 54
3.7.2 CRIS composition 54

4 The Simple Leaky-Box Transport Model 61
4.1 Inputs to the model 64
4.2 Analytical solution 69
4.3 Numerical solution 72
4.4 Model #1: Davis escape mean free path 80
4.4.1 Analytical solution results 83
4.4.2 Comparison with GALPROP 85
4.4.3 Summary of observations 90
4.5 Model #2: simple R-dependent escape mean free path 91
4.5.1 Comparison with GALPROP 98
4.5.2 Summary of observations 100
4.6 Simple leaky-box model conclusions 101

5 The Nested Leaky-Box Transport Model 104
5.1 Inputs to the model 107
5.2 Analytical solution 108
5.3 Numerical solution 114
5.4 Model #1 116
5.4.1 Analytical solution results 120
5.4.2 Comparison with GALPROP 121
5.4.3 Summary of observations 124
5.5 Model #2 125
5.5.1 Comparison with GALPROP 128
5.5.2 Summary of observations 131
5.6 Nested leaky-box model conclusions 131

6 Conclusions 135

Bibliography 138

A CRIS Solar Minimum Data 147

B CRIS Solar Maximum Data 152

C Updates to the Leaky-Box Transport Models 161
C.1 Production cross sections 161
C.2 Selected production cross sections 164
C.2.1 ^{20}Ne production 168
C.2.2 ^{21}Ne production 170

C.2.3 ^{22}Ne production . . . 172
C.2.4 ^{22}Na production . . . 175
C.2.5 ^{24}Na production . . . 177
C.2.6 ^{26}Al production . . . 179
C.2.7 ^{36}Ar production . . . 181
C.2.8 ^{38}Ar production . . . 182
C.2.9 ^{42}K production . . . 184
C.2.10 ^{43}K production . . . 186
C.2.11 ^{47}Ca production . . . 188
C.2.12 ^{43}Sc production . . . 189
C.2.13 ^{47}Sc production . . . 190
C.2.14 ^{48}V production . . . 191
C.2.15 ^{48}Cr production . . . 194
C.2.16 ^{49}Cr production . . . 195
C.2.17 ^{51}Cr production . . . 196
C.2.18 ^{52}Mn production . . . 198
C.2.19 ^{55}Co production . . . 201
C.2.20 ^{56}Co production . . . 202
C.2.21 ^{57}Co production . . . 204
C.2.22 ^{56}Ni production . . . 206
C.2.23 ^{57}Ni production . . . 207
C.3 Electron-capture decay nuclides . . . 208

D Simple and Nested Leaky-box Model Spectra **210**
D.1 Simple leaky-box model . . . 210
D.1.1 Model #1: Davis escape mean free path . . . 212
D.1.2 Model #2: simple R-dependent escape mean free path . . . 222
D.2 Nested leaky-box model . . . 231
D.2.1 Model #1 . . . 233
D.2.2 Model #2 . . . 241

List of Figures

1.1 Total cosmic-ray flux 3
1.2 GCR versus solar system composition 4

2.1 The CRIS instrument 20
2.2 CRIS, top view 21
2.3 ΔE vs. E' cross plot 24
2.4 CRIS cross section 27

3.1 Calculated charge versus E3 stop depth 37
3.2 Instrument livetime 39
3.3 CRIS oxygen flux, Bartels rotation averages 41
3.4 Geometry factor for $\theta \leq 30°$ 43
3.5 Spallation survival probability 47
3.6 SOFT hodoscope efficiency 48
3.7 CRIS solar minimum energy spectra, B-Ne 57
3.8 CRIS solar minimum energy spectra, Na-S 58
3.9 CRIS solar minimum energy spectra, Cl-Ti 59
3.10 CRIS solar minimum energy spectra, V-Ni 60

4.1 Escape mean free path form, SLBM 68
4.2 1997-98 secondary-to-primary ratios, SLB Model #1 81
4.3 2009-10 secondary-to-primary ratios, SLB Model #1 82
4.4 1997-98 secondary-to-primary ratios, SLB Model #1 with GALPROP . . 87
4.5 2009-10 secondary-to-primary ratios, SLB Model #1 with GALPROP . . 88
4.6 1997-98 secondary-to-primary ratios, SLB Model #2 92
4.7 2009-10 secondary-to-primary ratios, SLB Model #2 93
4.8 ^{10}B production cross sections 95
4.9 ^{11}B production cross sections 96
4.10 1997-98 secondary-to-primary ratios, SLB Model #2 with GALPROP . . 98
4.11 2009-10 secondary-to-primary ratios, SLB Model #2 with GALPROP . . 99

5.1 Escape mean free path form, NLBM 109
5.2 1997-98 secondary-to-primary ratios, NLB Model #1 118
5.3 2009-10 secondary-to-primary ratios, NLB Model #1 119
5.4 1997-98 secondary-to-primary ratios, NLB Model #1 with GALPROP . 122

5.5 2009-10 secondary-to-primary ratios, NLB Model #1 with GALPROP . 123
5.6 1997-98 secondary-to-primary ratios, NLB Model #2 126
5.7 2009-10 secondary-to-primary ratios, NLB Model #2 127
5.8 1997-98 secondary-to-primary ratios, NLB Model #2 with GALPROP . 129
5.9 2009-10 secondary-to-primary ratios, NLB Model #2 with GALPROP . 130

B.1 CRIS solar maximum energy spectra, B-Ne 155
B.2 CRIS solar maximum energy spectra, Na-S 156
B.3 CRIS solar maximum energy spectra, Cl-Ti 157
B.4 CRIS solar maximum energy spectra, V-Ni 158

C.1 ^{20}Ne production cross sections 168
C.2 ^{21}Ne production cross sections 170
C.3 ^{22}Ne production cross sections 172
C.4 ^{22}Na production cross sections 175
C.5 ^{24}Na production cross sections 177
C.6 ^{26}Al production cross sections 179
C.7 ^{36}Ar production cross sections 181
C.8 ^{38}Ar production cross sections 182
C.9 ^{42}K production cross sections 184
C.10 ^{43}K production cross sections 186
C.11 ^{47}Ca production cross sections 188
C.12 ^{43}Sc production cross sections 189
C.13 ^{47}Sc production cross sections 190
C.14 ^{48}V production cross sections 191
C.15 ^{48}Cr production cross sections 194
C.16 ^{49}Cr production cross sections 195
C.17 ^{51}Cr production cross sections 196
C.18 ^{52}Mn production cross sections 198
C.19 ^{55}Co production cross sections 201
C.20 ^{56}Co production cross sections 202
C.21 ^{57}Co production cross sections 204
C.22 ^{56}Ni production cross sections 206
C.23 ^{57}Ni production cross sections 207

D.1 1997-98 B and C energy spectra, SLB Model #1 212
D.2 1997-98 Sc, Ti, V, and Fe energy spectra, SLB Model #1 213
D.3 Adjusted 1997-98 B and C energy spectra, SLB Model #1 214
D.4 Adjusted 1997-98 Sc, Ti, V, and Fe energy spectra, SLB Model #1 . 215
D.5 2009-10 B and C energy spectra, SLB Model #1 217
D.6 2009-10 Sc, Ti, V, and Fe energy spectra, SLB Model #1 218
D.7 Adjusted 2009-10 B and C energy spectra, SLB Model #1 219
D.8 Adjusted 2009-10 Sc, Ti, V, and Fe energy spectra, SLB Model #1 . 220
D.9 ϕ vs. time for C, O, Mg, Si, and Fe 221

D.10 1997-98 B and C energy spectra, SLB Model #2 222
D.11 1997-98 Sc, Ti, V, and Fe energy spectra, SLB Model #2 223
D.12 Adjusted 1997-98 B and C energy spectra, SLB Model #2 224
D.13 Adjusted 1997-98 Sc, Ti, V, and Fe energy spectra, SLB Model #2 . 225
D.14 2009-10 B and C energy spectra, SLB Model #2 227
D.15 2009-10 Sc, Ti, V, and Fe energy spectra, SLB Model #2 228
D.16 Adjusted 2009-10 B and C energy spectra, SLB Model #2 229
D.17 Adjusted 2009-10 Sc, Ti, V, and Fe energy spectra, SLB Model #2 . 230
D.18 1997-98 B and C energy spectra, NLB Model #1 232
D.19 1997-98 Sc, Ti, V, and Fe energy spectra, NLB Model #1 233
D.20 Adjusted 1997-98 B and C energy spectra, NLB Model #1 234
D.21 Adjusted 1997-98 Sc, Ti, V, and Fe energy spectra, NLB Model #1 . 235
D.22 2009-10 B and C energy spectra, NLB Model #1 237
D.23 2009-10 Sc, Ti, V, and Fe energy spectra, NLB Model #1 238
D.24 Adjusted 2009-10 B and C energy spectra, NLB Model #1 239
D.25 Adjusted 2009-10 Sc, Ti, V, and Fe energy spectra, NLB Model #1 . 240
D.26 1997-98 B and C energy spectra, NLB Model #2 242
D.27 1997-98 Sc, Ti, V, and Fe energy spectra, NLB Model #2 243
D.28 Adjusted 1997-98 B and C energy spectra, NLB Model #2 244
D.29 Adjusted 1997-98 Sc, Ti, V, and Fe energy spectra, NLB Model #2 . 245
D.30 2009-10 B and C energy spectra, NLB Model #2 246
D.31 2009-10 Sc, Ti, V, and Fe energy spectra, NLB Model #2 247
D.32 Adjusted 2009-10 B and C energy spectra, NLB Model #2 248
D.33 Adjusted 2009-10 Sc, Ti, V, and Fe energy spectra, NLB Model #2 . 249

List of Tables

3.1 `xpick` data selections 35
3.2 Dead layer cuts for E2-E8 38
3.3 SOFT efficiency fit parameters 49
3.4 Solar minimum relative abundances 55

4.1 Estimated secondary fractions of select cosmic-ray isotopes 84

A.1 CRIS 1997-98 solar minimum spectra 148
A.2 CRIS 2009-10 solar minimum spectra 149
A.3 CRIS 1997-98 solar minimum spectra, interpolated 150
A.4 CRIS 2009-10 solar minimum spectra, interpolated 151

B.1 CRIS 2001-03 solar maximum spectra 154
B.2 CRIS 2001-03 solar maximum spectra, interpolated 159
B.3 Solar maximum relative abundances 160

C.1 Cross section references 167

Chapter 1

Introduction

1.1 Galactic cosmic rays

Cosmic rays (CRs) are highly energetic charged particles that are extraterrestrial in origin. They were originally discovered by Victor Hess in 1912 during manned balloon experiments, where he determined that the average ionization increased relative to the ionization at sea-level above 1.5 km (Longair 1992). Originally believed to be incident gamma-rays, we now know that about 98% of cosmic rays are nuclei, while the remaining 2% are electrons and positrons. Of the nuclei, approximately 89% are hydrogen (protons), 10% are helium (alpha particles), and 1% are heavier nuclei.

These particles have been observed to have energies that range from tens of MeV per nucleon up to $\sim 10^{20}$ eV. Above a few GeV/nucleon, the energy spectrum of CRs follows a power law proportional to $E^{-2.7}$. At $\sim 10^{15}$ eV there is a break in the spectrum, which is typically referred to as the "knee"; below this energy the CRs are certainly Galactic in origin. From the "knee" up to $\sim 10^{18}$ eV the power law falls as $E^{-3.0}$. A second kink in the spectrum occurs at 10^{18} eV, usually called the "ankle,"

where the spectrum flattens. At this energy it is possible that an extragalactic component to the cosmic-ray spectrum emerges. The CR spectrum continues up to $\sim 10^{20}$ eV, which is the current high-energy limit for observations of the spectrum. Cosmic rays with energies above 6 x 10^{19} eV will interact with the 2.7 K cosmic microwave background, and these CRs traveling over distances greater than 50 Mpc should not be observed at Earth (Greisen 1966). This is known as the Greisen-Zatsepin-Kuzmin (GZK) cutoff. A compilation of the flux of all cosmic rays is shown in Figure 1.1. The focus of this dissertation is on the study of galactic cosmic-ray (GCR) nuclei from boron through nickel with energies between ∼50-550 MeV/nucleon.

Galactic cosmic rays are classified into two categories: primary and secondary nuclei. Primary species are those nuclei produced at the source, accelerated to high energies, transported through the Galaxy, and then detected at Earth. Secondary species are nuclei produced from the fragmentation (spallation) of heavier nuclei from collisions with the interstellar medium, which is composed of mostly hydrogen and some helium. Primary species like carbon, oxygen, silicon, and iron have similar relative abundances as we see in the solar system, as is shown in Figure 1.2. Due to spallation, secondary species are typically more abundant in the cosmic rays than in the solar system, most notably seen in the light elements lithium, beryllium, and boron, and the sub-iron species scandium, titanium, and vanadium. These results indicate that the CR source material at the time of acceleration is of a similar composition to the solar system material. Where the GCR elemental and isotopic abundances differ from the solar system abundances, we find a key to determining the sources of GCRs.

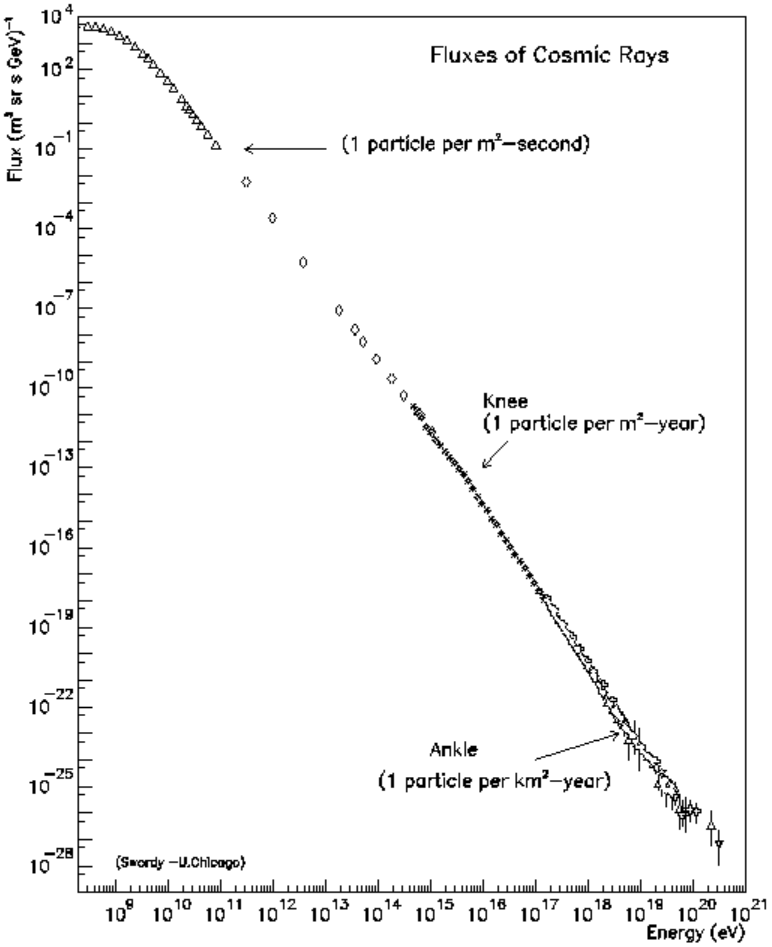

Figure 1.1: The total flux of all cosmic rays (Swordy 2001).

Galactic cosmic rays (and pre-solar meteoritic dust grains) are the only matter that can be directly studied that originated outside our solar system. GCR composition and energy spectra can be used to determine their sources, acceleration mechanisms, transport processes in the Galaxy and our heliosphere, and other high-energy phenomena. Since the most exciting frontiers of astrophysics involve physical processes and environments that can not be reproduced in the laboratory, these studies of GCRs will ultimately unlock a greater understanding of our universe.

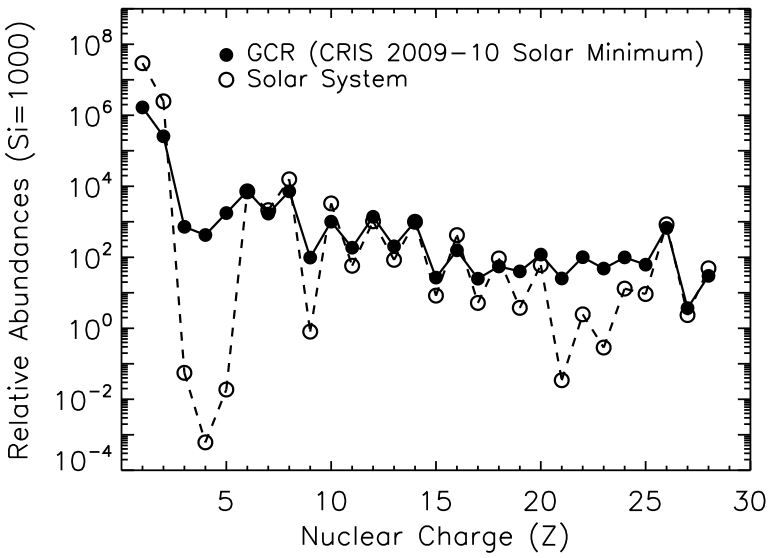

Figure 1.2: A comparison of the GCR solar minimum abundances (filled circles) at 160 MeV/nucleon and the solar system abundances (open circles) from Lodders et al. (2009). The GCR data for Z<5 come from Wang et al. (2002) and de Nolfo et al. (2006), while the Z>5 abundances are the 2009-10 CRIS solar minimum results reported in this work (Section 3.7.2).

1.2 Sources and acceleration mechanism

Since their discovery in 1912, scientists have been trying to determine the sources and acceleration mechanism of GCRs. It is likely that GCRs with energies below $\sim 10^{15}$ eV are accelerated in supernovae (SN) shocks. Under steady-state conditions, the power requirement for SN to maintain the CR flux is $\sim 10^{41}$ ergs/sec (Ginzburg and Syrovatskii 1964). Supernovae, which have a rate of about three per century per galaxy, have ejecta kinetic energies of $\sim 10^{51}$ ergs (Woosley and Weaver 1995). Therefore, the necessary power is achievable if at least 10% of the SN kinetic energy goes into the acceleration of GCRs.

Though SN inject freshly synthesized material into the surrounding space, we can use long-lived radioactive isotopes to determine whether this ejecta is accelerated directly or at a later time by subsequent SN shocks. The electron-capture decay of ^{59}Ni to ^{59}Co has a half-life of 7.6 x 10^4 years in the laboratory. Since GCRs propagating through the ISM at energies greater than ∼50 MeV/nucleon are stripped of their electrons, ^{59}Ni is a stable isotope. CRIS observations (Wiedenbeck et al. 1999) showing that essentially all ^{59}Ni has decayed indicate that there is a long delay (>10^5 years) between nucleosynthesis and acceleration, and therefore it is the older stellar ejecta or interstellar material, not the freshly ejected material, that is accelerated in SN shocks.

Most core-collapse supernovae are believed to occur in OB associations, which are unbound clusters of massive (>8 $M_\odot$) O and B type stars (Higdon et al. 1998). Those stars with the greatest initial mass ($\gtrsim$35 $M_\odot$) evolve into short-lived (∼3-6 x 10^6 years) Wolf-Rayet (W-R) stars. Powerful stellar winds from these stars and the successive SN carve out giant (>150 pc) cavities in the local ISM to form superbubbles. Streitmatter et al. (1985) were the first to propose that GCRs are created and accelerated in these regions.

The composition of the material inside superbubbles is not well known, so we compare observations of GCR elemental and isotopic abundances with solar system abundances and stellar modeling calculations. Models based on the first ionization potential (FIP) of nuclei were originally used to explain the observed enhancements of certain GCRs relative to the solar system abundances (Casse and Goret 1978). With

these models, elements with low FIP should be ionized and preferentially accelerated by SN shocks, and their GCR abundances would be enhanced. However, some species with similar FIP had relative abundances that differed by over a factor of two, and there was a large amount of scatter in the transition from low- to high-FIP. These ambiguities led to the consideration of volatility models.

Species that have high condensation temperatures (referred to as refractory, or low-volatility, elements) will more easily condense into grains. Because of UV surface ionization, these dust grains will attain a small positive charge and very high rigidity (momentum per unit charge), and so they are easily accelerated by the SN shocks. Atoms that sputter off of these energetic grains through collisions with the hydrogen and helium in the ISM are accelerated to CR energies more efficiently than atoms in the gas that did not have the benefit of that grain acceleration (Meyer et al. 1997). Therefore, refractory elements should be enhanced in the CRs relative to volatile elements. Isotopes of the same element have essentially the same condensation temperatures, so there should be very little difference in their acceleration efficiencies.

Casse and Paul (1982) first postulated that the enhanced $^{22}Ne/^{20}Ne$ ratio seen in the GCRs relative to the solar system was due to the enriched W-R outflow. This material, which is rich in ^{22}Ne and other high-metallicity matter, mixes with the low-density pre-supernova material (stellar wind outflow) inside the superbubble (Higdon and Lingenfelter 2003, 2005). This material resides within the superbubble for longer than the $\sim 10^5$ years required before the first stars explode and accelerate the ambient material (Higdon et al. 1998). Using a stellar model with non-rotating or rotating

W-R stars with 40M≤M≤85 $M_{\odot}$, Binns et al. (2005, 2007, 2008) demonstrated that observations of the GCR $^{22}Ne/^{20}Ne$ ratio (enhanced by a factor of ∼5 over solar system abundances) can be reproduced if they assume a GCR source composition that is ∼80% solar system material mixed with ∼20% W-R and supernova material. They also confirmed similar enhancements for $^{12}C/^{16}O$ (after correcting for the different acceleration efficiencies of C and O) and $^{58}Fe/^{56}Fe$. Using this same model, Rauch et al. (2009) found that refractory GCRs with charge Z≤40 are preferentially accelerated (enhanced by a factor of ∼4 over volatile GCRs), and when plotted versus atomic mass there is similar ordering.

Gamma-ray observations of supernova remnants (SNR), molecular clouds, and OB associations provide fairly compelling evidence that supernovae shocks accelerate electrons and nuclei up to $\sim 10^{14}$ eV/nucleon. Recently, the *Fermi* Large Area Telescope (LAT) and the VERITAS ground-based gamma-ray observatory have detected gamma-ray emission, covering energies between ∼400 MeV and ∼10 TeV, from the Type 1A SNR G120.1+1.4 known as *Tycho*'s SNR (Giordano et al. (2012); Acciari et al. (2011)). The photon flux is shown to be very well fit by a model that includes the production of gamma-rays from π^o production and decay, with only a small fraction of the observed flux due to inverse Compton emission and bremsstrahlung. This is good evidence that the gamma-ray emission is due to proton acceleration in the forward shock in the SNR.

Additionally, Ackermann et al. (2011) reported observations with the *Fermi* LAT of a cocoon of distributed gamma-ray emission in the 0.1- to 100-GeV energy band

from freshly accelerated CRs in the Cygnus X region of the sky. This emission extends over a ∼50 parsec region between the Cygnus OB2 association, a very large cluster with more than 500 O and B type stars, and the γ Cygni supernova near the open cluster NGC 6910. After subtracting background emission, they found that most of this distributed emission came from the two massive clusters. This emission region is bounded by 8 μm infrared emission coming from the compressed ionized gas of the shell of the Cygnus superbubble that represents the cocoon region. The energy spectra from various regions inside the cocoon are consistent and indicate that the emission is diffuse (i.e., not from individual point sources). Milagro observations (Abdo et al. 2007a,b) of this region suggest proton acceleration as the origin of the emission, since their results are inconsistent with gamma-ray emission from accelerated electrons. With these observations, there is now compelling evidence that CRs are accelerated in superbubbles.

1.3 Propagation and reacceleration

Once cosmic rays are accelerated, they propagate through the interstellar medium and into the heliosphere where we detect them. Since there are regions of space with varying densities and interstellar magnetic fields, CRs will be significantly affected by the environments they travel through.

Cosmic rays diffuse through the ISM and scatter off the inhomogeneities in the interstellar magnetic fields, effectively randomizing their arrival directions. Only the

highest energy particles travel through the ISM without significant deflection from the magnetic fields they may encounter. The deflection is characterized by the particle's gyromagnetic radius, or the radius at which a charged particle will spiral around a magnetic field line. For relativistic particles this radius is defined to be:

$$r_g = \frac{Rsin\theta}{Bc}\,, \tag{1.1}$$

where B is the magnetic field strength (measured in teslas), c is the speed of light, R is the particle's rigidity (typically reported in units of gigavolts), and θ is the pitch angle. As an example, consider a 10^9-eV proton traveling through an interstellar magnetic field with strength B=5 μG (1 G = 10^{-4} T) (Opher et al. 2009). The maximum radius of curvature, when the pitch angle is 90°, will be $\sim 10^{10}$ m or about 0.08 AU. To put this into perspective, cosmic rays with this energy would spiral around an interstellar magnetic field line with a radius that is about one-fifth of the distance between the Sun and Mercury (0.39 AU). Any kinks in the field line that are comparable or larger in size to r_g will significantly deflect the particle from its original trajectory (Parker 1965). Therefore, the arrival direction of GCRs gives no information about the sources, and we must instead study the composition of GCRs observed at Earth. By accurately describing the gain and loss processes that will affect GCRs during their transport through the Galaxy, we can construct models that enable us to infer the source composition from the observed composition.

During transport, CRs will interact with the ambient material of the ISM, which

is approximately 90% hydrogen and 10% helium. Cosmic rays lose energy to the ionization of the ISM hydrogen and helium, as well as attach or strip off orbital electrons, changing their charge states. They also suffer nuclear interactions with the ISM to produce lighter daughter nuclei that have approximately the same velocity as the parent cosmic ray. These collisions are the reason for the observed GCR enhancements of secondary elements relative to the solar system, as seen in Figure 1.2. Additionally, any unstable daughter nuclei (except for electron-capture decay nuclei, which when fully stripped of their electrons are stable in the CRs) may decay if they remain in the Galaxy comparable to or longer than their half-life.

While laboratory measurements of the production cross sections for high-energy particles incident on hydrogen and helium targets are available, they cover only a small energy range and a limited set of parent-daughter combinations. Therefore, results from semi-empirical models are used to fill in the missing cross section information. We note that critical updates made to the cross section database used in this work are detailed in Appendix D.

The relative abundances of long-lived radionuclides produced as secondary species (^{10}Be, ^{26}Al, ^{36}Cl, and ^{54}Mn) have been used to estimate the mean density of the ISM. This requires a parameterization of the escape mean free path (MFP) of these GCRs in the Galaxy, which is commonly taken to be a function of the particle rigidity and velocity and given in units of areal density (g/cm^2). After assuming an escape MFP that yielded results consistent with observations of the relative abundances of the radionuclides, Yanasak et al. (2001) calculated a mean ISM number density of 0.34

$\pm$ 0.04 cm^{-3}. Knowing this and the mean amount of material GCRs traverse before escape (given by Equation 4.3 in Chapter 4.1), the mean confinement time in the Galaxy was determined to be 15.0 $\pm$ 1.6 Myr. If GCRs could travel for this period of time near the speed of light without suffering nuclear interactions or scattering from irregularities in the magnetic fields in the ISM, they would travel a distance of nearly 5 Mpc (the plane of the visible Galaxy has a diameter of about 30 kpc).

Since GCRs are accelerated in supernovae shockwaves at their sources, it is plausible that randomly moving magnetohydrodynamic (MHD) waves in the ISM will also scatter GCRs, resulting in stochastic reacceleration. This process increases the energy of GCRs, and subsequently more secondary GCRs will be produced at higher energies. Some galactic transport models have incorporated small amounts of reacceleration at energies below $\sim$1 GeV/nucleon. Their results indicate that certain secondary-to-primary ratios, such as B/C, can be well fit with these models (de Nolfo et al. 2006; Strong et al. 2007).

1.4 GCRs in the heliosphere

Before galactic cosmic rays can be observed at Earth they must travel through the heliosphere, the region of space directly affected by Sun's influence. In this final leg of their journey to Earth, GCRs with energies below several GeV/nucleon in interstellar space will be affected by the outward flowing solar wind, resulting in significant changes to their energy spectra. Since the Sun dynamically changes over a

period of ∼22 years its effect on GCRs, referred to as solar modulation, also changes with time. The next sections will describe the solar cycle, the transport of GCRs through the heliosphere, and the solar modulation model used in this work.

1.4.1 The solar cycle

The Sun's influence within the heliosphere changes over a period of ∼22 years. This time can be divided into two ∼11-year periods, $A > 0$ and $A < 0$, defined according to the polarity of the Sun's magnetic field. At the beginning of the $A > 0$ phase, the solar magnetic field is relatively stable with a positive polarity at the solar north pole. During the next ∼11 years, the field will reorient itself until the solar south pole has a positive polarity, signaling the start of the $A < 0$ phase. Again, the magnetic field will reorient over the course of ∼11 years until the next $A > 0$ phase begins.

In both the $A > 0$ and $A < 0$ phases there are periods of high and low solar activity, which is typically measured by the number of sunspots. Both phases begin with solar minimum, where the magnetic field is stable and the solar activity is lowest. Other solar properties, including the mean solar magnetic field strength, the tilt angle of the heliospheric current sheet, and the solar-wind pressure are at their lowest (Mewaldt et al. 2010). During this period of time, GCRs in the heliosphere will suffer the least amount of solar modulation. As the solar magnetic field proceeds to flip its polarity the sun transitions into a period of solar maximum, where the magnetic field is complex and the solar activity is highest. The energy spectra of GCRs are most affected during this time.

1.4.2 Cosmic ray transport in the heliosphere

The plasma from the Sun flows radially outward at approximately a constant velocity, dragging the dipolar solar magnetic field with it. Since the Sun rotates about its axis once every 26 days, the field lines are warped into the the shape of an Archimedean spiral with the Sun at its center (Parker 1965). A wavy neutral current sheet, which may be tilted at an angle with respect to the ecliptic plane, separates the northern and southern polarities of the magnetic field.

As CRs diffuse inward into the heliosphere the outward convection of the solar wind reduces their density. In addition, the solar wind expands as it flows outward. The GCRs diffuse in this expanding medium and continuously lose energy in a process called adiabatic deceleration (Parker 1966). Therefore, by the time the GCRs are observed at Earth, particles with interstellar energies less than a few GeV/nucleon may have lost a significant fraction of their energies.

The magnitudes of the losses due to diffusion, convection, and adiabatic deceleration depend on the phase of the solar cycle. During the $A > 0$ phase, GCR nuclei entering the heliosphere in the northern solar hemisphere tend to drift in from the polar region and out along the wavy current sheet in the opposite direction of the solar rotation (due to curvature drift) (Jokipii et al. 1977). When the field polarity is flipped in the $A < 0$ phase, GCR nuclei will instead tend to drift inward along the current sheet in the same direction as the Sun's rotation. Drift directions are opposite for negatively-charged particles. Additionally, as the angle between the current

sheet and the ecliptic increases in the progression from solar minimum to maximum, the waviness of the current sheet will increase (Jokipii and Thomas 1981). For these reasons, GCRs lose the most energy during $A < 0$ solar maximum periods since they travel along the complex, wavy current sheet before observation. In contrast, GCRs entering the heliosphere during $A > 0$ solar minimum periods tend to lose the least amount of energy before observation since they have the shortest path to Earth along the current sheet. These changes will modulate the energies of GCRs as they travel through the heliosphere.

1.4.3 Solar modulation

The effects of diffusion, convection, adiabatic deceleration, and particle drift may be described using the spherically-symmetric Fokker-Planck equation (Goldstein et al. 1970):

$$\frac{1}{r^2}\frac{\partial}{\partial r}(r^2VU) - \frac{1}{3}\left(\frac{1}{r^2}\frac{\partial}{\partial r}(r^2V)\right)\left(\frac{\partial}{\partial T}(\alpha TU)\right) = \frac{1}{r^2}\frac{\partial}{\partial r}\left(r^2\kappa\frac{\partial U}{\partial r}\right) . \tag{1.2}$$

Here, $U(r,T)$ is the cosmic-ray number density and is a function of distance r and kinetic energy T. The solar wind speed is given by $V(r)$, $\kappa(r,T)$ is the interplanetary diffusion coefficient, and $\alpha(T) = (T+2mc^2)/(T+mc^2)$ (where mc^2 is the rest energy of the particle). This equation can be solved using the Crank-Nicholson technique described by Fisk (1971). By separating the diffusion coefficient in Equation 1.2 into radially- and ridigity-dependent parts, Gleeson and Axford (1968) were able to

describe the cosmic-ray intensities anywhere in the heliosphere with respect to their interstellar intensities using a single parameter, ϕ, that represented the mean energy loss of CRs as they moved through the interplanetary medium. This is called the "force field solution" and is given by:

$$\phi = \frac{R}{3} \int_{1\mathrm{AU}}^{D} \frac{V_{\mathrm{SW}}(r)}{\kappa(r,R)/\beta} dr \,, \tag{1.3}$$

where β is the particle's velocity and R is its ridigity (typically in GV), $V_{\mathrm{SW}}(r)$ is the solar wind speed ($\sim$400 km/sec), $\kappa(r,R)$ is the diffusion coefficient, and D is the the radius of the heliospheric boundary ($\sim$120 AU).

For the work in this dissertation, we have chosen to describe solar modulation using the Fisk (1971) solution to Equation 1.2, though we do approximate values of ϕ for different time periods. We do this by assuming that the diffusion coefficient has the form $\kappa(r,R) = \kappa_o \beta R/R_o$, where an absolute value κ_o is defined at rigidity R_o. Equation 1.3 then simplifies to

$$\phi = \frac{R_o V_{\mathrm{SW}}(D - 1\mathrm{AU})}{3\kappa_o} \,. \tag{1.4}$$

Typical values of ϕ for solar minimum periods are below 400 MV, while periods of solar maximum have ϕ values above 800 MV. We note that the energy spectra of different GCR species are sometimes best fit using slightly different values of ϕ, as seen in Figure D.9. This is unsurprising since Equation 1.2 over-simplifies the solar

environment by describing it as spherically-symmetric with no differences in the drift directions of particles in the $A > 0$ and $A < 0$ phases.

1.5 Cosmic ray detection

There are three different categories for CR experiments: satellites, balloon-borne detectors, and ground detectors. The lowest energy cosmic rays (less than a few hundred MeV/nucleon) must be observed via experiments onboard space-based satellites because these particles are easily deflected in the Earth's magnetosphere or absorbed in the upper atmosphere. PAMELA and AMS are examples of space-based CR detectors; HEAO, Fermi, Voyagers 1 and 2, and ACE are all examples of satellites carrying CR detectors (among other science instruments).

Instruments that observe CRs with energies from a few hundred MeV/nucleon up to $\sim 10^{15}$ eV are often flown on high-altitude balloons because they are too big or costly to launch into space. Large detectors are required to measure the higher-energy CRs (ATIC, CREAM, and TRACER are example instruments), as well as the rarer ultra-heavy CR nuclei (using the TIGER instrument) or CR antiparticles (using BESS and HEAT). Additionally, prototypes of CR detectors may be flown on balloons to develop, improve, and test future experiments.

Ground-based detector arrays indirectly observe the highest energy cosmic rays, since these particles interact in the Earth's atmosphere to produce massive electromagnetic air showers. Therefore, these detectors must be very large in order to observe

these rare CRs. The Pierre Auger Observatory is an example of a ground-based CR detector.

1.5.1 The Advanced Composition Explorer

The Advanced Composition Explorer (ACE) is a satellite carrying nine instruments designed to study the solar corona, wind, and magnetic field, as well as the elemental, isotopic, and ionic charge state composition of nuclei with charge $1 \leq Z \leq 30$ and energies between $\sim$1 keV/nucleon to $\sim$550 MeV/nucleon (Stone et al. 1998b). Observations of solar energetic particle events, anomalous cosmic rays (which are partially ionized nuclei that originate in the neutral gas of the ISM), and GCRs are used to study particle transport in both the heliosphere and the ISM. ACE was launched on August 25, 1997 and is located $\sim$1.5 million km sunward from Earth in a halo orbit about the L1 Lagrangian point.

Of the nine instruments, The Cosmic Ray Isotope Spectrometer (CRIS) is the only one capable of observing galactic cosmic rays (Stone et al. 1998a). It is designed to measure the charge, mass, and energy of GCRs with nuclear charge $3 \leq Z \leq 30$ at energies between $\sim$50-550 MeV/nucleon. Chapter 2 will discuss the instrument and its capabilities in great detail. In this dissertation, new CRIS observations of the elemental composition and energy spectra during the two most recent periods of solar minimum will be presented (Chapter 3)

1.6 Scope of this work

The objective of this dissertation is to use high-precision GCR observations of secondary species and their primary progenitors to test interstellar transport models that can be used to make predictions of the CR source composition. The work presented here is three-fold, where the first part discusses significant improvements in the data analysis techniques that were applied to the CRIS elemental GCR observations for the 1997-1998 solar minimum and 2003-2005 solar maximum periods, which were presented in our previous work (George et al. 2009). These changes include an improved approach to the error analysis for the energy spectra and relative abundances, and a more careful selection of the 1997-98 solar minimum dataset to avoid introducing charge-dependent biases in the results. The revised data are presented in Chapter 3.

The second part of this work presents the first measurements from CRIS of the elemental composition and energy spectra for the 2009-2010 solar minimum, which boasts the highest measured intensities of the space era. This period of time is notable for exhibiting very low levels of solar activity, which means that these GCR observations within the inner solar system are considered to be the closest we have ever come to observing nuclei heavier than helium in ISM conditions. These data (also found in Chapter 3) are the most detailed and statistically-significant GCR observations at low energies (< 1 GeV/nucleon) and low levels of solar modulation, and in future work they may be used to better estimate the GCR source abundances.

For the third part of this dissertation, we compare our CRIS solar minima ob-

servations to the results from two different models for GCR transport outside of the heliosphere. Before this work could be accomplished, extensive updates to our database of measured and semi-empirical interaction cross sections were required, with all additions and corrections documented here (Appendix C). Since these cross sections are one of the most critical inputs to any transport model, the new data substantially improves our confidence in the model results.

The first model studied (Chapter 4) was the simple leaky-box transport model. We used the new and improved CRIS solar minima data to determine if the model used in our previous work (George et al. 2009) was still able to provide a good fit to the observations, as well as whether or not a simpler model could provide equally good predictions. The numerical code used for the simple leaky-box model was then adapted to allow us to investigate what was thought to be the more realistic nested leaky-box transport model (Chapter 5). This model treats interstellar GCR transport as occurring in two separate volumes: high-density cocoon regions around the sources and a low-density Galactic region. By adjusting the input parameters we found two models that best fit the data. The strengths and weaknesses of each model are discussed, and their results are compared with those of the commonly-used GALPROP transport code. For each model we also developed a simplified analytical model for comparison with the numerical results. Though it is beyond the scope of this work, the best-fit models to the data may be used to determine new GCR source abundances, which will help us find the sources themselves.

Chapter 2

The Cosmic Ray Isotope Spectrometer

Figure 2.1: The Cosmic Ray Isotope Spectrometer (CRIS). The large, gold-colored square is the top of the SOFT hodoscope (Section 2.2). Other visible elements include the high-voltage power supplies, the image intensifier/CCD system, and the camera electronics.

The Cosmic Ray Isotope Spectrometer (CRIS) onboard the Advanced Composition Explorer (ACE) was launched on August 25, 1997 and placed into a halo orbit at the L1 Lagrangian point 1.5×10^6 kilometers sunward of Earth. It is designed to measure the charge, mass, and energy of galactic cosmic rays from $3 \leq Z \leq 30$ at ener-

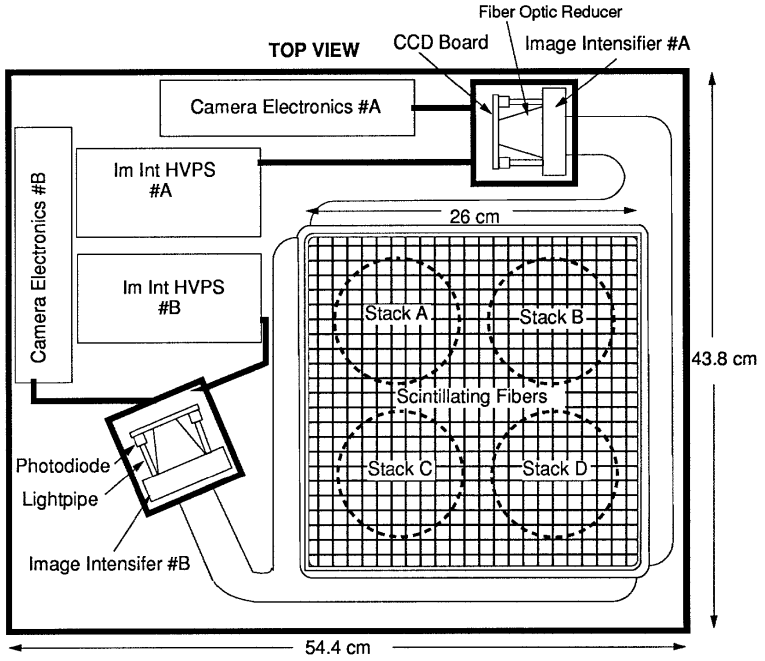

Figure 2.2: CRIS schematic, top view. Shown are the four silicon detector stacks beneath the scintillating fiber planes. The fibers are connected to two image-intensified CCD cameras. Also shown here are the high voltage power supplies and the camera electronics.

gies between ∼50-550 MeV/nucleon. Incident cosmic rays pass through a scintillating optical fiber trajectory (SOFT) hodoscope and into one of four silicon solid-state detector stacks. CRIS has a large geometrical acceptance of ∼250 cm^{2}sr and excellent mass resolution ($\sigma_A \leq 0.25$ amu at Fe). A complete description of CRIS is available in Stone et al. (1998a). As of this writing, its operation has exceeded the proposed 2-year mission, and it remains fully operational with minimal deterioration after 14 years.

2.1 The dE/dx versus E' technique

A particle with charge Z, mass number A, and initial kinetic energy E will penetrate an amount of material L and emerge with residual kinetic energy E' such that

$$R\left(Z, A, \frac{E}{A}\right) - R\left(Z, A, \frac{E'}{A}\right) = L = L_o \sec(\theta) \,, \tag{2.1}$$

where R is the range of the particle as a function of energy per nucleon in the given material, L_o is the detector thickness, and θ is the angle of incidence with respect to the detector normal. Given measurements of E', $\Delta E = E - E'$, and L in the CRIS detector, the charge, mass, and energy of an incident cosmic ray may be determined.

As discussed in Stone et al. (1998a), we can adopt a range-energy relation of the form

$$R\left(Z, A, \frac{E}{A}\right) \approx \frac{kA}{Z^2}\left(\frac{E}{A}\right)^a \,. \tag{2.2}$$

Values of k and a have been tabulated for the isotopes of boron through nickel in Table B.1 in Scott (2005); typically, the values for k range from $\sim$3-5x10^{-3}, while α has a range of values between $\sim$1.6-1.8. Substituting this relation into Equation 2.1 and solving for the mass A we obtain:

$$A \approx \left(\frac{k}{Z^2 L}\right)^{1/(a-1)} ((\Delta E + E')^a - E'^a)^{1/(a-1)} \,. \tag{2.3}$$

Uncertainties in the measurements of ΔE, E', and $L = L_o \sec(\theta)$ will introduce an

uncertainty in the calculated mass, which we call the mass resolution. Ogliore (2006) discusses the important contributions to the mass resolution for CRIS, which is 0.25-0.30 amu for the iron-group elements and as low as ∼0.1 amu for the lightest species.

If we assume a mass-to-charge ratio of $A/Z \approx 2 + \epsilon$ (for $Z \geq 3$) with $0 \leq \epsilon \leq 0.4$ (since Galactic cosmic rays with A/Z values outside this range have short half-lives and will not be observed before decay), we can use Equation 2.3 to solve for the charge of the particle:

$$Z \approx \left(\frac{k}{L(2+\epsilon)^{a-1}} \right)^{1/(a+1)} ((\Delta E + E')^a - E'^a)^{1/(a+1)} \, . \tag{2.4}$$

In practice, one first calculates the charge of each incident cosmic ray using Equation 2.4 (ΔE, E', and L are known for each event). A histogram of the results will yield well-separated element peaks which are used to assign the integer charge of each particle. Using this value and Equation 2.3, the particle's mass can be determined.

We can confirm that the dE/dx versus E' technique yields well-separated species by considering a second approach to defining the relationship between the charge, mass, and energy of cosmic rays. For a charged particle, the Bethe-Bloch formula gives the energy deposited per unit length:

$$-\frac{dE}{dx} = \frac{4\pi}{m_e c^2} \cdot \frac{n_e Z^2}{\beta^2} \cdot \left(\frac{e^2}{4\pi\epsilon_o} \right)^2 \cdot \left(\ln \left(\frac{2 m_e c^2 \beta^2}{I(1-\beta^2)} \right) - \beta^2 \right) \, . \tag{2.5}$$

Here, m_e is the rest mass of the electron, c is the speed of light, n_e is the electron

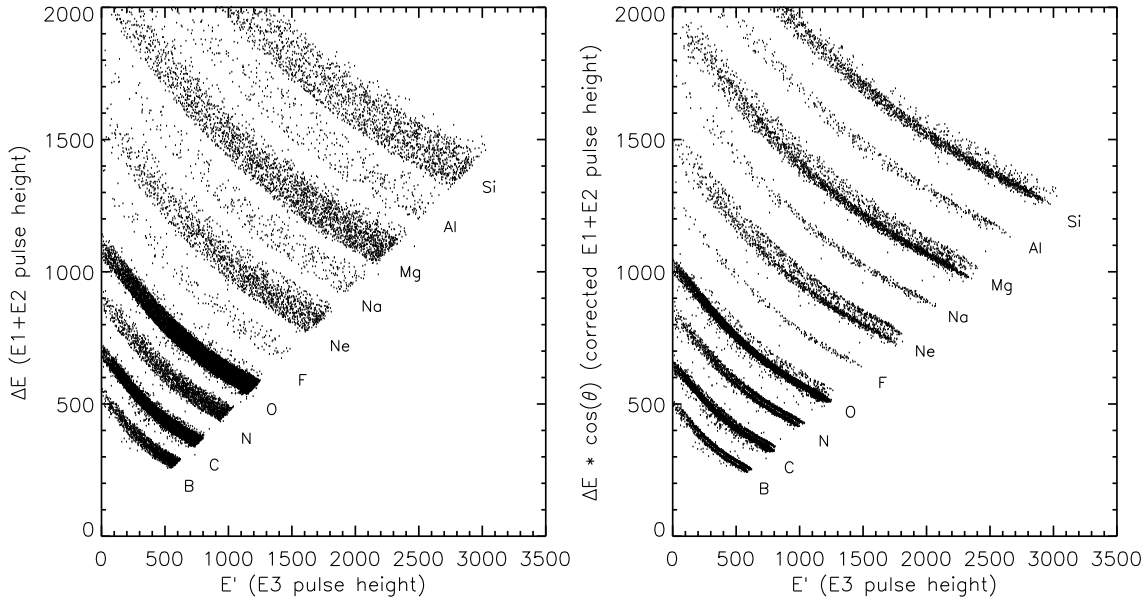

Figure 2.3: Cross plot of ΔE versus E', for particles with charge $5 \leq Z \leq 14$ stopping in detector E3 of telescope 1. In the left-hand panel ΔE has not been corrected for incident angle, though charge bands are visible. In the right-hand panel ΔE has been multiplied by the cosine of the incident angle θ. This correction clearly separates individual elements from one another and shows some isotope separation.

density of the target material, Z is the particle charge, β is the particle velocity in units of c, e is the electron charge, ϵ_o is the vacuum permittivity, and I is the mean excitation potential of the target material. In simpler terms, this equation specifies that the energy loss per unit length is a function of the charge and velocity of the particle:

$$\frac{\Delta E}{L} \approx \frac{dE}{dx} = Z^2 \cdot f(\beta) \, . \tag{2.6}$$

We can also write down the total energy of the particle as a function of its mass and velocity:

$$E = A \cdot g(\beta) \, . \tag{2.7}$$

Multiplying Equations 2.6 and 2.7 gives

$$\frac{\Delta E}{L} \cdot E = Z^2 A \cdot f(\beta) \cdot g(\beta) \, . \tag{2.8}$$

No two stable or long-lived isotopes have the same Z^2A, so plotting the energy loss per unit length versus the total energy will yield discrete isotope bands. As an example, Figure 2.3 plots ΔE versus E' for particles with charge $5 \leq Z \leq 14$ stopping in detector E3 of telescope 1. In the left panel of Figure 2.3, ΔE has not been corrected for the incident angle of the particle, and so we see wide charge bands that partially overlap one another, and no isotope resolution is visible. When the angle correction is included we arrive at the results in the right panel, where each element is nicely separated from its nearest neighbors. Some mass separation is now visible within the charge bands; for example, ^{14}N and ^{15}N can be identified as separate tracks, while oxygen is dominated by the highly abundant isotope ^{16}O.

2.2 The SOFT hodoscope

The Scintillating Optical Fiber Trajectory (SOFT) hodoscope was built at Washington University and is created from ∼10,000 polystyrene fibers doped with scintillating dye. Each fiber is 180 μm square with 10 μm of acrylic cladding on each side. The cladding on each fiber is coated in a black ink to prevent optical coupling between neighbors. The fibers are laid parallel to one another to create a single plane with an active area of 26 cm x 26 cm. Two orthogonal planes (x and y) at the top of

the instrument serve as the trigger layer. Six additional planes, each orthogonal to the prior plane, form three xy layers used to determine the trajectory of incident particles.

In each plane the fibers are bonded together into a 3 mm x 24 mm rectangular output, which at each end is coupled to the face of an image intensifier. A 244 x 550 pixel charge-coupled device (CCD) coupled to each image intensifier records the lit pixels. Even though there are two image intensifier/CCD systems, only one has been used for readout (with the other assembly serving as a backup should the primary camera system fail). The arrangement of the fiber planes is shown in Figure 2.4.

2.3 Silicon solid-state detector system

After passing through the SOFT hodoscope, incident cosmic rays will enter one of four telescopes of stacked silicon detectors. These detectors measure the energy loss of charged particles, with the deposited energy used to determine their charge and mass according the dE/dx versus E' technique described in Section 2.1. Each wafer is $\sim$3 mm thick and cylindrical in shape, with a diameter of 10 cm. These detectors were produced using the lithium compensation technique (Allbritton et al. 1996), which yielded nearly pure silicon wafers.

A single telescope is composed of 15 wafers arranged to form 9 separate detectors; six detectors (E3-E8) are made of electrically-paired wafers, each with a combined thickness of $\sim$6 mm (see Figure 2.4). Preflight testing found that the surface of each

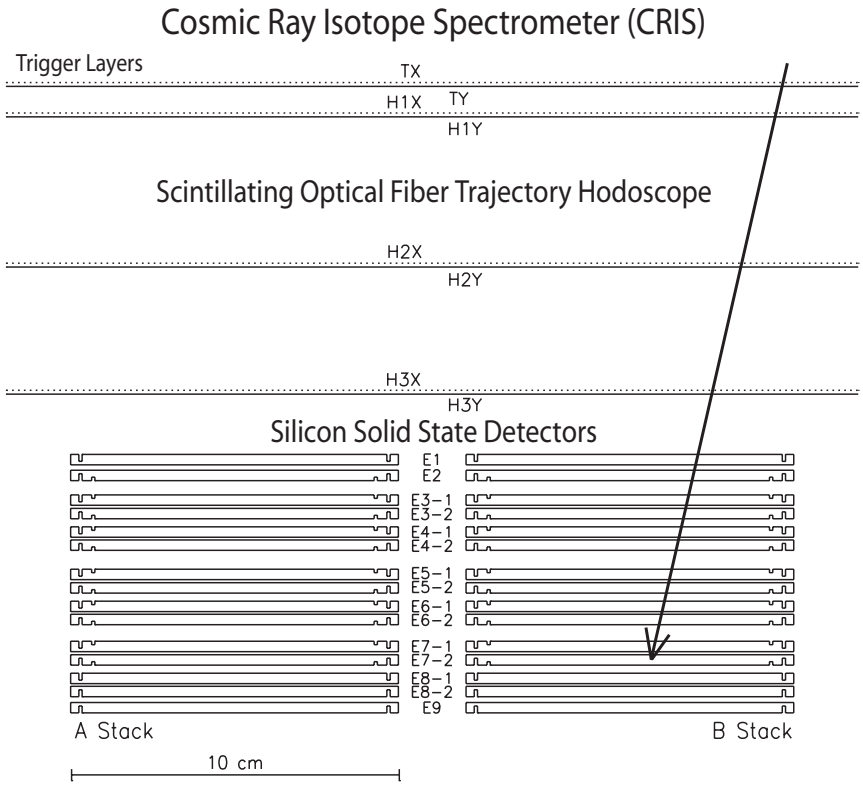

Figure 2.4: Cross section of the CRIS instrument. Particle trajectories are determined using three xy layers of scintillating optical fibers, with a fourth xy layer at the top of the instrument providing the trigger signal. Below the fiber hodoscope are four circular silicon solid-state detector stacks (2 of the 4 are shown here). The arrow represents the trajectory of a particle that stops in the bottom wafer of detector E7.

wafer had a small "dead layer" of approximate thickness between 55-70 μm, which was mostly likely caused by heavily lithiated regions in the silicon. Therefore, the arrangement of the wafers in each stack was chosen so that these dead layers were located at the top and bottom of each pair of wafers; Section 3.1.2 addresses our treatment of these dead layers during data selection.

Each wafer has a single outer groove used to mount it to the stack frame, while the inner 11 wafers in each telescope (corresponding to detectors E2-E7) have a second

inner groove. These additional grooves provide active guard rings that are used to flag particles as they enter or exit the stack through the side. Single-grooved detectors have an active inner radius of 4.65 cm, while double-grooved detectors have an active inner radius of 4.26 cm. For this work, good events must pass through SOFT into a single telescope and stop inside detectors E2-E8 without coming within 0.5 mm of the guard rings (additional information on these restrictions may be found in Section 3.1.1).

Data from the silicon detector stacks are read out using 32 pulse-height analyzers (PHAs). Each of the four E1 detectors is read out by separate PHAs. For detectors E2-E9, two telescopes are paired and their signals summed, with each telescope pair read out by one PHA (for a total of 16 PHAs). The signals in the guard rings in detectors E2-E7 are also summed between pairs of telescopes, with each pair read out by one PHA (for a total of 12 PHAs).

2.4 CRIS data output

Most data sent down by CRIS are "events" that contain the trajectory and pulse height information for a single detected nucleus. Valid events must produce a signal in the SOFT trigger plane and penetrate to at least detector E2 in one of the silicon stacks. For each of these events, the CRIS microprocessor reads a 12-bit pulse height from all silicon detectors PHAs with signals higher than the low-level discriminator threshold, and the SOFT video data (positions and intensities in the hodoscope layers

for every pixel above the threshold). The pixel data are used to identify the two brightest "clusters" (contiguous groups of bright pixels) in each fiber layer and at most six additional clusters, for a maximum of 18 clusters per event. Events, which have variable lengths from 31 to 162 bytes, are compressed onboard and sent to the ground in the 464-bits/second telemetry rate.

A smaller fraction of the data is information categorized as "housekeeping" or "diagnostic" measurements. Voltages, currents, temperatures, and trigger rates for each fiber plane (and the coincidence of the trigger planes) are recorded. Livetime rates are determined separately for species with charge Z=1, Z=2, and $Z \geq$3. These data, which can be used to identify potential instrument problems, are all multiplexed over a 256-second instrument cycle and sent to the ground.

Chapter 3

Data Analysis

The data selected for this dissertation have undergone rigorous selection criteria to guarantee the most accurate energy spectra and relative abundances. Data from the SOFT hodoscope were used to calculate the trajectories of particles, while the silicon detectors recorded the energy losses of particles as they passed through the instrument. Combining the information from the hodoscope and silicon detectors, we are able to determine the charge, mass, and incident energy of cosmic rays that stopped in the detectors. Using Monte Carlo techniques we calculated the instrument's geometrical acceptance as a function of the penetrated range in each detector. The energy spectra presented here were corrected for fragmentations that may have occurred in the instrument and the efficiency of the hodoscope.

In this chapter we present the CRIS elemental energy spectra and relative abundances for cosmic-ray species with nuclear charge $5 \leq Z \leq 28$. We consider only those particles that stop in detectors E2-E8 (see Section 2.3), covering an energy range of $\sim 50 - 500$ MeV/nucleon. Since the ACE spacecraft has been operational for 14 years, we have data that cover two solar minima and one solar maximum period of

the ∼23-year solar cycle. This work will focus on presenting and utilizing the solar minima data, though we have included our improved results from the solar maximum period in Appendix B.

3.1 CRIS data selection

On-board the spacecraft, events are sorted into 61 prioritized data buffers based on a rough nuclear charge estimation ($Z = 1$, $Z = 2$, $3 \leq Z \leq 9$, and $Z \geq 10$, determined solely by the triggers of low, medium, and high thresholds for the stack detector discriminators), the final detector penetrated, and the quality of the hodoscope data used to determine their trajectories (Stone et al. 1998a). Once sent down, these events are subjected to a rigorous set of cuts and calculations to extract an initial set of usable data. This is done using the `xpick` routine (version 1.16) developed at Caltech (see Section 3.1.1). Any additional data cuts or corrections are implemented in special programming developed by the user; Sections 3.1.2 and 3.1.3 describe the selections used for this work.

3.1.1 Data selection using `xpick`

We first used `xpick` to select our initial pool of data by choosing the data buffers appropriate for analysis. For this work we selected data from buffers 55-62 (see Table 12 in Stone et al. (1998a)), which included those events with nuclear charge $Z \geq 3$ stopping in detectors E2-E8 that had signals in at least five of the six SOFT

fiber planes and no hazard flags (which removes events that trigger within 130 ms of another event).

The first cut, GOOD_TRAJ, checks that a good trajectory can be found using the signals in the hodoscope layers. Events will fail this cut if (1) they do not have at least six 'blobs' in the hodoscope layers (three x- and y-coordinates are required to compute a trajectory), (2) there is at least one missing coordinate in layers 2 and 3, (3) there are no coordinates in layer 1, (4) the trajectory projects to the fiber bundles, (5) the x- or y-coordinates cannot be fit with a straight line (where coordinate 2 is more than 0.5 mm from the straight line defined by coordinates 1 and 3), and (6) no trajectory is found even when coordinate 'hopping' is considered (upon striking the solid matrix of the microchannel plate, photoelectrons may hop to nearby channels that can be up to several hundred microns away; this is especially problematic for the lightest species since there are fewer photoelectrons per event than for the heavier species).

About 43% of the initial dataset is removed by the GOOD_TRAJ cut, with ∼92% of these rejected events belonging to the data buffers for charges $3 \leq Z \leq 9$. If we were to estimate the charge of these events using a normal-incidence trajectory, more than 75% of these events would have charge $Z < 5$. The true charge of these events will almost always be less than this estimated charge, so we can be confident that the particles rejected by this cut are among the lightest cosmic rays, and CRIS is most inefficient at detecting these species (see Figure 3.6). We also note that there is a range dependence for this cut. For species with charge $3 \leq Z \leq 9$, ∼55% of the

rejected particles stopped in E2, ∼50% stopped in E3-E7, and ∼40% stopped in E8; for species with charge $Z \geq 10$, ∼27% stopped in E2, ∼20% stopped in E3-E4, and ∼16% stopped in E5-E8.

After making the cut on GOOD_TRAJ, we then removed those events where the SOFT coordinates were more than 5σ from the straight line trajectory through the hodoscope (DX_NORM and DY_NORM). To ensure that particles only passed through the active areas of the instrument, we also cut events with trajectories that were within 0.5 mm of the edge of the SOFT trigger plane (MARGIN_SOFT_TRIG), the guard rings at the top of detectors E1 and E2 (MARGIN_E1 and MARGIN_E2), and the guard ring at the top of the detector following the stop detector (MARGIN_NEXT). Note that we do not use the guard ring signals to eliminate these particles. In our analysis we noted that some events which stopped in E7 had trajectories that passed outside of the active area of E7 but were within the active area of E8 (this is due to the larger active area of detector E8; see Figure 2.4). We excluded these particles from our analysis by requiring that E7 events had trajectories that did not pass within 0.5 mm of the active radius of E7 at the top of E8.

After checking that the particles had valid trajectories, we used the silicon detector pulse height information to perform a charge consistency check for particles stopping in detectors E3-E8 (particles stopping in E2 have only one charge estimate, and therefore cannot be subjected to this test). This calculation helped remove from the dataset any events that fragmented in the silicon detector stacks. We first obtained charge estimates (see Section 2.1) using three different combinations of de-

tectors: (1) detector E1 as ΔE and all of the remaining detectors through the stop detector as E' (ZEST_E1), (2) the detector preceding the stop detector as ΔE and the stop detector as E' (ZEST_LAST), and (3) all detectors preceding the stop detector as ΔE and the stop detector as E' (ZEST). We then calculated the ratios ZEST_E1/ZEST and ZEST_LAST/ZEST, subtracted from them the mean of their empirically-derived distributions (which are a function of charge, range, and detector stack), and then divided each by the standard deviation of their distribution. If either of these normalized charge consistency ratios was greater than 10σ we rejected the event; the combination of these two cuts removed $\sim$12% of the dataset. Depending on the detector stack and the range, these cuts corresponded to charge estimates with a difference of 0.2-0.4 charge units for a carbon nucleus, and a difference of 0.5-0.8 charge units for an iron nucleus.

The selections made with `xpick` remove $\sim$68% of the events from chosen data buffers. Table 3.1 summarizes the parameters used in the cut set for this work. For each cut, the percentage of events remaining from the initial pool of data is given.

3.1.2 Geometrical cuts

Once the initial dataset was determined using `xpick`, we made two additional geometrical cuts to the data. First, we chose to remove events that entered the instrument at too large an incident angle relative to the detector normal. Multiple Coulomb scattering causes particles to deviate from the trajectories calculated using the hodoscope data, while Landau fluctuations affect the energy losses in the detectors (Stone et al.

`xpick` Cut	% of Initial Events Remaining	Usage
GOOD_TRAJ	57.0%	Selects events with valid, calculable trajectories
DX_NORM DY_NORM	56.6% 55.8%	Removes events with SOFT coordinates more than 5σ from their straight-line trajectory
MARGIN_E1 MARGIN_E2 MARGIN_NEXT MARGIN_SOFT_TRIG	54.3% 52.8% 37.3% 36.4%	Removes events passing $\leq$5 mm from the edge of an individual detector element
ZRAT_E1_NORM ZRAT_L_NORM	32.5% 32.0%	Removes events that fail the charge consistency checks

Table 3.1: CRIS `xpick` data selections for this analysis. The initial dataset was selected from buffers 55-62, which included $Z \geq 3$ particles stopping in detectors E2-E8. These events did not occur within 130 ms of another event, and were not stimulated diagnostic events. The data in these buffers represent $\sim$34% of the total number of events detected by CRIS (most of which are hydrogen and helium events). These cuts are described in greater detail in Section 3.1.1.

1998a). Both of these processes affect the mass resolution, causing it to decrease with increasing path length (and therefore incident angle). Ogliore (2006) studied the effects of each of these contributions and determined that incident angles $< 25^\circ$ yielded the highest resolution data, with a recommended cut-off at a maximum of 50°. We have chosen to accept only those events with incident angles $\leq 30^\circ$.

The second geometrical cut concerns the calculated depth (Section 2.1) for a particle stopping in a given detector. On one face of every silicon wafer is a surface dead layer ($\sim$60 μm) where the deposited energy is partially lost. Since the pulse height data are used to determine the charge, mass, and incident energy of a particle, and this information is used to calculate its range in the instrument, the missing information causes a slight miscalculation of the particle's final depth. This is most

prominent for particles stopping in the vicinity of a dead layer at the top of a detector, since the majority of the energy deposited in that detector (E') is missing. Particles stopping in all other depths of the stop detector are only slightly affected since a small fraction of the total deposited energy is lost. This effect is easily seen as small tail regions in the charge distributions shown in Figure 3.1.

We avoid this effect by requiring that particles do not stop within 160 μm of the top or bottom surface of a detector, since in each detector stack, each pair of wafers was positioned so that the dead layers were located at the top and bottom of the pair. Therefore, the E1 dead layer is at the top of E1, the E2 dead layer is on the bottom of E2, and there are dead layers on both the top and bottom of E3-E8. Table 3.2 lists the minimum and maximum depths allowed in detectors E2-E8 after application of the 160-μm cuts.

3.1.3 Instrument performance cuts

Following the inclusion of the geometrical cuts described in Section 3.1.2, there are a few additional temporal cuts used to ensure that the instrument is operating during optimum conditions. During the quiet periods of the solar cycle the instrument "livetime" is typically $\sim$80%, with the remaining time devoted to the onboard analysis of incident cosmic rays. The solar maximum period has a higher livetime near $\sim$86% since there are fewer events recorded during each duty cycle. A noisy guard ring was responsible for the decreased livetime seen prior to January 20, 1998, which was corrected by increasing the channel threshold for that guard. For our work, we have

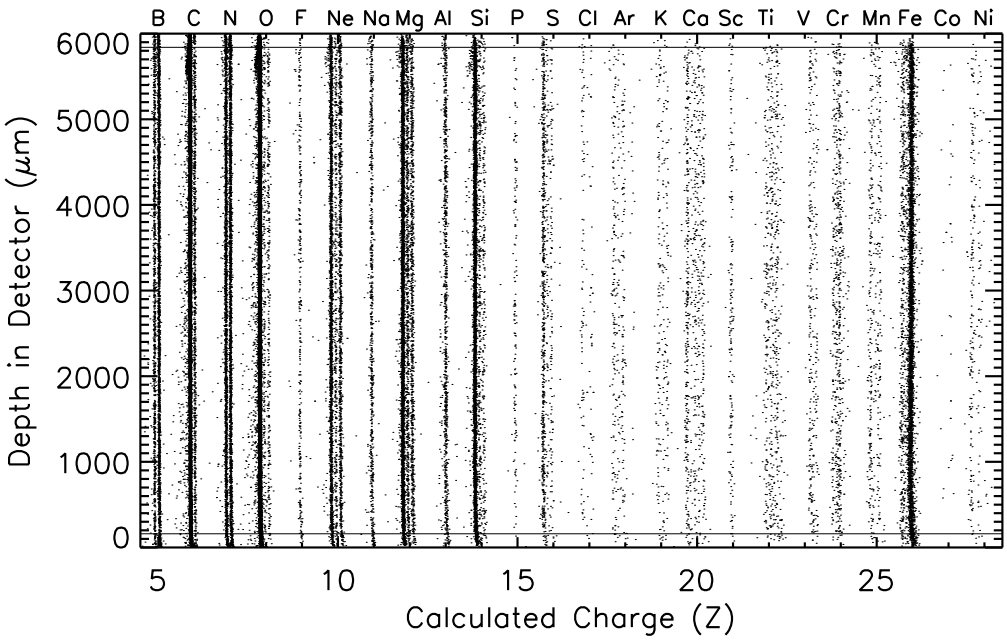

Figure 3.1: Calculated charge as a function of depth for particles stopping in the E3 detector. The horizontal lines indicate the 160 μm depth cuts from the top and bottom faces of the detector used to remove particles falling within the tail regions of the charge distributions. Particles in these regions stopped in or near the detector dead layers, where the collection of the deposited energy is inefficient.

chosen to include only those events that were recorded when the instrument livetime was above 60%. CRIS is perfectly capable of operating below this level, however including those events would require a large correction to the calculated intensities. Figure 3.2 plots the fractional livetime for all particles with charge $Z > 2$ for each of the periods of time considered in this work.

CRIS is programmed to shut down during large solar energetic particle (SEP) events, when the instrument is bombarded with large bursts of energetic particles from solar flares. The hodoscope trigger and coincidence rates, which are recorded every 256 seconds, are used to monitor the instrument for higher levels of solar activ-

Telescope	Detector	Depth in Detector (μm) Minimum	Maximum
0	2	0	2820
	3	160	5847
	4	160	5881
	5	160	5848
	6	160	5795
	7	160	5775
	8	160	5915
1	2	0	2857
	3	160	5866
	4	160	5756
	5	160	5843
	6	160	5814
	7	160	5789
	8	160	5804
2	2	0	2867
	3	160	5839
	4	160	5832
	5	160	5805
	6	160	5831
	7	160	5810
	8	160	5787
3	2	0	2806
	3	160	5813
	4	160	5890
	5	160	5789
	6	160	5848
	7	160	5779
	8	160	5865

Table 3.2: Minimum and maximum allowed depths in detectors E2-E8 after 160-μm dead layers have been removed from the measured thicknesses.

ity that could potentially saturate the image intensifiers. We implemented a limit of 10-500 triggers/second for the coincidence rate (trigger 0 AND 1) and <300 triggers/second for the E1 detector to guarantee that the instrument was not only operating at a minimum performance level, but also to ensure that SEP particles did not contaminate our dataset meant to contain only pure GCR events. The minimum SOFT

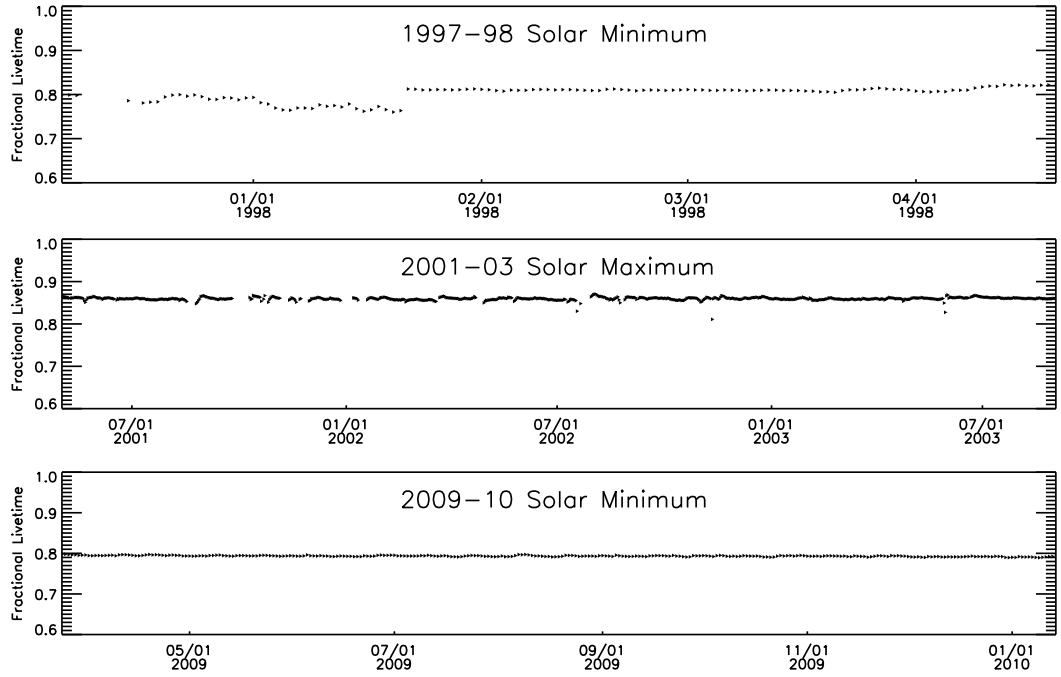

Figure 3.2: CRIS daily average fractional livetime for $Z > 2$ particles during two solar minimum periods and one solar maximum period. Missing days correspond to times when the instrument was turned off, typically for spacecraft maneuvers and solar energetic particle events. A noisy guard ring was responsible for decreased livetime prior to January 20, 1998.

coincidence rate and the E1 rate are used to remove time during SEP events when SOFT transitions from normal operation to a partially saturated state. During quiet periods of the solar cycle, the average coincidence rate is typically less than ∼100 triggers/second and the E1 rate is less than ∼50 triggers/second.

3.2 Final dataset

Our data from the first solar minimum period were selected from observations taken from December 5, 1997 through April 19, 1998. In our previous work (George et al. 2009) we used 99 earlier days of observation time for our analysis (August 28, 1997 through December 4, 1998). We have determined that the inclusion of those earlier days introduced a bias to the high-Z data that was due to a change in the discriminator threshold for the image intensifier for Camera B (which has been used exclusively throughout the mission). Prior to December 4, 1997 the threshold allowed the camera to record a larger number of pixels for each event. Heavier particles sometimes exceeded the limits on the number of allowed pixels or data segments, causing those events to be discarded from the analysis. When the threshold was raised to its current level (CAMDSC=119), we were able to record the high-Z events with higher efficiency. So we would not introduce a bias in the high-Z data, we chose to start our observations on the day following the threshold change. On April 20, 1998 there was a large solar energetic particle event and Forbush decrease, marking the end of the solar minimum conditions. From the 136-day period currently defined for this solar minimum, we removed approximately 8 days from the analysis due to solar energetic particle (SEP) events. During the remaining 128 days the instrument had an average livetime of ∼80%, giving us ∼102 days of data.

The more recent solar minimum was characterized by a long period of record-setting cosmic-ray intensities (Mewaldt et al. 2010), as seen in the CRIS oxygen

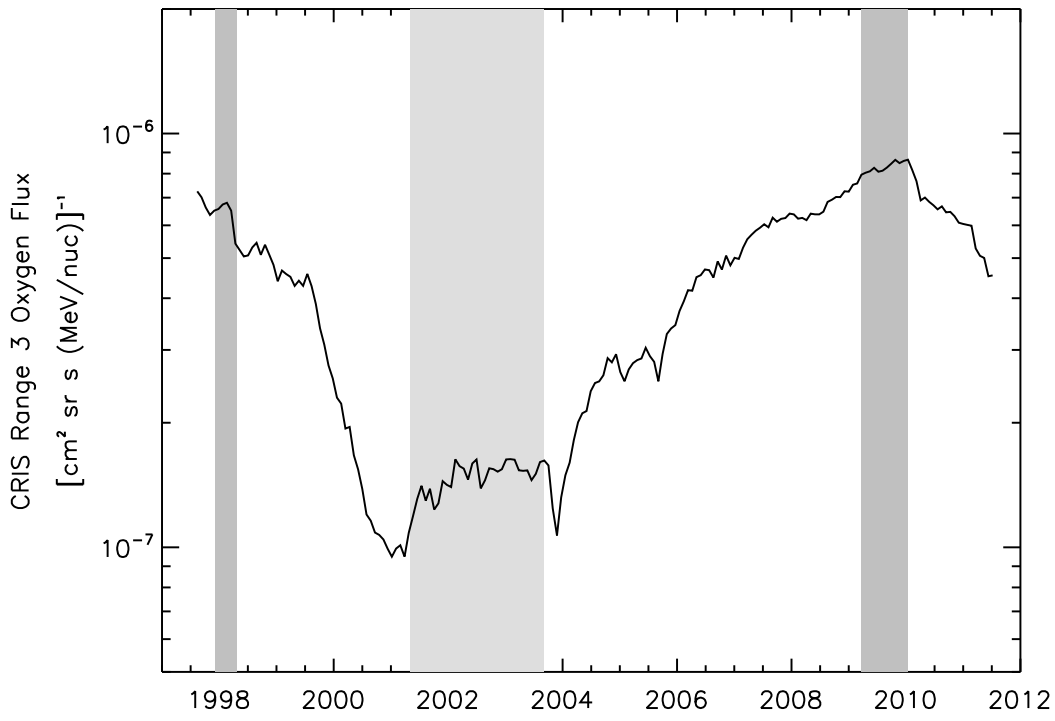

Figure 3.3: The CRIS oxygen flux, averaged over the 27-day Bartels rotation, for the duration of the mission. These data cover an energy range of 91.0-122.5 MeV/nucleon. The shaded regions indicate the beginning and end dates of the solar minimum (darker gray) and maximum (lighter gray) periods analyzed in this work.

Bartels rotation averages plotted in Figure 3.3. From the full solar minimum period we have chosen to consider only the time characterized by the highest cosmic-ray intensities, which covers 297 days from March 23, 2009 through January 13, 2010. During this time there were no SEP events, so with an average livetime of ∼79% we have ∼235 days of data for the more recent solar minimum period.

3.3 Geometry factors

The geometrical acceptance of the CRIS instrument varies according to where particles stop in the silicon detector stacks. We have used a Monte Carlo program that calculates the geometry factor as a function of depth for particles stopping in detectors E2-E8. We have reproduced the physical geometries of each stack of detectors and the SOFT hodoscope (see Sections 2.2 and 2.3). Our calculation includes our limitations on the maximum incident angle (30°), the edge cuts discussed in Section 3.1.1, and the dead layer cuts (Table 3.2).

The program was used to generate a total of 10 million particles, and each was given a random starting position and incident angle above the top of the instrument. Particles that satisfied the angle cut were propagated through the hodoscope and subjected to the SOFT edge cut. In steps of 10 μm, the remaining particles were propagated through the detector stacks to the bottom of the instrument, with the edge cuts and dead layer cuts applied along the way. This gave us over $\sim$50,000 tracks per range bin, yielding a statistical uncertainty of $<$0.5%. To account for possible systematic errors in the program, we conservatively assign an overall uncertainty of 2% to our results. Figure 3.4 shows our geometry factors $A\Omega$ (cm^2 sr) as a function of depth in the silicon detectors. The dotted lines show the geometry factors for individual ranges, while the solid line represents the total geometrical acceptance.

By using the range-energy relation (Equation 2.2), the endpoints of the individual geometry factors can be used to determine the minimum and maximum energies for

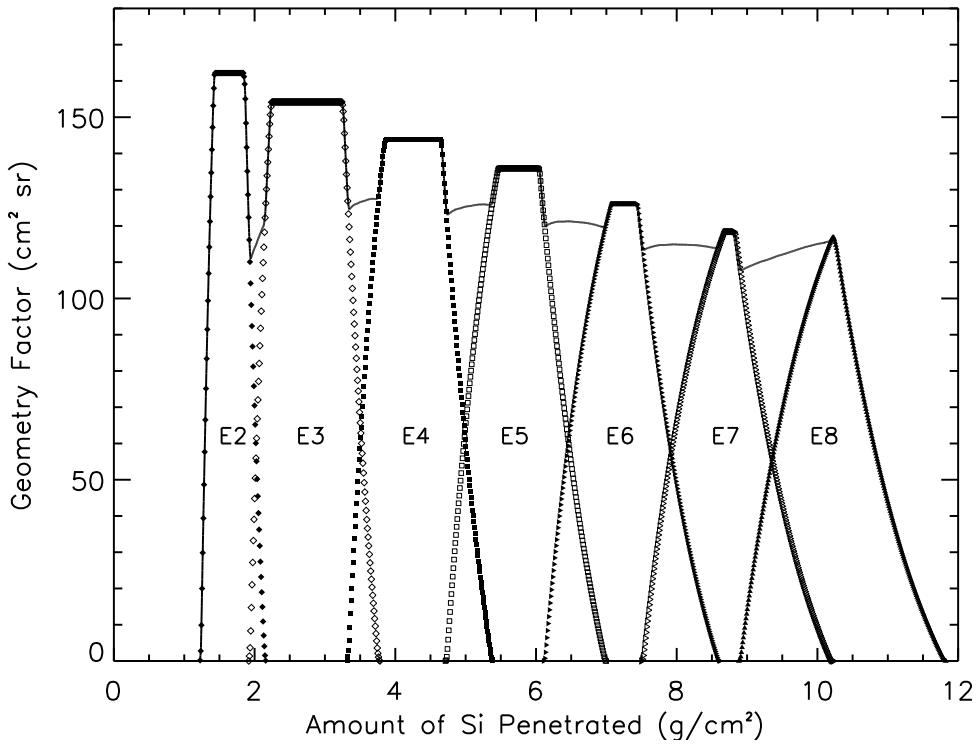

Figure 3.4: The CRIS geometry factor as a function of depth in the silicon detectors. The solid line plots the total geometrical acceptance of the instrument. The dotted lines with symbols show the contributions to the total geometry factor for particles stopping in individual detectors. The drops between detectors are due to the 160-μm dead layer cuts.

particles stopping in the detectors. These energies are calculated for each isotope, weighted according to the isotopic abundance, and summed to find the energy endpoints for each element. Even for relatively large uncertainties (10%) in the isotopic composition, the calculated energies for each element are negligibly affected. The central energy, or arithmetic mean of the energy endpoints, for particles stopping in a given detector is then used when plotting the energy spectra. Using these calculated

energies and geometry factors, we define the quantity

$$\Gamma = \int A\Omega d\varepsilon \, , \tag{3.1}$$

where the integral is taken over the energies of the particles that stop in the given detector.

3.4 Fragmentation correction

Incident cosmic rays may suffer nuclear interactions as they pass through the CRIS hodoscope or silicon detectors. Most of these particles are eliminated from our analysis due to consistency cuts performed during our initial selection of data (Section 3.1). Therefore, we need to take into account the number of particles thus eliminated when we calculate the intensities and abundances at the top of the instrument.

To calculate the survival probability, we need to determine the amount of material a particle traverses. A particle will first travel through the hodoscope, which we will approximate is made of aluminum and scintillator material (see Table 4 in Stone et al. (1998a) for a listing of all the materials and their thicknesses). After passing through the hodoscope the particle will enter the silicon detector stacks and stop. For the calculation, we will make a second approximation that the particles stop at the middle depth of a detector. Therefore, the total amount of material traversed is the sum of the hodoscope thickness and the silicon thickness up to the stop depth, corrected for the incident angle (here we use the average secant of the angle as a

function of range, which corresponds to angles between 19.7° and 20.7°).

The probability that a particle with nuclear charge Z will survive without interacting in the CRIS instrument is given by:

$$\epsilon_{spall}(Z,D) = \sum_{i=isotopes} w(Z,A_i) exp\left(-\frac{t_{Al}}{\Lambda_{Al}(A_i)} - \frac{t_{scint}}{\Lambda_{scint}(A_i)} - \frac{t_{Si}(D)}{\Lambda_{Si}(A_i)}\right) , \quad (3.2)$$

where t_{Al} is the thickness of aluminum, t_{scint} is the thickness of scintillator material, $t_{Si}(D)$ is the amount of silicon traversed if the particle stops in the middle depth of detector D (D=E2,E3,...,E8), and $\Lambda_{Al}(A_i)$, $\Lambda_{scint}(A_i)$, and $\Lambda_{Si}(A_i)$ are the interaction lengths in aluminum, scintillator, and silicon. The material thicknesses used here are the actual thicknesses divided by the cosine of the average angle. Since we are interested in an average correction factor for a given Z, we perform a summation over all its isotopes i (with atomic weights A_i). Each contributing term is weighted according to its isotopic fraction observed by CRIS, $w(Z,A_i)$.

For a nucleus with mass A_i (g/mol), the interaction length (g/cm^2) in a target material with mass A_T (g/mol) is given by

$$\Lambda(A_i) = \frac{A_T}{N_{Av}\sigma(A_i,A_T)} , \quad (3.3)$$

where N_{Av} is Avogadro's number and $\sigma(A_i,A_T)$ is the total mass-changing cross section (cm^2). We have chosen for the cross sections the mass-changing interaction

parameterization given by Webber et al. (1990c):

$$\sigma(A_i, A_T) = \pi r_o^2 (A_i^{1/3} + A_T^{1/3} - b)^2 \,, \tag{3.4}$$

with $r_o = 1.47$ fm and

$$b = 1.36 - (0.018 A_T) - (0.065 A_i^{1/3} A_T^{1/3}) \,. \tag{3.5}$$

Here we have not included the Letaw energy dependence (Letaw et al. 1983) recommended by the authors for the cross sections at low energies since that term is only valid for hydrogen and helium targets.

Survival factors for particles stopping in detectors E2-E8 are plotted in Figure 3.5 as a function of nuclear charge. The values range from ∼96% for boron in detector E2 to ∼60% for nickel in detector E8. We assigned to the interaction cross sections a 10% uncertainty, which yields <1% uncertainty for the survival factions of nuclei stopping in the top silicon detectors, and ∼3-6% uncertainty for nuclei stopping in the bottom silicon detectors.

In using this correction, we assumed that all particles suffering charge- or mass-changing interactions were eliminated from the analysis. This is likely true for charge-changing interactions since the stripped-off nuclei will penetrate deeper into the instrument, leading to event rejection based on the multiple charge estimates discussed in Section 3.1.1 or due to one fragment penetrating the E9 detector. However, we

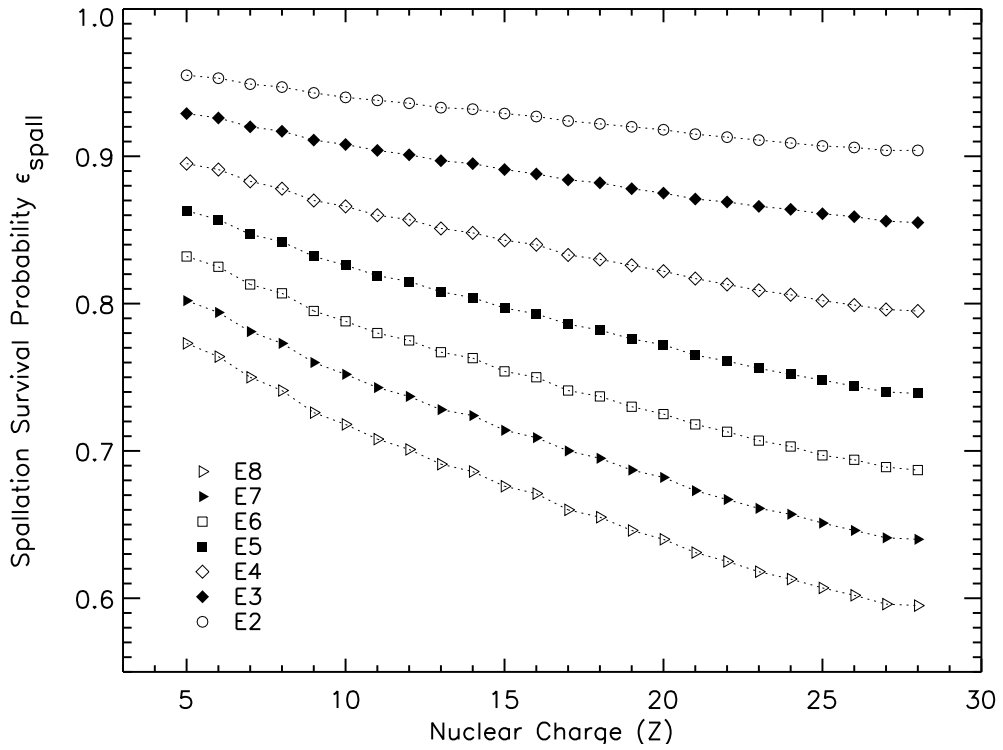

Figure 3.5: Spallation survival probability as a function of nuclear charge. These correction factors are specified for particles stopping in CRIS detectors E2-E8.

do not expect all mass-changing interactions to be recognized, especially when only one or two neutrons are stripped from the incident nucleus. In assigning the 10% overall uncertainty, we include our uncertainty in the number of events that should have been removed but still remain in the analysis.

3.5 Hodoscope efficiency correction

Though the SOFT hodoscope is an efficient means of determining the trajectory of particles as they enter the CRIS instrument, it is possible that some nuclei are not properly detected. An incident nucleus that passes through the acrylic cladding sur-

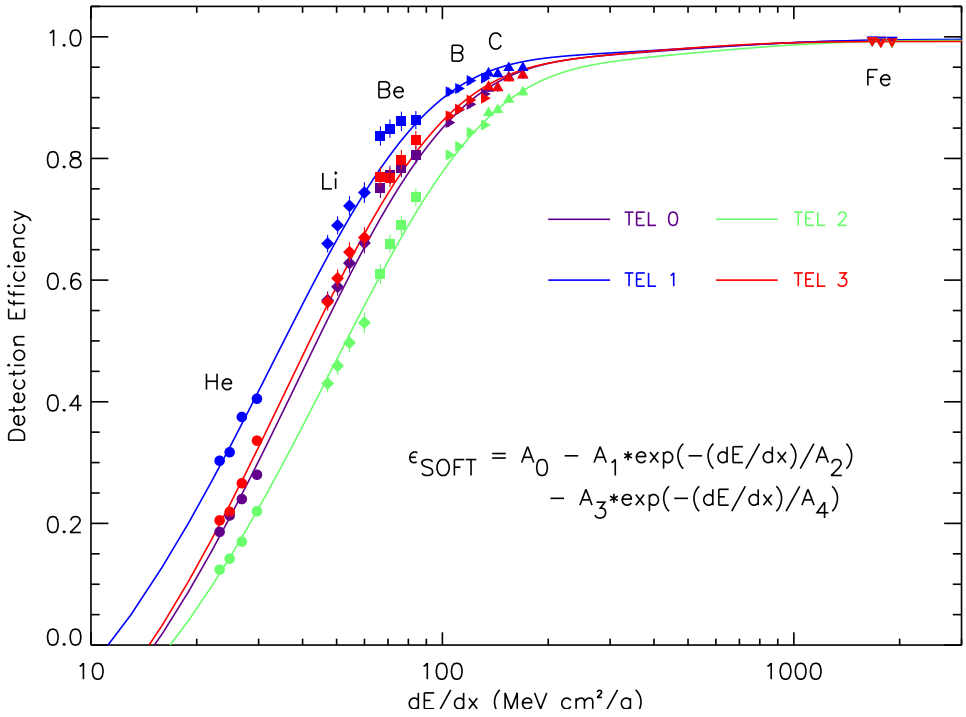

Figure 3.6: SOFT hodoscope efficiency by telescope for select cosmic-ray species stopping in detectors E5 (right-most data points) through E8 (left-most data points). The corrections are parameterized by the energy loss in silicon at the top of the instrument. The solid lines represent fits to the data and their functional forms are given by the equation, with the coefficients A_0 through A_4 given in Table 3.3. These data, which are reproduced with the permission of de Nolfo (2010), were previously used in the work of de Nolfo et al. (2006).

rounding a fiber will produce a signal from knock-on electrons which is much weaker than the strong signal produced when it passes through a fiber. More importantly, signal attenuation in the fibers results in fewer photons reaching the image intensifier. This effect is most significant for low-Z particles that produce weak signals. Both of these effects can cause a mis-identification of the particle's trajectory and possibly its rejection as a valid event due to a failure in detecting the signal in one or more fiber planes.

$$\epsilon_{SOFT} = A_0 - A_1 * e^{-(dE/dx)/A_2} - A_3 * e^{-(dE/dx)/A_4}$$

Telescope	A_0	A_1	A_2	A_3	A_4
0	0.995	1.402	38.76	0.049	422.4
1	0.996	1.347	32.80	0.041	490.4
2	0.994	1.325	48.16	0.062	468.0
3	0.992	1.404	36.23	0.059	298.4

Table 3.3: Parameterization of the SOFT hodoscope efficiencies given by telescope, plotted as solid lines in Figure 3.6.

The hodoscope efficiencies were calculated by de Nolfo (2010) by determining the fraction of observed events that have valid trajectories using only the silicon detector pulse height data. The analysis was restricted to those events stopping in detectors E5-E8 whose incident angles were within 30°, since for these angles some of the most abundant elements could be resolved without knowing the hodoscope trajectory information. These efficiencies were previously used in the work of de Nolfo et al. (2006).

Figure 3.6 plots the correction factors calculated for each telescope, parameterized by the energy loss in silicon at the top of the instrument. We have included fits to the data for each of the four telescopes (solid lines), given by the indicated equation and the parameters listed in Table 3.3, which allows us to determine the efficiencies for those species not shown. Telescope 1 has the highest efficiency since it is located closest to the active camera, with better than 90% efficiency in all ranges for all species with $5 \leq Z \leq 28$. Telescope 2, being farthest from the camera, has the lowest efficiency with 78% for range 8 boron; however, this improves to greater than 94% for species heavier than nitrogen. We used these parameterizations to calculate the

average efficiency for the whole instrument, which we then used to correct the calculated energy spectra. We assign a 2% uncertainty to these values due to systematics in the method used to determine these efficiencies.

This calculation used CRIS data collected prior to 2004. Recently de Nolfo (2010) recalculated the range 5 efficiencies for telescopes 1 and 2 using data from the more recent solar minimum period. While there was no evidence that the efficiency for telescope 1 had changed, there was a 2-3% decrease in the efficiency for boron and carbon in telescope 2. Further work must be done to determine the appropriate parameterization for the more recent solar minimum period. However, since the efficiencies for all four telescopes converge to high values for species heavier than carbon, we can avoid this problem by simply excluding from the 2009-10 dataset the boron and carbon events from telescope 2. Both species are quite abundant, so the loss of statistics will not be detrimental to our results. For the 1997-98 solar minimum (which has lower statistics for all species) the parameterizations are known, so we have chosen to keep the data from all four telescopes.

3.6 Intensity and composition

For the i^{th} cosmic-ray species the differential intensity, $(\frac{dJ}{dE})_i$, at the top of the CRIS instrument is given by:

$$\left(\frac{dJ}{dE}\right)_i = \frac{N_i}{\Gamma_i \, \epsilon_{spall,i} \, \epsilon_{SOFT,i} \, t_{live}} \, . \tag{3.6}$$

Here N_i is the number of counts of species i, Γ_i is the geometry factor integrated over energy (Equation 3.1), $\epsilon_{spall,i}$ is the spallation survival probability (Equation 3.2), $\epsilon_{SOFT,i}$ is the efficiency of the SOFT hodoscope (see Figure 3.6 for the parameterization), and t_{live} is the active exposure time. The total uncertainty is calculated by combining in quadrature the statistical and systematic uncertainties:

$$\sigma_{\left(\frac{dJ}{dE}\right)_i} = \left(\frac{dJ}{dE}\right)_i \sqrt{\left(\frac{\sigma_{N_i}}{N_i}\right)^2 + \left(\frac{\sigma_{\Gamma_i}}{\Gamma_i}\right)^2 + \left(\frac{\sigma_{spall,i}}{\epsilon_{spall,i}}\right)^2 + \left(\frac{\sigma_{SOFT,i}}{\epsilon_{SOFT,i}}\right)^2} . \tag{3.7}$$

The CRIS energy spectra for both solar minimum periods are presented in Section 3.7.1 and tabulated in Appendix A (Tables A.1 and A.2).

From the energy spectra we may also compute ratios of secondary and primary species as a function of energy. For a given energy $E^{'}$, the ratio is given by:

$$\frac{\left(\frac{dJ(Z_1,E^{'})}{dE}\right)}{\left(\frac{dJ(Z_2,E^{'})}{dE}\right)} = f\frac{N_1}{N_2} , \tag{3.8}$$

where N_1 and N_2 are the number of counts of species 1 and 2, and f takes into account the differences in geometry factor, energy interval, spallation survival probability, and SOFT efficiencies. Since the CRIS energy bands are different for each species and each detector, the spectra must be interpolated to a common energy grid. For this work we used a linear interpolation between adjacent data points in $\log(Intensity)$ versus $\log(Energy/nucleon)$, with the results tabulated in Appendix A (Tables A.3 and A.4). For some species, small extrapolations at the minimum or maximum energies

were included. Statistical uncertainties on the interpolated data are determined by a linear interpolation of the number of events in the adjacent energy bins, while systematic uncertainties are assigned the same value as the measured point closest in energy to the interpolated data point. These interpolated intensities are used to calculate the B/C and $(Sc + Ti + V)/Fe$ ratios, which are presented in Chapters 4 and 5 and are used to test various cosmic ray transport models.

Relative abundances have been determined by fitting a parabola to each spectrum in $\log(Intensity)$ versus $\log(Energy/nucleon)$ and taking ratios of the fits at a single energy. Letting $y_i = \ln(I_i)$ and $x = \ln(E) - \ln(E_o)$, the intensity for the i^{th} species at energy E according to the quadratic fit is given by:

$$y_i = a_i + b_i x + c_i x^2 \,, \tag{3.9}$$

where a_i, b_i, and c_i are the fit coefficients. At the interpolation energy $E = E_o$, $x = 0$ and $y_i = a_i$, which yields $I_i = exp(a_i)$. The statistical uncertainty on I_i is determined by the uncertainty on the fit coefficient a_i. This is found by calculating $C_i[1,1]$, the first diagonal element of the correlation matrix (Bevington and Robinson 2003).

If a species has insufficient statistics to achieve a good fit to the data, a nearby element can be used as a template for the shape and only the overall normalization is fit. In this work, only Cl and Co in the 1997-98 solar minimum required a template to fit the shape. Using the same definitions for x and y as used above, we may calculate

the intensity at energy E using:

$$y_i = a_t + b_t x + c_t x^2 + d_i \,, \tag{3.10}$$

where a_t, b_t, and c_t are the fit coefficients from the template, and d_i is the normalization coefficient. At $E = E_o$, $y_i = a_t + d_i$, which yields $I_i = exp(a_t + d_i)$. The statistical uncertainty on I_i is the quadratic sum of the uncertainties on a_t and d_i (where we use the standard deviation of the fit to the data).

The systematic uncertainties on these intensities are taken to be the same as the measured data point closest in energy to E_o. For the ratios of adjacent elements, the residual systematic uncertainties tend to cancel. In most cases, the systematic uncertainties are larger than the statistical uncertainties owing to the large number of events recorded for each species in each solar minimum period.

3.7 CRIS solar minimum results

We present the CRIS solar minimum energy spectra (Section 3.7.1) and abundances relative to silicon (Section 3.7.2) for the two periods of solar minimum defined in Section 3.2. For each species, the energy spectra were calculated (using Equation 3.6) at seven unique energies corresponding to those particles stopping in detectors E2-E8. Relative abundances were computed with Equation 3.8 at 160 MeV/nucleon, with the data normalized such that Si≡1000.

3.7.1 CRIS energy spectra

Figures 3.7 through 3.10 present the CRIS energy spectra. For each species, both solar minimum spectra are plotted in the same panel to allow for direct comparison of the shape and intensity over the two time periods. The data plotted here are tabulated in Appendix A in Tables A.1 and A.2. We have also interpolated the data to a common energy grid, given in Tables A.3 and A.4, with our method and uncertainties described in Section 3.6. Vertical dotted lines are drawn at 160 MeV/nucleon to indicate where the relative abundances were calculated.

The solid and dashed lines represent the quadratic fits in $\log(Intensity)$ versus $\log(Energy/nucleon)$ to the seven data points. For the 1997-98 chlorine and cobalt spectra we did not have sufficient statistics to yield a good fit to the data, so we used sulfur and manganese as templates for the shapes and only the overall normalization was fit.

3.7.2 CRIS composition

CRIS abundances relative to silicon were calculated at 160 MeV/nucleon following the calculation described in Section 3.6. Table 3.4 gives the relative abundances for both solar minimum periods, with the data normalized such that Si≡1000; only statistical uncertainties are given. The absolute intensities for silicon at 160 MeV/nucleon are also given. As expected, our results show good agreement between the two solar minima.

Element	1997–1998	2009–2010
B	1824.5± 25.7	1758.8± 17.2
C	7329.7± 31.1	7339.0± 21.3
N	1726.9± 13.9	1700.3± 8.3
O	7127.7± 28.3	7198.1± 17.0
F	100.2± 3.4	98.1± 2.0
Ne	1012.3± 10.8	1005.6± 6.4
Na	191.2± 4.6	186.0± 2.7
Mg	1378.7± 11.9	1379.6± 7.1
Al	199.7± 4.4	203.6± 2.6
Si	1000.0± 9.2	1000.0± 5.5
P	26.7± 1.4	26.7± 0.9
S	155.9± 3.4	157.2± 2.0
Cl	26.1± 1.7	24.9± 0.8
Ar	58.2± 2.0	55.1± 1.2
K	39.9± 1.7	40.1± 1.0
Ca	125.9± 3.1	118.9± 1.8
Sc	27.4± 1.4	25.3± 0.8
Ti	102.4± 2.9	100.5± 1.7
V	46.0± 2.0	48.1± 1.2
Cr	100.5± 3.1	99.1± 1.9
Mn	63.2± 2.6	61.9± 1.5
Fe	673.3± 9.0	671.0± 5.4
Co	4.4± 0.4	3.7± 0.4
Ni	31.6± 2.2	29.9± 1.3

Table 3.4: CRIS solar minimum relative abundances at 160 MeV/nucleon, normalized to Si≡1000. Only the statistical uncertainties are given. The absolute intensity for silicon at 160 MeV/nucleon is (110.1 ± 3.6)x10^{-9} (cm^2 s sr MeV/nucleon)$^{-1}$ for the 1997-98 solar minimum, and (134.8 ± 4.3)x10^{-9} (cm^2 s sr MeV/nucleon)$^{-1}$ for the 2009-10 solar minimum.

From Table 3.4, we see that there is less than a 2σ difference between the relative abundances for nearly all of the species. The three exceptions are for boron (2.1σ), oxygen (2.1σ), and calcium (2.0σ). For boron, the difference may be due to a lower hodoscope efficiency in the more recent solar minimum (the same parameterization was used for both solar minima; see Section 3.5 for details). It is also possible that there are some spectral differences, since our measurements for each solar minimum

correspond to slightly different interstellar energies. However, since the difference is only 2.1σ we will not investigate this any further.

The probability of having a 2σ difference in the measurements is $\sim$5%, or 1 out of the 24 species considered here. If we neglect the difference for boron, that means two species (oxygen and calcium) out of 24 have relative abundances that are different by 2σ, which corresponds to $\sim$8% of the species. This is reasonable, especially considering the small sample size.

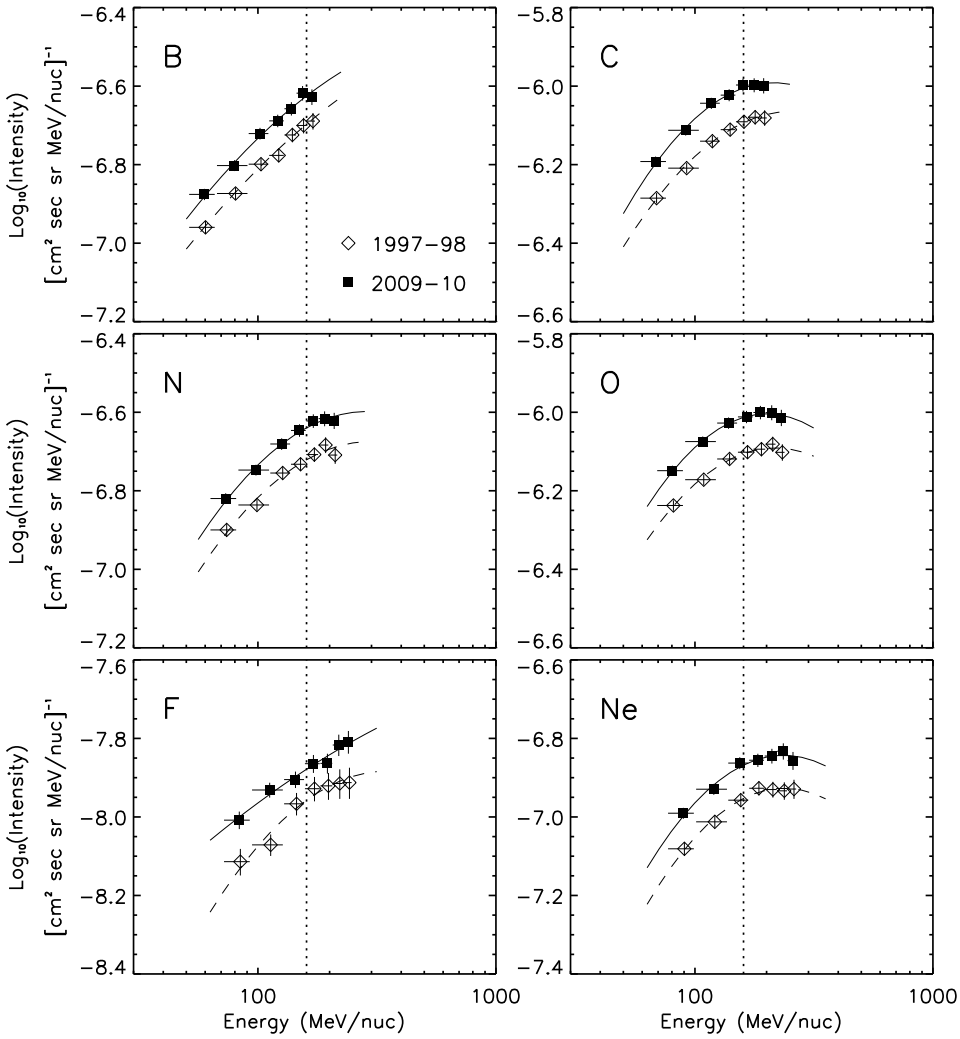

Figure 3.7: CRIS energy spectra for boron through neon. Results from both solar minima are shown to allow for direct comparison of the data. The solid and dashed lines represent quadratic fits to the data. The vertical lines at 160 MeV/nucleon indicate the energy at which the relative abundances were calculated. The data shown here are tabulated in Tables A.1 and A.2 in Appendix A.

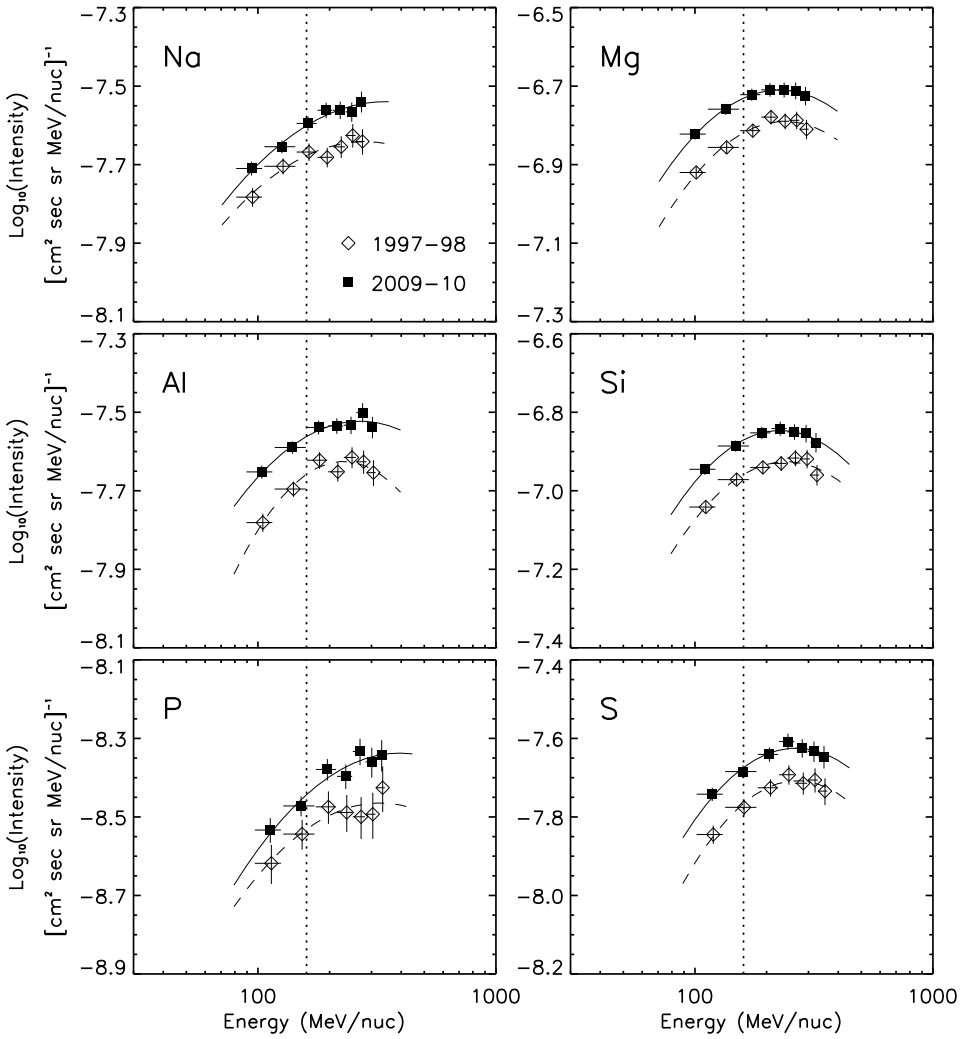

Figure 3.8: CRIS energy spectra for sodium through sulfur. Results from both solar minima are shown to allow for direct comparison of the data. The solid and dashed lines represent quadratic fits to the data. The vertical lines at 160 MeV/nucleon indicate the energy at which the relative abundances were calculated. The data shown here are tabulated in Tables A.1 and A.2 in Appendix A.

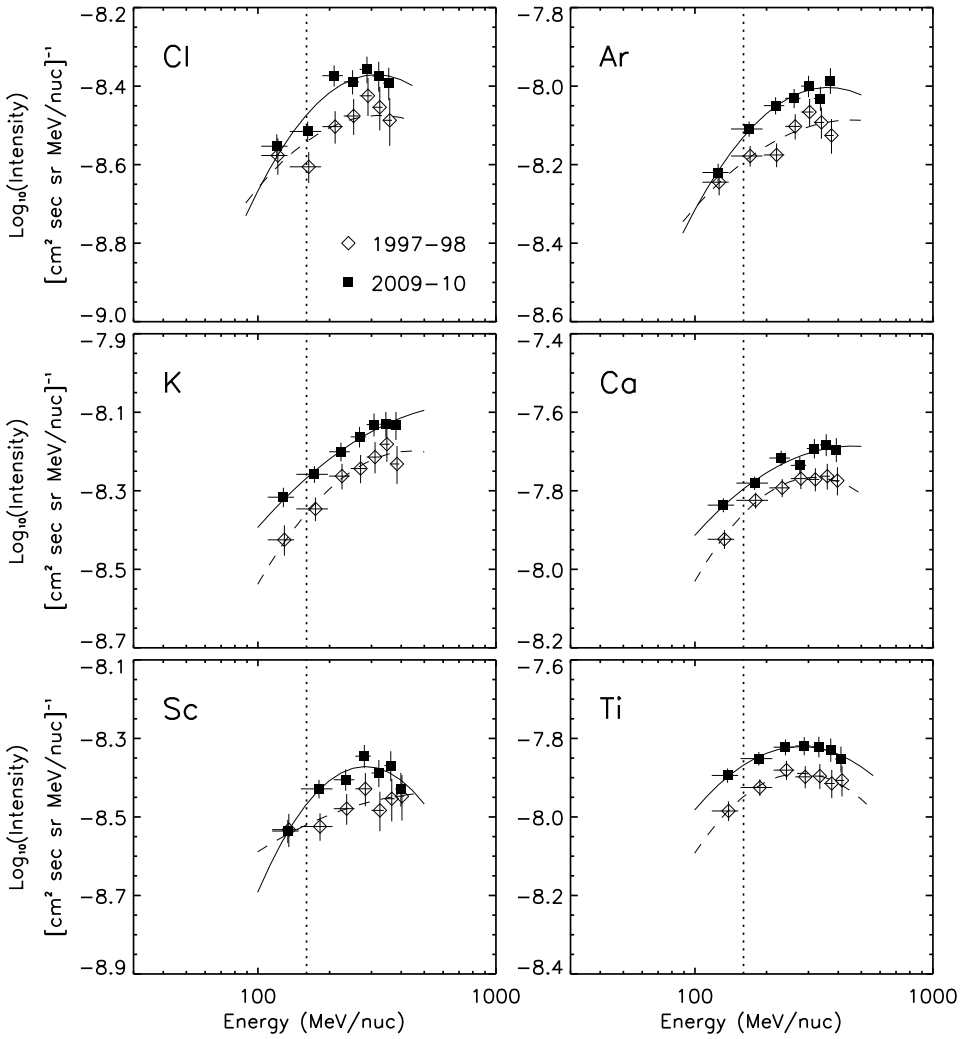

Figure 3.9: CRIS energy spectra for chlorine through titanium. Results from both solar minima are shown to allow for direct comparison of the data. The solid and dashed lines represent quadratic fits to the data. The vertical lines at 160 MeV/nucleon indicate the energy at which the relative abundances were calculated. The data shown here are tabulated in Tables A.1 and A.2 in Appendix A.

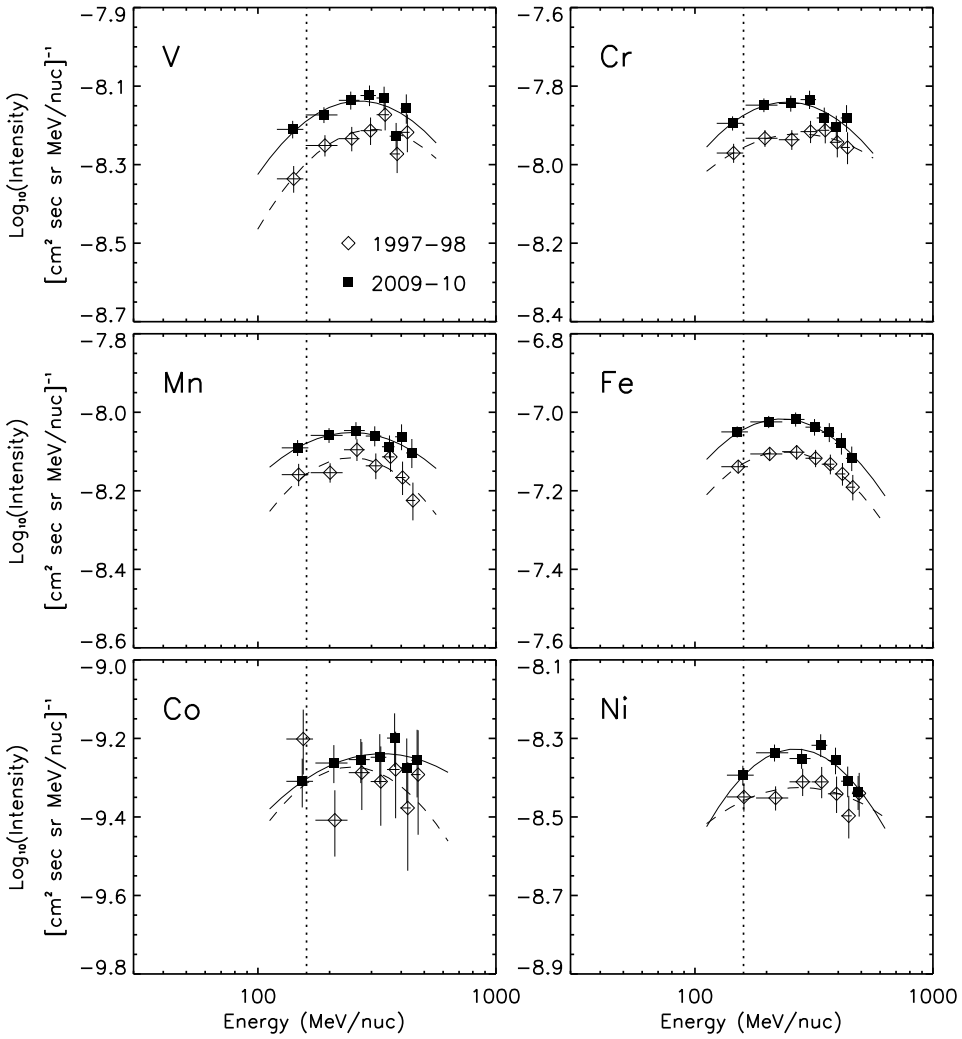

Figure 3.10: CRIS energy spectra for vanadium through nickel. Results from both solar minima are shown to allow for direct comparison of the data. The solid and dashed lines represent quadratic fits to the data. The vertical lines at 160 MeV/nucleon indicate the energy at which the relative abundances were calculated. The data shown here are tabulated in Tables A.1 and A.2 in Appendix A.

Chapter 4

The Simple Leaky-Box Transport Model

The simple leaky-box transport model (Cowsik et al. 1967) is a steady-state solution for the transport of cosmic rays through the ISM. It has a few built-in assumptions: (1) the sources of cosmic rays are uniformly distributed throughout the Galaxy, (2) cosmic rays are accelerated at their sources with identical spectra, (3) cosmic rays will freely diffuse through the homogeneous volume of the Galaxy in an energy-dependent fashion, (4) escape from the Galaxy is dependent on the energy of the cosmic ray, and (5) there is no additional acceleration (reacceleration) during transport.

For a cosmic ray with atomic number Z_i, mass number A_i, ionic charge Q_i, and energy per nucleon ε, its number density $N_i(\varepsilon)$ in the Galaxy is described using a steady-state ($\frac{dN_i}{dt} = 0$) leaky-box formalism (Gloeckler and Jokipii 1969; Meneguzzi et al. 1971; Cowsik and Wilson 1973):

$$\frac{dN_i}{dt} = 0 = C_i + \sum_j N_j \left\{ n\beta c\sigma_{ji}^{\rm spall} + \frac{1}{\gamma\tau_{ji}^{\rm decay}} + n\beta c\left(\sigma_{ji}^{\rm attach} + \sigma_{ji}^{\rm strip}\right)\right\} - N_i \left\{ n\beta c\sigma_i^{\rm spall} + \frac{1}{\gamma\tau_i^{\rm decay}} + n\beta c\left(\sigma_i^{\rm attach} + \sigma_i^{\rm strip}\right) + \frac{1}{\tau_i^{\rm esc}}\right\} - \frac{d\left(b_i N_i\right)}{d\varepsilon} \ . \quad (4.1)$$

The first five terms on the right-hand side of this equation describe the production of species i. In the first term we account for the injection of cosmic rays into the Galaxy by the sources, with the number density per unit time C_i. The second term represents the production of species i from a species j interacting with the nuclei in the ISM, where n is the number density of the ISM, βc is the velocity of the projectile (and in fact, we assume the spallation reactions produce daughter nuclei with the same velocity as the parent and the products are fully stripped with $Q_i = Z_i$), and $\sigma_{ji}^{\text{spall}}$ is the partial cross section for spallation of a nuclide of type j producing a nuclide of type i. We can rewrite this contribution in terms of the amount of material the particle traverses. This areal density, or mean free path (MFP), is related to the cross section for interaction by $\Lambda_{ji}^{\text{spall}} = m/\sigma_{ji}^{\text{spall}}$, where m is the nuclear mass.

The third term gives the production from the radioactive decay of species j into species i, where $\gamma = (1 - \beta^2)^{-1/2}$ is the Lorentz factor and τ_{ji}^{decay} is the mean time for decay in the rest frame of the nucleus. This decay time will be infinite for stable nuclei and electron-capture nuclei that have been stripped of all their electrons ($Q_i = Z_i$); τ^{decay} will be finite for unstable nuclei and electron-capture nuclei that have at least one attached electron ($Q_i \leq Z_i - 1$). For this work we only consider fully stripped nuclei ($Q_i = Z_i$) and nuclei with only one attached electron ($Q_i = Z_i - 1$). We can rewrite the decay contribution in terms of its associated MFP: $\Lambda_{ji}^{\text{decay}} = mn\beta c\gamma\tau_{ji}^{\text{decay}}$. The final fourth and fifth terms give the production of species i from species j gaining or losing an orbital electron, which are expressed in terms of the attachment and stripping cross sections ($\sigma_{ji}^{\text{attach}}$ and $\sigma_{ji}^{\text{strip}}$). These cross sections are related to their

respective MFPs by $\Lambda_{ji}^{\text{attach/strip}} = m/\sigma_{ji}^{\text{attach/strip}}$.

The remaining six terms in Equation 4.1 represent the losses of species i. These include the losses from interaction, radioactive decay, and the gain or loss of an electron. These contributions may be expressed in terms of their associated MFPs using the same relationships defined for the production terms. Cosmic rays may also 'leak' out of the Galaxy over some mean time for escape τ_i^{esc}, which is represented by the tenth term on the right-hand side of this equation. We can express the MFP for escape as $\Lambda_i^{\text{esc}} = mn\beta c\tau_i^{\text{esc}}$. The last term accounts for the amount of ionization energy loss a cosmic ray will suffer during transport, where $b_i = mn\beta c w_i$ (and $w_i \equiv d\varepsilon/dx$ is the specific ionization per nucleon).

Letting $C_i(\varepsilon) = mnq_i(\varepsilon)$ (where $q_i(\varepsilon)$ is the source production of species i per gram of ISM per unit time), and $\varphi_i(\varepsilon) = \beta c N_i(\varepsilon)$ be the equilibrium interstellar intensity for species i, we can rewrite Equation 4.1 in terms of the various mean free paths:

$$\begin{aligned} q_i + \sum_j \varphi_j \left(\frac{1}{\Lambda_{ji}^{\text{spall}}} + \frac{1}{\Lambda_{ji}^{\text{decay}}} + \frac{1}{\Lambda_{ji}^{attach}} + \frac{1}{\Lambda_{ji}^{strip}} \right) \\ = \varphi_i \left(\frac{1}{\Lambda_i^{\text{spall}}} + \frac{1}{\Lambda_i^{\text{decay}}} + \frac{1}{\Lambda_i^{attach}} + \frac{1}{\Lambda_i^{strip}} + \frac{1}{\Lambda_i^{\text{esc}}} \right) - \frac{d\left(w_i \varphi_i\right)}{d\varepsilon} \,. \end{aligned} \tag{4.2}$$

This equation may be used to determine either the source composition q_i (given φ_i) or the observed intensity φ_i (given q_i).

In Section 4.2 we first use a simplified form of Equation 4.1 to calculate the secondary-to-primary ratios B/C and $(Sc + Ti + V)/Fe$. These two ratios are com-

monly used to test propagation models since B, Sc, Ti, and V are almost entirely produced from the fragmentation of heavier nuclei, most notably the nearly pure primary nuclei C and Fe. With a successful fit of a model to these observed ratios, one can determine the mean amount of matter cosmic rays will traverse before they escape from the Galaxy. Then in Section 4.3, we introduce a numerical solution for the φ_i in Equation 4.2. The density ratios calculated in Section 4.2 are identical to the ratios of the φ_i at the same energy per nucleon, and they are a check of our results from the numerical calculation.

This chapter presents two simple leaky-box models for the transport of cosmic rays through the Galaxy. We derive a simple analytical solution to the models in Section 4.2, and provide an overview of the numerical code used to extract results (Section 4.3). Models #1 and #2 are discussed in detail in Sections 4.4 and 4.5, respectively. We use the secondary-to-primary ratios B/C and $(Sc + Ti + V)/Fe$ to test how well each model reproduces the observations, and then we compare the results for these ratios with with the plain diffusion and diffusive reacceleration models from the commonly used `GALPROP` cosmic-ray transport code. For the associated energy spectra for each model, refer to Appendix D.

4.1 Inputs to the model

The three most important inputs to the simple leaky-box model are the form of the injection spectrum, the parameterization of the energy dependence for escape

from the Galaxy, and the partial interaction cross sections of cosmic-ray nuclei on hydrogen and helium target atoms. In this model, we first assume that all cosmic rays are injected by the sources with the same power law spectrum. For this work, we used an injection spectrum that is a power law in momentum per nucleon, with a spectral index of -2.35. This form has been previously shown (George et al. 2009) to reproduce the energy dependence of the observed GCR intensities at energies between 1-100 GeV/nucleon.

We then used two parameterizations for escape from the Galaxy. The first is the form used by Davis et al. (2000):

$$\Lambda^{esc} = \frac{29.5\beta}{(\frac{\beta R}{1.0GV})^{0.6} + (\frac{\beta R}{1.3GV})^{-2.0}}\, g/cm^2\,, \tag{4.3}$$

where β is the velocity of the particle and R is its rigidity (GV). The rigidity is dependent on the charge Z, mass A, and energy ε (GeV/nucleon) by

$$R = \frac{A}{Z}\left(\varepsilon^2 + 2\varepsilon m_{\rm amu}\right)^{1/2}\,, \tag{4.4}$$

where $m_{\rm amu} = 0.9315$ GeV. The dependence on the charge and mass of the particle means that the energy dependence of Λ^{esc} will be slightly different for each cosmic ray species. At high rigidities ($\sim$1 GV) Equation 4.3 was shown to match the observed secondary-to-primary ratios quite well (Davis et al. 2000). However, the amount of material traversed by cosmic rays at low energies (less than $\sim$1 GeV/nucleon) is

artificially decreased in order to better fit the low-energy CRIS data, which is counter to what we would expect for the following reason. Above ∼1 GV Equation 4.3 gives a decreasing escape path length with increasing rigidity, which seems natural if we expect higher-rigidity particles to escape the Galaxy more easily. Below ∼1 GV this equation gives a decreasing escape path length with decreasing rigidity, though there is no reason to expect lower-rigidity particles to also escape more easily. So this shape is counter to expectation and is therefore artificial, though it seems to be needed to fit the CRIS data.

We note that a similar parameterization given by Yanasak et al. (2001) was also considered for this work; it has the form:

$$\Lambda^{esc} = \frac{26.7\beta}{(\frac{\beta R}{1.0GV})^{0.58} + (\frac{\beta R}{1.4GV})^{-1.4}}\ g/cm^2\ . \tag{4.5}$$

For B/C and $(Sc+Ti+V)/Fe$, we found that the Yanasak model yielded ratios that were an average of ∼3-4% lower than our results with the Davis model. Due to this difference, the ratios are generally better fit with the Davis model than the Yanasak model. Therefore, we chose to use the Davis escape form for our study of the simple leaky-box model.

The second escape form used in this work assumes a much simpler and more physically reasonable dependence on the particle rigidity:

$$\Lambda^{esc} = \Lambda_o \beta R^{\gamma}\ g/cm^2\ . \tag{4.6}$$

Here, Λ_o is an energy-independent normalization factor. For the simple leaky-box model we adopted $\Lambda_o = 29.5$ g/cm^2 and $\gamma = -0.6$ since at high energies, where the data are well fit, Equation 4.3 is proportional to $R^{-0.6}$. The advantage to using this parameterization is that we can compare our results using this escape form to those using the first in order to determine how strongly the artificial decrease affects the low-energy model results.

Figure 4.1 plots the escape parameterization for both models for ^{12}C and ^{56}Fe. At high energies the escape forms are identical, though at energies below ∼1 GeV/nucleon they quickly diverge. Since cosmic rays will lose energy during transport through the heliosphere, only interstellar energies above ∼300 MeV/nucleon will be relevant for this study. For reference, we have shown the total interaction mean free paths (Webber et al. (1990c); Letaw et al. (1983)) for each species, which are calculated using Equations 4.13 and 4.14.

Finally, we used a combination of measured data and semi-empirical cross sections for the interaction production cross sections over an energy range from 10 MeV/nucleon to 100 GeV/nucleon. Though we are only concerned with interstellar energies above ∼300 MeV/nucleon, the measured cross sections at lower energies are used to determine if any renormalization of the semi-empirical cross sections is necessary (see Appendix C). We made use of two different types of experimental data: direct measurements (where the isotope of interest is produced and measured before it decays) and cumulative measurements (where indirect production routes via the decays of radioactive species are combined with direct measurements). All measured data

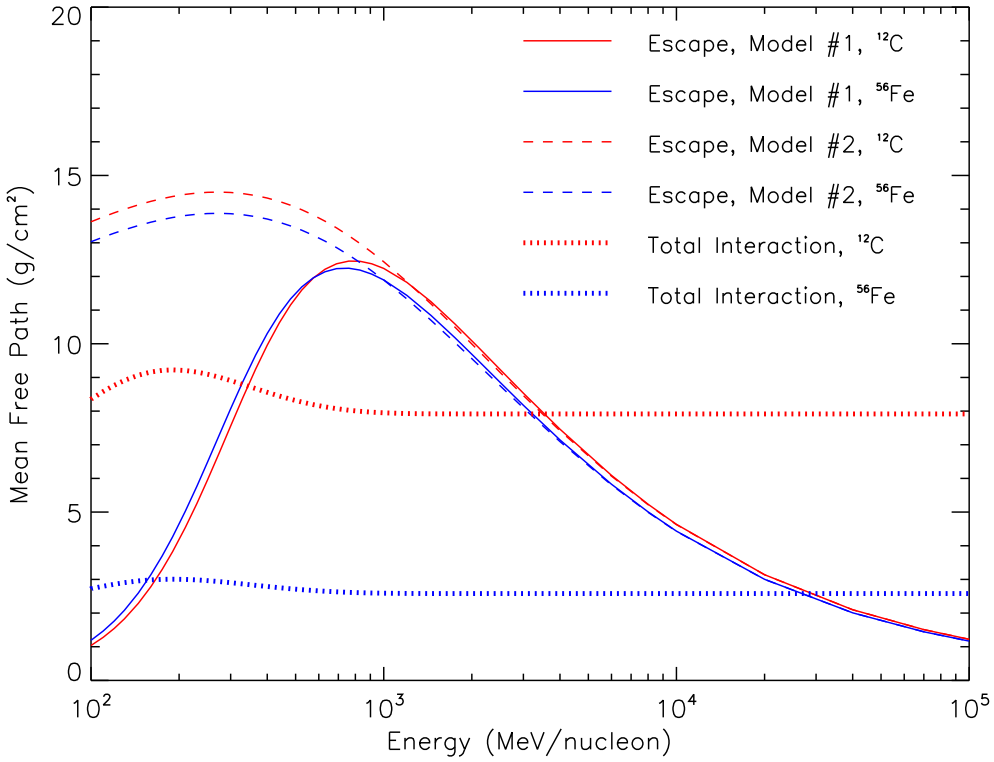

Figure 4.1: The escape mean free path parameterizations for ^{12}C and ^{56}Fe for the leaky-box models #1 and #2. The solid and dashed curves are calculated using Equations 4.3 and 4.6 (with $\Lambda_o = 29.5$ g/cm^2 and $\gamma = -0.6$), respectively. For reference the total interaction mean free path for each species, based on the cross sections calculated with Equations 4.13 and 4.14 (Webber et al. (1990c); Letaw et al. (1983)), are shown as dotted lines. Note that the shapes of these curves below ∼300 MeV/nucleon are not relevant for this study since cosmic rays with these interstellar energies will not be seen by CRIS due to solar modulation.

were compiled using the National Nuclear Data Center (Pritychenko et al. (2005); `http://www.nndc.bnl.gov/`).

Since available cross section measurements only cover small energy bands and a limited set of parent-daughter interactions, we filled in the missing cross section information using the semi-empirical formulae of Silberberg et al. (1998) and Tsao

et al. (1998) (hereafter referred to as the S&T cross sections). In our previous work (George et al. 2009), the cross sections were calculated using the `yieldx_080999.for` version of their code. These cross sections were updated with the help of A. F. Barghouty (Barghouty 2010), who provided us with a new set of data based on the most up-to-date version of their code. Appendix C offers a partial study of their new data and discusses its usage in our leaky-box models.

4.2 Analytical solution

The simple leaky-box model (Equation 4.1) specifies the gains and losses of particles as they are transported from their sources through the Galaxy. We begin by considering cosmic rays with energies above a few GeV/nucleon. In this regime, nuclear interaction cross sections are nearly energy independent, and we can also neglect ionization energy loss since these changes in energy will be negligible compared to the total energy of the particle. For this derivation we will also neglect losses and gains due to radioactive decays of unstable nuclei (most of which have half-lives shorter than their residence times in the Galaxy), as well as the attachment or stripping of an orbital electron (since at energies above a few GeV/nucleon the attachment of electrons is very unlikely and nuclei are nearly always fully stripped). Since we are neglecting energy changes, the energies of the primary particles injected into the Galaxy by the source do not need to be specified here.

With the above approximations, Equation 4.1 reduces to:

$$\frac{dS}{dt} = 0 = cn \sum_{N_k} N_k \, \sigma_{N_k \to S} - S \left(\frac{1}{\tau} + cn\sigma_S \right) . \tag{4.7}$$

Here, $N_i = S$ (cm^{-3}) denotes the number density of a purely secondary cosmic ray in the Galaxy (a species not present in the sources). On the right-hand side of this equation, the first term represents the gains due to fragmentation of the heavier species N_k (cm^{-3}) in the Galaxy. It involves the partial interaction cross sections $\sigma_{N_k \to S}$ (cm^2) for cosmic rays incident on hydrogen, producing the secondary particle; the summation is over all species heavier than S in the Galaxy. The final two terms represent the losses due to escape from the Galaxy and fragmentation of the secondary cosmic ray. The total charge-changing cross section of the secondary particle S is given by σ_S. In this equation, τ (seconds) is the cosmic-ray leakage lifetime from the Galaxy, c is the speed of light ($\beta \approx 1$ in this energy regime), and n represents the number density (cm^{-3}) of hydrogen target atoms in the Galaxy. Under steady-state conditions ($\frac{dS}{dt} = 0$) and letting $\lambda = cn\tau$ be the mean column density (cm^{-2}) to escape from the Galaxy, we can rewrite Equation 4.7 as

$$S = \frac{\lambda}{1 + \lambda\sigma_S} \sum_{N_k} N_k \, \sigma_{N_k \to S} . \tag{4.8}$$

We may determine the ratio of a secondary cosmic ray to one of the heavier species N_k using Equation 4.8. These interstellar equilibrium abundances are identical to the

ratios of cosmic-ray intensities measured at the same energy per nucleon (or velocity). As an example, the ratio of boron to carbon would be given as

$$\frac{B}{C} = \frac{\lambda}{1+\lambda\sigma_B} \sum_{N_k>B} \frac{N_k}{C}\, \sigma_{N_k \to B}\ . \tag{4.9}$$

Another example is the ratio for the sum of several sub-iron secondary cosmic rays to the primary iron: $(Sc+Ti+V)/Fe$. Here, we simply add together the individual ratios of scandium/iron, titanium/iron, and vanadium/iron:

$$\begin{aligned}\frac{Sc+Ti+V}{Fe} = \lambda \Bigg\{ & \sum_{N_k>Sc} \frac{N_k}{Fe} \frac{\sigma_{N_k \to Sc}}{(1+\lambda\sigma_{Sc})} + \\ & \sum_{N_k>Ti} \frac{N_k}{Fe} \frac{\sigma_{N_k \to Ti}}{(1+\lambda\sigma_{Ti})} + \sum_{N_k>V} \frac{N_k}{Fe} \frac{\sigma_{N_k \to V}}{(1+\lambda\sigma_{V})} \Bigg\}\ .\end{aligned} \tag{4.10}$$

In both of the above examples, the ratios N_k/C and N_k/Fe are the observed relative abundances of cosmic rays. Also, note that in these derivations the helium component of the ISM has been neglected. It is easily introduced by letting

$$\sigma_x = f_H \sigma_x^H + f_{He} \sigma_x^{He}\ , \tag{4.11}$$

where f_H and f_{He} are the fractions of hydrogen and helium in the ISM; the subscript x denotes the particular cross section for fragmenting into or out of the species of interest (for example: $N_k \to S$, the partial interaction cross section on hydrogen for the heavier species N_k producing the secondary S).

In the above solutions, we chose to describe the interstellar equilibrium abundances by λ instead of τ because the fraction of radioactive isotopes that survive transport through the Galaxy is dependent on the density of the ISM (Ptuskin and Soutoul 1998). It may be convenient to convert λ from a column number density (cm^{-2}) to an areal density ($\mathrm{g/cm}^2$), since there are a variety of parameterizations of the latter that have been used by the astrophysics community (e.g.: Swordy et al. 1990; Leske 1993; Yanasak et al. 2001; Ave et al. 2009; George et al. 2009). To do so one simply has to account for the masses of the hydrogen and helium atoms:

$$\Lambda^{\mathrm{esc}} = \lambda \left(f_H m_H + f_{He} m_{He} \right) \ . \tag{4.12}$$

Since the ratios B/C and $(Sc+Ti+V)/Fe$ are frequently used to test the validity of transport models, Equations 4.9 and 4.10 provide a simple test of the model results for two widely different charge regimes. Sections 4.4 and 4.5 will discuss these two ratios in detail for Models #1 and #2, respectively, using these analytical solutions and the full numerical simple leaky-box model (Section 4.3).

4.3 Numerical solution

In this section we describe a numerical solution (Wiedenbeck (2010) and Appendix C of George et al. (2009)) of Equation 4.2 to determine the equilibrium interstellar spectra (φ_i) for all species from boron to nickel ($5 \leq Z \leq 28$), covering energies between $10-10^5$ MeV/nucleon. In doing this work several improvements were made to

the code (described in Appendix C), the most important of which was a comprehensive update of the required partial interaction cross sections.

The calculation begins by specifying a set of isotopic source spectra (see Section 4.1). For the source composition we adopted the elemental solar system values given by Lodders et al. (2009). The only exception was for the ^{22}Ne/^{20}Ne ratio, where instead we used the value derived by Binns et al. (2005). After fixing the relative source isotopic abundances within each element, we defined an initial set of guesses for the elemental source abundances using the values derived by Duvernois and Thayer (1996). The resulting nuclidic abundances were propagated, and the local elemental abundances were calculated and compared to measured values from CRIS. Source abundances for those elements with a significant fraction of primary material (C-O, Ne-Si, S, Ar, Ca, Fe, and Ni) were adjusted so that they reproduced GCR measurements near Earth. For elements that are dominantly secondary, we assumed a source abundance using the solar value relative to a nearby primary element with a comparable first ionization potential. This process was repeated until the adjusted source abundances yielded results that converged with the CRIS measurements.

In the Galaxy, we assumed the ISM had a hydrogen number density of 0.34 cm^{-3} and a helium-to-hydrogen ratio of 0.11 by number. Yanasak et al. (2001) determined this value of the ISM density by calculating the cosmic-ray confinement times for the radionuclides ^{10}Be, ^{26}Al, ^{36}Cl, and ^{54}Mn. We accounted for ionized hydrogen in the ISM by increasing the ionization energy loss in hydrogen by a factor of 1.4 (Soutoul et al. 1990). Total cross sections for cosmic rays interacting with the nuclei in the

ISM were based on the work of Webber et al. (1990c):

$$\sigma^{\text{spall,tot}} = 57.3 * \left(A_P^{1/3} + A_T^{1/3} - \left[1.36 - 0.018 A_T - 0.065 (A_P A_T)^{1/3} \right] \right)^2 . \quad (4.13)$$

In this equation A_P and A_T are the mass numbers of the projectile and target nuclei, respectively, and ε is the energy of the projectile (in MeV/nucleon). This parameterization worked well at high energies for a variety of [A_T,A_P] combinations, though they found that the cross section measurements on hydrogen targets showed a distinct energy dependence in the range 300-1600 MeV/nucleon. They found that this could be fit by multiplying Equation 4.13 by an energy-dependent function $f(\varepsilon)$ given by Letaw et al. (1983):

$$f(\varepsilon) = 1 - 0.62 e^{-\varepsilon/200} \sin(10.9 \varepsilon^{-0.28}) . \quad (4.14)$$

Webber et al. (1990c) found that the energy dependence was nearly the same for helium targets, but not for heavier targets. Yanasak (2000) found a better fit to the data by comparing the Webber-Letaw cross sections with the measurements compiled in Tripathi et al. (1997). For each A_P, a normalization factor was determined which gave the best fit of these calculated cross sections to the measured data; the normalization varies from $0.942 - 0.979$ for $A_P = 1 - 64$. We have chosen to apply these renormalization factors to the Webber-Letaw cross sections for this work.

Partial interaction cross sections on hydrogen were based on measured data and

the S&T semi-empirical formulae (see Section 4.1). The cross sections for a projectile P (mass A_P) interacting on hydrogen ($T = H$) and producing the fragment F (mass A_F) may be used to determine the cross sections for interactions on helium ($T = He$) according to the work of Hirzebruch et al. (1993):

$$\frac{\sigma_{partial}(P, T = He, F)}{\sigma_{partial}(P, T = H, F)} = g(P, F)\sqrt{\frac{\sigma_{total}(P, T = He)}{\sigma_{total}(P, T = H)}}\,, \tag{4.15}$$

$$g(P, F) = \begin{cases} 1, & \text{if } A_F \geq \frac{2}{3}A_P \\ exp\left[1.63A_P^{-1.03}\left(\frac{2}{3}A_P - A_F\right)\right], & \text{if } A_F < \frac{2}{3}A_P \end{cases}. \tag{4.16}$$

Converting the partial interaction cross sections on hydrogen targets to those on helium targets depends on the ratio of the total interaction cross sections, which we calculated using the formulae of Kox et al. (1987):

$$\sigma_{total} = \pi R_{int}^2 \left[1 - \frac{B_C}{E_{cm}}\right]. \tag{4.17}$$

In this equation, E_{cm} is the collision energy (MeV) in the center of mass frame and B_C is the Coulomb barrier of the projectile-target system. It is defined to be

$$B_C = \frac{kZ_T Z_P e^2}{r_C\left(A_T^{1/3} + A_P^{1/3}\right)}\,, \tag{4.18}$$

where Z_T and Z_P are the target and projectile atomic charges, $k = 8.9876 \times 10^9$ $\mathrm{Nm^2/C^2}$ is Coulomb's constant, e is the electron charge, and $r_C = 1.3$ fm is the

electrostatic interaction radius. The variable R_{int} in Equation 4.17 is the projectile-target interaction radius, and it is the sum of a surface and a volume term:

$$R_{int} = R_{surf} + R_{vol} \, , \tag{4.19}$$

$$R_{surf} = r_o \left(a \frac{A_P^{1/3} A_T^{1/3}}{A_P^{1/3} + A_T^{1/3}} - c \right) \, , \tag{4.20}$$

$$R_{vol} = r_o \left(A_P^{1/3} + A_T^{1/3} \right) \, . \tag{4.21}$$

The values for r_o, a, and c are given in Table III of Kox et al. (1987).

For those parent-daughter reactions with measurements of the direct or cumulative partial interaction cross sections, we calculated an unweighted least-squares fit of the S&T cross sections to the data to find the energy-independent scale factors that would give the best fit to the measurements. Interactions where both types of data were available were considered on a case-by-case basis to determine what kind of rescaling was necessary. For more information on the cross sections and our rescaling procedure, please refer to Appendix C.

For the attachment or stripping of an orbital electron, we used cross sections based on the work of Wilson (1978) and Crawford (1979) (we note that there are typographical errors in both works, and the proper corrections have been made here). We calculate the stripping cross section using the following corrected equation:

$$\sigma^{\text{strip}} = \frac{4\pi d_1 \alpha^2 R_{\text{Bohr}}^2}{\beta^2 Z_P^2} (Z_T^2 + Z_T) \left(\ln(\frac{4\beta^2\gamma^2}{d_2 Z_P^2 \alpha^2}) - \beta^2 \right) \, . \tag{4.22}$$

In this equation, Z_P and Z_T are the charges of the parent and target nuclei; α is the fine structure constant; β is the velocity of the parent nucleus (in units of c) and γ is its Lorentz factor; $R_{\text{Bohr}} = 0.0529$ fm is the classical electron radius; and the coefficients d_1 and d_2 have values 0.285 and 0.048, respectively.

The attachment of an electron can be either radiative (where the attachment is accompanied by the emission of a photon) or non-radiative (where no photon is emitted). For the radiative process, the cross section for attachment is given by

$$\sigma^{\text{attach,rad}} = 1.803 Z_T Z_P^5 \alpha^4 \sigma_{\text{Thom}} G(\beta) F_{\text{corr}} \,, \tag{4.23}$$

where $\sigma_{\text{Thom}} = \frac{8}{3}\pi r_e^2$ is the Thompson cross section with the classical electron radius $r_e = 2.818$ fm. The function $G(\beta)$ is given by the following equations:

$$G(\beta) = \frac{\beta^3 \gamma^3 M(\beta)}{(\gamma^2 - 1)(\gamma - 1)^3} \,, \tag{4.24}$$

$$M(\beta) = \frac{4}{3} + \frac{\gamma(\gamma - 2)}{\gamma + 1}\left(1 - \frac{\ln(\gamma + \gamma\beta)}{\beta\gamma^2}\right) \,. \tag{4.25}$$

Finally, F_{corr} is a correction term given by

$$F_{\text{corr}} = (\alpha Z_P)^{\xi} exp\left[-2\alpha Z_P \arccos(\alpha Z_P)/\beta\right](1 + \pi\alpha Z_P N(\beta) M(\beta)) \,, \tag{4.26}$$

$$\xi = \sqrt{1 - Z_P^2\alpha^2} - 1 \,, \tag{4.27}$$

$$N(\beta) = \frac{1}{\beta^3}\left(\frac{-4\gamma}{15} + \frac{34}{15} - \frac{21}{5\gamma} + \frac{5}{3\gamma^2} + \frac{8}{15\gamma^3} - \frac{(\gamma - 2)(\gamma - 1)\ln(\gamma + \gamma\beta)}{\beta\gamma^3}\right) \,. \tag{4.28}$$

Non-radiative attachment cross sections are given by the Brinkman-Kramers relation discussed in Wilson (1978) and Crawford (1979), though we have updated the formula for applicability at relativistic energies:

$$\sigma^{\text{attach,non-rad}} = \sigma_o \left[\frac{\beta^2\gamma^2}{\alpha^2} + (Z_P + Z_{T,eff})^2\right]^{-5} \left[\frac{\beta^2\gamma^2}{\alpha^2} + (Z_P - Z_{T,eff})^2\right]^{-5}, \quad (4.29)$$

$$\sigma_o = \frac{(1.202)(2^{18})\pi}{5}\gamma^2 R_{\text{Bohr}}^2 (Z_P Z_{T,eff})^5 \left(\frac{\beta\gamma}{\alpha}\right)^8, \quad (4.30)$$

where $Z_{T,eff}$ is the effective charge of the target material; it has a value of 1 for hydrogen and 1.7 for helium.

We included in our calculation $\beta^{\pm}$-decay isotopes with half lives longer than ^{14}C (5730 yr), as well as any isotopes that decay only by electron capture. For the electron-capture nuclides with a single attached orbital electron we increased the half life by a factor of $\sim$2 from the laboratory value since the probability of decay with only one attached electron is half that for a neutral atom (see Appendix C.3 for the calculation). All β-decay isotopes with shorter half lives were considered to decay immediately after production.

The equilibrium interstellar intensities $\varphi_i(\varepsilon)$ are calculated for every species of interest by numerically solving the set of ordinary, first-order differential equations defined by Equation 4.2. By changing ε to $\ln(\varepsilon)$ and applying finite-difference tech-

niques, we converted each equation into a tri-diagonal matrix equation:

$$\begin{bmatrix} q_i(\varepsilon_1) \\ q_i(\varepsilon_2) \\ . \\ . \\ . \\ q_i(\varepsilon_k) \end{bmatrix} = \begin{bmatrix} \frac{1}{\Lambda_1^{Tot}} & c_2 & & & & \\ a_1 & \frac{1}{\Lambda_2^{Tot}} & c_3 & & & \\ & . & . & . & & \\ & & . & . & . & \\ & & & . & . & . \\ & & & & a_{k-1} & \frac{1}{\Lambda_k^{Tot}} \end{bmatrix} \begin{bmatrix} \varphi_i(\varepsilon_1) \\ \varphi_i(\varepsilon_2) \\ . \\ . \\ . \\ \varphi_i(\varepsilon_k) \end{bmatrix} . \tag{4.31}$$

Here, the Λ_i^{Tot} terms contain all of the gain and loss mean free paths of Equation 4.2. The off-diagonal terms (a_i and c_i) contain the ionization energy loss information. This matrix can be inverted to obtain the φ_i by using standard numerical techniques (Press et al. 1992). We solved these equations by working from the heaviest to the lightest nuclides (and in order of increasing atomic number for a given mass) so that we properly accounted for the production of nuclides in spallation reactions. The β^+ and electron-capture decays have daughter nuclides that are produced earlier in the calculation sequence, so we used iteration loops to recalculate the contributions to those species. Once these interstellar $\varphi_i(\varepsilon)$ were calculated, we used a spherically symmetric solar modulation model to find the intensities observed near Earth (see Chapter 1.4.3 for information on this calculation).

4.4 Model #1: Davis escape mean free path

In this Section we present the secondary-to-primary ratios B/C and $(Sc+Ti+V)/Fe$ for Model #1, which uses the Davis form (Equation 4.3) for the escape mean free path in the Galaxy. Figures 4.2 and 4.3 plot the ratios for the 1997-98 and 2009-10 solar minima, respectively. These ratios are an important test of any transport model since they probe the mean amount of material cosmic rays will traverse before escaping the Galaxy. B/C is the most well-studied ratio with multiple experiments providing measurements at energies from tens of MeV/nucleon up to 100 GeV/nucleon. It is almost always used to test transport models because boron is a purely secondary species and carbon is very nearly a pure primary species. $(Sc + Ti + V)/Fe$ has also been used to test models; however there have been fewer experiments with the capabilities to study the sub-iron species.

B/C and $(Sc + Ti + V)/Fe$ are determined by taking ratios of the elemental cosmic-ray spectra at Earth (see Appendix D.1.1). CRIS data presented in this work, as well as various experiments that cover higher energies ($\sim 500 - 10^5$ MeV/nucleon), are used to evaluate how well each model reproduces the observations. We have used data from the space missions CRN (Swordy et al. 1990), AMS-01 (Aguilar et al. 2010), and HEAO-3 (Engelmann et al. 1990), as well as data from the balloon experiments ATIC-2 (Panov et al. 2008), CREAM (Ahn et al. 2008), and TRACER (Obermeier et al. 2011). Note that some of the experiments listed here are not used in the discussion of the energy spectra in Appendix D (and visa versa). This is simply due

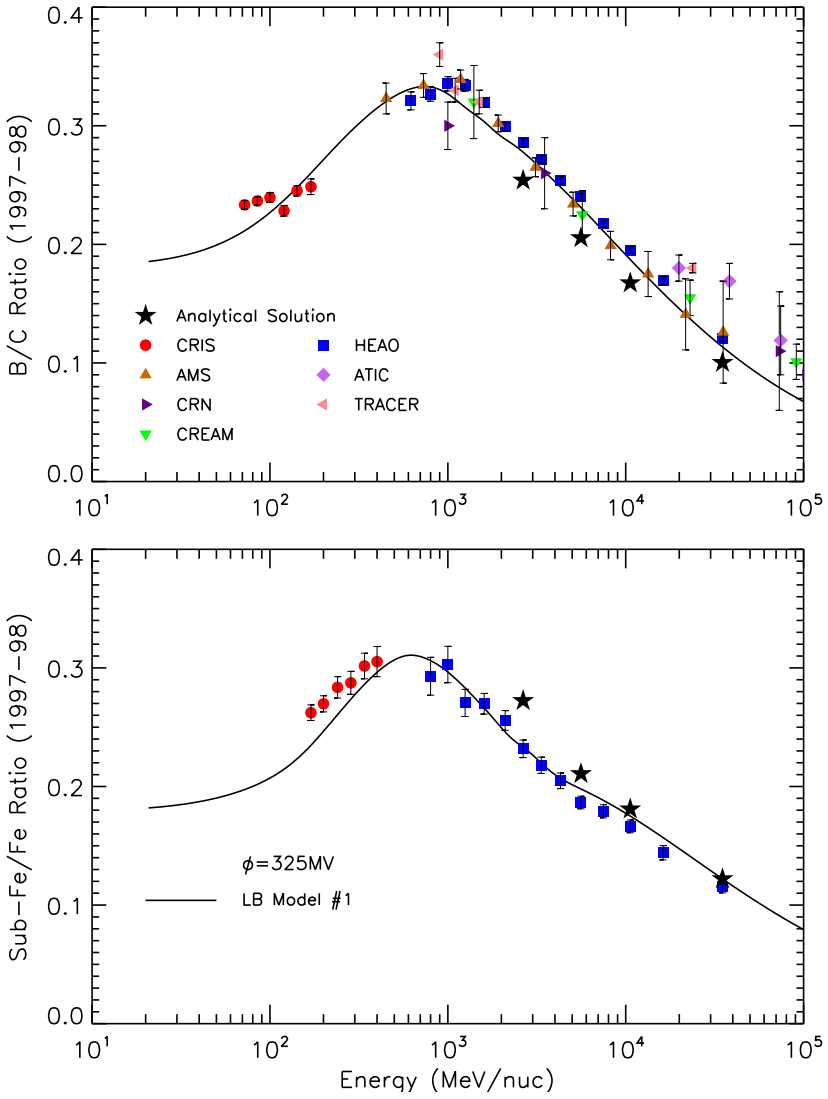

Figure 4.2: B/C and $(Sc+Ti+V)/Fe$ ratios for the 1997-98 solar minimum. CRIS observations discussed in this work are shown as filled red circles; for references to all other data used here, refer to Section 4.4. The solid curves are calculated from ratios of the cosmic-ray spectra at 1 AU (Appendix D.1.1), which result from an interstellar transport model using the Davis form of the escape mean free path (Equation 4.3) and a solar modulation level of $\phi = 325$ MV. The injection spectrum was taken to be a power law in momentum per nucleon, with a spectral index of -2.35.

to which energy spectra and/or secondary-to-primary ratios have been reported.

In each time period this model gives a good fit to both ratios at energies above

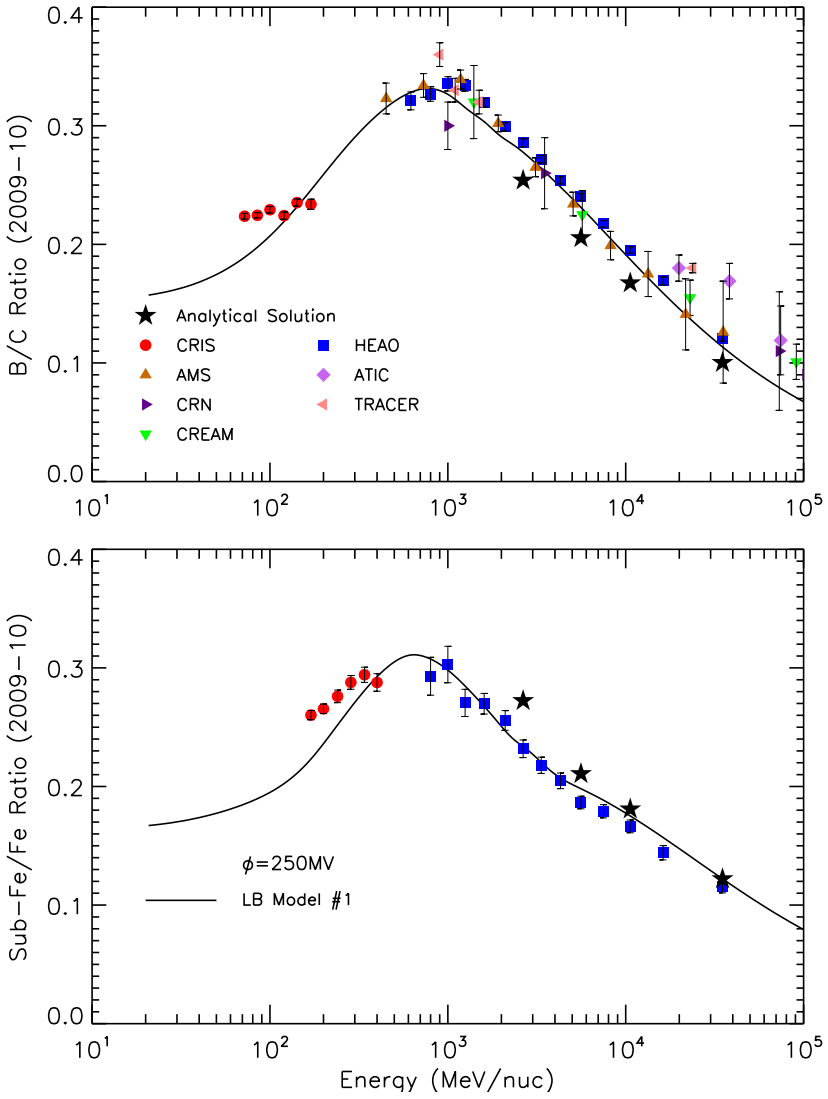

Figure 4.3: B/C and $(Sc+Ti+V)/Fe$ ratios for the 2009-10 solar minimum. For additional information concerning the data and interstellar transport models used here, refer to the caption of Figure 4.2.

several hundred MeV/nucleon. However, it is at the lower CRIS energies where we see substantial deviations of the model from the data. For B/C the model more steeply increases with increasing energy than the data suggest, with an average deviation of 5% for the 1997-98 solar minimum and 10% for the 2009-10 solar minimum. The

$(Sc + Ti + V)/Fe$ ratio predicted by the model has the right shape, but it is systematically lower than the data in both solar minimum periods by 7% (1997-98) and 10% (2009-10). We note that these differences are comparable to or smaller than the uncertainties in the cross sections for producing the secondary nuclei, which are estimated to be as large as ∼30% (Silberberg et al. 1985). The ratios given by the model have characteristic peaks between ∼600-700 MeV/nucleon. For B/C the data suggest that the peak is just above 1 GeV/nucleon. Though there are no measurements of $(Sc + Ti + V)/Fe$ between 400-800 MeV/nucleon, a peak near 700 MeV/nucleon is consistent with the data that is available.

4.4.1 Analytical solution results

As a test of the numerical model results, we have also calculated the ratios from our analytical solution presented in Section 4.2. To simplify the calculation, we have restricted the summations in Equations 4.9 and 4.10 to include only those parent species that most significantly produce the secondary species. Parent species that have the largest observed abundances in the cosmic rays and whose isotopic abundances are greater than 30% of the elemental abundance are chosen. Most remaining heavier species will have small or negligible contributions to the total production of the secondary nuclei. For the production of boron we considered ^{12}C, ^{14}N, ^{15}N, ^{16}O, ^{20}Ne, ^{22}Ne, ^{24}Mg, and ^{28}Si for the parent species; for the production of scandium, titanium, and vanadium we chose to use ^{52}Cr, ^{53}Mn, ^{55}Mn, ^{56}Fe, and ^{58}Ni for the parent species.

Species	Isotopic Fraction	Secondary Fraction
^{12}C	0.94	0.10
^{14}N	0.49	0.60
^{15}N	0.51	0.89
^{16}O	0.97	0.03
^{20}Ne	0.56	0.18
^{22}Ne	0.32	0.44
^{24}Mg	0.70	0.08
^{28}Si	0.87	0.03
^{52}Cr	0.43	0.66
^{53}Mn	0.50	0.66
^{55}Mn	0.39	0.70
^{56}Fe	0.83	<0.01
^{58}Ni	0.64	<0.01

Table 4.1: The estimated secondary fractions of select cosmic-ray isotopes (Wiedenbeck et al. 2008). Isotopic fractions are taken from Wiedenbeck (2006) and represent the isotopic composition of the GCRs as measured by CRIS.

Some of these parents are not purely primary species and they have their own significant secondary components. Using the derived cosmic-ray secondary fractions of Wiedenbeck et al. (2008), the observed CRIS relative abundances (Table 3.4), and the isotopic composition reported by CRIS (see Wiedenbeck (2006) and the references therein), we estimate that ∼12% of the boron and ∼10% of the sub-iron nuclei are tertiary products that come from interactions involving secondary parent species; Table 4.1 summarizes the relevant information. Therefore, for the purposes of these calculations, the thirteen parent isotopes we chose can be approximated as primary nuclei.

In Equations 4.9 and 4.10 we have used the high-energy HEAO observations (Engelmann et al. 1990) to compute the ratios N_k/C and N_k/Fe. The analytical solutions are computed at four different energies, 2.65, 5.60, 10.6, and 35.0 GeV/nucleon, cor-

responding to several HEAO energy bins; the results are plotted in Figures 4.2 and 4.3 as filled stars. For both time periods we see that the analytical solution generally underestimates the B/C numerical model by an average of 13%, while it overestimates $(Sc + Ti + V)/Fe$ by an average of 6%. We note that in the case of the sub-iron ratio the analytical solution deviates from the numerical model by 14% at 2.65 GeV/nucleon, while the remaining three points are higher by less than 6%.

The discrepancies seen between the analytical solution and the numerical model are most likely caused by our simplification that only a small number of primary isotopes are important for the production of the secondary species. There are certainly other parent species that are highly abundant secondary isotopes, and they can undergo further interactions in the interstellar medium to produce tertiary boron, scandium, titanium, and vanadium. However, the analytical solution presented in Section 4.2 specifies that these interactions are neglected.

4.4.2 Comparison with `GALPROP`

Next we have chosen to compare our leaky-box model results with `GALPROP` (Strong and Moskalenko 1998), a numerical code that uses current information about galactic structures and source distributions to simultaneously predict the observations of all relativistic charged particles, including cosmic-ray nuclei, electrons, and positrons, as well as compute the diffuse γ-ray and synchrotron radiation. The code is a numerical solution to the Parker transport equation (Parker 1965), which includes the physical processes of diffusion, convection, diffusive reacceleration, energy loss, nuclear

fragmentation, and radioactive decay:

$$\frac{\delta\psi}{\delta t} = q + \vec{\nabla}\cdot(D_{xx}\vec{\nabla}\psi - \vec{V}\psi) + \frac{\delta}{\delta p}p^2 D_{pp}\frac{\delta}{\delta p}\frac{\psi}{p^2} - \frac{\delta}{\delta p}\left[\frac{dp}{dt}\psi - \frac{p}{3}(\vec{\nabla}\cdot\vec{V})\psi\right] - \frac{\psi}{\tau_f} - \frac{\psi}{\tau_r}\,. \tag{4.32}$$

In this equation $\psi = \psi(\vec{r}, p, t)$ is the cosmic ray density per unit of total particle momentum p at position $\vec{r}$ and time t. The source term $q = q(\vec{r}, p, t)$ includes contributions from primary particles, as well as spallation and radioactive decay contributions. D_{xx} gives the diffusion coefficient, while diffusive reacceleration is described in terms of the diffusion in momentum space, D_{pp}. The convection velocity is given by $\vec{V}$, τ_f is the timescale for loss due to fragmentation, and τ_r is the timescale for loss due to radioactive decay. For a very thorough description of the various parameters, boundary conditions, and assumptions used for the numerical solution of Equation 4.32, please refer to Strong et al. (2007).

There are two publicly-available sample models programmed using `GALPROP` Version 54.1.984 (released 09/07/2011) at `http://galprop.stanford.edu/webrun/`. The first is a plain diffusion model (parameter file `galdef_44_999726pub`) published in Ptuskin et al. (2006), and the second is a conventional reacceleration model (parameter file `galdef_44_599278pub`) published in Ptuskin et al. (2006) and Strong and Moskalenko (2001). Both models are tuned to reproduce the isotopic abundances from CRIS reported in Wiedenbeck et al. (2001). Figures 4.4 and 4.5 compare the B/C and $(Sc + Ti + V)/Fe$ ratios from these two models with the results from our

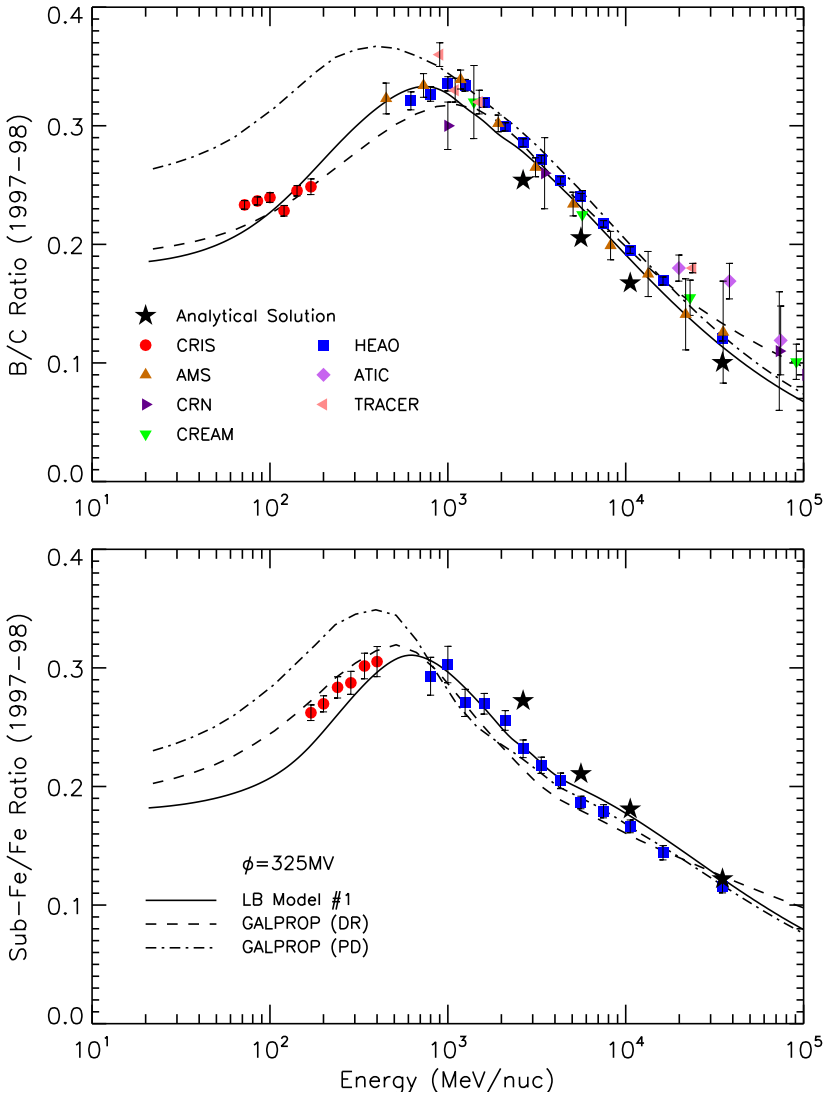

Figure 4.4: B/C and $(Sc+Ti+V)/Fe$ ratios for the 1997-98 solar minimum. Data and the Model #1 results are identical to those shown in Figure 4.2. Here we now show the results from the `GALPROP` numerical code for the case of plain diffusion (PD, dot-dashed line) and diffusive reacceleration (DR, dashed line).

Model #1 and the available observations. Note that we have used the same modulation levels for the `GALPROP` results that were previously used for each time period (325 MV for 1997-98 and 250 MV for 2009-10).

The plain diffusion (PD) model predicts a low-energy B/C ratio that is an average

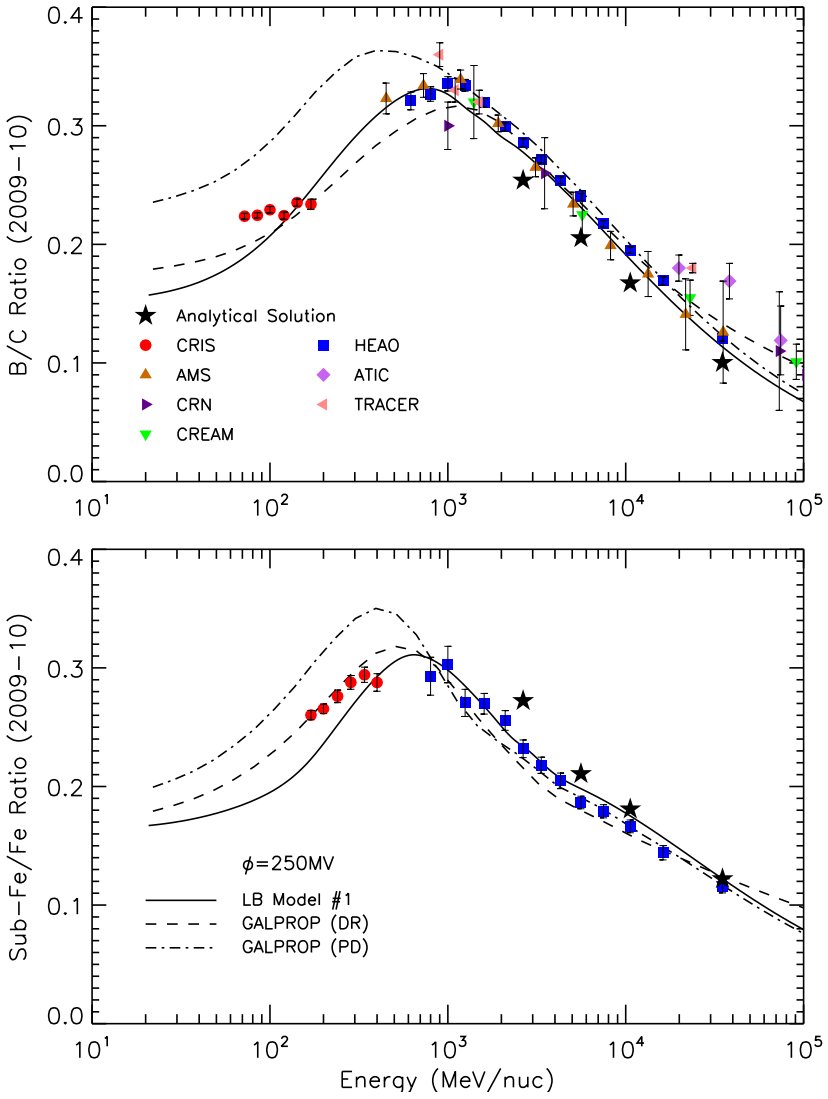

Figure 4.5: B/C and $(Sc+Ti+V)/Fe$ ratios for the 2009-10 solar minimum. Data and the Model #1 results are identical to those shown in Figure 4.3. Here we now show the results from the `GALPROP` numerical code for the case of plain diffusion (PD, dot-dashed line) and diffusive reacceleration (DR, dashed line).

of 33% and 23% larger than the CRIS 1997-98 and 2009-10 data, respectively. The results are not much better for $(Sc+Ti+V)/Fe$, where the PD model differs from the CRIS data by 18% (1997-98) and 16% (2009-10). This is far worse than the results seen with our Model #1, however we must remember that the Davis model uses an

artificial parameterization for the low-energy escape mean free path.

The diffusive reacceleration (DR) model is more successful at reproducing both the low-energy ratios. For B/C we find that the average difference between the DR model and the CRIS data is 4% (1997-98) and 10% (2009-10). $(Sc + Ti + V)/Fe$ is even more well-fit by the DR model, with average differences of 4% and 1% for the 1997-98 and 2009-10 solar minima, respectively. We note that overall the DR model yields results for B/C that are quite similar to our own using Model #1, and slightly better results for $(Sc + Ti + V)/Fe$. Therefore, we postulate that the energy dependence of the Davis escape mean free path may be mimicing the effect of reacceleration.

For both ratios, we see that all three models yield good fits to the high-energy B/C and $(Sc + Ti + V)/Fe$ ratios. Perhaps some of the differences in the models at low energies are due to the production cross sections. For the leaky-box model we have used the S&T semi-empirical formulae (Silberberg et al. (1998) and Tsao et al. (1998)); `GALPROP` uses a combination of S&T and the formulae of Webber et al. (1990a). Yanasak et al. (2001) found differences between these two formulae when studying the production cross sections of secondary radionuclides, and it is possible that the same is true for the relevant reactions that produce the secondary species discussed here. Though energy spectra are significantly affected by the type of solar modulation model used, the ratios of species with similar charge and mass are less affected by the chosen model. However, it may be possible that some of the differences at low energies are due to the different types of modulation models used here. With

GALPROP the heliospheric modulation is determined from the numerical solution of the Parker transport equation (Parker 1965), while Model #1 uses the spherically symmetric Fisk (1971) model (Chapter 1.4.3).

4.4.3 Summary of observations

To summarize the Davis model results for the secondary-to-primary ratios, we see good agreement for both B/C and $(Sc+Ti+V)/Fe$ at the highest energies. At CRIS energies, the model has a stronger energy-dependence than the B/C data suggest, though it does appear to have the right shape (but not the right magnitude) for $(Sc+Ti+V)/Fe$; also, both the model and the data exhibit peaks at similar energies. Since the Davis model is tailored to decrease the escape mean free path length at low energies to better fit the CRIS observations, it is not surprising that the secondary-to-primary ratios fit those data to within 10%. The analytical solution most closely agrees with the numerical model at the highest energies, though it is systematically lower for B/C. This suggests that the analytical solution is a good approximation to the full numerical calculation, despite the simplifications introduced.

We see that Model #1 better fits the observations than the GALPROP plain diffusion model, though the two calculations should be comparable since neither include convection nor reacceleration. The differences between these two models at low energies are due to the parameterization of the escape mean free path used in Model #1, which seems to mimic the energy dependence we see with the GALPROP diffusive reacceleration model. Both Model #1 and the reacceleration model yield comparable

results that give good fits to the data, though the reacceleration model gives a slightly better fit to the $(Sc + Ti + V)/Fe$ ratio.

4.5 Model #2: simple R-dependent escape mean free path

In this Section we present the secondary-to-primary ratios B/C and $(Sc+Ti+V)/Fe$ for Model #2, which uses a simple rigidity-dependent form (Equation 4.6 with $\Lambda_o = 29.5$ g/cm^2 and $\gamma = -0.6$) for the escape mean free path in the Galaxy. Figures 4.6 and 4.7 plot the ratios for the 1997-98 and 2009-10 solar minima, respectively. These ratios are calculated from the elemental cosmic-ray spectra at Earth (see Appendix D.1.2). CRIS data presented in this work, as well as various experiments that cover higher energies ($\sim 500 - 10^5$ MeV/nucleon), are used to evaluate how well each model reproduces the observations; see Section 4.4 for references to the data from other experiments.

Since the escape mean free path length for this model is not artificially lower at low energies, we find that the ratios are higher than those seen using Model #1. For B/C the 1997-98 model has approximately the same energy dependence as the CRIS data, however it is systematically higher by an average of 13%. For the 2009-10 B/C ratio the average difference is smaller at 7%, though the model increases more rapidly with increasing energy than the CRIS data suggest. The $(Sc + Ti + V)/Fe$ ratio has the right shape, though it is systematically lower than the data in both solar

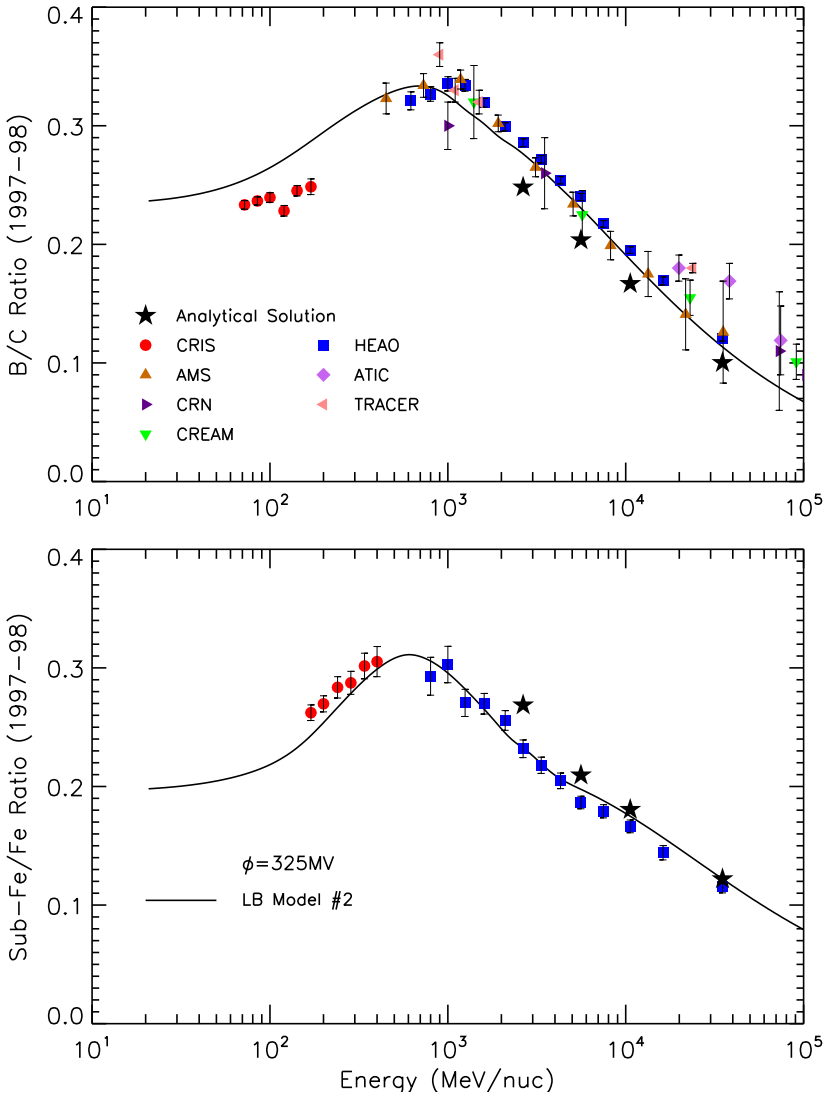

Figure 4.6: B/C and $(Sc+Ti+V)/Fe$ ratios for the 1997-98 solar minimum. CRIS observations discussed in this work are shown as filled red circles; for references to all other data used here, refer to Section 4.4. The solid curves are calculated from ratios of the cosmic-ray spectra at 1 AU (Appendix D.1.2), which result from an interstellar transport model using the simple rigidity-dependent form of the escape mean free path (Equation 4.6 with $\Lambda_o = 29.5$ g/cm^2 and $\gamma = -0.6$) and a solar modulation level of $\phi = 325$ MV. The injection spectrum was taken to be a power law in momentum per nucleon, with a spectral index of -2.35.

minimum periods by 5% (1997-98) and 7% (2009-10). The model results for these ratios have characteristic peaks near ~600-700 MeV/nucleon. This is consistent with

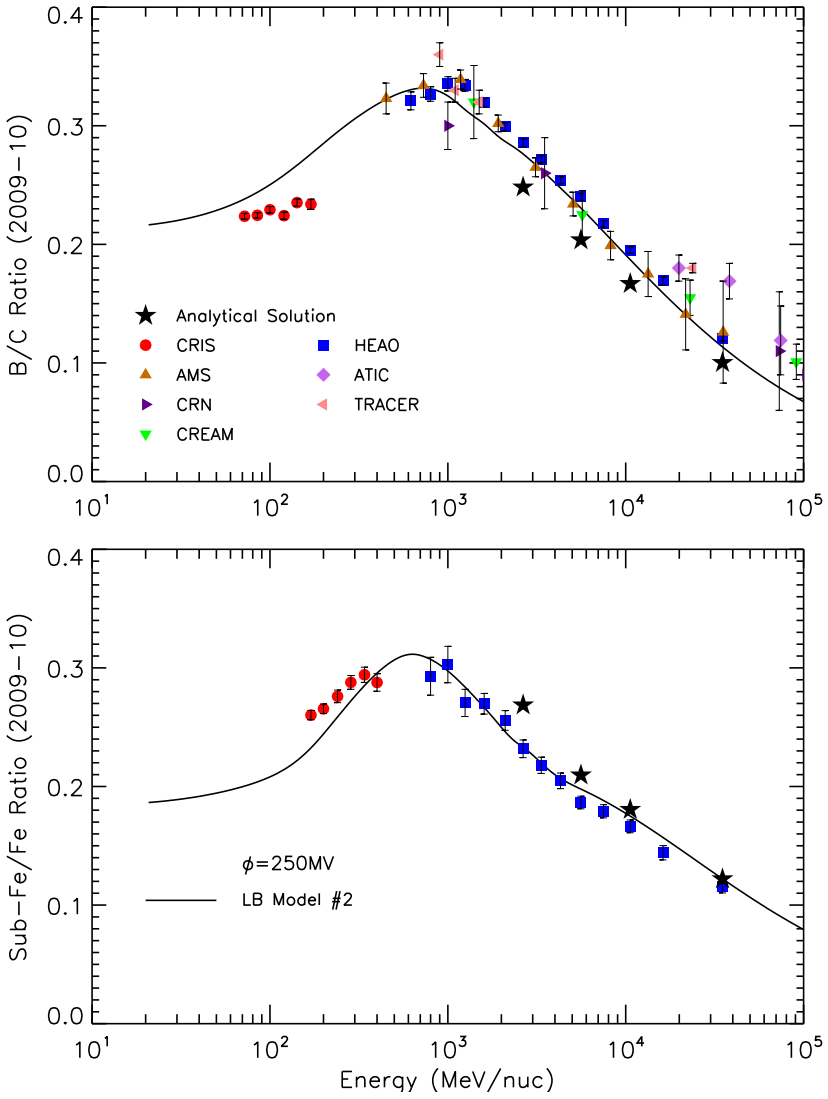

Figure 4.7: B/C and $(Sc+Ti+V)/Fe$ ratios for the 2009-10 solar minimum. For additional information concerning the data and interstellar transport models used here, refer to the caption of Figure 4.6.

the available $(Sc+Ti+V)/Fe$ observations, though the B/C data suggest that the peak should be just above 1 GeV/nucleon.

Additionally, since the escape mean free path for Model #2 is virtually identical to Model #1 at higher energies, we still see a good fit to both ratios at energies

above several hundred MeV/nucleon for both solar minima. Therefore, the analytical solution to the model, which is only calculated at energies above ∼1 GeV/nucleon, yields the same results we saw in Model #1 (Section 4.4.1).

We note that the higher B/C ratio at CRIS energies in Model #2, compared to Model #1, is expected since in Model #2 the carbon nuclei will propagate further and produce more boron before escape (see Figure 4.1). The $(Sc + Ti + V)/Fe$ ratio is not sensitive to the differences in these two models because the effective total propagation length (escape plus interaction) for a high-Z particle is virtually identical in both models. As seen in Figure 4.1, the interaction mean free path for iron is much shorter than the escape mean free path for either model, and so losses due to interactions will dominate. These results indicate that while a simpler escape mean free path parameterization still yields a great fit to $(Sc + Ti + V)/Fe$, we can not achieve similar results with the B/C ratio.

To better fit the low-energy B/C ratio we may consider adjusting some of the most important cross sections for producing boron. Carbon and oxygen are the most abundant parent species, and their cross sections for producing boron are large. Figures 4.8 and 4.9 give the ^{10}B and ^{11}B cross sections, respectively, for ^{12}C and ^{16}O incident on hydrogen. In these figures, measurements of the direct production of the boron isotopes are plotted as filled symbols, while cumulative measurements (direct, plus indirect contributions from unstable daughter nuclei that decay to the stable boron isotopes) are shown as open symbols.

Also shown are the S&T semi-empirical cross sections: the unscaled direct or indi-

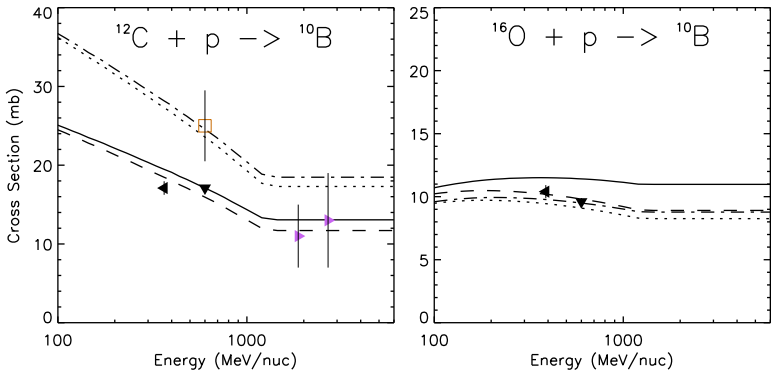

Figure 4.8: Selected cross sections for the production of ^{10}B. Direct (filled points) and cumulative measurements (open points) are shown. Original, unscaled direct S&T cross sections (Silberberg et al. (1998) and Tsao et al. (1998)) are given by black dotted lines, while unscaled cumulative S&T cross sections are given by black dot-dashed lines. Rescaled direct S&T cross sections are given by black dashed lines, while rescaled cumulative S&T cross sections (which are used in the numerical transport code) are given by black solid lines. All references for the data shown in these panels are listed in Table C.1 in Appendix C.

rect cross sections (dotted lines); the unscaled cumulative cross sections (dot-dashed lines), which combine all direct and indirect routes for production; the direct or indirect cross sections that have been rescaled according to the measurements (dashed lines); and the new cumulative cross sections that include the rescaled direct and indirect contributions (solid lines). For a thorough explanation of the data and semi-empirical cross sections plotted here, refer to Appendix C. The rescaled cumulative S&T production cross sections are used in the numerical code for the transport models.

In Figure 4.8 there are only two direct measurements for each reaction at low energies (Webber et al. (1990b); Webber et al. (1998a); Webber et al. (1998b)), and these measurements have very small uncertainties (1.5-5.0%). The direct and indirect

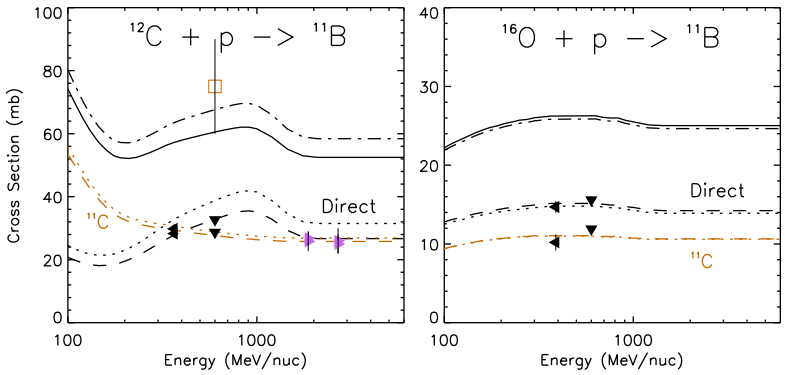

Figure 4.9: Selected cross sections for the production of ^{11}B. Refer to the caption of Figure 4.8 for information on the measurements and semi-empirical cross sections shown here. Note that the S&T cross sections for the indirect production route from the decay of ^{11}C are given as brown lines. The cumulative S&T cross sections are the sum of the direct and all indirect production routes.

(not shown) S&T cross sections were rescaled with an unweighted least-squares fit to these data. Since the Webber measurements are well fit by the rescaled S&T cross sections (dashed lines) and the data have very small uncertainties, additional low-energy adjustments to the S&T cross sections may not be allowed.

Also shown is a single cumulative measurement for ^{12}C producing ^{10}B, which has a large uncertainty (18%). The rescaled cumulative S&T cross section (solid line) includes the rescaled direct and indirect contributions, and it is lower than the single cumulative measurement by ∼30%. We also note that this data point originally agreed well with the unscaled cumulative S&T cross section (dot-dashed line). Since there are not enough cumulative measurements for either reaction to judge how well the cumulative S&T cross sections are known, it may still be possible that adjustments to decrease these cross sections are allowable (especially given the large uncertainty

on the single measurement).

For the production of ^{11}B, shown in Figure 4.9, we see very similar results. Note that in the two reactions shown, the indirect contribution from the decay of ^{11}C into ^{11}B is as equally important as the direct production route, with the unscaled and rescaled S&T cross sections given as brown dotted and dashed lines, respectively. Though the Webber measurements would again seem to disallow further adjustments to the S&T cross sections, the few available data (direct, indirect, and cumulative) do not rule out possible changes to S&T.

As Appendix C discusses, we must be careful to draw conclusions about those reactions that have Webber measurements, as these data have very small uncertainties and some cross sections have been found to disagree significantly with other measurements. While the direct and indirect measurements of these cross sections suggest that further adjustments to S&T are not allowed, there are only a few measurements for each reaction at low energies, and we do not trust the quoted uncertainties for the Webber data. More cumulative measurements are needed as well if we are to have a better understanding of the cross sections we use as inputs to the transport model. Since we are uncertain about the measurements of these boron production cross sections, we can not rule out the application of further adjustments (on the order of a $\sim$10% decrease) to better fit the low-energy B/C ratio with Model #2.

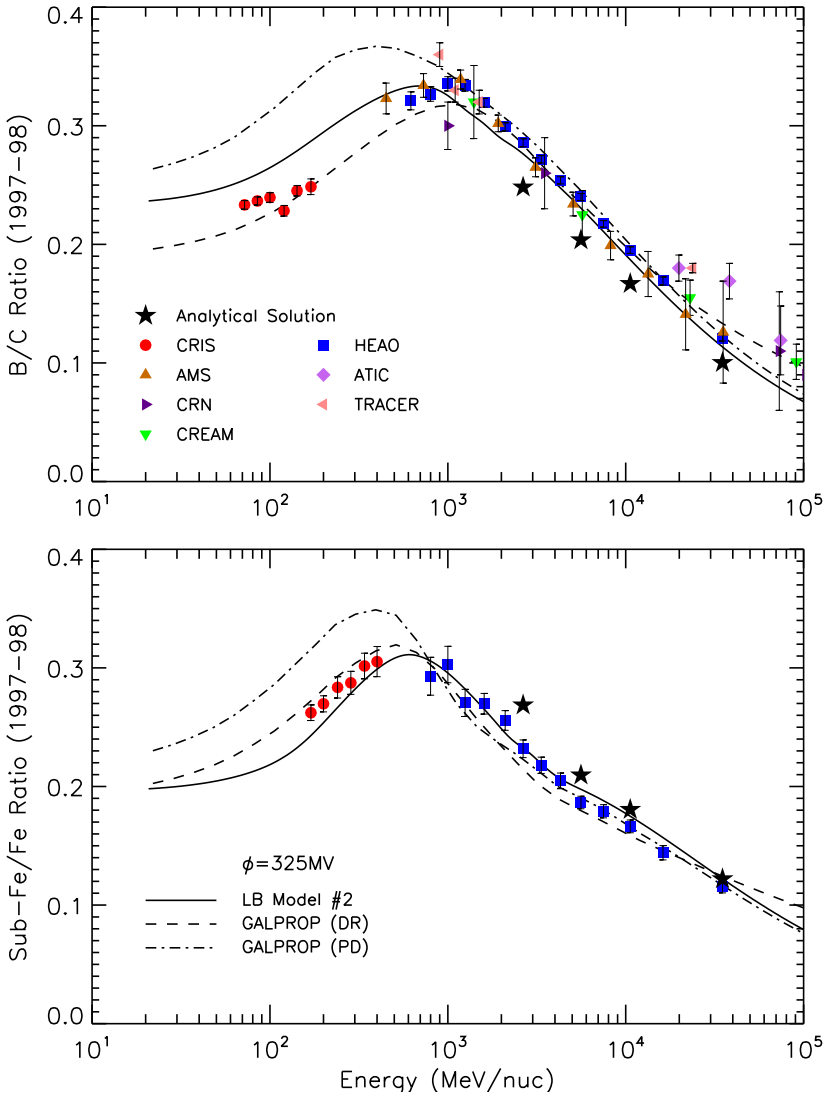

Figure 4.10: B/C and $(Sc+Ti+V)/Fe$ ratios for the 1997-98 solar minimum. Data and the leaky-box model results are identical to those shown in Figure 4.6. Here we now show the results from the GALPROP numerical code for the case of plain diffusion (PD, dot-dashed line) and diffusive reacceleration (DR, dashed line).

4.5.1 Comparison with GALPROP

Figures 4.10 and 4.11 show the results comparing our Model #2 with the plain diffusion (PD) and diffusive reacceleration (DR) GALPROP models. First, we note that the GALPROP models and the plotted data are the same as those shown in Section 4.4.2.

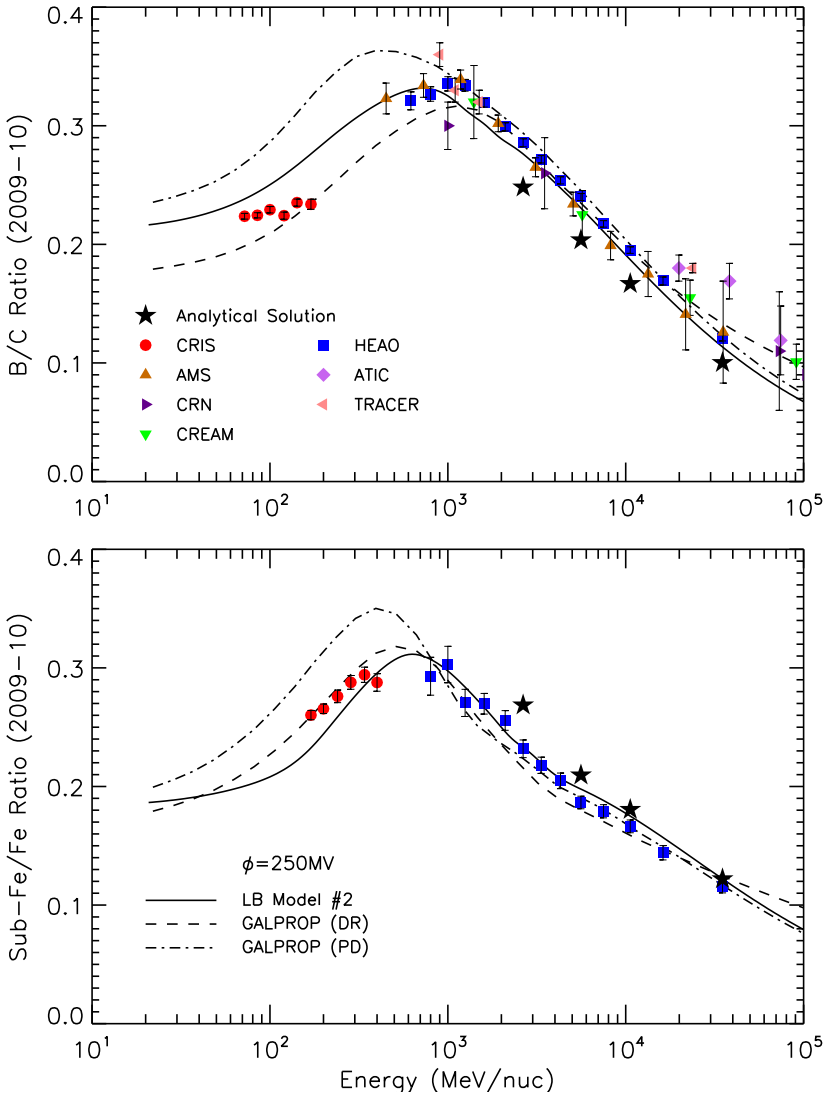

Figure 4.11: B/C and $(Sc+Ti+V)/Fe$ ratios for the 2009-10 solar minimum. Data and the leaky-box model results are identical to those shown in Figure 4.7. Here we now show the results from the `GALPROP` numerical code for the case of plain diffusion (PD, dot-dashed line) and diffusive reacceleration (DR, dashed line).

Also, Model #2 is only different from Model #1 for B/C, so we shall only compare the models for this ratio at low energies.

The most important feature to note here is that the PD model is still higher than our simple leaky-box results for both ratios, even though our Model #2 does not have

any special adjustments to the escape mean free path length below 1 GeV/nucleon. In theory, the PD model and Model #2 should account for the same physical processes in the transport of relativistic charged particles, and the results should be similar. It is unclear why these two models do not yield the same results, however the discrepancy may be due to the differing production cross sections and solar modulation models, as discussed in Section 4.4.2.

4.5.2 Summary of observations

To summarize the simple rigidity-dependent leaky-box model results, we see good agreement between the two simple leaky-box models and the data for both B/C and $(Sc + Ti + V)/Fe$ at the highest energies. However, at CRIS energies there are disagreements in the magnitude and shape of the model compared with these data. Model #2 is high compared to the CRIS data for the B/C ratio in both solar minima, and the energy dependences are somewhat steeper than the data suggest. While the differences in magnitude are attributed to the parameterization for the escape mean free path, the differences in the shapes are likely due to imperfections in the solar modulation model. We see that the $(Sc + Ti + V)/Fe$ ratio has the right shape but is slightly systematically low for both solar minimum. Also, both the model and the solar minima data exhibit peaks near the same energies.

These differences, however, may be within the allowed uncertainties of the production cross sections. Though the direct and indirect cross section measurements have very small uncertainties, the cumulative data have uncertainties larger than the

differences seen in the low-energy B/C ratio. Therefore, we propose that by using an escape mean free path distribution that is physically more reasonable than Model #1, it is still possible to reproduce the observations of these secondary-to-primary ratios.

Model #2 better fits the observations than the `GALPROP` plain diffusion (PD) model, even though the low-energy parameterization of the escape mean free path does not have an artificial energy dependence. This difference is likely due to each model's approach to characterizing the diffusion of CRs through the Galaxy, where the simple leaky-box model assumes all particles have an equal probability of escaping the Galaxy no matter where they are located, and particles in the `GALPROP` PD model must diffuse to the edge of the Galaxy to escape. It is also possible that the differences in the modulation models or the production cross sections contribute to the discrepancy. Compared with the diffusive reacceleration model, we find that Model #2 gives similar or slightly better results for $(Sc + Ti + V)/Fe$; for B/C the reacceleration model gives the best fit to the data.

4.6 Simple leaky-box model conclusions

In this chapter we have studied two simple leaky-box models for the transport of cosmic rays through the Galaxy. Each model is defined by a specific energy dependence of the escape mean free path in the Galaxy, where Model #1 uses the Davis escape parameterization (Equation 4.3; Davis et al. (2000)) and Model #2 uses a simpler

rigidity-dependent escape (Equation 4.6 with $\Lambda_o = 29.5$ g/cm^2 and $\gamma = -0.6$). The analytical and numerical solutions to these models are discussed in detail in Sections 4.2 and 4.3, respectively.

In Section 4.4 we presented the results for the secondary-to-primary ratios B/C and $(Sc+Ti+V)/Fe$ for Model #1. The CRIS data discussed in this work, covering energies between ∼50-550 MeV/nucleon, and data from several other experiments at higher energies were used to test the results of the model. We find that Model #1 gives a good fit to both ratios for both time periods. This is not surprising since the model was originally tuned to fit the CRIS data in Davis et al. (2000). Compared with the `GALPROP` plain diffusion and reacceleration models, we find that Model #1 is comparable to the reacceleration model at all energies for both ratios.

Section 4.5 presented the B/C and $(Sc + Ti + V)/Fe$ ratios for Model #2. We find that this model provides a marginally better fit to the $(Sc + Ti + V)/Fe$ ratio than Model #1 in both solar minima, while B/C is overestimated at low energies. Model #2 fits the $(Sc + Ti + V)/Fe$ ratio about as well as the `GALPROP` diffusive reacceleration (DR) model, though the low-energy B/C ratio is better fit with the DR model than Model #2. Though the `GALPROP` plain diffusion model should be comparable to Model #2 , we still see a better fit to both ratios with Model #2.

In general, we find that Models #1 and #2 are virtually indistinguishable for high-Z species since nuclear interactions are the dominating loss mechanism (see Figure 4.1). Low-Z species are very sensitive to the escape path length, and so we see larger differences between the two models at low energies. We confirm the Davis

et al. (2000) conclusion that an artificial escape form in the simple leaky-box model seems necessary to correctly fit the low-energy B/C ratio and the boron and carbon energy spectra. However, we do note that a simpler, more realistic model may fit the ratios within uncertainties, since the cumulative measurements for some of the boron production cross sections have large uncertainties. This is in contrast to the GALPROP models, which show that diffusive reacceleration (DR) is necessary to fit both the B/C and $(Sc + Ti + V)/Fe$ ratios.

We note that the energy spectra, which were used to calculated the secondary-to-primary ratios, are not discussed in this Chapter. Unlike the ratios, which are mostly affected by the interstellar transport model, the spectra are seriously affected by the injection spectrum, the interstellar transport model, and the solar modulation model. Since, it is difficult to use energy spectra to draw conclusions about the interstellar model, the primary focus of this thesis, the spectra are not discussed in this Chapter but are instead presented in Appendix D.

Since Model #1 fits the ratios as well as the GALPROP DR model, we postulate that the artificial escape mean free path form mimics the effect of including reacceleration during transport. With reacceleration the low-energy particles are moved up to higher energies, thus reducing the amount of time that particles remain in the Galaxy at low energies. In a similar way, the artificial escape form reduces the amount of material low-energy particles will travel through prior to escape, which in turn reduces the time they are present in the Galaxy.

Chapter 5

The Nested Leaky-Box Transport Model

The nested leaky-box model was first developed by Cowsik and Wilson (1975) as an extension of their earlier work (Cowsik and Wilson 1973) describing near-Earth observations of GCR spectra and relative abundances. This model has some of the same assumptions as the simple leaky-box model (Chapter 4): the cosmic ray sources are uniformly distributed throughout the Galaxy, cosmic rays are accelerated to identical spectra at their sources, and there is no reacceleration during transport. For the nested leaky-box model we now define a slightly different manner of transport through the Galaxy.

First, cosmic rays are briefly stored in the immediate vicinity of their sources (hereafter referred to as the 'cocoon' regions) prior to their transport through the rest of the Galaxy. The original publication by Cowsik and Wilson (1975) stated that the cocoons are the regions immediately surrounding the sources, though there was no speculation of whether the cocoons surround individual stars or clusters of stars. Work by Binns et al. (2005) has shown that the isotopic abundances measured

by CRIS are consistent with cosmic-ray sources that are a mix of ∼80% interstellar material with solar system abundances and ∼20% Wolf-Rayet star ejecta (stellar wind and core-collapse supernova ejecta). More recently (Ackermann et al. 2011), the Fermi Large Area Telescope has identified distributed gamma-ray emission from freshly accelerated cosmic rays in the energy range of 1-100 GeV from a 50-parsec-wide region in the Cygnus X OB association. Since most Wolf-Rayet stars and core-collapse supernovae (believed to be cosmic-ray accelerators) reside in OB associations that form superbubbles within giant molecular clouds (Higdon et al. 1998), these studies suggest that the cosmic-ray sources are the stars in OB associations and that superbubbles are the cocoons.

Cosmic rays will escape from the cocoons in an energy-dependent fashion, and diffuse through the remaining Galactic volume. In this nested leaky-box model, escape from the Galactic region is taken as being independent of energy. This parameterization of the escape mean free path in the Galaxy is motivated by studies of cosmic-ray anisotropies at high energies (above 100 GeV/nucleon). In the simple leaky-box model, an escape mean free path that decreases with increasing energy above ∼1 GeV/nucleon implies that anisotropies that increase with increasing energy would be observed, since higher-energy cosmic rays would escape more freely from the Galaxy. However, this conflicts with observational evidence of large-scale anisotropies (Takeda et al. (1999); Antoni et al. (2004); Strong et al. (2007)). According to Cowsik and Burch (2010), the energy-independent escape from the Galaxy used in the nested leaky-box model results in constant anisotropies up to several hundred TeV, which is

consistent with the observations (as shown in their Figure 3).

Equations 4.1 and 4.2 can still be used to describe the number density or equilibrium interstellar intensity of a particular species of cosmic ray, however we must now consider each transport region separately. We solve for the equilibrium densities or intensities in the cocoons (N_i^{cocoon} and φ_i^{cocoon}) given the gains and losses from source injection, nuclear fragmentation, radioactive decay, electron stripping or attachment, escape, and ionization energy losses. Then we again use Equations 4.1 and 4.2 to solve for the equilibrium N_i^{Galaxy} or φ_i^{Galaxy} given the appropriate gains and losses for this region. In this part of the calculation, the source injection terms are now replaced by the injection of cosmic rays into the Galaxy due to their escape from the cocoons (C_i^{Galaxy} and q_i^{Galaxy}).

As in the case of the simply leaky-box model, we will first use an analytic solution of a simplified form of Equation 4.1 to determine the B/C and $(Sc + Ti + V)/Fe$ ratios in the Galaxy for the nested leaky-box model (see Section 5.2). In Section 5.3 we then introduce our numerical solution for the interstellar equilibrium intensities φ_i^{Galaxy} given by Equation 4.2. The density ratios we derive in Section 5.2 will be identical to the ratios of the φ_i^{Galaxy} at the same energy per nucleon, and they provide us with a way to test the results from our numerical calculation.

5.1 Inputs to the model

Similar to Section 4.1, there are four important inputs to the nested leaky-box model. The partial interaction cross sections, determined using both measured data and calculated numbers based on semi-empirical formulae, are again a crucial piece of information. The source injection spectrum is a power law in momentum per nucleon, though according to Cowsik and Burch (2010) we must now choose for the power-law index the value from the observed cosmic-ray spectra at energies above $\sim$ 10 GeV/nucleon. After exploring a range of spectral indices (from -2.5 to -2.9), we found that the spectra are best fit using an index of -2.8 for this model.

Since cosmic rays may escape out of the cocoon and the Galaxy, there are two definitions for the the escape path length (given by $\Lambda_C^{\rm esc}$ and $\Lambda_G^{\rm esc}$). In the cocoon, the path length for escape depends on the energy of a cosmic ray. We have chosen to use the simple rigidity-dependent escape mean free path form given by Equation 4.6, and have explored the parameter space to find the values of Λ_o and γ that best fit the model to the observed data. For Λ_o we considered values in the range of 12.5-43.0 g/cm^2, and values for γ between -0.6 and -0.8. In this Chapter we will present the results from two different parameterizations: Model #1: $\Lambda_o = 16.5$ g/cm^2 and $\gamma = -0.6$; Model #2: $\Lambda_o = 23.0$ g/cm^2 and $\gamma = -0.6$.

In the Galaxy, the path length for escape $\Lambda_G^{\rm esc}$ is considered to be independent of energy. We explored a range of constant values, from 0.5-2.0 g/cm^2, and determined that $\Lambda_G^{\rm esc} = 0.5$ g/cm^2 yields the best fit for both models to the observed data. Sections

5.4 and 5.5 will present the secondary-to-primary ratios using these parameterizations for $\Lambda_C^{\rm esc}$ and $\Lambda_G^{\rm esc}$ (the energy spectra are found in Appendix D.2). As will be seen, Model #1 gives an excellent fit to the $(Sc + Ti + V)/Fe$ ratio at all energies and to the B/C ratio at CRIS energies, while Model #2 gives an good fit only for B/C at high energies. No set of parameters could be found that simultaneously fit both ratios at all energies.

Figure 5.1 plots the cocoon escape parameterizations for both models for ^{12}C and ^{56}Fe. Though each model uses a different value of Λ_o, at high energies both escape forms begin to converge. Since cosmic rays will lose energy during transport through the heliosphere, only interstellar energies above ∼300 MeV/nucleon will be relevant for this study. For reference, we have shown the total interaction mean free paths for each species, as calculated using Equations 4.13 and 4.14 (Webber et al. (1990c); Letaw et al. (1983)).

5.2 Analytical solution

The analytical solution to the nested leaky-box model, based on Equation 4.1, is similar to the derivation for the simple leaky-box model outlined in Section 4.2. In this case we now divide the propagation region into two parts: the cocoon regions (which are all considered to be identical and uniformly distributed throughout the Galaxy) and the remaining volume of the Galaxy. Again, we begin by considering cosmic rays with energies above a few GeV/nucleon. Ionization energy losses, electron

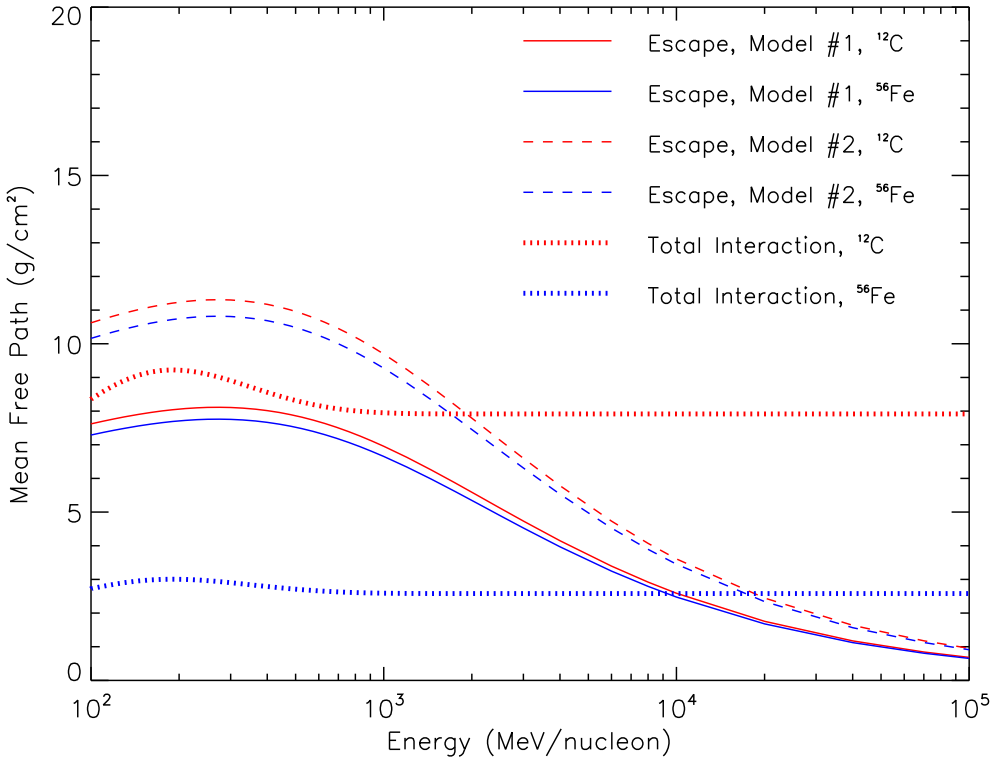

Figure 5.1: The escape mean free path parameterizations in the cocoon for ^{12}C and ^{56}Fe for the nested leaky-box models. The solid and dashed curves are calculated using Equation 4.6, where Model #1 (solid lines) uses $\Lambda_o = 16.5$ g/cm^2 and $\gamma = -0.6$, and Model #2 (dashed lines) uses $\Lambda_o = 23.0$ g/cm^2 and $\gamma = -0.6$. For reference the total interaction mean free path for each species (Webber et al. (1990c); Letaw et al. (1983)), based on the cross sections calculated with Equations 4.13 and 4.14, are shown (dotted lines). Note that the shapes of these curves below ~300 MeV/nucleon are not relevant for this study since cosmic rays with these interstellar energies will not be seen by CRIS due to solar modulation.

stripping and attachment, and radioactive decays are all neglected here.

First, we distinguish between the two propagation regions with the subscripts C and G for the cocoon regions and the Galaxy, respectively. The number density (cm^{-3}) of cosmic ray sources (i.e., the number density of cocoons) is given by h. The

number density of interstellar hydrogen atoms is given by j in each cocoon and n in the Galaxy.

Let $a(\varepsilon)$ be the number of primary particles accelerated by the source inside each cocoon per unit time. These cosmic rays have a leakage lifetime out of the cocoons of τ_C (seconds). Under steady-state conditions ($\frac{dQ}{dt} = 0$), the number of primary particles of species $Q(\varepsilon)$ in each cocoon is controlled by losses due to escape and fragmentation, and gains via injection by the source:

$$\frac{dQ}{dt} = 0 = a - Q\left(\frac{1}{\tau_C} + cj\sigma_P\right) , \tag{5.1}$$

$$Q = \frac{a\tau_C}{1 + \lambda_C\sigma_P} . \tag{5.2}$$

Here, c is the speed of light; σ_P gives the total charge-changing cross section (cm^2) for a primary particle interacting on hydrogen. Let the mean column density (cm^{-2}) for escape from the cocoons be given by $\lambda_C = cj\tau_C$. We note that Equation 5.2 assumes that Q is not produced from the fragmentation of heavier elements. This simplification is good for iron since the most abundant element that can contribute to iron production is nickel, and its abundance is 5% of the iron abundance. The approximation is not as good for carbon, since oxygen is equally abundant and nitrogen's abundance is ∼25% of carbon's abundance.

These cosmic rays may escape from the cocoons into the Galaxy. This injection of primary cosmic rays is directly proportional to Q and the leakage rate $1/\tau_C$. In the Galaxy, these primaries can be lost by escape and fragmentation. The steady-state

equation that controls the number density $P(\varepsilon)$ (cm^{-3}) of the primary cosmic rays in the Galaxy is given by

$$\frac{dP}{dt} = 0 = \frac{hQ}{\tau_C} - P\left(\frac{1}{\tau_G} + cn\sigma_P\right) , \tag{5.3}$$

$$P = \frac{hQ\tau_G}{\tau_C\left(1 + \lambda_G\sigma_P\right)} . \tag{5.4}$$

Here we define the mean column density (cm^{-2}) for escape from the Galaxy as $\lambda_G = cn\tau_G$, where τ_G is the leakage time (seconds) from the Galaxy.

For the nested leaky-box model, secondary cosmic rays in the Galaxy are the sum of two parts: those secondaries produced in the cocoons that have escaped into the Galaxy, and those secondaries that were produced within the Galaxy from heavier species. Beginning in each cocoon, the number $s(\varepsilon)$ of some purely secondary cosmic ray is controlled by a steady-state equation balancing losses due to escape and fragmentation and gains due to the fragmentation of heavier species into the secondary particle:

$$\frac{ds}{dt} = 0 = cj\sum_{Q_k>S} Q_k\sigma_{Q_k\to S} - s\left(\frac{1}{\tau_C} + cj\sigma_S\right) , \tag{5.5}$$

$$s = \frac{\lambda_C}{1 + \lambda_C\sigma_S}\sum_{Q_k>S} Q_k\sigma_{Q_k\to S} . \tag{5.6}$$

Here, σ_S gives the total charge-changing interaction cross section (cm^2) of the secondary particle on hydrogen. In the summation, $\sigma_{Q_k\to S}$ is the partial interaction cross

section (cm^2) of a heavier primary species $Q_k(\varepsilon)$ incident on hydrogen.

These secondary cosmic rays will leak into the Galaxy, at a rate $q = hs/\tau_C$ (cm^{-3} s^{-1}). Accounting for losses due to escape from the Galaxy and fragmentation, and gains from the secondaries leaking out of the cocoons, we may write the steady-state equation describing the first piece of the secondary number density in the Galaxy as:

$$\frac{dR}{dt} = 0 = -R\left(\frac{1}{\tau_G} + cn\sigma_S\right) + q\,, \tag{5.7}$$

$$R = \frac{h\tau_G\lambda_C \sum_{Q_k>S} Q_k\sigma_{Q_k\to S}}{\tau_C\left(1+\lambda_C\sigma_S\right)\left(1+\lambda_G\sigma_S\right)}\,. \tag{5.8}$$

Using Equation 5.4 to substitute $P_k(\varepsilon)$ for $Q_k(\varepsilon)$, Equation 5.8 becomes

$$R = \frac{\lambda_C \sum_{P_k>S} P_k\sigma_{P_k\to S}\left(1+\lambda_G\sigma_{P_k}\right)}{\left(1+\lambda_C\sigma_S\right)\left(1+\lambda_G\sigma_S\right)}\,. \tag{5.9}$$

In this equation, we consider secondary production from primary species only in order to simplify the solution.

To determine the number density of purely secondary cosmic rays $S(\varepsilon)$ produced in the Galaxy, we may refer to Equation 4.8 of the simple leaky-box model:

$$S = \frac{\lambda_G}{1+\lambda_G\sigma_S}\sum_{P_k>S} P_k\sigma_{P_k\to S}\,. \tag{5.10}$$

The total number density of secondary cosmic rays in the Galaxy is the sum of $R(\varepsilon)$ (the component dependent on the secondary particles that leaked out of the cocoons

into the Galaxy) and $S(\varepsilon)$ (the component dependent on primary particles in the Galaxy interacting in the ISM to form the secondary particles):

$$S + R = \frac{1}{1 + \lambda_G \sigma_S} \sum_{P_k > S} P_k \sigma_{P_k \to S} \left\{ \lambda_G + \frac{\lambda_C \left(1 + \lambda_G \sigma_{P_k}\right)}{1 + \lambda_C \sigma_S} \right\} . \tag{5.11}$$

From Equation 5.11 we can determine the ratio of secondary cosmic rays (denoted by $S + R$) in the Galaxy to one of the heavier primary particles $P_k(\varepsilon)$. These ratios (or interstellar equilibrium abundances) are identical to ratios of intensities measured at the same energy/nucleon. As an example, the ratio of boron to carbon would be given as

$$\frac{B}{C} = \frac{1}{1 + \lambda_G \sigma_B} \sum_{P_k > B} \frac{P_k}{C} \sigma_{P_k \to B} \left\{ \lambda_G + \frac{\lambda_C \left(1 + \lambda_G \sigma_{P_k}\right)}{1 + \lambda_C \sigma_B} \right\} , \tag{5.12}$$

while the ratio $(Sc + Ti + V)/Fe$ has the form

$$\begin{aligned} \frac{Sc + Ti + V}{Fe} \quad = \quad & \sum_{P_k > Sc} \frac{P_k}{Fe} \left\{ \frac{\sigma_{P_k \to Sc}}{1 + \lambda_G \sigma_{Sc}} \left(\lambda_G + \frac{\lambda_C \left(1 + \lambda_G \sigma_{P_k}\right)}{1 + \lambda_C \sigma_{Sc}} \right) + \right. \\ & \frac{\sigma_{P_k \to Ti}}{1 + \lambda_G \sigma_{Ti}} \left(\lambda_G + \frac{\lambda_C \left(1 + \lambda_G \sigma_{P_k}\right)}{1 + \lambda_C \sigma_{Ti}} \right) + \\ & \left. \frac{\sigma_{P_k \to V}}{1 + \lambda_G \sigma_V} \left(\lambda_G + \frac{\lambda_C \left(1 + \lambda_G \sigma_{P_k}\right)}{1 + \lambda_C \sigma_V} \right) \right\} . \end{aligned} \tag{5.13}$$

The summation covers any primary species heavier than vanadium. For Equations 5.12 and 5.13, P_k/C and P_k/Fe are the observed abundance ratios of cosmic rays.

As in Section 4.2, we can also include in these solutions the helium component of the ISM. For the nested leaky-box model, we need to define the fractions of hydrogen and helium in both the cocoons and the Galaxy. Let f_C^H and f_C^{He} represent the

appropriate fractions in each cocoon, while f_G^H and f_G^{He} give the fractions in the Galaxy. Then we make the replacement

$$\lambda_x \sigma_y = \lambda_x \left(f_x^H \sigma_y^H + f_x^{He} \sigma_y^{He} \right) , \tag{5.14}$$

where the subscript x indicates propagation region (C or G), and y specifies the type of cross section (P_k, S, or $P_k \rightarrow S$). If we wish to convert λ_C and λ_G from column number densities (cm^{-2}) to areal densities ($\mathrm{g/cm}^2$), we may use Equation 4.12 with λ_C or λ_G taking the place of the original λ.

Sections 5.4 and 5.5 will discuss the analytical solutions presented above for both models considered here, as well as the results from the numerical nested leaky box model (Section 5.3).

5.3 Numerical solution

The numerical solution for the nested leaky-box model is very similar to the calculation for the simple leaky-box model (Wiedenbeck (2010) and Appendix C of George et al. (2009)). The source spectra and composition are calculated in the manner described in Section 4.3. Ionization energy losses were again adjusted by a factor of 1.4 to account for the presence of ionized hydrogen in the ISM. Total and partial interaction cross sections and the attachment and stripping cross sections were calculated with the formulae given by Equations 4.13-4.30. We again considered only the

long-lived radioactive isotopes in this calculation.

The differences between the solutions for the simple and nested leaky-box models arise when we consider that in the nested model there are now two regions for cosmic-ray transport. Cowsik and Burch (2010) proposed a range of hydrogen densities in each region, with $0.1 - 0.2$ cm^{-3} representative of the Galaxy and $\sim 100 - 10^7$ cm^{-3} in the cocoons. They argued that the cocoons should be much denser than the Galaxy so that the majority of secondary production can take place during the short residence time of the cosmic rays in the cocoons. The wide range of values they proposed reflect the various densities of the candidates that may serve as the cocoon regions (i.e., circumstellar envelopes, dark clouds, molecular clouds, and giant molecular complexes). We explored Galactic hydrogen densities in the range of 0.025-0.4 cm^{-3}, and cocoon hydrogen densities in the range of 25-100 cm^{-3}, though our results were insensitive to the chosen values. Therefore we have adopted a Galactic hydrogen density of 0.2 cm^{-3} and a cocoon hydrogen density of 100 cm^{-3}, with a helium-to-hydrogen ratio of 0.11 by number in both regions. In Sections 5.4 and 5.5 we will present the model results for the parameterizations that yielded the best fits to the secondary-to-primary ratio observations.

We solved for the interstellar equilibrium intensities $\varphi_i^{Galaxy}(\varepsilon)$ of Equation 4.2 using a matrix solution similar to the one defined by Equation 4.31. However, for the nested leaky-box model this required a three-step processing scheme. We first solved Equation 4.2 for the equilibrium intensities in the cocoons, $\varphi_i^{cocoon}(\varepsilon)$. In the second step, we 'leaked' the cosmic rays out of the cocoons and into the Galaxy. This

required that we divide the $\varphi_i^{cocoon}(\varepsilon)$ by the escape time in the cocoons (τ_C). For the final step we solved Equation 4.2 for the $\varphi_i^{Galaxy}(\varepsilon)$, given the injection of cosmic rays from the cocoons (which was determined in the second step of this calculation).

As in the leaky-box model, we processed the species in order of decreasing mass and increasing atomic number per mass. Iteration loops were used to calculate radioactive decay contributions that occurred out of order in the processing sequence. Once the $\varphi_i^{Galaxy}(\varepsilon)$ were found, we used a spherically symmetric solar modulation model to find the intensities observed near Earth (see Chapter 1.4.3).

5.4 Model #1

In this Section we present the secondary-to-primary ratios B/C and $(Sc+Ti+V)/Fe$ for the nested leaky-box Model #1. This model uses a simple rigidity-dependent form for the escape mean free path in the cocoon (Equation 4.6 with $\Lambda_o = 16.5$ g/cm^2 and $\gamma = -0.6$), and an energy-independent form in the Galaxy (given by $\Lambda_G = 0.5$). Figures 5.2 and 5.3 plot the ratios for the 1997-98 and 2009-10 solar minima, respectively.

B/C and $(Sc + Ti + V)/Fe$ are determined by taking ratios of the elemental cosmic-ray spectra at Earth (see Appendix D.2.1). We have used higher-energy data from the space missions CRN (Swordy et al. 1990), AMS-01 (Aguilar et al. 2010), and HEAO-3 (Engelmann et al. 1990), as well as data from the balloon experiments ATIC-2 (Panov et al. 2008), CREAM (Ahn et al. 2008), and TRACER (Obermeier

et al. 2011) to evaluate how well each model reproduces the observations. Note that some of the experiments listed here are not used in the discussion of the energy spectra in Appendix D (and visa versa). This is simply due to which energy spectra and/or secondary-to-primary ratios have been reported.

For both solar minima, this model gives a very good fit to the B/C ratio at CRIS energies and the $(Sc + Ti + V)/Fe$ ratio at all energies. The average differences between the model and the CRIS data for both ratios are 2-3%. However, at higher energies the model underestimates the B/C ratio by $\sim$20% on average. Despite this difference the model peaks near the same energies as suggested by the available data, though the B/C peak occurs at a slightly lower energy than the data.

To explain why we only see significant differences in the B/C ratio above a few hundred MeV/nucleon, we might consider that one or more of the partial interaction cross sections for producing boron are too low in this energy regime. Carbon and oxygen are the most abundant parent species, and their cross sections for producing boron are large; therefore, we might expect that increasing these cross sections at high energies would have a positive effect on the final results. We can use Equation 5.12 to estimate the changes we would see.

The uncertainties in the S%T semi-empirical production cross sections may be as high as 30% (Silberberg et al. 1985). If the high-energy cross sections for carbon or oxygen producing boron are increased by 30% this would translate to a 25% increase in the B/C ratio, which nearly makes up the difference. However, of the few measured cross sections we have at high energies some of the data have reported uncertainties

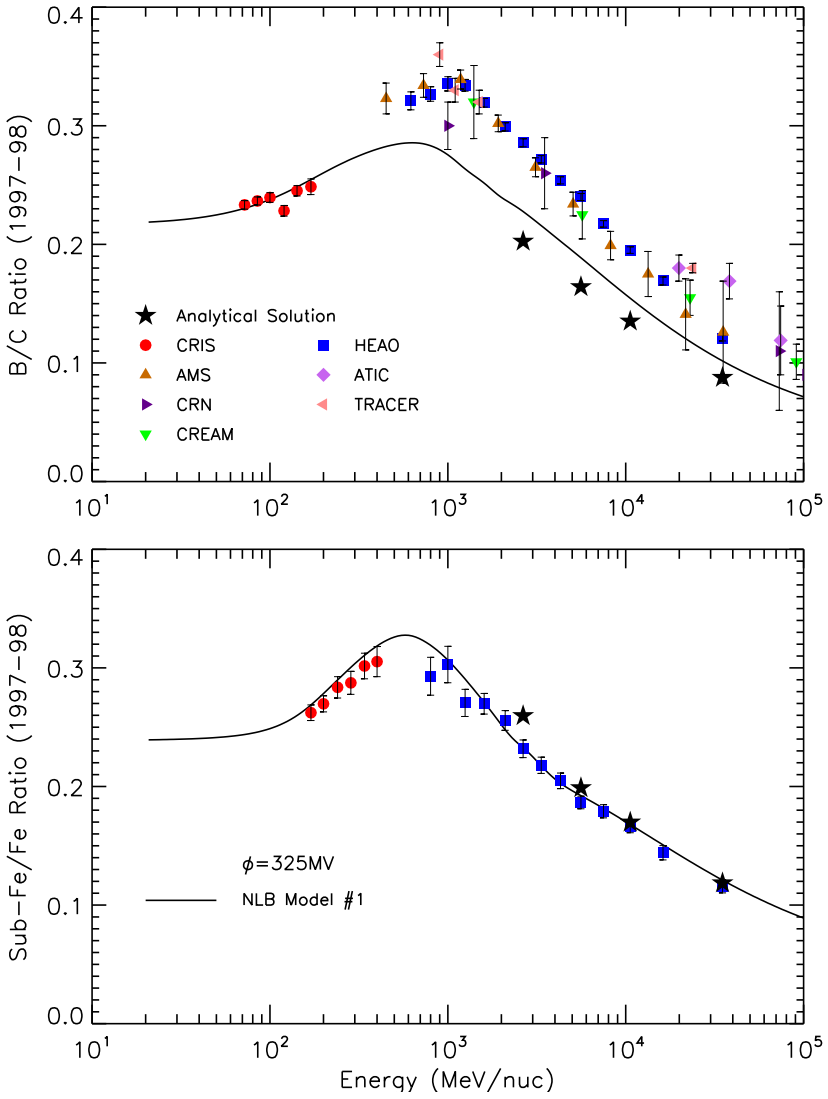

Figure 5.2: B/C and $(Sc + Ti + V)/Fe$ ratios for the 1997-98 solar minimum. CRIS observations discussed in this work are shown as filled red circles; for references to all other data used here, refer to Section 5.4. The solid curves are calculated from ratios of the cosmic-ray spectra at 1 AU (Appendix D.2.1), which result from an interstellar transport model using a simple rigidity-dependent form of the escape mean free path in the cocoon (given by Equation 4.6, where $\Lambda_o = 16.5$ g/cm^2 and $\gamma = -0.6$) and an energy-independent form in the Galaxy ($\Lambda_G = 0.5$ g/cm^2), and a solar modulation level of $\phi = 325$ MV. The injection spectrum was taken to be a power law in momentum per nucleon, with a spectral index of -2.8.

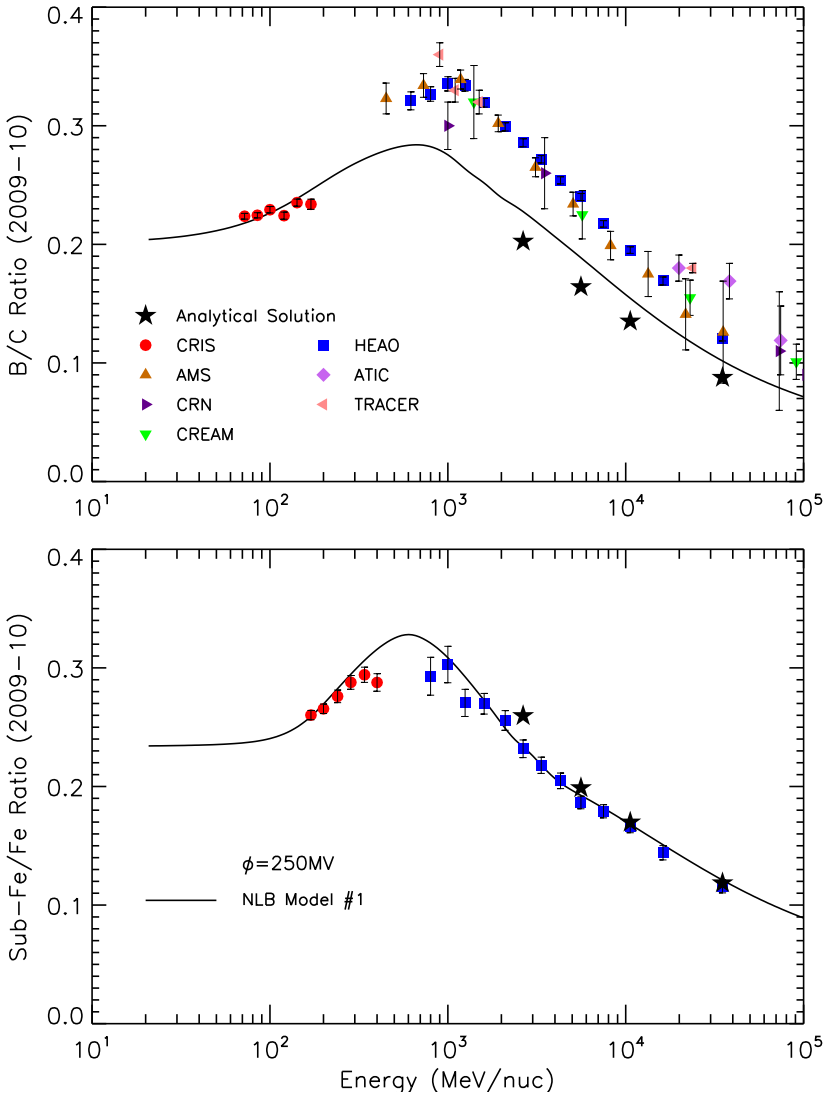

Figure 5.3: B/C and $(Sc+Ti+V)/Fe$ ratios for the 2009-10 solar minimum. For additional information concerning the data and interstellar transport models used here, refer to the caption of Figure 5.2.

that are less than 15% (see Figures 4.8 and 4.9 in Chapter 4.5). Therefore, the adjustments required to better fit the high-energy B/C ratio are beyond what could be reasonably allowed. We also know that such an increase is unnecessary to fit the B/C ratio using the simple leaky-box models in Chapter 4. So while this increase

would almost make up for the total difference, it is unlikely that the cross sections are the only problem.

5.4.1 Analytical solution results

The ratios from our numerical model are compared with the analytical solutions computed from Equations 5.12 and 5.13; our procedure was previously discussed in Section 4.4.1. We computed the ratios at four energies, 2.65, 5.60, 10.6, and 35.0 GeV/nucleon, corresponding to several HEAO energy bins and the results are plotted in Figures 5.2 and 5.3 as filled stars. The B/C ratio is underestimated by an average of 14%, while the $(Sc + Ti + V)/Fe$ ratio is overestimated by an average of 4%. The largest difference for the sub-iron ratio is 10% at 2.65 GeV/nucleon, while the difference is less than 3% at the three higher energies.

These results comparing the analytical and numerical models are quite similar to those seen with the two simple leaky-box models presented in Chapter 4. This is likely due to the fact that the escape mean free path in the cocoon region, where the majority of the secondaries are produced, has a similar energy-dependence above $\sim$1 GeV/nucleon as those parameterizations used in both simple leaky-box models. Therefore, we again propose that the discrepancies seen here are most likely caused by our simplifications to the calculation and the uncertainties in the interaction cross sections.

5.4.2 Comparison with GALPROP

GALPROP (Strong and Moskalenko 1998), which has been previously described in Section 4.4.2, is a numerical code that uses current information about galactic structures and source distributions to simultaneously predict the observations of all relativistic charged particles and the diffuse γ-ray and synchrotron radiation. In this Section we will compare our nested leaky-box results from Model #1 with publicly available sample models using GALPROP Version 54.1.984 (released 09/07/2011) at http://galprop.stanford.edu/webrun/. We have chosen to use two pre-programmed models that are tuned to reproduce the CRIS isotopic abundances (Wiedenbeck et al. 2001): the first is a plain diffusion (PD) model (parameter file galdef_44_999726pub) published in Ptuskin et al. (2006), and the second is a diffusive reacceleration (DR) model (parameter file galdef_44_599278pub) published in Ptuskin et al. (2006) and Strong and Moskalenko (2001). Figures 5.4 and 5.5 compare the B/C and $(Sc+Ti+V)/Fe$ ratios from these models with the results from our Model #1 and the available observations. Note that we have specified the same modulation levels for all of the models (325 MV for 1997-98 and 250 MV for 2009-10).

We note that the data and the GALPROP results shown here are identical to those shown in Sections 4.4.2 and 4.5.1. Therefore, the comparisons between the GALPROP models and the CRIS data remain the same, and only the comparison between the three models will be important for this discussion.

It is clear that our results with Model #1 better fit the CRIS data than the

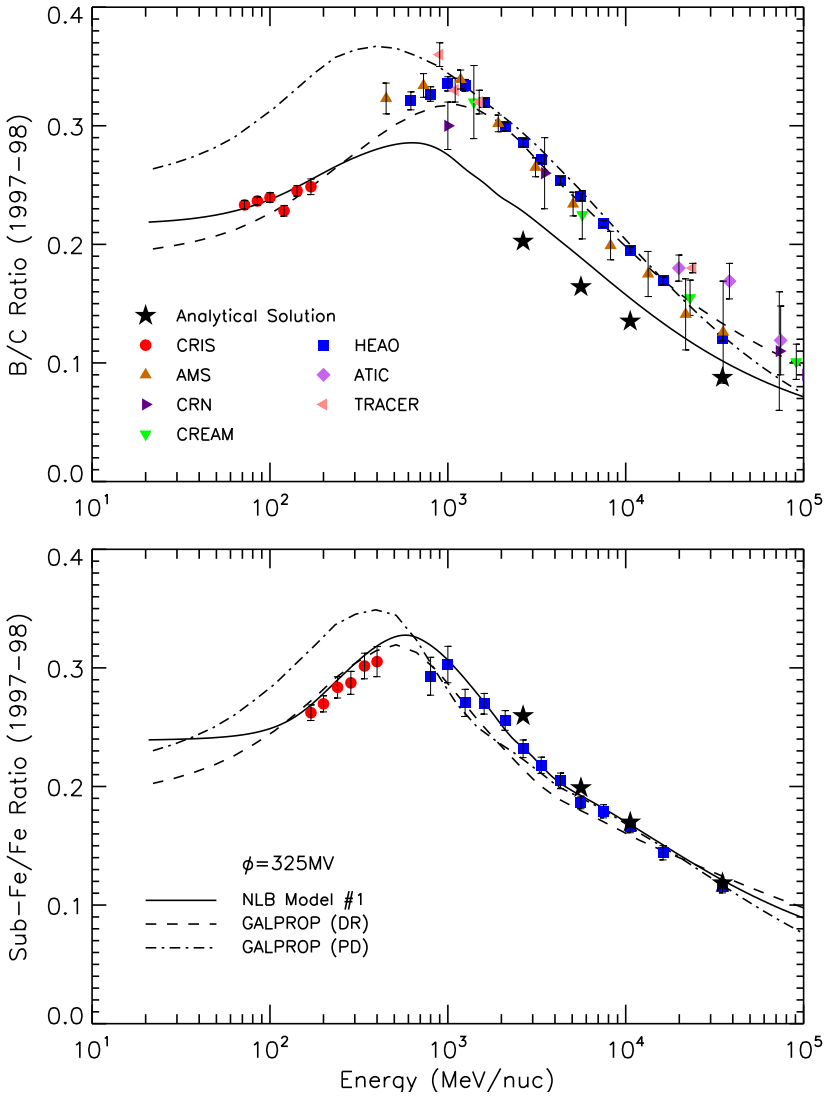

Figure 5.4: B/C and $(Sc+Ti+V)/Fe$ ratios for the 1997-98 solar minimum. Data and the leaky-box model results are identical to those shown in Figure 5.2. Here we now show the results from the GALPROP numerical code for the case of plain diffusion (PD, dot-dashed line) and diffusive reacceleration (DR, dashed line).

GALPROP plain diffusion (PD) model. Compared with the diffusive reacceleration (DR) model, our Model #1 is as successful or better at reproducing both of the low-energy ratios, especially for the low-energy B/C ratio. The CRIS B/C data suggest a relatively flat ratio that Model #1 is able to fit, while the too-steep DR model can

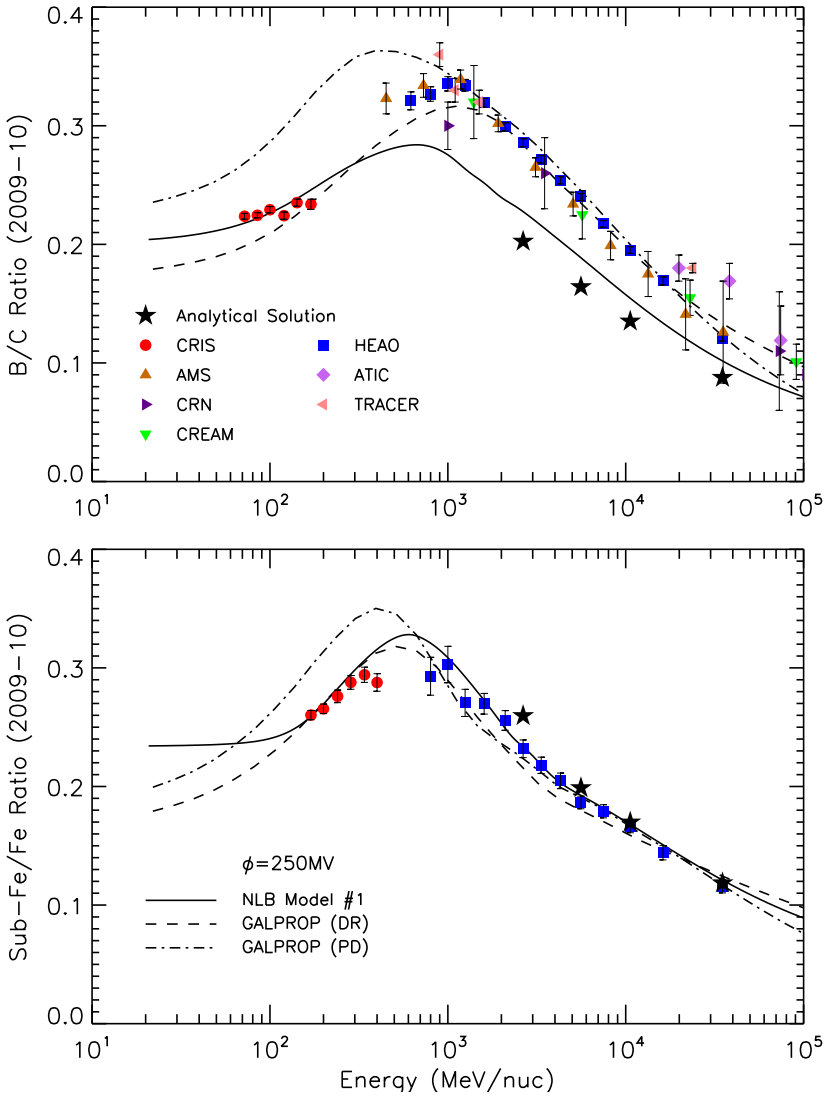

Figure 5.5: B/C and $(Sc+Ti+V)/Fe$ ratios for the 2009-10 solar minimum. Data and the leaky-box model results are identical to those shown in Figure 5.3. Here we now show the results from the `GALPROP` numerical code for the case of plain diffusion (PD, dot-dashed line) and diffusive reacceleration (DR, dashed line).

only fit the highest energy observations. This is important to note because our nested leaky-box model does not require an artificial escape form (as in the simple leaky-box Model #1 in Section 4.4) or reacceleration to fit either low-energy ratio.

At higher energies, Model #1 seems to yield a slightly better fit to the $(Sc+$

$Ti + V)/Fe$ ratio than either GALPROP model. However, the same is not true for the high-energy B/C ratio since Model #1 is unable to fit these data.

5.4.3 Summary of observations

To summarize the results from Model #1 for the secondary-to-primary ratios, we see very good fits to the low-energy B/C and $(Sc + Ti + V)/Fe$ ratios in each solar minimum period. However, while the high-energy $(Sc+Ti+V)/Fe$ ratio is also very well fit with this model, the high-energy B/C ratio is underestimated by an average of 20%. We have considered that the production cross sections for boron are too low, however the available cross section measurements limit our ability to adjust the production of boron. The analytical solution yields results that are quite similar to those seen with the simple leaky-box models in Chapter 4. Therefore, we again conclude that the analytical solution to the nested leaky-box model is a good approximation to the full numerical calculation, despite the simplifications introduced.

We see that Model #1 fits the low-energy observations as well as or better than both of the GALPROP models. This is interesting because the GALPROP results assert that the low-energy ratios can only be fit if reacceleration is included in the transport model, and our Model #1 does not include any reacceleration. At higher energies, Model #1 gives a slightly better fit to the $(Sc + Ti + V)/Fe$ ratio than the GALPROP models. However, the B/C ratio is better fit with either GALPROP model since Model #1 significantly underestimates these observations.

5.5 Model #2

In this Section we present the secondary-to-primary ratios B/C and $(Sc+Ti+V)/Fe$ for Model #2, which uses a simple rigidity-dependent form of the escape mean free path in the cocoon (Equation 4.6, with $\Lambda_o = 23.0$ g/cm^2 and $\gamma = -0.6$) and an energy-independent escape form in the Galaxy ($\Lambda_G = 0.5$ g/cm^2). Figures 5.6 and 5.7 plot the ratios for the 1997-98 and 2009-10 solar minima, respectively. These ratios are calculated from the elemental cosmic-ray spectra at Earth (see Appendix D.2.2). CRIS data presented in this work, as well as various experiments that cover higher energies ($\sim 500 - 10^5$ MeV/nucleon), are used to evaluate how well each model reproduces the observations; see Section 5.4 for references to the data from other experiments.

In each time period this model gives a fairly good fit to B/C at energies above several hundred MeV/nucleon. At CRIS energies B/C seems to have the right energy dependence, though it is systematically high compared to the data (with an average deviation of 14% for both solar minimum periods). The $(Sc + Ti + V)/Fe$ ratio predicted by the model also has the right shape, but again it is systematically higher than the data in both solar minimum periods by 11%.

As seen in Figures 4.8 and 4.9 in Chapter 4.5, the uncertainties on the few boron production cross section measurements may be large enough to allow for adjustments that would yield better fits to the low-energy B/C ratio. However, the production of the scandium, titanium, and vanadium isotopes from ^{56}Fe (the most abundant

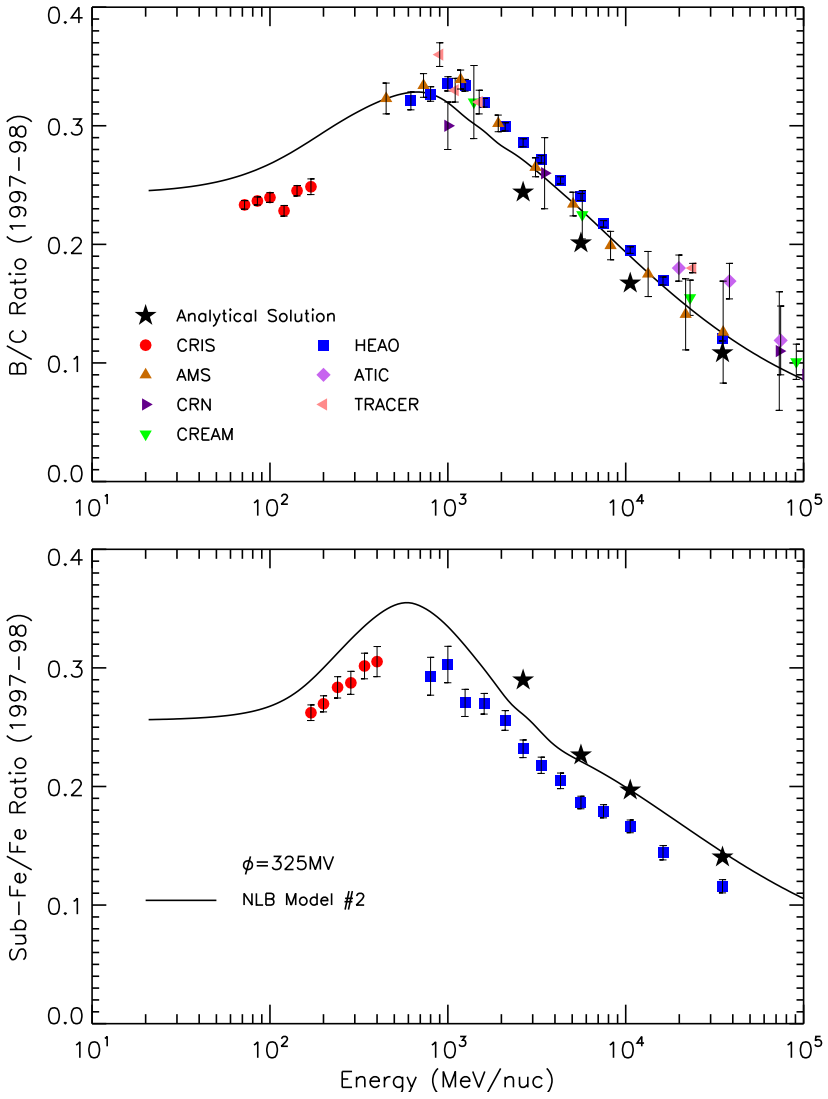

Figure 5.6: B/C and $(Sc + Ti + V)/Fe$ ratios for the 1997-98 solar minimum. CRIS observations discussed in this work are shown as filled red circles; for references to all other data used here, refer to Section 5.4. The solid curves are calculated from ratios of the cosmic-ray spectra at 1 AU (Appendix D.2.2), which result from an interstellar transport model using a simple rigidity-dependent form of the escape mean free path in the cocoon (given by Equation 4.6, where $\Lambda_o = 23.0$ g/cm^2 and $\gamma = -0.6$) and an energy-independent form in the Galaxy ($\Lambda_G = 0.5$ g/cm^2), and a solar modulation level of $\phi = 325$ MV. The injection spectrum was taken to be a power law in momentum per nucleon, with a spectral index of -2.8.

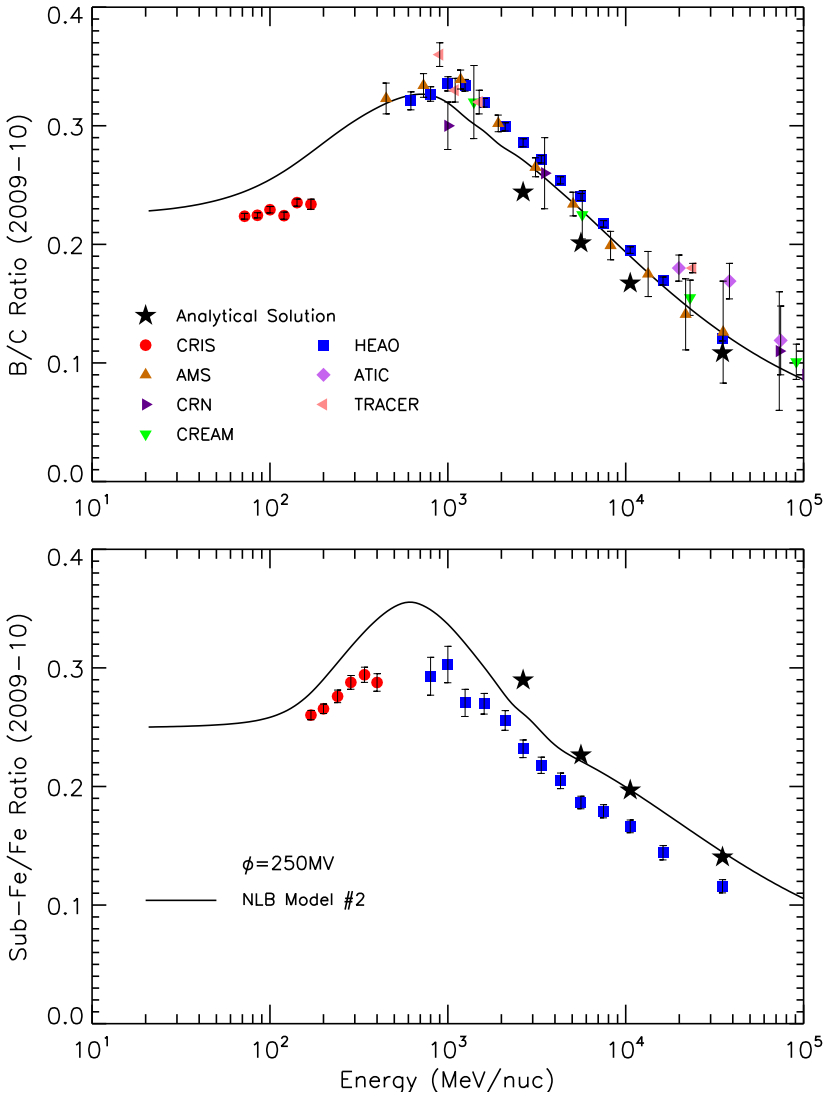

Figure 5.7: B/C and $(Sc+Ti+V)/Fe$ ratios for the 2009-10 solar minimum. For additional information concerning the data and interstellar transport models used here, refer to the caption of Figure 5.6.

primary progenitor) are better studied than the boron cross sections, with measurements covering a large range in energies. This is seen is several of the example cross sections shown in Appendix C. The differences we see for the $(Sc+Ti+V)/Fe$ ratio are a little larger than the $\lesssim$10% uncertainties on the cross section measurements.

Therefore, it is unlikely that the discrepancies between Model #2 and both ratios may be the rectified with adjustments to all of the relevant production cross sections.

In Section 5.4 we saw that Model #1 could not fit the high-energy B/C ratio, and so we chose for Model #2 a higher value of Λ_o for escape from the cocoon region. This change allowed the primary nuclei to travel farther and produce more secondary nuclei before escape from the cocoon region. However, it strongly affected both ratios at all energies, leading to the large disagreements we see here. This was to be expected since losses due to interaction are now equally or more important than losses due to escape (see Figure 5.1).

We also tested the numerical model results using the calculated ratios from our analytical solution (Equations 5.12 and 5.13) described in Section 5.2. We find that the results are quite similar to those discussed in Section 5.4.1 and the simple leaky-box models in Chapter 4.

5.5.1 Comparison with GALPROP

The nested leaky-box models we have used here do not include the effects of diffusive reacceleration, which has been used in other studies to better fit the low-energy secondary-to-primary ratios. Therefore, in this Section we will compare our model results with the GALPROP transport models (Strong and Moskalenko (1998); Moskalenko et al. (2003)), which were previously described in Section 4.4.2. Figures 5.8 and 5.9 compare the GALPROP plain diffusion (PD) and diffusive reacceleration (DR) models with our Model #2.

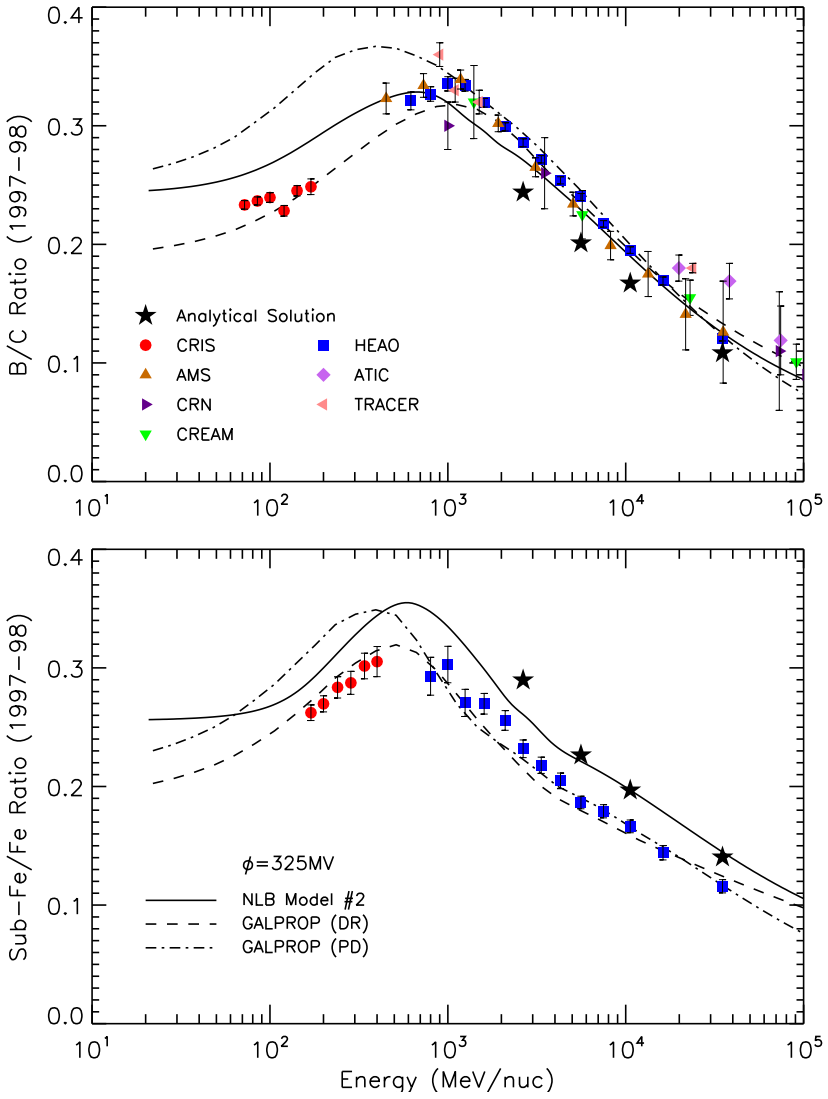

Figure 5.8: B/C and $(Sc+Ti+V)/Fe$ ratios for the 1997-98 solar minimum. Data and the leaky-box model results are identical to those shown in Figure 5.6. Here we now show the results from the GALPROP numerical code for the case of plain diffusion (PD, dot-dashed line) and diffusive reacceleration (DR, dashed line).

Note that the GALPROP models and the plotted data are identical to those shown in Section 5.4.2. Therefore, we will only focus on the comparison between the three models. We see that the ratios using the PD model are still higher than our nested leaky-box results at CRIS energies, even though Model #2 significantly overestimates

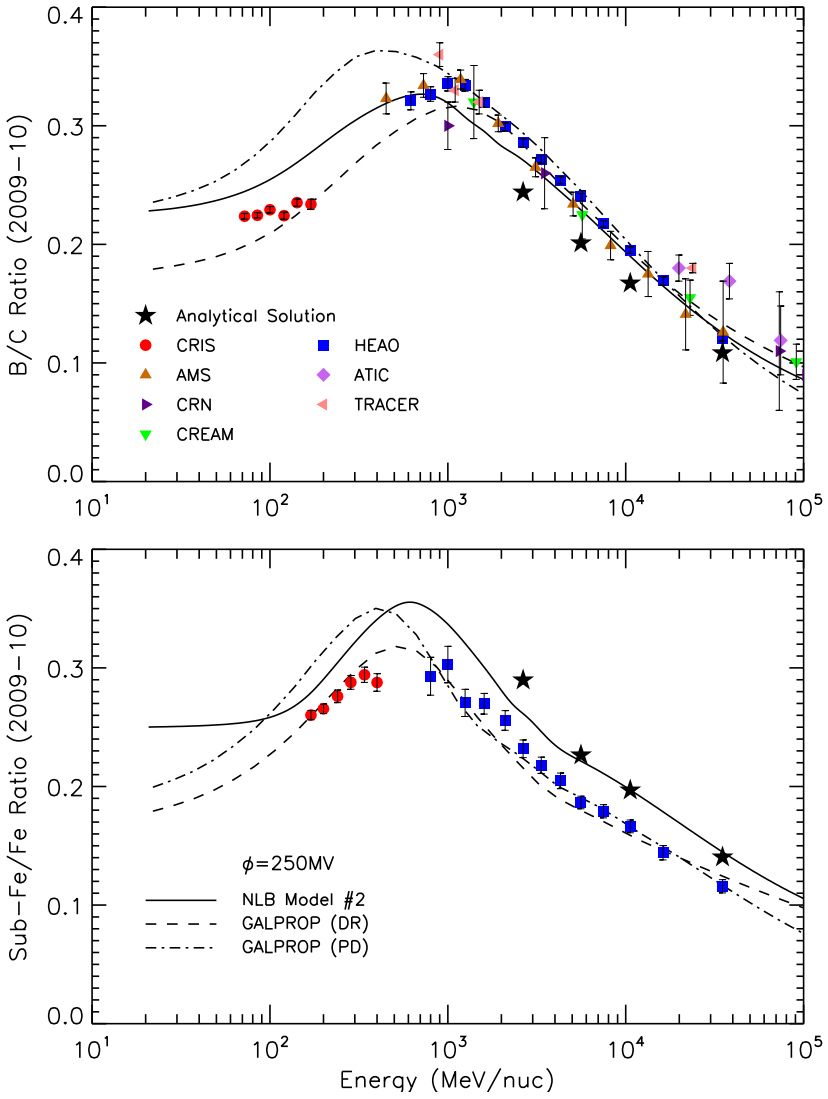

Figure 5.9: B/C and $(Sc+Ti+V)/Fe$ ratios for the 2009-10 solar minimum. Data and the leaky-box model results are identical to those shown in Figure 5.7. Here we now show the results from the GALPROP numerical code for the case of plain diffusion (PD, dot-dashed line) and diffusive reacceleration (DR, dashed line).

$(Sc+Ti+V)/Fe$ at all energies and B/C at low energies. As expected, the GALPROP DR model better fits both ratios at all energies, though the high-energy B/C ratio is about as equally well fit with Model #2.

5.5.2 Summary of observations

To summarize the results for the secondary-to-primary ratios using Model #2, we see a good fit to the high-energy B/C ratio in each solar minimum period. We achieved this good fit by adopting a longer escape mean free path length in the cocoon region than the form used in Model #1 (Section 5.4). However, this change results in a poorer fit to the low-energy B/C ratio and the $(Sc+Ti+V)/Fe$ ratio at all energies (specifically, the ratios are overestimated by 11-14% at CRIS energies). The analytical solution yields results that are quite similar to those seen with the simple leaky-box models in Chapter 4 and the nested leaky-box Model #1 in Section 5.4.1. Therefore, we again conclude that the analytical solution to the nested leaky-box model is a good approximation to the full numerical calculation, despite the simplifications introduced.

Finally, we see that in most cases the `GALPROP` diffusive reacceleration model yields the best fit to both ratios at all energies. Only at high energies does Model #2 yield a comparably good fit to the B/C ratio. Even though Model #2 overestimates both ratios at CRIS energies, we see that Model #2 still yields better results than the `GALPROP` plain diffusion model.

5.6 Nested leaky-box model conclusions

In this chapter we studied a range of nested leaky-box models in which we varied the input parameters to find models that best fit the B/C and $(Sc + Ti + V)/Fe$

ratios. This search included: the injection spectrum index (varied from -2.5 to -2.9); Λ_o (varied from 12.5-43.0 g/cm^2) and γ (varied from -0.6 and -0.8) for the cocoon escape mean free path (given by Equation 4.6); and Λ_G (varied from 0.5-2.0 g/cm^2) for the energy-independent Galactic escape mean free path. We present here two models, one of which gave the best fit to $(Sc + Ti + V)/Fe$ at all energies and the B/C ratio only at low energies, and a second which best fit only the high-energy B/C ratio. We were unable to find a model that best fit these ratios at all energies. Model #1 uses $\Lambda_o = 16.5$ g/cm^2, $\gamma = -0.6$, and $\Lambda_G = 0.5$ g/cm^2; Model #2 uses $\Lambda_o = 23.0$ g/cm^2, $\gamma = -0.6$, and $\Lambda_G = 0.5$ g/cm^2. The analytical and numerical solutions to these models are discussed in detail in Sections 5.2 and 5.3, respectively.

In Section 5.4 we presented the results for the secondary-to-primary ratios B/C and $(Sc+Ti+V)/Fe$ using Model #1. We find that this model gives a very good fit to the low-energy B/C and $(Sc + Ti + V)/Fe$ ratios in each solar minimum period. However, while the high-energy $(Sc+Ti+V)/Fe$ ratio is also very well fit with this model, the high-energy B/C ratio is underestimated by an average of 20%. Compared with the `GALPROP` plain diffusion (PD) and diffusive reacceleration (DR) models, we see that Model #2 gives a comparable or better fit to the data than the PD and DR models (except for high-energy B/C).

Section 5.5 discussed our results with Model #2. Due to the poor fit of the high-energy B/C ratio using Model #1, we used a longer escape mean free path length in this model. For both solar minima we do see that this change allows for a good fit to the high-energy B/C ratio for both time periods. However, the low-energy

B/C ratio and the $(Sc + Ti + V)/Fe$ ratio at all energies are overestimated. This is expected since the longer path length allows for the production of more secondary species due to nuclear interactions (see Figure 5.1). Because of these overestimations, the GALPROP DR model better fits the ratios than Model #2. Only for the high-energy B/C ratio does Model #2 give a comparable fit.

As discussed in Section 5.4, it might be plausible that the production cross sections for boron at high energies are too low and some adjustments would allow a better fit to B/C using Model #1. However, the uncertainties on the relevant cross sections do not allow large enough changes at high energies. We may also consider similar cross section adjustments to yield better fits to the ratios using Model #2. Yet, the production of scandium, titanium, and vanadium from ^{56}Fe are fairly well studied and have somewhat smaller uncertainties than the differences we see for the $(Sc + Ti + V)/Fe$ ratio. Therefore, it is unlikely that the problems we see fitting the B/C and $(Sc + Ti + V)/Fe$ ratios are only due to our treatment of the production cross sections.

Perhaps the problem here may be that our nested leaky-box model is missing fundamental physics that is most important for secondary production, or some of the assumptions we have made are limiting our results. Despite these issues, we believe that the nested leaky-box model shows promise as a cosmic-ray transport model since it can be used to fit some of the secondary-to-primary ratios very well, if not better than the standard approaches using the simple leaky-box model and the GALPROP DR model. However, to better reproduce the results at all energies, further work

with this model and the interaction cross sections are required. Until this model is better understood, it can not be considered an alternative to the simple leaky-box and GALPROP models.

Chapter 6

Conclusions

In this dissertation, observations of galactic cosmic rays with nuclear charge $5 \leq Z \leq 28$ in the energy range $\sim$50-550 MeV/nucleon using the CRIS instrument are presented. Improvements to the data analysis techniques originally used in George et al. (2009) are discussed in Chapter 3. These changes include a more careful selection of the data for the 1997-98 solar minimum period to avoid discriminator threshold changes that introduced a bias in the high-Z dataset, as well an improved approach to the error analysis for the energy spectra and relative abundances. New data from the 2009-2010 solar minimum are also presented. This period featured very low levels of solar activity, and we find that the GCR intensities observed during this time are the highest recorded during the space age. These measurements are considered to be the closest we have ever come to observing the interstellar energy spectra of nuclei heavier than helium.

These high-precision CRIS measurements were then used to study the interstellar transport of galactic cosmic rays. For this work, extensive updates to our database of measured and semi-empirical production cross sections were required. This informa-

tion is critical when modeling interstellar transport since GCRs will suffer interactions with the ambient hydrogen and helium atoms in the the interstellar medium. Appendix C documents the work required to update our transport code.

The secondary-to-primary ratios B/C and $(Sc+Ti+V)/Fe$ were then used to test the simple and nested leaky-box transport models (Chapters 4 and 5, respectively). The new and improved CRIS observations presented in this work were used to evaluate the predictions of these models at energies below $\sim$1 GeV/nucleon. Comparing the simple leaky-box model results to the data, we find the ratios and energy spectra are well fit at all energies only when an artificial, unphysical form for the galactic escape mean free path below $\sim$1 GeV/nucleon is used. A more realistic energy dependence for escape from the Galaxy resulted in poorer fits to the boron and carbon observations. We also found that the results using the artificial escape parameterization mimicked the results of the `GALPROP` transport model that fits the CRIS data by including a small amount of reacceleration at low energies.

For the nested leaky-box model, we were unable to find a single set of transport parameters that would yield a simultaneous fit of the B/C and $(Sc + Ti + V)/Fe$ ratios at all energies. To achieve a better fit to the data, this model would have required adjustments to the high-energy boron production cross sections that were larger than the uncertainties on the cross section measurements. Though some of the results are promising, further work is required before the nested leaky-box model can be considered an alternative transport model to `GALPROP` and the simple leaky-box model.

While this work focuses on the study of the interstellar transport models, we have not explored alternative models for the transport of GCRs through the heliosphere. Solar modulation significantly affects GCRs with energies below ∼1 GeV/nucleon, so a robust heliospheric transport model is required in order to best fit the CRIS observations. In this work, we have used a simplified spherically symmetric solar modulation model that includes diffusion, convection, and adiabatic deceleration, as described by the Fokker-Planck equation (refer to Equation 1.2 in Chapter 1.4.3). Our results with this model seem to fit the secondary-to-primary ratios well, though these observations are a better test of the interstellar propagation model. Future work should include a careful examination of the solar modulation model used here, as well as the consideration of more physically accurate models.

Once we have found heliospheric and interstellar models that yield the best fits to GCR observations at Earth, these models can be used to derive the GCR source abundances. These predictions will provide additional insight into source models, particularly the OB association/superbubble model (Higdon and Lingenfelter (2003); Binns et al. (2005)) that predicts a source mixture of ∼80% solar system material and ∼20% massive star ejecta.

Bibliography

Abdo, A. A., Allen, B., Berley, D., Blaufuss, E., Casanova, S., Chen, C., Coyne, D. G., Delay, R. S., Dingus, B. L., Ellsworth, R. W., Fleysher, L., Fleysher, R., Gebauer, I., Gonzalez, M. M., Goodman, J. A., Hays, E., Hoffman, C. M., Kolterman, B. E., Kelley, L. A., Lansdell, C. P., Linnemann, J. T., McEnery, J. E., Mincer, A. I., Moskalenko, I. V., Nemethy, P., Noyes, D., Ryan, J. M., Samuelson, F. W., Saz Parkinson, P. M., Schneider, M., Shoup, A., Sinnis, G., Smith, A. J., Strong, A. W., Sullivan, G. W., Vasileiou, V., Walker, G. P., Williams, D. A., Xu, X. W., and Yodh, G. B.: 2007a, *Astrophys. J.* **658**, L33

Abdo, A. A., Allen, B., Berley, D., Casanova, S., Chen, C., Coyne, D. G., Dingus, B. L., Ellsworth, R. W., Fleysher, L., Fleysher, R., Gonzalez, M. M., Goodman, J. A., Hays, E., Hoffman, C. M., Hopper, B., Hüntemeyer, P. H., Kolterman, B. E., Lansdell, C. P., Linnemann, J. T., McEnery, J. E., Mincer, A. I., Nemethy, P., Noyes, D., Ryan, J. M., Saz Parkinson, P. M., Shoup, A., Sinnis, G., Smith, A. J., Sullivan, G. W., Vasileiou, V., Walker, G. P., Williams, D. A., Xu, X. W., and Yodh, G. B.: 2007b, *Astrophys. J.* **664**, L91

Acciari, V. A., Aliu, E., Arlen, T., Aune, T., Beilicke, M., Benbow, W., Bradbury, S. M., Buckley, J. H., Bugaev, V., Byrum, K., Cannon, A., Cesarini, A., Ciupik, L., Collins-Hughes, E., Cui, W., Dickherber, R., Duke, C., Errando, M., Finley, J. P., Finnegan, G., Fortson, L., Furniss, A., Galante, N., Gall, D., Gillanders, G. H., Godambe, S., Griffin, S., Grube, J., Guenette, R., Gyuk, G., Hanna, D., Holder, J., Hughes, J. P., Hui, C. M., Humensky, T. B., Kaaret, P., Karlsson, N., Kertzman, M., Kieda, D., Krawczynski, H., Krennrich, F., Lang, M. J., LeBohec, S., Madhavan, A. S., Maier, G., Majumdar, P., McArthur, S., McCann, A., Moriarty, P., Mukherjee, R., Ong, R. A., Orr, M., Otte, A. N., Pandel, D., Park, N. H., Perkins, J. S., Pohl, M., Quinn, J., Ragan, K., Reyes, L. C., Reynolds, P. T., Roache, E., Rose, H. J., Saxon, D. B., Schroedter, M., Sembroski, G. H., Senturk, G. D., Slane, P., Smith, A. W., Tešić, G., Theiling, M., Thibadeau, S., Tsurusaki, K., Varlotta, A., Vassiliev, V. V., Vincent, S., Vivier, M., Wakely, S. P., Ward, J. E., Weekes, T. C., Weinstein, A., Weisgarber, T., Williams, D. A., Wood, M., and Zitzer, B.: 2011, *Astrophys. J.* **730**, L20

Ackermann, M., Ajello, M., Allafort, A., Baldini, L., Ballet, J., Barbiellini, G., Bastieri, D., Belfiore, A., Bellazzini, R., Berenji, B., Blandford, R. D., Bloom, E. D., Bonamente, E., Borgland, A. W., Bottacini, E., Brigida, M., Bruel, P., Buehler, R., Buson, S., Caliandro, G. A., Cameron, R. A., Caraveo, P. A., Casand-

jian, J. M., Cecchi, C., Chekhtman, A., Cheung, C. C., Chiang, J., Ciprini, S., Claus, R., Cohen-Tanugi, J., de Angelis, A., de Palma, F., Dermer, C. D., do Couto e Silva, E., Drell, P. S., Dumora, D., Favuzzi, C., Fegan, S. J., Focke, W. B., Fortin, P., Fukazawa, Y., Fusco, P., Gargano, F., Germani, S., Giglietto, N., Giordano, F., Giroletti, M., Glanzman, T., Godfrey, G., Grenier, I. A., Guillemot, L., Guiriec, S., Hadasch, D., Hanabata, Y., Harding, A. K., Hayashida, M., Hayashi, K., Hays, E., Jóhannesson, G., Johnson, A. S., Kamae, T., Katagiri, H., Kataoka, J., Kerr, M., Knödlseder, J., Kuss, M., Lande, J., Latronico, L., Lee, S.-H., Longo, F., Loparco, F., Lott, B., Lovellette, M. N., Lubrano, P., Martin, P., Mazziotta, M. N., McEnery, J. E., Mehault, J., Michelson, P. F., Mitthumsiri, W., Mizuno, T., Monte, C., Monzani, M. E., Morselli, A., Moskalenko, I. V., Murgia, S., Naumann-Godo, M., Nolan, P. L., Norris, J. P., Nuss, E., Ohsugi, T., Okumura, A., Orlando, E., Ormes, J. F., Ozaki, M., Paneque, D., Parent, D., Pesce-Rollins, M., Pierbattista, M., Piron, F., Pohl, M., Prokhorov, D., Rainò, S., Rando, R., Razzano, M., Reposeur, T., Ritz, S., Parkinson, P. M. S., Sgrò, C., Siskind, E. J., Smith, P. D., Spinelli, P., Strong, A. W., Takahashi, H., Tanaka, T., Thayer, J. G., Thayer, J. B., Thompson, D. J., Tibaldo, L., Torres, D. F., Tosti, G., Tramacere, A., Troja, E., Uchiyama, Y., Vandenbroucke, J., Vasileiou, V., Vianello, G., Vitale, V., Waite, A. P., Wang, P., Winer, B. L., Wood, K. S., Yang, Z., Zimmer, S., and Bontemps, S.: 2011, *Science* **334**, 1103

Aguilar, M., Alcaraz, J., Allaby, J., Alpat, B., Ambrosi, G., Anderhub, H., Ao, L., Arefiev, A., Arruda, L., Azzarello, P., Basile, M., Barao, F., Barreira, G., Bartoloni, A., Battiston, R., Becker, R., Becker, U., Bellagamba, L., Béné, P., Berdugo, J., Berges, P., Bertucci, B., Biland, A., Bindi, V., Boella, G., Boschini, M., Bourquin, M., Bruni, G., Buénerd, M., Burger, J. D., Burger, W. J., Cai, X. D., Cannarsa, P., Capell, M., Casadei, D., Casaus, J., Castellini, G., Cernuda, I., Chang, Y. H., Chen, H. F., Chen, H. S., Chen, Z. G., Chernoplekov, N. A., Chiueh, T. H., Choi, Y. Y., Cindolo, F., Commichau, V., Contin, A., Cortina-Gil, E., Crespo, D., Cristinziani, M., Dai, T. S., dela Guia, C., Delgado, C., Di Falco, S., Djambazov, L., D'Antone, I., Dong, Z. R., Duranti, M., Engelberg, J., Eppling, F. J., Eronen, T., Extermann, P., Favier, J., Fiandrini, E., Fisher, P. H., Flügge, G., Fouque, N., Galaktionov, Y., Gervasi, M., Giovacchini, F., Giusti, P., Grandi, D., Grimm, O., Gu, W. Q., Haino, S., Hangarter, K., Hasan, A., Hermel, V., Hofer, H., Hungerford, W., Ionica, M., Jongmanns, M., Karlamaa, K., Karpinski, W., Kenney, G., Kim, D. H., Kim, G. N., Kim, K. S., Kirn, T., Klimentov, A., Kossakowski, R., Kounine, A., Koutsenko, V., Kraeber, M., Laborie, G., Laitinen, T., Lamanna, G., Laurenti, G., Lebedev, A., Lechanoine-Leluc, C., Lee, M. W., Lee, S. C., Levi, G., Lin, C. H., Liu, H. T., Lu, G., Lu, Y. S., Lübelsmeyer, K., Luckey, D., Lustermann, W., Maña, C., Margotti, A., Mayet, F., McNeil, R. R., Menichelli, M., Mihul, A., Mujunen, A., Oliva, A., Palmonari, F., Park, H. B., Park, W. H., Pauluzzi, M., Pauss, F., Pereira, R., Perrin, E., Pevsner, A., Pilo, F., Pimenta, M., Plyaskin, V., Pojidaev, V., Pohl, M., Produit, N., Quadrani, L., Rancoita, P. G., Rapin, D., Ren, D., Ren, Z., Ribordy, M., Richeux, J. P.,

Riihonen, E., Ritakari, J., Ro, S., Roeser, U., Sagdeev, R., Santos, D., Sartorelli, G., Sbarra, C., Schael, S., Schultz von Dratzig, A., Schwering, G., Seo, E. S., Shin, J. W., Shoumilov, E., Shoutko, V., Siedenburg, T., Siedling, R., Son, D., Song, T., Spada, F. R., Spinella, F., Steuer, M., Sun, G. S., Suter, H., Tang, X. W., Ting, S. C. C., Ting, S. M., Tomassetti, N., Tornikoski, M., Torsti, J., Trümper, J., Ulbricht, J., Urpo, S., Valtonen, E., Vandenhirtz, J., Velikhov, E., Verlaat, B., Vetlitsky, I., Vezzu, F., Vialle, J. P., Viertel, G., Vité, D., Von Gunten, H., Waldmeier Wicki, S., Wallraff, W., Wang, J. Z., Wiik, K., Williams, C., Wu, S. X., Xia, P. C., Xu, S., Xu, Z. Z., Yan, J. L., Yan, L. G., Yang, C. G., Yang, J., Yang, M., Ye, S. W., Zhang, H. Y., Zhang, Z. P., Zhao, D. X., Zhou, F., Zhou, Y., Zhu, G. Y., Zhu, W. Z., Zhuang, H. L., Zichichi, A., Zimmermann, B., and Zuccon, P.: 2010, *Astrophys. J.* **724**, 329

Ahn, H. S., Allison, P. S., Bagliesi, M. G., Beatty, J. J., Bigongiari, G., Boyle, P. J., Brandt, T. J., Childers, J. T., Conklin, N. B., Coutu, S., Duvernois, M. A., Ganel, O., Han, J. H., Hyun, H. J., Jeon, J. A., Kim, K. C., Lee, J. K., Lee, M. H., Lutz, L., Maestro, P., Malinin, A., Marrocchesi, P. S., Minnick, S. A., Mognet, S. I., Nam, S., Nutter, S. L., Park, I. H., Park, N. H., Seo, E. S., Sina, R., Swordy, S. P., Wakely, S. P., Wu, J., Yang, J., Yoon, Y. S., Zei, R., and Zinn, S. Y.: 2008, *Astroparticle Physics* **30**, 133

Allbritton, G. L., Andersen, H., Barnes, A., Christian, E. R., Cummings, A. C., Dougherty, B. L., Jensen, L., Lee, J., Leske, R. A., Madden, M. P., Mewaldt, R., Milliken, B., Nahory, B. W., O'Donnell, R., Schmidt, P., Sears, B. R., von Rosenvinge, T. T., Walton, J. T., Wiedenbeck, M. E., and Wong, Y. K.: 1996, *IEEE Transactions on Nuclear Science* **43**, 1505

Antoni, T., Apel, W. D., Badea, A. F., Bekk, K., Bercuci, A., Blümer, H., Bozdog, H., Brancus, I. M., Büttner, C., Daumiller, K., Doll, P., Engel, R., Engler, J., Fessler, F., Gils, H. J., Glasstetter, R., Haungs, A., Heck, D., Hörandel, J. R., Kampert, K.-H., Klages, H. O., Maier, G., Mathes, H. J., Mayer, H. J., Milke, J., Müller, M., Obenland, R., Oehlschläger, J., Ostapchenko, S., Petcu, M., Rebel, H., Risse, A., Risse, M., Roth, M., Schatz, G., Schieler, H., Scholz, J., Thouw, T., Ulrich, H., van Buren, J., Vardanyan, A., Weindl, A., Wochele, J., Zabierowski, J., and KASCADE Collaboration: 2004, *Astrophys. J.* **604**, 687

Ave, M., Boyle, P. J., Gahbauer, F., Höppner, C., Hörandel, J. R., Ichimura, M., Müller, D., and Romero-Wolf, A.: 2008, *Astrophys. J.* **678**, 262

Ave, M., Boyle, P. J., Höppner, C., Marshall, J., and Müller, D.: 2009, *Astrophys. J.* **697**, 106

Barghouty, A. F.: 2010, *Partial interaction cross sections of protons on heavy nuclei*, private communication

Bevington, P. R. and Robinson, D. K.: 2003, *Data reduction and error analysis for the physical sciences*

Binns, W. R., Wiedenbeck, M. E., Arnould, M., Cummings, A. C., de Nolfo, G. A., Goriely, S., Israel, M. H., Leske, R. A., Mewaldt, R. A., Meynet, G., Scott, L. M., Stone, E. C., and von Rosenvinge, T. T.: 2007, *Space Sci. Rev.* **130**, 439

Binns, W. R., Wiedenbeck, M. E., Arnould, M., Cummings, A. C., de Nolfo, G. A., Goriely, S., Israel, M. H., Leske, R. A., Mewaldt, R. A., Stone, E. C., and von Rosenvinge, T. T.: 2008, *New Astronomy Rev.* **52**, 427

Binns, W. R., Wiedenbeck, M. E., Arnould, M., Cummings, A. C., George, J. S., Goriely, S., Israel, M. H., Leske, R. A., Mewaldt, R. A., Meynet, G., Scott, L. M., Stone, E. C., and von Rosenvinge, T. T.: 2005, *Astrophys. J.* **634**, 351

Bodemann, R., Lange, H.-J., Leya, I., Michel, R., Schiekel, T., Rösel, R., Herpers, U., Hofmann, H. J., Dittrich, B., Suter, M., Wölfli, W., Holmqvist, B., Condé, H., and Malmborg, P.: 1993, *Nuclear Instruments and Methods in Physics Research B* **82**, 9

Casse, M. and Goret, P.: 1978, *Astrophys. J.* **221**, 703

Casse, M. and Paul, J. A.: 1982, *Astrophys. J.* **258**, 860

Chen, C.-X., Albergo, S., Caccia, Z., Costa, S., Crawford, H. J., Cronqvist, M., Engelage, J., Greiner, L., Guzik, T. G., Insolia, A., Knott, C. N., Lindstrom, P. J., McMahon, M., Mitchell, J. W., Potenza, R., Russo, G. V., Soutoul, A., Testard, O., Tull, C. E., Tuve, C., Waddington, C. J., Webber, W. R., and Wefel, J. P.: 1997a, *Astrophys. J.* **479**, 504

Chen, C.-X., Albergo, S., Caccia, Z., Costa, S., Crawford, H. J., Cronqvist, M., Engelage, J., Greiner, L., Guzik, T. G., Insolia, A., Knott, C. N., Lindstrom, P. J., McMahon, M., Mitchell, J. W., Potenza, R., Russo, G. V., Soutoul, A., Testard, O., Tull, C. E., Tuvé, C., Waddington, C. J., Webber, W. R., and Wefel, J. P.: 1997b, *Phys. Rev. C* **56**, 1536

Cowsik, R. and Burch, B.: 2010, *Phys. Rev. D* **82(2)**, 023009

Cowsik, R., Pal, Y., Tandon, S. N., and Verma, R. P.: 1967, *Physical Review* **158**, 1238

Cowsik, R. and Wilson, L. W.: 1973, in *International Cosmic Ray Conference*, Vol. 1 of *International Cosmic Ray Conference*, pp 500–+

Cowsik, R. and Wilson, L. W.: 1975, in *International Cosmic Ray Conference*, Vol. 2 of *International Cosmic Ray Conference*, pp 659–+

Crawford, H. J.: 1979, *Ph.D. thesis*, California Univ., Berkeley.

Davis, A. J., Mewaldt, R. A., Binns, W. R., Christian, E. R., Cummings, A. C., George, J. S., Hink, P. L., Leske, R. A., von Rosenvinge, T. T., Wiedenbeck, M. E., and Yanasak, N. E.: 2000, in R. A. Mewaldt, J. R. Jokipii, M. A. Lee, E. Möbius, & T. H. Zurbuchen (ed.), *Acceleration and Transport of Energetic Particles Observed in the Heliosphere*, Vol. 528 of *American Institute of Physics Conference Series*, pp 421–424

de Nolfo, G. A.: 2010, *CRIS SOFT efficiencies parameterized by telescope*, private communication

de Nolfo, G. A., Moskalenko, I. V., Binns, W. R., Christian, E. R., Cummings, A. C., Davis, A. J., George, J. S., Hink, P. L., Israel, M. H., Leske, R. A., Lijowski, M., Mewaldt, R. A., Stone, E. C., Strong, A. W., von Rosenvinge, T. T., Wiedenbeck, M. E., and Yanasak, N. E.: 2006, *Advances in Space Research* **38**, 1558

Derrickson, J. H., Parnell, T. A., Austin, R. W., Selig, W. J., and Gregory, J. C.:

1992, *International Journal of Radiation Applications and Instrumentation D Nuclear Tracks and Radiation Measurements* **20**, 415

Duvernois, M. A. and Thayer, M. R.: 1996, *Astrophys. J.* **465**, 982

Engelmann, J. J., Ferrando, P., Soutoul, A., Goret, P., and Juliusson, E.: 1990, *Astron. Astrophys.* **233**, 96

Firestone, R. B. and Shirley, V. S.: 1998, *Table of Isotopes, 2 Volume Set*

Fisk, L. A.: 1971, *J. Geophys. Res.* **76**, 221

Garcia-Munoz, M., Mason, G. M., Simpson, J. A., and Wefel, J. P.: 1977, in *International Cosmic Ray Conference*, Vol. 1 of *International Cosmic Ray Conference*, pp 230–235

George, J. S.: 1999, *Electron capture half-life corrections*, private communication

George, J. S., Lave, K. A., Wiedenbeck, M. E., Binns, W. R., Cummings, A. C., Davis, A. J., de Nolfo, G. A., Hink, P. L., Israel, M. H., Leske, R. A., Mewaldt, R. A., Scott, L. M., Stone, E. C., von Rosenvinge, T. T., and Yanasak, N. E.: 2009, *Astrophys. J.* **698**, 1666

Ginzburg, V. L. and Syrovatskii, S. I.: 1964, *The Origin of Cosmic Rays*

Giordano, F., Naumann-Godo, M., Ballet, J., Bechtol, K., Funk, S., Lande, J., Mazziotta, M. N., Rainò, S., Tanaka, T., Tibolla, O., and Uchiyama, Y.: 2012, *Astrophys. J.* **744**, L2

Gleeson, L. J. and Axford, W. I.: 1968, *Astrophys. J.* **154**, 1011

Gloeckler, G. and Jokipii, J. R.: 1969, *Physical Review Letters* **22**, 1448

Goldstein, M. L., Fisk, L. A., and Ramaty, R.: 1970, *Physical Review Letters* **25**, 832

Greisen, K.: 1966, *Physical Review Letters* **16**, 748

Higdon, J. C. and Lingenfelter, R. E.: 2003, *Astrophys. J.* **590**, 822

Higdon, J. C. and Lingenfelter, R. E.: 2005, *Astrophys. J.* **628**, 738

Higdon, J. C., Lingenfelter, R. E., and Ramaty, R.: 1998, *Astrophys. J.* **509**, L33

Hirzebruch, S. E., Winkel, E., and Heinrich, W.: 1993, in *International Cosmic Ray Conference*, Vol. 2 of *International Cosmic Ray Conference*, pp 175–+

Jokipii, J. R., Levy, E. H., and Hubbard, W. B.: 1977, *Astrophys. J.* **213**, 861

Jokipii, J. R. and Thomas, B.: 1981, *Astrophys. J.* **243**, 1115

Knott, C. N., Albergo, S., Caccia, Z., Chen, C.-X., Costa, S., Crawford, H. J., Cronqvist, M., Engelage, J., Greiner, L., Guzik, T. G., Insolia, A., Lindstrom, P. J., Mitchell, J. W., Potenza, R., Russo, G. V., Soutoul, A., Testard, O., Tull, C. E., Tuvé, C., Waddington, C. J., Webber, W. R., and Wefel, J. P.: 1997, *Phys. Rev. C* **56**, 398

Korejwo, A., Giller, M., Dzikowski, T., Perelygin, V. V., and Zarubin, A. V.: 2002, *Journal of Physics G Nuclear Physics* **28**, 1199

Kox, S., Gamp, A., Perrin, C., Arvieux, J., Bertholet, R., Bruandet, J. F., Buenerd, M., Cherkaoui, R., Cole, A. J., El-Masri, Y., Longequeue, N., Menet, J., Merchez, F., and Viano, J. B.: 1987, *Phys. Rev. C* **35**, 1678

Leske, R. A.: 1993, *Astrophys. J.* **405**, 567

Letaw, J. R., Silberberg, R., and Tsao, C. H.: 1983, *Astrophys. J. Supp.* **51**, 271

Lezniak, J. A. and Webber, W. R.: 1978, *Astrophys. J.* **223**, 676

Lodders, K., Palme, H., and Gail, H.-P.: 2009, in *Landolt-Börnstein - Group VI Astronomy and Astrophysics Numerical Data and Functional Relationships in Science and Technology Volume 4B: Solar System. Edited by J.E. Trümper, 2009, 4.4.*, pp 44–+

Longair, M. S.: 1992, *High energy astrophysics. Vol.1: Particles, photons and their detection*

Meneguzzi, M., Audouze, J., and Reeves, H.: 1971, *Astron. Astrophys.* **15**, 337

Mewaldt, R. A., Davis, A. J., Lave, K. A., Leske, R. A., Stone, E. C., Wiedenbeck, M. E., Binns, W. R., Christian, E. R., Cummings, A. C., de Nolfo, G. A., Israel, M. H., Labrador, A. W., and von Rosenvinge, T. T.: 2010, *Astrophys. J.* **723**, L1

Meyer, J.-P., Drury, L. O., and Ellison, D. C.: 1997, *Astrophys. J.* **487**, 182

Michel, R., Bodemann, R., Busemann, H., Daunke, R., Gloris, M., Lange, H.-J., Klug, B., Krins, A., Leya, I., Lüpke, M., Neumann, S., Reinhardt, H., Schnatz-Büttgen, M., Herpers, U., Schiekel, T., Sudbrock, F., Holmqvist, B., Condé, H., Malmborg, P., Suter, M., Dittrich-Hannen, B., Kubik, P.-W., Synal, H.-A., and Filges, D.: 1997, *Nuclear Instruments and Methods in Physics Research B* **129**, 153

Michel, R., Gloris, M., Lange, H.-J., Leya, I., Lüpke, M., Herpers, U., Dittrich-Hannen, B., Rösel, R., Schiekel, T., Filges, D., Dragovitsch, P., Suter, M., Hofmann, H.-J., Wölfli, W., Kubik, P. W., Baur, H., and Wieler, R.: 1995, *Nuclear Instruments and Methods in Physics Research B* **103**, 183

Michel, R., Peiffer, F., Theis, S., Begemann, F., Weber, H., Signer, P., Wieler, R., Cloth, P., Dragovitsch, P., Filges, D., and Englert, P.: 1989, *Nuclear Instruments and Methods in Physics Research B* **42**, 76

Moskalenko, I. V., Strong, A. W., Mashnik, S. G., and Ormes, J. F.: 2003, *Astrophys. J.* **586**, 1050

Napolitani, P., Schmidt, K.-H., Botvina, A. S., Rejmund, F., Tassan-Got, L., and Villagrasa, C.: 2004, *Phys. Rev. C* **70(5)**, 054607

Niebur, S. M., Scott, L. M., Wiedenbeck, M. E., Binns, W. R., Christian, E. R., Cummings, A. C., Davis, A. J., George, J. S., Hink, P. L., Israel, M. H., Leske, R. A., Mewaldt, R. A., Stone, E. C., von Rosenvinge, T. T., and Yanasak, N. E.: 2003, *Journal of Geophysical Research (Space Physics)* **108**, 8033

Obermeier, A., Ave, M., Boyle, P., Höppner, C., Hörandel, J., and Müller, D.: 2011, *Astrophys. J.* **742**, 14

Ogliore, R. C.: 2006, *Ph.D. thesis*, California Institute of Technology

Opher, M., Bibi, F. A., Toth, G., Richardson, J. D., Izmodenov, V. V., and Gombosi, T. I.: 2009, *Nature* **462**, 1036

Panov, A. D., Sokolskaya, N. V., Adams, Jr., J. H., and et al.: 2008, in *International Cosmic Ray Conference*, Vol. 2 of *International Cosmic Ray Conference*, pp 3–6

Parker, E. N.: 1965, *Planetary Space Sci.* **13**, 9

Parker, E. N.: 1966, *Planetary Space Sci.* **14**, 371

Press, W. H., Teukolsky, S. A., Vetterling, W. T., and Flannery, B. P.: 1992, *Numerical recipes in C. The art of scientific computing*

Pritychenko, B., Arcilla, R., Burrows, T. W., Dunford, C. L., Herman, M. W.,

McLane, V., Obložinský, P., Sonzogni, A. A., Tuli, J. K., and Winchell, D. F.: 2005, in R. C. Haight, M. B. Chadwick, T. Kawano, & P. Talou (ed.), *International Conference on Nuclear Data for Science and Technology*, Vol. 769 of *American Institute of Physics Conference Series*, pp 132–135

Ptuskin, V. S., Moskalenko, I. V., Jones, F. C., Strong, A. W., and Zirakashvili, V. N.: 2006, *Astrophys. J.* **642**, 902

Ptuskin, V. S. and Soutoul, A.: 1998, *Astron. Astrophys.* **337**, 859

Rauch, B. F., Link, J. T., Lodders, K., Israel, M. H., Barbier, L. M., Binns, W. R., Christian, E. R., Cummings, J. R., de Nolfo, G. A., Geier, S., Mewaldt, R. A., Mitchell, J. W., Schindler, S. M., Scott, L. M., Stone, E. C., Streitmatter, R. E., Waddington, C. J., and Wiedenbeck, M. E.: 2009, *Astrophys. J.* **697**, 2083

Schiekel, T., Sudbrock, F., Herpers, U., Gloris, M., Lange, H.-J., Leya, I., Michel, R., Dittrich-Hannen, B., Synal, H.-A., Suter, M., Kubik, P. W., Blann, M., and Filges, D.: 1996, *Nuclear Instruments and Methods in Physics Research B* **114**, 91

Scott, L. M.: 2005, *Ph.D. thesis*, Washington University

Silberberg, R., Tsao, C. H., and Barghouty, A. F.: 1998, *Astrophys. J.* **501**, 911

Silberberg, R., Tsao, C. H., and Letaw, J. R.: 1985, *Astrophys. J. Supp.* **58**, 873

Soutoul, A., Ferrando, P., and Webber, R. W.: 1990, in *International Cosmic Ray Conference*, Vol. 3 of *International Cosmic Ray Conference*, pp 337–+

Stone, E. C., Cohen, C. M. S., Cook, W. R., Cummings, A. C., Gauld, B., Kecman, B., Leske, R. A., Mewaldt, R. A., Thayer, M. R., Dougherty, B. L., Grumm, R. L., Milliken, B. D., Radocinski, R. G., Wiedenbeck, M. E., Christian, E. R., Shuman, S., Trexel, H., von Rosenvinge, T. T., Binns, W. R., Crary, D. J., Dowkontt, P., Epstein, J., Hink, P. L., Klarmann, J., Lijowski, M., and Olevitch, M. A.: 1998a, *Space Sci. Rev.* **86**, 285

Stone, E. C., Frandsen, A. M., Mewaldt, R. A., Christian, E. R., Margolies, D., Ormes, J. F., and Snow, F.: 1998b, *Space Sci. Rev.* **86**, 1

Streitmatter, R. E., Balasubrahmanyan, V. K., Ormes, J. F., and Protheroe, R. J.: 1985, *Astron. Astrophys.* **143**, 249

Strong, A. W. and Moskalenko, I. V.: 1998, *Astrophys. J.* **509**, 212

Strong, A. W. and Moskalenko, I. V.: 2001, *Advances in Space Research* **27**, 717

Strong, A. W., Moskalenko, I. V., and Ptuskin, V. S.: 2007, *Annual Review of Nuclear and Particle Science* **57**, 285

Swordy, S. P.: 2001, *Space Sci. Rev.* **99**, 85

Swordy, S. P., Mueller, D., Meyer, P., L'Heureux, J., and Grunsfeld, J. M.: 1990, *Astrophys. J.* **349**, 625

Takeda, M., Hayashida, N., Honda, K., Inoue, N., Kadota, K., Kakimoto, F., Kamata, K., Kawaguchi, S., Kawasaki, Y., Kawasumi, N., Kusano, E., Matsubara, Y., Murakami, K., Nagano, M., Nishikawa, D., Ohoka, H., Osone, S., Sakaki, N., Sasaki, M., Shinozaki, K., Souma, N., Teshima, M., Torii, R., Tsushima, I., Uchihori, Y., Yamamoto, T., Yoshida, S., and Yoshii, H.: 1999, *Astrophys. J.* **522**, 225

Titarenko, Y. E., Batyaev, V. F., Titarenko, A. Y., Butko, M. A., Pavlov, K. V., Florya, S. N., Tikhonov, R. S., Mashnik, S. G., Ignatyuk, A. V., Titarenko, N. N., Gudowski, W., Těšínský, M., Persson, C.-M. L., Abderrahim, H. A., Kumawat, H., and Duarte, H.: 2008, *Phys. Rev. C* **78(3)**, 034615

Tripathi, R. K., Cucinotta, F. A., and Wilson, J. W.: 1997, *Universal Parameterization of Absorption Cross Sections*, Technical Paper 3621

Tsao, C. H., Silberberg, R., and Barghouty, A. F.: 1998, *Astrophys. J.* **501**, 920

Usoskin, I. G., Bazilevskaya, G. A., and Kovaltsov, G. A.: 2011, *Journal of Geophysical Research (Space Physics)* **116**, 2104

Villagrasa-Canton, C.: 2003, *Ph.D. thesis*, Université de Paris XI, France

Villagrasa-Canton, C., Boudard, A., Ducret, J.-E., Fernandez, B., Leray, S., Volant, C., Armbruster, P., Enqvist, T., Hammache, F., Helariutta, K., Jurado, B., Ricciardi, M.-V., Schmidt, K.-H., Sümmerer, K., Vivès, F., Yordanov, O., Audouin, L., Bacri, C.-O., Ferrant, L., Napolitani, P., Rejmund, F., Stéphan, C., Tassan-Got, L., Benlliure, J., Casarejos, E., Fernandez-Ordoñez, M., Pereira, J., Czajkowski, S., Karamanis, D., Pravikoff, M., George, J. S., Mewaldt, R. A., Yanasak, N., Wiedenbeck, M., Connell, J. J., Faestermann, T., Heinz, A., and Junghans, A.: 2007, *Phys. Rev. C* **75(4)**, 044603

Vonach, H., Pavlik, A., Wallner, A., Drosg, M., Haight, R. C., Drake, D. M., and Chiba, S.: 1997, *Phys. Rev. C* **55**, 2458

Wang, J. Z., Seo, E. S., Anraku, K., Fujikawa, M., Imori, M., Maeno, T., Matsui, N., Matsunaga, H., Motoki, M., Orito, S., Saeki, T., Sanuki, T., Ueda, I., Yoshimura, K., Makida, Y., Suzuki, J., Tanaka, K., Yamamoto, A., Yoshida, T., Mitsui, T., Matsumoto, H., Nozaki, M., Sasaki, M., Mitchell, J., Moiseev, A., Ormes, J., Streitmatter, R., Nishimura, J., Yajima, Y., and Yamagami, T.: 2002, *Astrophys. J.* **564**, 244

Webber, W. R., Kish, J. C., Rockstroh, J. M., Cassagnou, Y., Legrain, R., Soutoul, A., Testard, O., and Tull, C.: 1998a, *Astrophys. J.* **508**, 949

Webber, W. R., Kish, J. C., and Schrier, D. A.: 1990a, *Phys. Rev. C* **41**, 566

Webber, W. R., Kish, J. C., and Schrier, D. A.: 1990b, *Phys. Rev. C* **41**, 547

Webber, W. R., Kish, J. C., and Schrier, D. A.: 1990c, *Phys. Rev. C* **41**, 520

Webber, W. R., Soutoul, A., Kish, J. C., Rockstroh, J. M., Cassagnou, Y., Legrain, R., and Testard, O.: 1998b, *Phys. Rev. C* **58**, 3539

Wiedenbeck, M. E.: 2006, *Galactic Cosmic Ray Isotopic Composition from CRIS*, `http://www.srl.caltech.edu/ACE/ASC/DATA/level3/cris/isotopic$_$composition.html`

Wiedenbeck, M. E.: 2010, *Leaky-box code for cosmic-ray transport*, private communication

Wiedenbeck, M. E.: 2011, *Time-varying solar modulation values for select primary species*, private communication

Wiedenbeck, M. E., Binns, W. R., Christian, E. R., Cummings, A. C., Dougherty, B. L., Hink, P. L., Klarmann, J., Leske, R. A., Lijowski, M., Mewaldt, R. A., Stone, E. C., Thayer, M. R., von Rosenvinge, T. T., and Yanasak, N. E.: 1999,

Astrophys. J. **523**, L61

Wiedenbeck, M. E., Binns, W. R., Cummings, A. C., and et al.: 2008, in *International Cosmic Ray Conference*, Vol. 2 of *International Cosmic Ray Conference*, pp 149–152

Wiedenbeck, M. E., Yanasak, N. E., Cummings, A. C., Davis, A. J., George, J. S., Leske, R. A., Mewaldt, R. A., Stone, E. C., Hink, P. L., Israel, M. H., Lijowski, M., Christian, E. R., and von Rosenvinge, T. T.: 2001, *Space Sci. Rev.* **99**, 15

Wilson, L. W.: 1978, *Ph.D. thesis*, California Univ., Berkeley.

Woosley, S. E. and Weaver, T. A.: 1995, *Astrophys. J. Supp.* **101**, 181

Yanasak, N. E.: 2000, *Total interaction cross section renormalization*, private communication

Yanasak, N. E., Wiedenbeck, M. E., Mewaldt, R. A., Davis, A. J., Cummings, A. C., George, J. S., Leske, R. A., Stone, E. C., Christian, E. R., von Rosenvinge, T. T., Binns, W. R., Hink, P. L., and Israel, M. H.: 2001, *Astrophys. J.* **563**, 768

Young, J. S., Freier, P. S., Waddington, C. J., Brewster, N. R., and Fickle, R. K.: 1981, *Astrophys. J.* **246**, 1014

Appendix A

CRIS Solar Minimum Data

The 1997-98 and 2009-10 CRIS solar minimum energy spectra (plotted in Figures 3.7 through 3.10 in Section 3.7.1) are given in Tables A.1 and A.2. These spectra have also been interpolated to a common energy grid, given in Tables A.3 and A.4. The reported uncertainties are the quadratic summation of the statistical and systematic contributions, as discussed in Section 3.6.

Element	Energies (MeV/nucleon) 1997-98 Intensities (10^{-9} [cm^2 s sr MeV/nucleon]$^{-1}$)						
B	59.6	79.7	102.0	121.1	138.2	154.0	168.6
	109.7 ± 4.0	133.8 ± 4.5	158.9 ± 5.8	167.3 ± 6.6	188.6 ± 7.9	199.4 ± 9.1	204.6 ± 10.0
C	68.3	91.4	117.2	139.2	159.1	177.3	194.4
	518.3 ± 15.8	618.2 ± 19.1	724.0 ± 23.8	774.6 ± 27.6	811.4 ± 31.0	833.2 ± 34.8	829.7 ± 37.7
N	73.2	98.1	125.8	149.5	170.9	190.6	209.1
	126.0 ± 4.4	145.8 ± 4.9	175.9 ± 6.3	185.2 ± 7.2	196.0 ± 8.3	207.3 ± 9.6	195.4 ± 9.8
O	80.4	107.8	138.4	164.7	188.4	210.2	230.7
	578.9 ± 17.6	673.4 ± 20.9	760.4 ± 25.6	791.3 ± 29.0	805.2 ± 32.2	829.5 ± 36.8	790.6 ± 38.2
F	83.5	112.0	143.8	171.1	195.9	218.6	240.0
	7.7 ± 0.6	8.5 ± 0.5	10.8 ± 0.7	11.8 ± 0.8	12.0 ± 0.9	12.2 ± 1.1	12.2 ± 1.1
Ne	89.4	120.0	154.3	183.8	210.5	235.1	258.2
	83.0 ± 3.0	97.2 ± 3.4	110.3 ± 4.2	118.3 ± 4.9	117.4 ± 5.4	116.6 ± 6.0	117.8 ± 6.6
Na	94.0	126.2	162.3	193.5	221.7	247.8	272.3
	16.5 ± 0.9	19.8 ± 0.9	21.5 ± 1.1	20.8 ± 1.2	22.2 ± 1.4	23.7 ± 1.6	22.9 ± 1.7
Mg	100.2	134.6	173.3	206.7	237.0	265.0	291.4
	120.2 ± 4.1	139.3 ± 4.7	153.6 ± 5.7	166.4 ± 6.8	162.4 ± 7.4	163.3 ± 8.4	154.9 ± 8.8
Al	103.8	139.6	179.8	214.5	246.1	275.3	302.8
	16.6 ± 0.9	20.2 ± 0.9	23.9 ± 1.2	22.3 ± 1.2	24.3 ± 1.5	23.7 ± 1.6	22.2 ± 1.7
Si	110.0	148.2	191.0	228.1	261.8	293.0	322.5
	90.9 ± 3.2	106.8 ± 3.7	114.7 ± 4.4	117.4 ± 5.1	121.2 ± 5.8	120.6 ± 6.5	109.7 ± 6.6
P	112.7	151.8	195.8	233.9	268.6	300.8	331.1
	2.4 ± 0.3	2.9 ± 0.2	3.4 ± 0.3	3.2 ± 0.4	3.2 ± 0.4	3.2 ± 0.4	3.8 ± 0.5
S	118.2	159.3	205.6	245.8	282.4	316.4	348.5
	14.3 ± 0.8	16.8 ± 0.8	18.8 ± 1.0	20.3 ± 1.2	19.3 ± 1.2	19.7 ± 1.4	18.4 ± 1.4
Cl	120.0	161.8	209.0	249.9	287.2	321.8	354.5
	2.7 ± 0.3	2.5 ± 0.2	3.1 ± 0.3	3.3 ± 0.3	3.8 ± 0.4	3.5 ± 0.4	3.3 ± 0.5
Ar	125.1	168.9	218.2	261.1	300.2	336.6	371.0
	5.7 ± 0.4	6.6 ± 0.4	6.7 ± 0.5	7.9 ± 0.6	8.6 ± 0.7	8.1 ± 0.7	7.5 ± 0.8
K	127.9	172.7	223.3	267.3	307.4	344.8	380.2
	3.8 ± 0.3	4.5 ± 0.3	5.5 ± 0.4	5.7 ± 0.5	6.1 ± 0.6	6.6 ± 0.6	5.9 ± 0.6
Ca	131.7	178.1	230.3	275.9	317.5	356.2	392.9
	11.9 ± 0.7	15.0 ± 0.7	16.1 ± 0.9	17.0 ± 1.0	16.9 ± 1.1	17.3 ± 1.3	16.8 ± 1.4
Sc	133.5	180.5	233.6	279.9	322.2	361.5	398.8
	2.9 ± 0.3	3.0 ± 0.2	3.3 ± 0.3	3.7 ± 0.4	3.3 ± 0.4	3.5 ± 0.4	3.6 ± 0.5
Ti	137.1	185.5	240.1	287.9	331.5	372.1	410.7
	10.4 ± 0.6	11.9 ± 0.6	13.2 ± 0.7	12.7 ± 0.8	12.7 ± 0.9	12.2 ± 1.0	12.4 ± 1.1
V	139.9	189.4	245.4	294.3	339.0	380.7	420.3
	4.6 ± 0.4	5.6 ± 0.3	5.8 ± 0.4	6.1 ± 0.5	6.7 ± 0.6	5.3 ± 0.6	6.1 ± 0.7
Cr	143.9	194.9	252.7	303.1	349.4	392.5	433.5
	10.7 ± 0.6	11.7 ± 0.6	11.6 ± 0.7	12.1 ± 0.8	12.2 ± 0.9	11.4 ± 1.0	11.1 ± 1.0
Mn	146.8	199.0	258.1	309.7	357.1	401.3	443.4
	6.9 ± 0.5	7.0 ± 0.4	8.0 ± 0.5	7.3 ± 0.5	7.7 ± 0.6	6.8 ± 0.7	6.0 ± 0.7
Fe	150.5	204.1	264.9	318.1	367.0	412.6	455.9
	72.7 ± 2.6	78.3 ± 2.9	79.1 ± 3.4	76.4 ± 3.9	73.7 ± 4.3	69.7 ± 4.6	64.5 ± 4.8
Co	153.5	208.4	270.6	325.1	375.2	422.0	466.5
	0.63 ± 0.12	0.39 ± 0.08	0.52 ± 0.10	0.49 ± 0.11	0.53 ± 0.13	0.42 ± 0.13	0.51 ± 0.15
Ni	159.0	216.0	280.7	337.5	389.7	438.5	485.0
	3.6 ± 0.3	3.5 ± 0.2	3.9 ± 0.3	3.9 ± 0.4	3.6 ± 0.4	3.2 ± 0.4	3.6 ± 0.5

Table A.1: CRIS 1997-98 solar minimum spectra. Systematic and statistical uncertainties are combined in quadrature.

Element	Energies (MeV/nucleon) 2009-10 Intensities (10^{-9} [cm^2 s sr MeV/nucleon]$^{-1}$)						
B	59.6 133.1 ± 4.4	79.7 157.6 ± 5.0	102.0 190.2 ± 6.4	121.1 204.9 ± 7.5	138.2 220.0 ± 8.6	154.0 241.0 ± 10.3	168.6 235.7 ± 10.8
C	68.3 642.6 ± 19.1	91.4 771.8 ± 23.5	117.2 904.4 ± 29.3	139.2 948.5 ± 33.3	159.1 1006.7 ± 37.9	177.3 1005.7 ± 41.3	194.4 1002.7 ± 44.9
N	73.2 151.5 ± 4.7	98.1 179.0 ± 5.6	125.8 208.5 ± 7.0	149.5 225.8 ± 8.3	170.9 238.6 ± 9.5	190.6 242.0 ± 10.5	209.1 239.0 ± 11.3
O	80.4 710.0 ± 21.0	107.8 842.0 ± 25.7	138.4 938.7 ± 31.2	164.7 973.3 ± 35.1	188.4 998.8 ± 39.4	210.2 998.1 ± 43.7	230.7 968.3 ± 46.2
F	83.5 9.8 ± 0.5	112.0 11.7 ± 0.5	143.8 12.4 ± 0.6	171.1 13.7 ± 0.7	195.9 13.7 ± 0.8	218.6 15.2 ± 1.0	240.0 15.5 ± 1.0
Ne	89.4 102.2 ± 3.3	120.0 117.6 ± 3.8	154.3 137.1 ± 4.8	183.8 139.5 ± 5.4	210.5 143.0 ± 6.2	235.1 147.0 ± 7.0	258.2 139.1 ± 7.3
Na	94.0 19.5 ± 0.8	126.2 22.2 ± 0.8	162.3 25.4 ± 1.0	193.5 27.4 ± 1.2	221.7 27.5 ± 1.4	247.8 27.2 ± 1.5	272.3 28.9 ± 1.8
Mg	100.2 150.6 ± 4.7	134.6 174.3 ± 5.6	173.3 189.8 ± 6.8	206.7 195.2 ± 7.7	237.0 195.2 ± 8.6	265.0 194.2 ± 9.6	291.4 188.4 ± 10.3
Al	103.8 22.3 ± 0.9	139.6 25.7 ± 0.9	179.8 28.9 ± 1.2	214.5 29.2 ± 1.3	246.1 29.3 ± 1.5	275.3 31.6 ± 1.8	302.8 29.0 ± 1.8
Si	110.0 113.5 ± 3.6	148.2 130.1 ± 4.2	191.0 140.5 ± 5.1	228.1 144.1 ± 5.9	261.8 141.2 ± 6.4	293.0 140.0 ± 7.2	322.5 132.7 ± 7.6
P	112.7 2.9 ± 0.2	151.8 3.4 ± 0.2	195.8 4.2 ± 0.3	233.9 4.0 ± 0.3	268.6 4.6 ± 0.4	300.8 4.4 ± 0.4	331.1 4.5 ± 0.4
S	118.2 18.1 ± 0.7	159.3 20.7 ± 0.8	205.6 22.9 ± 1.0	245.8 24.7 ± 1.2	282.4 23.7 ± 1.3	316.4 23.3 ± 1.4	348.5 22.5 ± 1.5
Cl	120.0 2.8 ± 0.2	161.8 3.1 ± 0.2	209.0 4.2 ± 0.3	249.9 4.1 ± 0.3	287.2 4.4 ± 0.3	321.8 4.2 ± 0.4	354.5 4.0 ± 0.4
Ar	125.1 6.0 ± 0.3	168.9 7.8 ± 0.3	218.2 8.9 ± 0.4	261.1 9.3 ± 0.5	300.2 10.0 ± 0.6	336.6 9.3 ± 0.7	371.0 10.3 ± 0.8
K	127.9 4.8 ± 0.3	172.7 5.5 ± 0.3	223.3 6.3 ± 0.3	267.3 6.9 ± 0.4	307.4 7.4 ± 0.5	344.8 7.4 ± 0.6	380.2 7.4 ± 0.6
Ca	131.7 14.6 ± 0.6	178.1 16.6 ± 0.6	230.3 19.2 ± 0.8	275.9 18.4 ± 0.9	317.5 20.3 ± 1.2	356.2 20.8 ± 1.3	392.9 20.2 ± 1.4
Sc	133.5 2.9 ± 0.2	180.5 3.7 ± 0.2	233.6 3.9 ± 0.2	279.9 4.5 ± 0.3	322.2 4.1 ± 0.3	361.5 4.3 ± 0.4	398.8 3.7 ± 0.4
Ti	137.1 12.8 ± 0.5	185.5 14.1 ± 0.6	240.1 15.1 ± 0.7	287.9 15.2 ± 0.8	331.5 15.1 ± 0.9	372.1 14.8 ± 1.0	410.7 14.0 ± 1.1
V	139.9 6.2 ± 0.3	189.4 6.7 ± 0.3	245.4 7.3 ± 0.4	294.3 7.5 ± 0.5	339.0 7.4 ± 0.5	380.7 5.9 ± 0.5	420.3 7.0 ± 0.6
Cr	143.9 12.7 ± 0.5	194.9 14.2 ± 0.6	252.7 14.3 ± 0.7	303.1 14.6 ± 0.8	349.4 13.2 ± 0.8	392.5 12.4 ± 0.9	433.5 13.1 ± 1.0
Mn	146.8 8.1 ± 0.4	199.0 8.7 ± 0.4	258.1 9.0 ± 0.5	309.7 8.7 ± 0.5	357.1 8.2 ± 0.6	401.3 8.7 ± 0.7	443.4 7.9 ± 0.7
Fe	150.5 89.1 ± 2.9	204.1 94.5 ± 3.4	264.9 95.9 ± 4.0	318.1 91.6 ± 4.5	367.0 88.9 ± 4.9	412.6 83.3 ± 5.3	455.9 76.3 ± 5.5
Co	153.5 0.49 ± 0.07	208.4 0.55 ± 0.06	270.6 0.56 ± 0.07	325.1 0.56 ± 0.08	375.2 0.63 ± 0.10	422.0 0.53 ± 0.10	466.5 0.56 ± 0.11
Ni	159.0 4.0 ± 0.2	216.0 4.6 ± 0.2	280.7 4.5 ± 0.3	337.5 4.8 ± 0.3	389.7 4.4 ± 0.3	438.5 3.9 ± 0.3	485.0 3.7 ± 0.4

Table A.2: CRIS 2009-10 solar minimum spectra. Systematic and statistical uncertainties are combined in quadrature.

	Energies (MeV/nucleon) 1997-98 Intensities (10^{-9} [cm^2 s sr MeV/nucleon]$^{-1}$)						
Element	**60**	**72**	**85**	**100**	**120**	**142**	**170**
B	110.2± 4.0	124.8± 4.1	140.0± 4.5	156.7± 5.6	166.9± 6.5	191.3± 7.7	205.1± 10.2
C		535.1± 16.1	591.6± 18.1	654.5± 19.9	730.7± 23.9	780.0± 27.6	824.7± 33.9
N		125.0± 4.4	135.8± 4.4	148.0± 4.9	169.7± 5.9	182.3± 6.8	195.6± 8.2
O			595.8± 17.8	647.9± 19.9	709.5± 21.8	764.9± 25.7	794.5± 28.9
F			7.7± 0.6	8.2± 0.4	9.1± 0.5	10.7± 0.7	11.8± 0.8
Ne			80.7± 3.1	88.1± 2.9	97.2± 3.4	105.8± 3.8	114.7± 4.5
Na				17.1± 0.8	19.2± 0.8	20.5± 0.8	21.3± 1.0
Mg				120.1± 4.1	131.5± 4.3	142.2± 4.7	152.5± 5.6
Al				16.2± 0.9	18.2± 0.8	20.4± 0.9	23.0± 1.0
Si					95.3± 3.1	104.3± 3.5	111.0± 4.1
P					2.5± 0.2	2.8± 0.2	3.1± 0.2
S					14.4± 0.7	15.8± 0.7	17.3± 0.7
Cl					2.7± 0.3	2.6± 0.2	2.6± 0.2
Ar					5.6± 0.5	6.1± 0.3	6.6± 0.4
K						4.0± 0.3	4.5± 0.3
Ca						12.6± 0.6	14.5± 0.6
Sc						2.9± 0.2	3.0± 0.2
Ti						10.5± 0.6	11.4± 0.5
V						4.7± 0.3	5.2± 0.3
Cr						10.7± 0.6	11.2± 0.5
Mn						6.9± 0.5	7.0± 0.4
Fe							74.9± 2.7
Co							0.54± 0.08
Ni							3.6± 0.2

	Energies (MeV/nucleon) 1997-98 Intensities (10^{-9} [cm^2 s sr MeV/nucleon]$^{-1}$)					
Element	**200**	**240**	**285**	**340**	**400**	**475**
C	828.6± 38.4					
N	201.0± 9.6					
O	818.4± 35.9	774.6± 38.3				
F	12.0± 0.8	12.2± 1.1				
Ne	117.8± 5.2	116.8± 5.8				
Na	21.1± 1.1	23.2± 1.4	22.5± 2.2			
Mg	163.9± 6.6	162.5± 7.4	156.8± 8.7			
Al	22.9± 1.1	23.9± 1.4	23.1± 1.4			
Si	115.4± 4.3	118.8± 5.0	120.7± 6.3			
P	3.3± 0.3	3.2± 0.3	3.2± 0.3	3.9± 0.7		
S	18.6± 0.9	20.1± 1.1	19.3± 1.2	18.7± 1.3		
Cl	3.0± 0.2	3.3± 0.3	3.7± 0.4	3.4± 0.4		
Ar	6.7± 0.4	7.3± 0.4	8.3± 0.6	8.0± 0.7		
K	5.0± 0.3	5.6± 0.3	5.9± 0.4	6.5± 0.6		
Ca	15.5± 0.6	16.3± 0.8	17.0± 0.9	17.1± 1.1	16.7± 1.5	
Sc	3.1± 0.2	3.4± 0.3	3.7± 0.3	3.4± 0.3	3.6± 0.5	
Ti	12.2± 0.5	13.2± 0.7	12.7± 0.8	12.6± 0.8	12.3± 1.0	
V	5.7± 0.3	5.8± 0.4	6.1± 0.4	6.7± 0.6	5.7± 0.5	
Cr	11.7± 0.5	11.6± 0.6	11.9± 0.7	12.2± 0.8	11.3± 0.9	
Mn	7.0± 0.4	7.7± 0.4	7.6± 0.5	7.6± 0.5	6.8± 0.7	
Fe	77.9± 2.9	78.8± 3.3	78.0± 3.3	75.1± 4.2	70.7± 4.6	62.4± 5.0
Co	0.42± 0.07	0.45± 0.06	0.51± 0.08	0.50± 0.09	0.47± 0.10	0.53± 0.19
Ni	3.5± 0.2	3.7± 0.2	3.9± 0.3	3.9± 0.3	3.5± 0.3	3.5± 0.4

Table A.3: CRIS 1997-98 solar minimum spectra, interpolated to a common energy grid. Systematic and statistical uncertainties are combined in quadrature.

	Energies (MeV/nucleon) 2009-10 Intensities (10^{-9} [cm^2 s sr MeV/nucleon]$^{-1}$)						
Element	**60**	**72**	**85**	**100**	**120**	**142**	**170**
B	133.6± 4.4	148.6± 4.6	165.5± 5.1	187.3± 6.3	204.1± 7.4	225.1± 8.6	235.2± 10.9
C		664.2± 19.6	737.3± 22.3	817.3± 24.7	910.3± 29.4	956.9± 33.5	1006.1± 41.0
N		150.0± 4.7	164.9± 5.1	181.1± 5.7	202.6± 6.8	220.5± 7.9	238.1± 9.5
O			733.4± 21.6	806.0± 24.6	882.2± 26.9	943.7± 31.3	979.2± 35.3
F			9.9± 0.5	10.9± 0.4	11.9± 0.5	12.4± 0.6	13.6± 0.7
Ne			99.8± 3.3	107.8± 3.3	117.6± 3.8	130.4± 4.5	138.4± 5.2
Na				20.0± 0.7	21.7± 0.8	23.6± 0.8	25.9± 1.0
Mg				150.5± 4.7	164.7± 5.2	177.5± 5.6	188.5± 6.7
Al				21.9± 0.9	23.9± 0.8	25.9± 0.9	28.2± 1.1
Si					118.1± 3.6	127.5± 4.1	135.6± 4.8
P					3.0± 0.2	3.3± 0.2	3.7± 0.2
S					18.2± 0.7	19.7± 0.7	21.2± 0.8
Cl					2.8± 0.2	2.9± 0.2	3.3± 0.2
Ar					5.8± 0.3	6.7± 0.3	7.8± 0.3
K						5.1± 0.2	5.5± 0.3
Ca						15.0± 0.6	16.3± 0.6
Sc						3.1± 0.2	3.5± 0.2
Ti						12.9± 0.5	13.7± 0.5
V						6.2± 0.3	6.5± 0.3
Cr						12.7± 0.5	13.5± 0.5
Mn						8.1± 0.4	8.4± 0.3
Fe							91.2± 3.2
Co							0.51± 0.05
Ni							4.2± 0.2

	Energies (MeV/nucleon) 2009-10 Intensities (10^{-9} [cm^2 s sr MeV/nucleon]$^{-1}$)					
Element	**200**	**240**	**285**	**340**	**400**	**475**
C	1001.8± 45.3					
N	240.4± 11.2					
O	998.4± 43.6	955.9± 46.0				
F	14.0± 0.7	15.5± 1.0				
Ne	141.6± 6.0	145.2± 6.8				
Na	27.4± 1.2	27.3± 1.4	29.7± 2.1			
Mg	194.2± 7.6	195.1± 8.5	189.7± 10.2			
Al	29.1± 1.2	29.3± 1.4	30.6± 1.6			
Si	141.4± 5.1	143.0± 5.8	140.3± 7.1			
P	4.2± 0.2	4.1± 0.3	4.5± 0.3	4.6± 0.5		
S	22.6± 0.9	24.4± 1.1	23.7± 1.2	22.7± 1.4		
Cl	4.0± 0.2	4.1± 0.3	4.4± 0.3	4.1± 0.3		
Ar	8.5± 0.4	9.1± 0.4	9.7± 0.5	9.4± 0.6		
K	6.0± 0.3	6.5± 0.3	7.1± 0.4	7.4± 0.5		
Ca	17.7± 0.6	19.0± 0.8	18.8± 0.9	20.6± 1.2	20.1± 1.5	
Sc	3.8± 0.2	4.0± 0.2	4.5± 0.3	4.2± 0.3	3.7± 0.4	
Ti	14.4± 0.5	15.1± 0.7	15.2± 0.8	15.0± 0.9	14.2± 1.0	
V	6.8± 0.3	7.3± 0.4	7.5± 0.4	7.4± 0.5	6.4± 0.5	
Cr	14.2± 0.6	14.3± 0.6	14.5± 0.7	13.4± 0.8	12.6± 0.9	
Mn	8.7± 0.4	8.9± 0.4	8.8± 0.5	8.3± 0.5	8.6± 0.6	
Fe	94.1± 3.3	95.4± 3.9	94.2± 3.9	90.4± 4.9	84.7± 5.3	73.6± 5.4
Co	0.54± 0.05	0.55± 0.05	0.56± 0.06	0.59± 0.07	0.58± 0.08	0.56± 0.13
Ni	4.5± 0.2	4.5± 0.2	4.5± 0.3	4.8± 0.3	4.3± 0.3	3.7± 0.3

Table A.4: CRIS 2009-10 solar minimum spectra, interpolated to a common energy grid. Systematic and statistical uncertainties are combined in quadrature.

Appendix B

CRIS Solar Maximum Data

In our previous work (George et al. 2009) we reported the 2001-03 CRIS solar maximum energy spectra and composition. Since that time, there have been updates to the analysis used to produced our results. In particular, we have adopted the SOFT hodoscope efficiencies from de Nolfo (2010) (Section 3.5), as well as refined our technique for calculating the uncertainties on the interpolated energy spectra (with our current method described in Section 3.6). In this appendix we present the updated solar maximum results, where we have used the data selections and corrections described in Chapter 3, as well as data from the same range of days given in the original work (covering data from May 1, 2001 through September 1, 2003).

The 2001-03 CRIS solar minimum energy spectra are plotted in Figures B.1 through B.4, with the data given in Table B.1. The solid lines are the quadratic fits to the data (see Section 3.6), and the dotted lines at 160 MeV/nucleon show where the relative abundances were calculated. These energy spectra have also been interpolated to a common energy grid, given in Table B.2. The reported uncertainties on the intensities are the quadratic summation of the statistical and systematic

contributions, as discussed in Section 3.6.

Table B.3 lists the abundances relative to silicon (Si≡1000); only statistical uncertainties are given. We note that several elements have solar maximum relative abundances that are different from the solar minima results (Table 3.4) by more than the statistical uncertainties. Even though these data are reported at the same energy at 1 AU, the cosmic rays observed during solar maximum had higher energies in the interstellar medium than those we observed during the solar minima. Therefore, the differences in the spectral shapes would contribute to the differences we see in the relative abundances. We also expect differences due to solar modulation, which depends on the mass-to-charge ratio of the cosmic ray. For those elements where the average A/Z is different from that of silicon, the effects due to modulation will be most apparent. Though the reasons for the differences between the solar minimum and maximum relative abundances are important to understand, further study is beyond the scope of this work.

Element	Energies (MeV/nucleon) 2001-03 Intensities (10^{-9} [cm^2 s sr MeV/nucleon]$^{-1}$)						
B	59.6	79.7	102.0	121.1	138.2	154.0	168.6
	30.1 ± 1.0	36.5 ± 1.2	44.0 ± 1.5	50.8 ± 1.9	55.3 ± 2.2	60.4 ± 2.6	61.7 ± 2.8
C	68.3	91.4	117.2	139.2	159.1	177.3	194.4
	110.1 ± 3.3	136.2 ± 4.2	166.5 ± 5.4	187.6 ± 6.6	207.1 ± 7.8	214.9 ± 8.9	224.9 ± 10.1
N	73.2	98.1	125.8	149.5	170.9	190.6	209.1
	31.4 ± 1.0	38.1 ± 1.2	47.5 ± 1.6	53.8 ± 2.0	58.3 ± 2.4	62.2 ± 2.8	62.4 ± 3.0
O	80.4	107.8	138.4	164.7	188.4	210.2	230.7
	123.1 ± 3.7	150.5 ± 4.6	183.8 ± 6.2	200.0 ± 7.3	215.5 ± 8.5	226.3 ± 10.0	231.1 ± 11.1
F	83.5	112.0	143.8	171.1	195.9	218.6	240.0
	2.4 ± 0.1	3.0 ± 0.1	3.5 ± 0.2	3.9 ± 0.2	4.1 ± 0.3	4.4 ± 0.3	4.7 ± 0.3
Ne	89.4	120.0	154.3	183.8	210.5	235.1	258.2
	20.8 ± 0.7	26.0 ± 0.9	30.9 ± 1.1	33.8 ± 1.3	38.0 ± 1.7	39.2 ± 1.9	38.5 ± 2.1
Na	94.0	126.2	162.3	193.5	221.7	247.8	272.3
	4.5 ± 0.2	5.5 ± 0.2	6.5 ± 0.3	6.8 ± 0.3	7.6 ± 0.4	8.2 ± 0.5	8.3 ± 0.5
Mg	100.2	134.6	173.3	206.7	237.0	265.0	291.4
	29.3 ± 1.0	36.3 ± 1.2	43.4 ± 1.6	47.3 ± 1.9	50.0 ± 2.2	53.4 ± 2.7	52.7 ± 2.9
Al	103.8	139.6	179.8	214.5	246.1	275.3	302.8
	4.7 ± 0.2	6.1 ± 0.2	7.3 ± 0.3	8.1 ± 0.4	8.7 ± 0.5	8.4 ± 0.5	9.1 ± 0.6
Si	110.0	148.2	191.0	228.1	261.8	293.0	322.5
	23.6 ± 0.8	28.5 ± 0.9	33.2 ± 1.2	35.4 ± 1.5	38.2 ± 1.8	40.8 ± 2.1	40.4 ± 2.3
P	112.7	151.8	195.8	233.9	268.6	300.8	331.1
	0.7 ± 0.1	1.1 ± 0.1	1.1 ± 0.1	1.3 ± 0.1	1.5 ± 0.1	1.7 ± 0.1	1.8 ± 0.2
S	118.2	159.3	205.6	245.8	282.4	316.4	348.5
	4.3 ± 0.2	5.2 ± 0.2	6.5 ± 0.3	7.2 ± 0.4	7.2 ± 0.4	8.0 ± 0.5	8.1 ± 0.5
Cl	120.0	161.8	209.0	249.9	287.2	321.8	354.5
	1.0 ± 0.1	1.1 ± 0.1	1.5 ± 0.1	1.5 ± 0.1	1.6 ± 0.1	2.0 ± 0.2	1.9 ± 0.2
Ar	125.1	168.9	218.2	261.1	300.2	336.6	371.0
	1.9 ± 0.1	2.3 ± 0.1	2.9 ± 0.2	3.3 ± 0.2	3.4 ± 0.2	3.6 ± 0.3	3.3 ± 0.3
K	127.9	172.7	223.3	267.3	307.4	344.8	380.2
	1.6 ± 0.1	1.9 ± 0.1	2.3 ± 0.1	2.6 ± 0.2	2.7 ± 0.2	2.7 ± 0.2	2.9 ± 0.2
Ca	131.7	178.1	230.3	275.9	317.5	356.2	392.9
	4.0 ± 0.2	5.1 ± 0.2	5.7 ± 0.3	6.2 ± 0.3	6.8 ± 0.4	7.0 ± 0.5	7.2 ± 0.5
Sc	133.5	180.5	233.6	279.9	322.2	361.5	398.8
	0.9 ± 0.1	1.1 ± 0.1	1.3 ± 0.1	1.3 ± 0.1	1.4 ± 0.1	1.5 ± 0.1	1.5 ± 0.1
Ti	137.1	185.5	240.1	287.9	331.5	372.1	410.7
	3.3 ± 0.2	4.1 ± 0.2	4.5 ± 0.2	4.8 ± 0.3	4.9 ± 0.3	5.2 ± 0.4	5.0 ± 0.4
V	139.9	189.4	245.4	294.3	339.0	380.7	420.3
	1.5 ± 0.1	1.8 ± 0.1	2.1 ± 0.1	2.2 ± 0.1	2.3 ± 0.2	2.2 ± 0.2	2.5 ± 0.2
Cr	143.9	194.9	252.7	303.1	349.4	392.5	433.5
	3.1 ± 0.1	3.8 ± 0.2	4.1 ± 0.2	4.3 ± 0.2	4.7 ± 0.3	4.8 ± 0.3	4.5 ± 0.4
Mn	146.8	199.0	258.1	309.7	357.1	401.3	443.4
	2.1 ± 0.1	2.2 ± 0.1	2.8 ± 0.1	2.8 ± 0.2	3.0 ± 0.2	3.1 ± 0.2	2.9 ± 0.2
Fe	150.5	204.1	264.9	318.1	367.0	412.6	455.9
	21.5 ± 0.7	24.5 ± 0.9	27.7 ± 1.2	28.9 ± 1.4	30.7 ± 1.7	30.7 ± 1.9	30.7 ± 2.2
Co	153.5	208.4	270.6	325.1	375.2	422.0	466.5
	0.10 ± 0.02	0.15 ± 0.02	0.20 ± 0.03	0.18 ± 0.03	0.19 ± 0.03	0.22 ± 0.04	0.21 ± 0.04
Ni	159.0	216.0	280.7	337.5	389.7	438.5	485.0
	1.0 ± 0.1	1.2 ± 0.1	1.4 ± 0.1	1.4 ± 0.1	1.7 ± 0.1	1.6 ± 0.1	1.5 ± 0.1

Table B.1: CRIS 2001-03 solar maximum spectra. Systematic and statistical uncertainties are combined in quadrature.

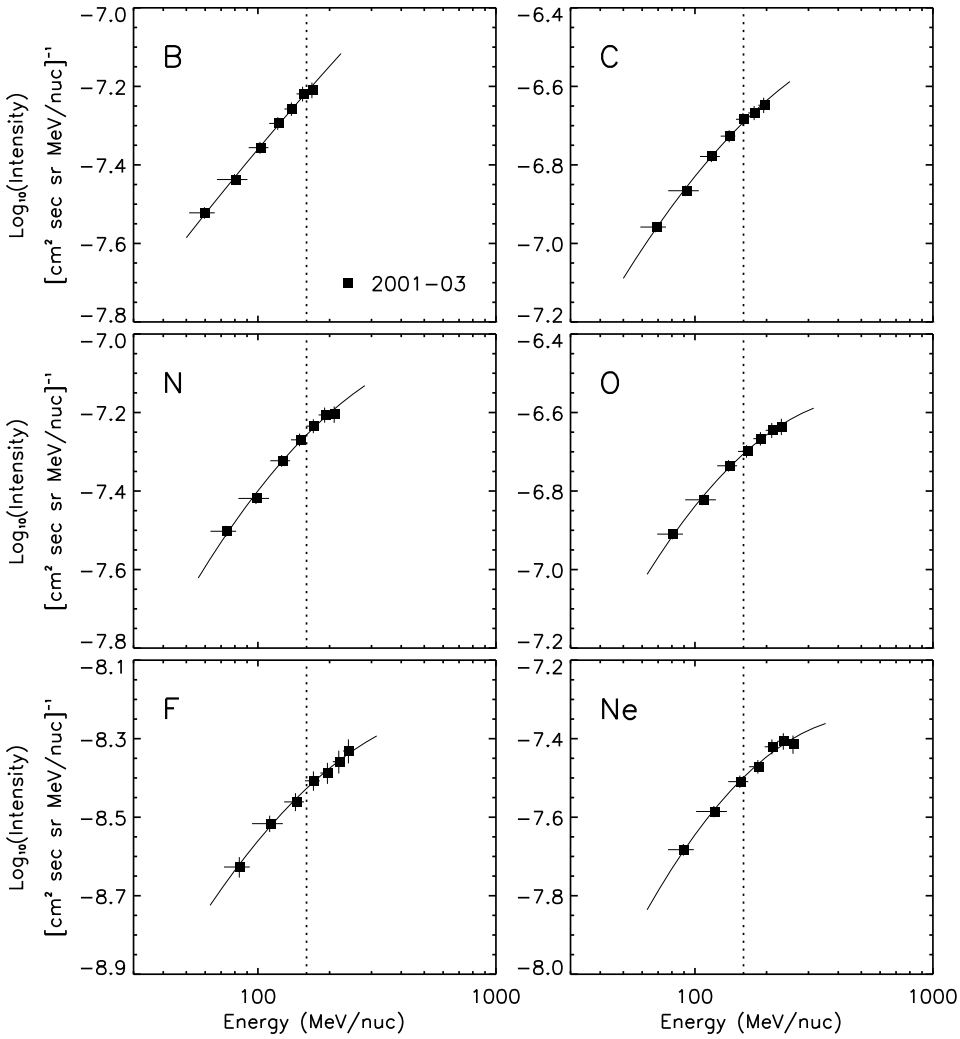

Figure B.1: CRIS solar maximum energy spectra for boron through neon. The solid lines represent quadratic fits to the data. The vertical lines at 160 MeV/nucleon indicate the energy at which the relative abundances were calculated. The data shown here are tabulated in Table B.1 in Appendix B.

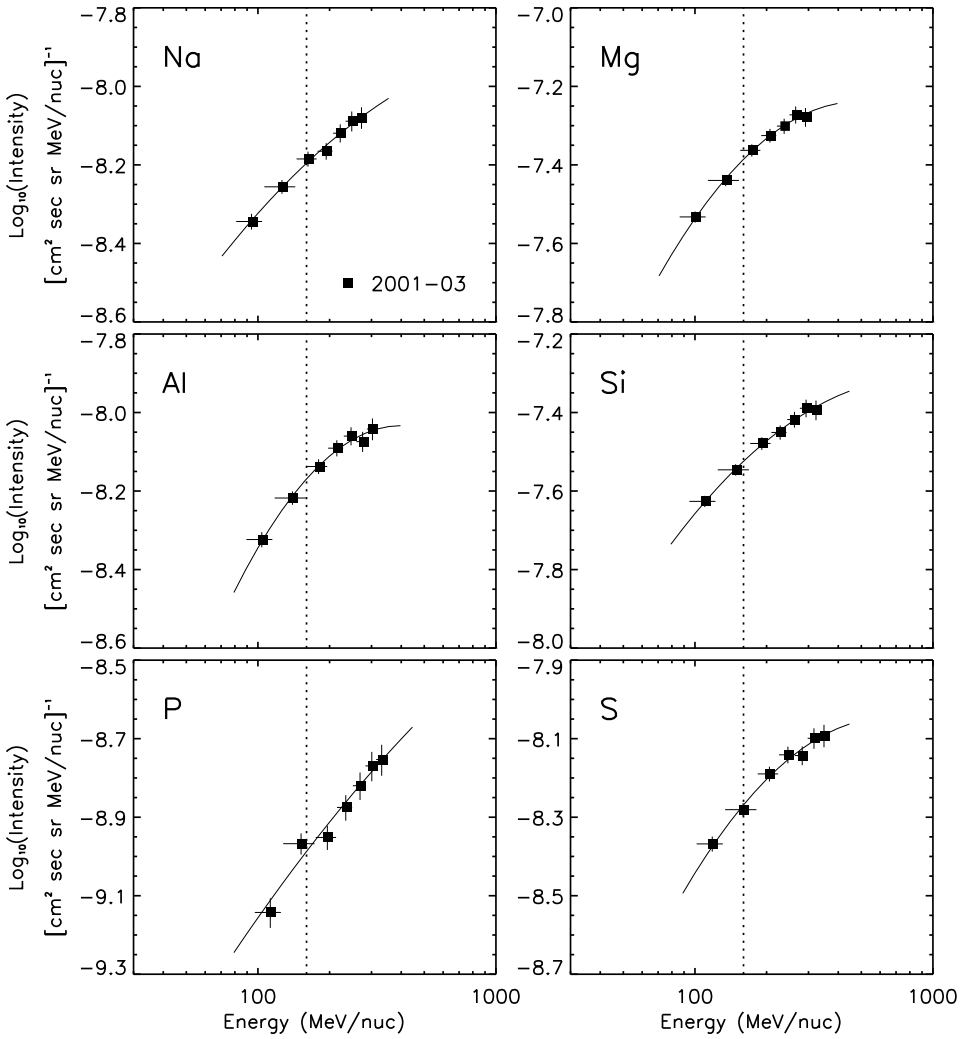

Figure B.2: CRIS solar maximum energy spectra for sodium through sulfur. The solid lines represent quadratic fits to the data. The vertical lines at 160 MeV/nucleon indicate the energy at which the relative abundances were calculated. The data shown here are tabulated in Table B.1 in Appendix B.

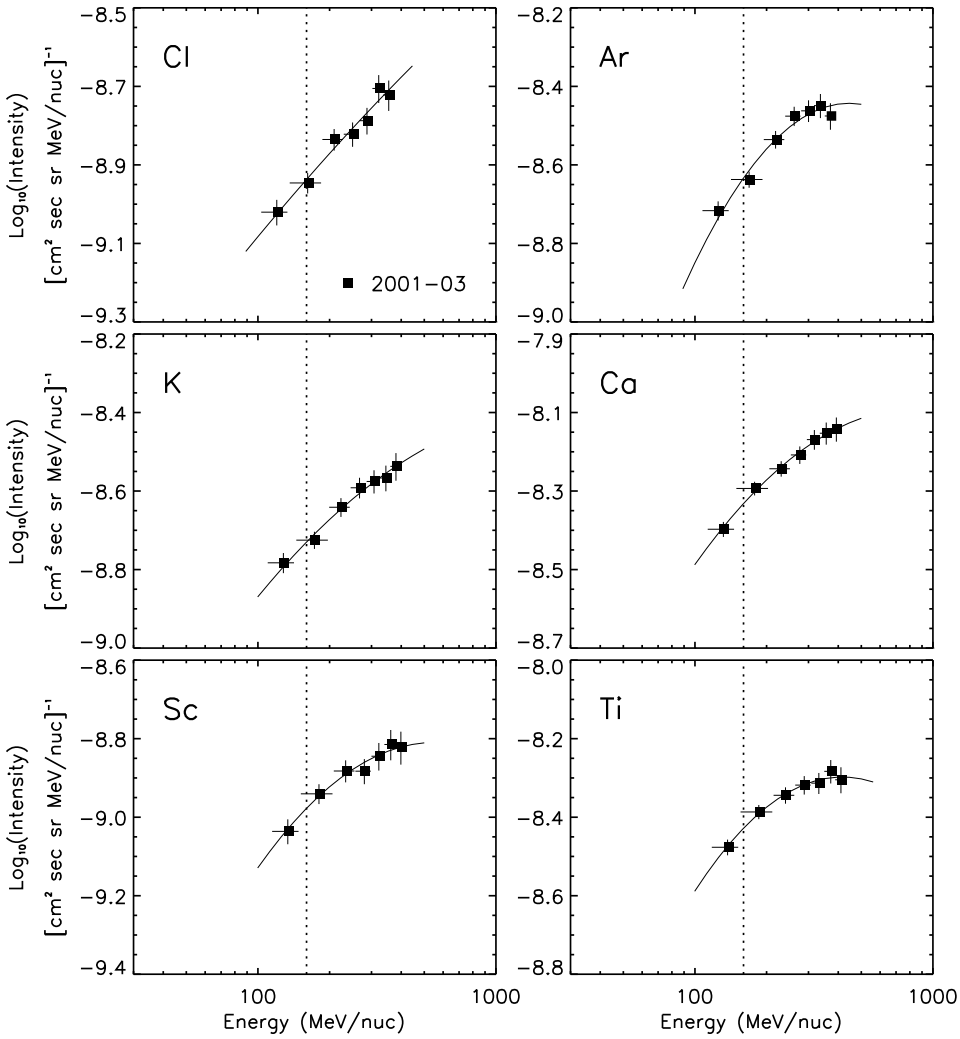

Figure B.3: CRIS solar maximum energy spectra for chlorine through titanium. The solid lines represent quadratic fits to the data. The vertical lines at 160 MeV/nucleon indicate the energy at which the relative abundances were calculated. The data shown here are tabulated in Table B.1 in Appendix B.

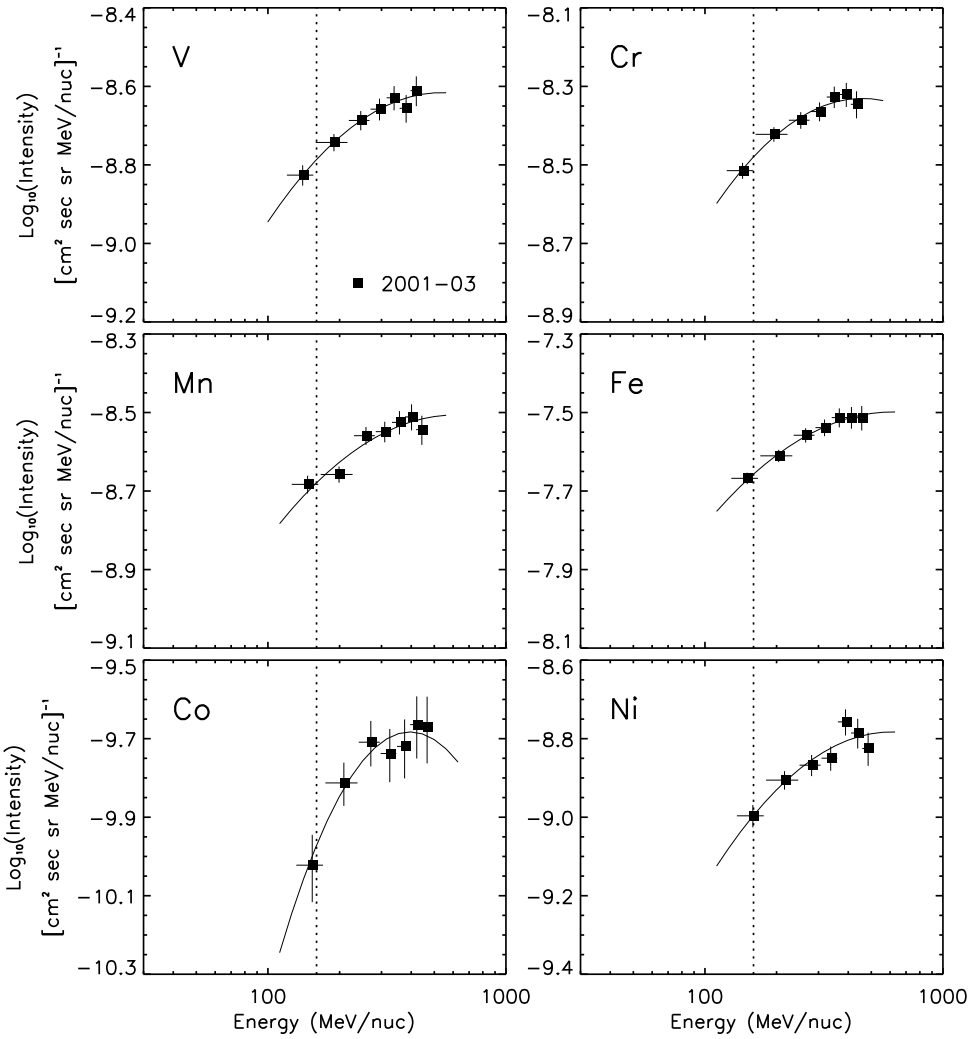

Figure B.4: CRIS solar maximum energy spectra for vanadium through nickel. The solid lines represent quadratic fits to the data. The vertical lines at 160 MeV/nucleon indicate the energy at which the relative abundances were calculated. The data shown here are tabulated in Table B.1 in Appendix B.

	Energies (MeV/nucleon) 2001-03 Intensities (10^{-9} [cm^2 s sr MeV/nucleon]$^{-1}$)						
Element	**60**	**72**	**85**	**100**	**120**	**142**	**170**
B	30.2± 1.0	34.1± 1.1	38.4± 1.2	43.4± 1.5	50.4± 1.8	56.5± 2.2	61.8± 2.9
C		114.4± 3.4	129.2± 3.9	146.5± 4.4	169.2± 5.5	190.4± 6.7	211.9± 8.7
N		31.1± 1.0	34.7± 1.1	38.8± 1.2	45.6± 1.5	51.8± 1.9	58.1± 2.3
O			127.9± 3.8	143.0± 4.4	164.0± 5.0	186.1± 6.2	203.5± 7.4
F			2.4± 0.1	2.8± 0.1	3.2± 0.1	3.4± 0.2	3.9± 0.2
Ne			20.0± 0.7	22.6± 0.7	26.0± 0.9	29.2± 1.0	32.5± 1.2
Na				4.7± 0.2	5.4± 0.2	6.0± 0.2	6.6± 0.3
Mg				29.3± 1.0	33.4± 1.1	37.7± 1.2	42.8± 1.5
Al				4.6± 0.2	5.3± 0.2	6.1± 0.2	7.0± 0.3
Si					25.0± 0.8	27.7± 0.9	30.9± 1.1
P					0.8± 0.1	1.0± 0.1	1.1± 0.1
S					4.3± 0.2	4.8± 0.2	5.5± 0.2
Cl					1.0± 0.1	1.1± 0.1	1.2± 0.1
Ar					1.9± 0.1	2.1± 0.1	2.3± 0.1
K						1.7± 0.1	1.9± 0.1
Ca						4.3± 0.2	4.9± 0.2
Sc						1.0± 0.1	1.1± 0.1
Ti						3.4± 0.1	3.9± 0.2
V						1.5± 0.1	1.7± 0.1
Cr						3.0± 0.1	3.4± 0.1
Mn						2.1± 0.1	2.1± 0.1
Fe							22.7± 0.8
Co							0.11± 0.02
Ni							1.1± 0.1

	Energies (MeV/nucleon) 2001-03 Intensities (10^{-9} [cm^2 s sr MeV/nucleon]$^{-1}$)					
Element	**200**	**240**	**285**	**340**	**400**	**475**
C	228.0± 10.4					
N	62.3± 2.9					
O	221.3± 9.7	233.1± 11.3				
F	4.1± 0.2	4.7± 0.3				
Ne	36.3± 1.5	39.1± 1.9				
Na	7.0± 0.3	8.0± 0.4	8.4± 0.6			
Mg	46.5± 1.8	50.3± 2.2	52.8± 2.9			
Al	7.8± 0.3	8.6± 0.4	8.7± 0.5			
Si	33.8± 1.2	36.4± 1.5	40.2± 2.0			
P	1.1± 0.1	1.4± 0.1	1.6± 0.1	1.8± 0.2		
S	6.3± 0.3	7.1± 0.3	7.3± 0.4	8.1± 0.5		
Cl	1.4± 0.1	1.5± 0.1	1.6± 0.1	1.9± 0.1		
Ar	2.7± 0.1	3.1± 0.2	3.4± 0.2	3.5± 0.2		
K	2.1± 0.1	2.4± 0.1	2.6± 0.1	2.7± 0.2		
Ca	5.4± 0.2	5.8± 0.2	6.3± 0.3	6.9± 0.4	7.2± 0.5	
Sc	1.2± 0.1	1.3± 0.1	1.3± 0.1	1.5± 0.1	1.5± 0.1	
Ti	4.2± 0.2	4.5± 0.2	4.8± 0.3	4.9± 0.3	5.0± 0.4	
V	1.9± 0.1	2.0± 0.1	2.2± 0.1	2.3± 0.2	2.3± 0.2	
Cr	3.8± 0.2	4.0± 0.2	4.2± 0.2	4.6± 0.3	4.7± 0.3	
Mn	2.2± 0.1	2.6± 0.1	2.8± 0.1	2.9± 0.2	3.1± 0.2	
Fe	24.3± 0.9	26.4± 1.1	28.2± 1.2	29.7± 1.6	30.7± 1.9	30.7± 2.2
Co	0.14± 0.02	0.18± 0.02	0.19± 0.02	0.19± 0.02	0.20± 0.03	0.21± 0.05
Ni	1.2± 0.1	1.3± 0.1	1.4± 0.1	1.4± 0.1	1.7± 0.1	1.5± 0.1

Table B.2: CRIS 2001-03 solar maximum spectra, interpolated to a common energy grid. Systematic and statistical uncertainties are combined in quadrature.

Element	2001–2003
B	2037.0± 21.1
C	6809.0± 23.2
N	1849.9± 11.3
O	6591.8± 21.4
F	125.1± 3.0
Ne	1060.6± 8.6
Na	213.1± 3.7
Mg	1375.5± 9.0
Al	226.6± 3.5
Si	1000.0± 7.0
P	34.4± 1.2
S	180.1± 2.8
Cl	38.6± 1.3
Ar	77.8± 1.8
K	62.2± 1.6
Ca	155.7± 2.6
Sc	35.2± 1.3
Ti	124.7± 2.5
V	54.7± 1.7
Cr	110.8± 2.6
Mn	70.0± 2.1
Fe	736.7± 7.3
Co	3.6± 0.5
Ni	33.8± 1.8

Table B.3: CRIS solar maximum relative abundances at 160 MeV/nucleon, normalized to Si≡1000. Only the statistical uncertainties are given. The absolute intensity for silicon at 160 MeV/nucleon is (29.91 ± 0.97)x10^{-9} (cm^2 s sr MeV/nucleon)$^{-1}$ for the 2001-03 solar maximum.

Appendix C

Updates to the Leaky-Box Transport Models

Before the leaky-box transport models were used for this work, extensive updates were made to our programming. The most important work involved updating our database of measured production cross sections and our semi-empirical cross section formulae. Section C.1 describes this work, with several example reactions presented and discussed in detail in Section C.2. Half-lives and branching ratios for unstable nuclei were also updated (see Section C.3).

C.1 Production cross sections

The most important update to our leaky-box transport code involved the expansion of our database of high-energy production cross section measurements. Prior to this work our database contained only direct, or undecayed, measurements for the production of stable and unstable daughter nuclei that were published before 2004. These data included reactions for parent nuclei with charge Z$\leq$28 interacting on hydrogen at energies between 300-1500 MeV/nucleon, and producing daughter nuclei from ^{7}Be

through ^{57}Ni. We searched for more recent publications of direct production cross sections using the extensive databases maintained by the National Nuclear Data Center (NNDC, `http://www.nndc.bnl.gov/nudat2/`). For a complete list of references for this work, see Table C.1.

Direct cross sections considered in this work were measured using a variety of beam-target combinations, which we briefly mention here. Nine experiments used isotope beams incident on hydrogen targets (typically liquid hydrogen, though Webber et al. (1990c) used CH_2 and subtracted the cross sections on carbon targets to infer the hydrogen values). In these reactions, the products have velocities similar to the beam energy and they are detected a short distance from the target with a magnetic spectrometer, so measurements are made a few nanoseconds after the interaction and most unstable nuclei will not have time to decay. Seven experiments used proton beams incident on element or isotope targets. X-ray, γ-ray, and mass spectrometry (accelerator and conventional) were used to measure the radioactive and stable daughter nuclei produced in the target materials.

Since available production cross section measurements cover only a small energy range and a limited set of parent-daughter interactions, we had to fill in the missing cross section information using a semi-empirical formula. We chose to use the work of Silberberg et al. (1998) and Tsao et al. (1998), hereafter referred to as the S&T cross sections. In our previous work (George et al. 2009), these cross sections were calculated using the `yieldx_080999.for` version of their code. Our new database of measured cross sections prompted us to update the S&T direct production cross

sections, which was done with the help of A. F. Barghouty (Barghouty 2010).

For all reactions where we had measured direct cross sections, we made a comparison between the data and S&T to determine if any readjustments needed to be made to the semi-empirical cross sections before their implementation in the transport code. Using an unweighted least-squares fit of S&T to the data, we calculated the energy-independent scale factors that would yield the best agreement between the two cross sections. We note that an unweighted fit was chosen because of the inclusion of the various Webber measurements (Webber et al. (1990b); Webber et al. (1998a); Webber et al. (1998b)). These data are quoted to have quite small uncertainties, and for many reactions there were other experimental data that disagreed significantly from the Webber data. By adopting the unweighted fit, we tried to avoid introducing any bias in the rescaling procedure.

After rescaling we calculated the cumulative S&T production cross sections; here we use the term 'cumulative' to refer to the cross sections after all short-lived, unstable daughter nuclei have decayed to a stable isotope. In the cosmic rays, short-lived nuclei have half-lives shorter than the cosmic-ray confinement time of $\sim$15 Myr (Yanasak et al. 2001). Some cosmic-ray species that decay only by electron capture have short half-lives, though they are essentially stable as long as they are fully stripped; the probability for electron attachment is highly energy-dependent at several hundred MeV/nucleon (Niebur et al. (2003); Scott (2005)).

For an example of the calculation of a cumulative cross section, consider the reaction ^{28}Si + p $\rightarrow$ ^{20}Ne. Besides the direct production of ^{20}Ne, there is the indirect

route ^{28}Si + p $\rightarrow$ ^{20}Na $\rightarrow$ ^{20}Ne, since ^{20}Na decays to ^{20}Ne in $\sim$450 milliseconds. When calculating the cumulative cross section, we add together the cross sections for the direct production and all indirect production routes (^{20}Na and all other unstable daughter isotopes that decay to ^{20}Ne).

In our prior work (George et al. 2009) we did not compare our cumulative S&T cross sections with available measurements. In this work we rectified this oversight by compiling a second database of cumulative cross sections (using the NNDC databases). All of these cross sections come from experiments where proton beams were incident on element or isotope targets. Using both γ-ray and mass spectrometry the targets were examined days or weeks following irradiation to allow for the decay of the shortest-lived radioactive nuclei. We compared our new cumulative S&T cross sections with these data, and for many reactions, S&T agreed quite well with the measurements. However, there were others that had significant discrepancies in the magnitude and/or the energy dependence of the cross sections. Therefore, we examined the cumulative cross sections on a case-by-case basis to determine the best form of the cumulative S&T to use. We note that only the cumulative cross sections are used as inputs in our transport code. Select examples are discussed in Section C.2.

C.2 Selected production cross sections

In this section we present a subset of the extensive compilation of production cross sections on hydrogen. These reactions all have measured cumulative cross sections

(though not necessarily direct measurements), and they required special consideration to determine the form of S&T that best fit the available data. All reactions not shown either had no measured data with which to compare to the cumulative S&T cross sections, or S&T was found to fit the data well enough without additional adjustments.

For some cases, a simple rescaling to the new cumulative data was required. This was done using an unweighted least-squares fit of the S&T cross section to the cumulative data. For these fits we restricted our energy band to 200-2000 MeV/nucleon. Cross sections below this range are unimportant for this work since particles with these energies in the ISM will have lost too much energy during transport to be observed by CRIS. We set an upper limit at 2 GeV/nucleon because the cumulative data from Michel et al. (1995) were reported to have large corrections at the highest energies; these corrections were largest when the mass difference between the parent and daughter nuclei was the smallest. For some reactions, the difference between the direct and cumulative measurements was larger than the difference suggested by S&T. For these cases we still rescaled S&T to the cumulative data.

We note that for a small number of cases, the cumulative cross section measurements were lower than the direct cross section measurements. This is simply unphysical, so we chose to fit S&T to the available cumulative cross section data, which we ultimately use in our transport code. In one case (^{27}Al + p $\rightarrow$ ^{26}Al), fitting to the cumulative data rather than the direct data allowed for better agreement among calculated cosmic-ray confinement times (Yanasak et al. 2001).

There are other cases where the energy dependence of S&T did not agree with the shape suggested by the data. For these cases, we chose to fit a flat line to the cumulative data. These lines represent the average value of the cross section in the energy range of 200-2000 MeV/nucleon.

The following table lists the references for the direct and cumulative cross section measurements used in this work, as well as the plotting symbols assigned to each. Direct measurements are given as filled symbols, while cumulative measurements are represented with open symbols.

Direct (Undecayed) Cross Sections	
Reference	**Symbol**
Bodemann et al. (1993)	■
† Chen et al. (1997a)	●
† Chen et al. (1997b)	▼
† Knott et al. (1997)	▲
Korejwo et al. (2002)	▶
Michel et al. (1989)	♦
Michel et al. (1995)	▶
Michel et al. (1997)	■
Napolitani et al. (2004)	★
Schiekel et al. (1996)	▲
Titarenko et al. (2008)	●
‡ Villagrasa-Canton et al. (2007)	♦
† Vonach et al. (1997)	◀
† Webber et al. (1990c)	▼
† Webber et al. (1998a)	◀
† Webber et al. (1998b)	★
Cumulative (Decayed) Cross Sections	
Reference	**Symbol**
Michel et al. (1989)	◇
Michel et al. (1995)	▷
Michel et al. (1997)	□
Schiekel et al. (1996)	△
Titarenko et al. (2008)	○

Table C.1: References for the production cross sections on hydrogen used in this work, and the plotting symbols assigned to each. Entries marked with a † are those references used in our previous work (George et al. 2009). The entry marked with a ‡ is the reference currently used in this work, though in our previous publication the data came from Villagrasa-Canton (2003).

C.2.1 ^{20}Ne production

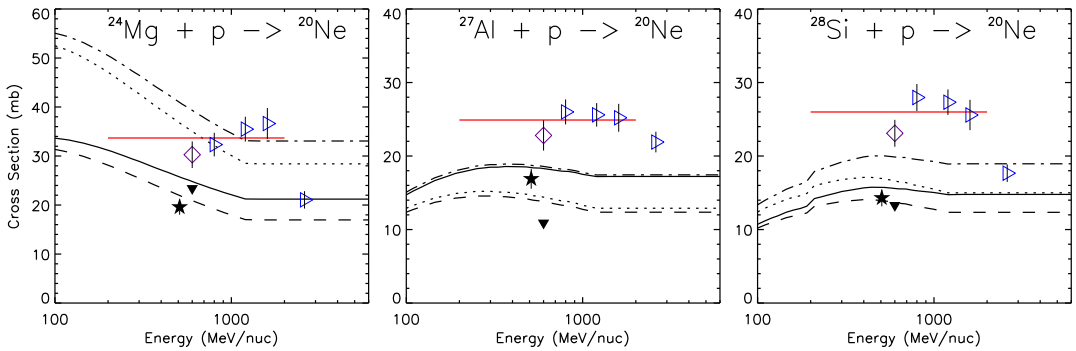

Figure C.1: Selected cross sections for the production of ^{20}Ne. Direct (filled points) and cumulative measurements (open points) are shown. Original, unscaled S&T cross sections are given by black dotted lines, while unscaled cumulative S&T cross sections are given by black dot-dashed lines. Rescaled direct S&T cross sections are given by black dashed lines, while rescaled cumulative S&T cross sections are given by black solid lines. A red solid line indicates that a different form was chosen for the definition of the cumulative cross section. All references for the data shown in these panels are listed in Table C.1.

^{24}Mg + p $\rightarrow$ ^{20}Ne: The original direct S&T production cross section (black dotted line) is too high compared to the direct Webber data (filled points), and it can be rescaled (black dashed line) to fit those data. The original cumulative S&T production cross section (black dot-dashed line) gives a better fit to the available cumulative data (open points) than the cumulative cross section calculated using the rescaled direct production (black solid line). However, the shape below ~1 GeV/nucleon is not right and so a flat value (red solid line) is adopted. This represents the average of the cumulative data in the energy band defined by this line.

^{27}Al + p $\rightarrow$ ^{20}Ne: The original direct S&T cross section (black dotted line) and its rescaled form (black dashed line) agree well with the direct Webber data (filled points). The cumulative S&T cross sections with and without rescaling due to the Webber data (black solid and dot-dashed lines, respectively) agree well with one another. However, the cumulative data (open points) indicate that larger cross sections are needed from S&T to achieve a good fit. Additionally, S&T has a broad peak that occurs at a lower energy than suggested by the data. A flat shape (red solid line, as described for ^{24}Mg + p $\rightarrow$ ^{20}Ne) is used instead of increasing the S&T production cross sections and shifting them so the peak is found at higher energies.

^{28}Si + p $\rightarrow$ ^{20}Ne: The original direct S&T cross section (black dotted line) is too high compared to the direct Webber data (filled points), and it can be rescaled (black dashed line). The original cumulative S&T cross section (black dot-dashed line) is closer to the available cumulative data (open points) than the cumulative cross section calculated using the rescaled direct production (black solid line). However, both of the cumulative S&T cross sections are too low in either case and the shape has the same problem as is seen in ^{27}Al + p $\rightarrow$ ^{20}Ne. Therefore, by the same reasoning, a flat shape (red solid line) is used for the cumulative cross section.

C.2.2 ^{21}Ne production

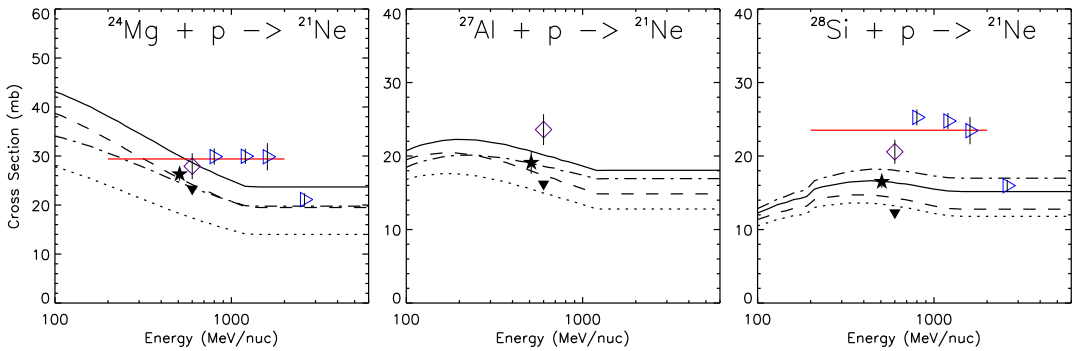

Figure C.2: Selected cross sections for the production of ^{21}Ne. For a definition of the data, please refer to the caption of Figure C.1.

^{24}Mg + p → ^{21}Ne: The original direct S&T cross section (black dotted line) is too low compared to the direct Webber data (filled points), and it can be rescaled (black dashed line) to fit those data. The cumulative S&T cross section calculated using the rescaled direct production (black solid line) gives a better fit to the available cumulative data (open points) than the unscaled cumulative S&T cross section (black dot-dashed line). However, the shape below ∼1 GeV/nucleon is not right and so a flat value (red solid line) is adopted. This represents the average of the cumulative data in the energy band defined by this line.

^{27}Al + p → ^{21}Ne: The original direct S&T cross section (black dotted line) is a little low compared to the direct Webber data (filled points) and so it can be rescaled (black dashed line). The cumulative S&T cross sections with and without rescaling

due to the Webber data (black solid and dot-dashed lines, respectively) are similar to one another, though the rescaled line gives a slightly larger cross section. The rescaled cumulative S&T cross section is used in this work. Since there is only one cumulative measurement (open point), no additional rescaling is used here.

^{28}Si + p $\rightarrow$ ^{21}Ne: This reaction has nearly the same features and problems as ^{27}Al + p $\rightarrow$ ^{20}Ne. Therefore, a flat shape (red solid line) is also used here.

C.2.3 ^{22}Ne production

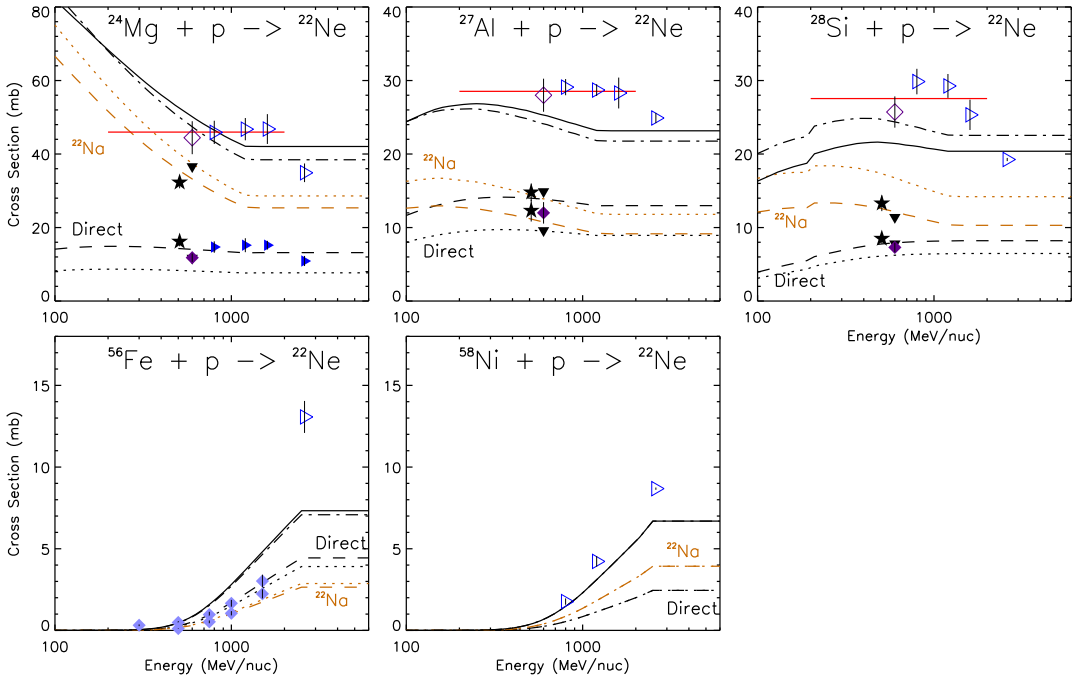

Figure C.3: Selected cross sections for the production of ^{22}Ne. For a definition of the data, please refer to the caption of Figure C.1. For these examples, the indirect production of ^{22}Ne via the decay of ^{22}Na is also shown (brown dotted and dashed lines) since this cross section is an important contribution to the cumulative cross section.

^{24}Mg + p → ^{22}Ne: The original direct S&T cross section (black dotted line) is too low compared to the available direct measurements (filled points), and it can be rescaled (black dashed line) to fit those data. The original S&T cross section for indirect production of ^{22}Ne via the decay of ^{22}Na (brown dotted line) is a little high compared to the associated Webber data (filled points) and can also be rescaled (brown dashed line). The cumulative S&T cross section calculated using the rescaled

direct and indirect production routes (black solid line) is a better fit to the available cumulative data (open points) than the unscaled cumulative S&T cross section (black dot-dashed line). The cumulative cross section below ∼1 GeV/nucleon has a strong energy dependence that can't be confirmed by the measurements, so instead a flat value (red solid line) is adopted that represents the average of the cumulative data in the energy band defined by this line.

^{27}Al + p → ^{22}Ne: The original direct S&T cross section (black dotted line) is a little low compared to the available direct data (higher two black and one purple filled points), and it can be rescaled (black dashed line) to fit those data. The indirect production of ^{22}Ne from ^{22}Na is a little high (brown dotted line) for the data (lower two black filled points), and so it can also be rescaled (brown dashed line). The cumulative S&T cross sections with and without the rescaling (black solid and dot-dashed lines, respectively) are similar to one another, though the rescaled curve gives a slightly higher cross section. However, the shape isn't right so a flat value (red solid line) is adopted.

^{28}Si + p → ^{22}Ne: This reaction has nearly the same features and problems as ^{27}Al + p → ^{22}Ne. Therefore, a flat shape (solid red line) is also used here.

^{56}Fe + p → ^{22}Ne: This reaction has very small cross sections compared to the first three examples, and Fe is less abundant than both Mg and Si. Therefore, this reaction is not very important for ^{22}Ne production. The direct and indirect data (filled points)

are well fit by both the original and rescaled S&T cross sections (black and brown dotted and dashed lines). The single cumulative measurement (open point) is high compared to the cumulative S&T cross section, but it is at an energy higher than we are interested. Therefore, no additional rescaling is used here.

^{58}Ni + p $\rightarrow$ ^{22}Ne: This reaction has very small cross sections compared to the first three examples, and Ni is less abundant than Fe. Therefore, this reaction is not very important for ^{22}Ne production. There are no direct or indirect cross section measurements, but there are cumulative data (open points) that can be used to rescale the cross sections. These data are fairly well fit by the unscaled cumulative S&T cross sections (black solid line), and so no additional rescaling is used for this reaction.

C.2.4 ^{22}Na production

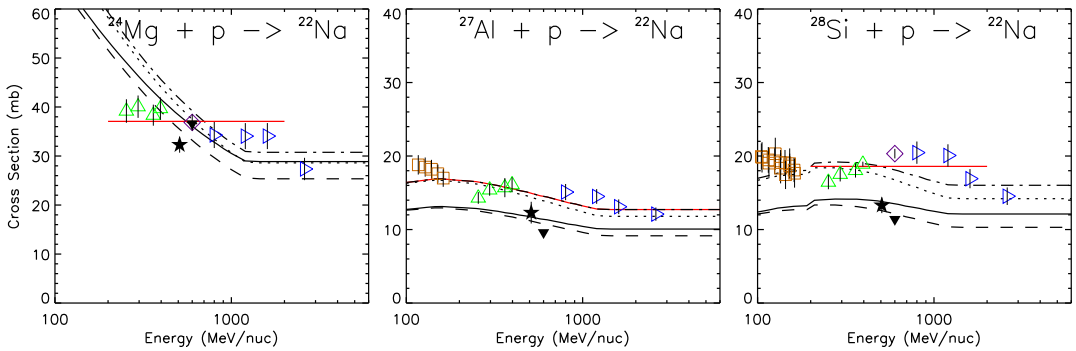

Figure C.4: Selected cross sections for the production of ^{22}Na. For a definition of the data, please refer to the caption of Figure C.1.

^{24}Mg + p $\rightarrow$ ^{22}Na: The original direct S&T cross section (black dotted line) is too high compared to the direct Webber measurements (filled points), and it can be rescaled (black dashed line) to fit those data. Both the unscaled and rescaled cumulative S&T cross sections (black dot-dashed and solid lines, respectively) have similar shapes with strong energy dependences, though below ~1 GeV/nucleon the cumulative data (open points) suggest a flatter shape. Therefore, a flat value (red solid line) is adopted that represents the average of the cumulative data in the energy band defined by this line.

^{27}Al + p $\rightarrow$ ^{22}Na: The original direct S&T cross section (black dotted line) is a little high compared to the direct Webber data (filled points), and so it can be rescaled (black dashed line) to fit those data. The available cumulative data (open

points) suggest a very broad peak that is almost well fit by the unscaled cumulative S&T cross section (black dot-dashed line), while the rescaled cumulative S&T cross section (black solid line) is too low compared to the cumulative data. Therefore, for this work we will not use the cumulative S&T cross section rescaled according to the direct Webber data. For clarity, the unscaled cumulative S&T cross section is overdrawn with a red solid line to indicate our choice.

^{28}Si + p $\rightarrow$ ^{22}Na: This reaction is very similar to ^{27}Al + p $\rightarrow$ ^{22}Na, however the cumulative data (open points) peak at a higher energy. Choosing the unscaled cumulative S&T cross section (black dot-dashed line), as was done in the previous reaction, is not quite right here so instead we adopted a flat value shown by the red solid line.

C.2.5 ^{24}Na production

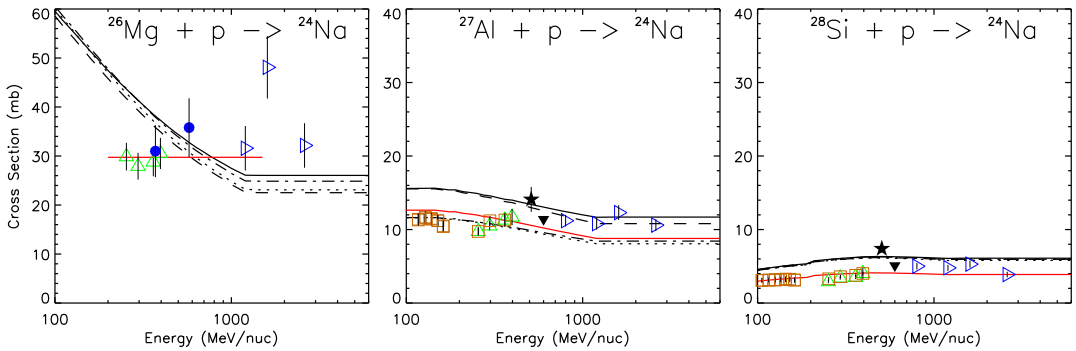

Figure C.5: Selected cross sections for the production of ^{24}Na. For a definition of the data, please refer to the caption of Figure C.1.

^{26}Mg + p → ^{24}Na: The original direct S&T cross section (black dotted line) is quite similar to the direct cross section when it is rescaled (black dashed line) to the direct measurements (filled points). This is also true of the unscaled (black dot-dashed line) and rescaled (black solid line) cumulative S&T cross sections. However, below ∼1 GeV/nucleon the cumulative data (open points) suggest a flatter shape. Therefore, a flat value (red solid line) is adopted that represents the average of the cumulative data in the energy band defined by this line. Note that the highest energy points were not used to determine the new shape since there were very large corrections made to these data (refer to Michel et al. (1995)).

^{27}Al + p → ^{24}Na: The original direct S&T cross section (black dotted line) is a little low compared to the direct Webber data (filled points), and it can be rescaled (black

dashed line) to fit those data. The unscaled cumulative S&T cross section (black dot-dashed line) gives a better fit to the cumulative data (open points) below ∼500 MeV/nucleon, while the rescaled cumulative S&T cross section (black solid line) gives a better fit to the data above ∼500 MeV/nucleon. Therefore, the cumulative S&T cross section is rescaled using the cumulative data between 200-2000 MeV/nucleon, which is shown as a red solid line.

^{28}Si + p → ^{24}Na: Both the unscaled (black dotted line) and rescaled (black dashed line) direct S&T cross sections fit the direct measurements (filled points) well. The unscaled (black dot-dashed line) and rescaled (black solid line) cumulative S&T cross sections are nearly identical, however they are a little high compared to the cumulative data (open points). Even though these cross sections are small compared to the previous two examples, we chose to rescale (red solid line) to the cumulative data since Si is a very abundant parent in the cosmic rays.

C.2.6 ^{26}Al production

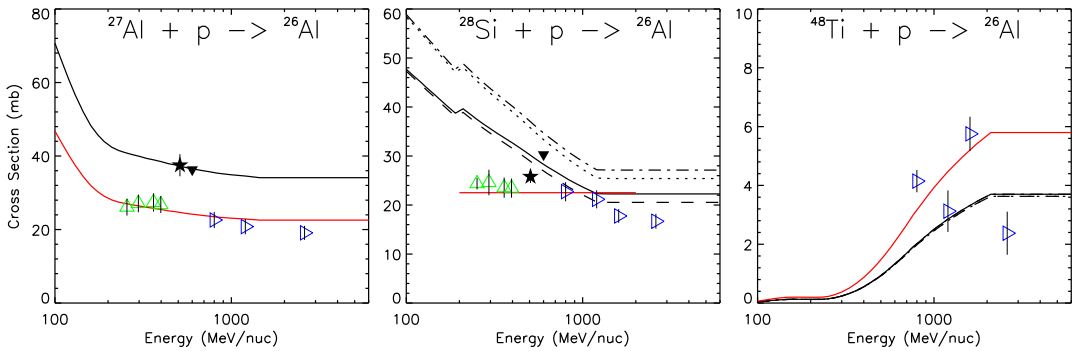

Figure C.6: Selected cross sections for the production of ^{26}Al. For a definition of the data, please refer to the caption of Figure C.1.

^{27}Al + p → ^{26}Al: For this reaction there are no indirect routes that contribute to the cumulative cross section; therefore, there is only the direct route to consider here. The original S&T cross section (black solid line) perfectly fits the Webber data (filled points). However, the other data (open points) suggest much lower cross sections. Yanasak et al. (2001) found agreement between the ^{10}Be, ^{26}Al, ^{36}Cl, and ^{54}Mn confinement times when the S&T cross section was rescaled to the lower non-Webber data. Therefore, the same choice is made to rescale to the non-Webber data, which is shown as a red solid line.

^{28}Si + p → ^{26}Al: The original direct S&T cross section (black dotted line) is too high compared to the direct Webber measurements (filled points). Therefore, it can be rescaled (black dashed line) to fit those data. The unscaled cumulative S&T cross

section (black dot-dashed line) is high compared to the cumulative data (open points), while the cumulative S&T cross section that is rescaled (black solid line) according to the direct measurements more closes fits the cumulative data. However, below ∼1 GeV/nucleon the cumulative data suggest a flatter shape. Therefore, a flat value (red solid line) is adopted which represents the average of the cumulative data in the energy band defined by this line.

^{48}Ti + p → ^{26}Al: This reaction has much smaller cross sections compared to the first two examples, and Ti is less abundant than Si. Therefore, this reaction is not very important for ^{26}Al production. There are no direct cross section measurements, and the cumulative data (open points) are widely scattered. For this reason we have chosen to rescale the cumulative S&T cross section to the data (red solid line) below 2 GeV/nucleon.

C.2.7 ^{36}Ar production

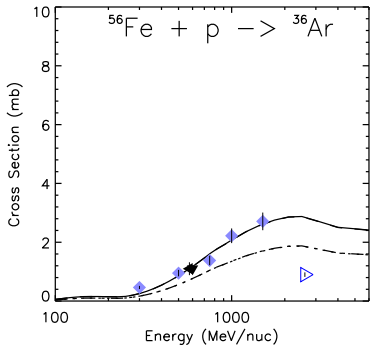

Figure C.7: Selected cross sections for the production of ^{36}Ar. For a definition of the data, please refer to the caption of Figure C.1.

^{56}Fe + p $\rightarrow$ ^{36}Ar: This reaction has very small cross sections. The original direct S&T cross section (black dotted line, under the black dot-dashed line) is too low given the direct measurements (filled points). After rescaling (black dashed line, under the black solid line), the direct measurements are very well fit by S&T. The original and rescaled cumulative S&T cross sections (black dot-dashed and solid lines, respectively) are also shown. The single cumulative measurement (open point) does not agree with either cumulative S&T cross section and it is lower than the highest energy direct data (which is unphysical); therefore we have chosen to use no additional rescaling to fit that single point.

C.2.8 ^{38}Ar production

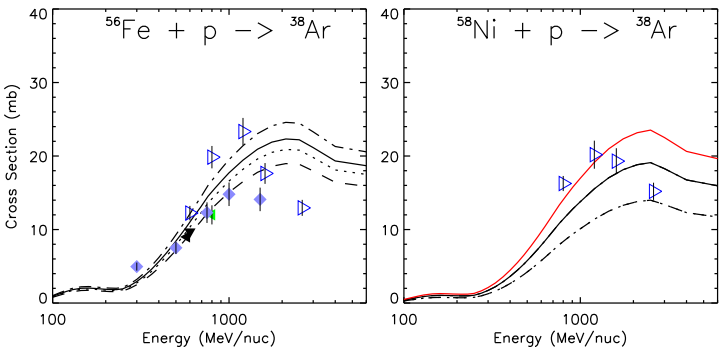

Figure C.8: Selected cross sections for the production of ^{38}Ar. For a definition of the data, please refer to the caption of Figure C.1.

^{56}Fe + p → ^{38}Ar: The original direct S&T cross section (black dotted line) is a little high given the direct measurements (filled points). After rescaling (black dashed line), these data are mostly well fit by S&T. The cumulative data (open points) are slightly better fit with the unscaled cumulative S&T cross section (black dot-dashed line) than the rescaled cumulative S&T cross section (black solid line). However, the cumulative data have a narrow peak with the highest energy points turning over very quickly. The rescaled cumulative S&T cross section fits the cumulative data well enough below 2 GeV/nucleon, so this form is used in this work.

^{58}Ni + p → ^{38}Ar: There are no direct data available, though there are cumulative data (open points) that can be used to rescale the original cumulative S&T cross section (black dot-dashed line). The cumulative data peak at a lower energy than

the rescaled S&T (black solid line), so S&T is rescaled according to the data below 2 GeV/nucleon. The red solid line gives the result, which is used in this work.

C.2.9 ^{42}K production

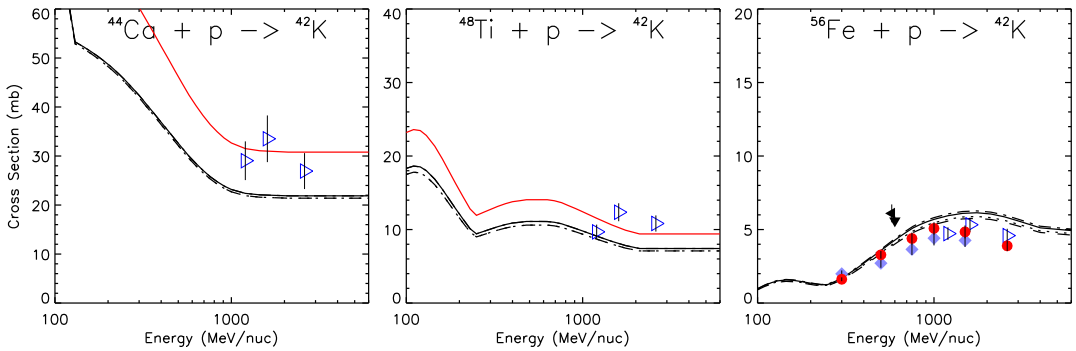

Figure C.9: Selected cross sections for the production of ^{42}K. For a definition of the data, please refer to the caption of Figure C.1.

^{44}Ca + p → ^{42}K: This reaction has no direct measurements, and the original cumulative S&T cross section is given by the black dot-dashed line (the black solid line is the cumulative S&T cross section after accounting for any rescaling in the indirect production routes). The cumulative data (open points) are higher than the cumulative S&T cross section, so S&T is rescaled (red solid line) according to these data.

^{48}Ti + p → ^{42}K: This reaction has the same features and problems as ^{44}Ca + p → ^{42}K. Therefore, the cumulative S&T (black solid line) is rescaled according to the cumulative data (open points). This is shown the the red solid line.

^{56}Fe + p → ^{42}K: The original direct S&T cross section (black dotted line) can be rescaled using the available direct measurements. The Webber data (black filled

points) are not in agreement with the rest of the direct data (other filled points), and so the rescaled S&T cross section (black dashed line) is a little high compared to the non-Webber data. The unscaled and rescaled cumulative S&T cross sections (black dot-dashed and solid lines, respectively) are nearly the same and also a little high compared to the cumulative data (open points). However, this reaction is not very important to ^{42}K production, so we have decided that no further rescaling is necessary for this reaction.

C.2.10 ^{43}K production

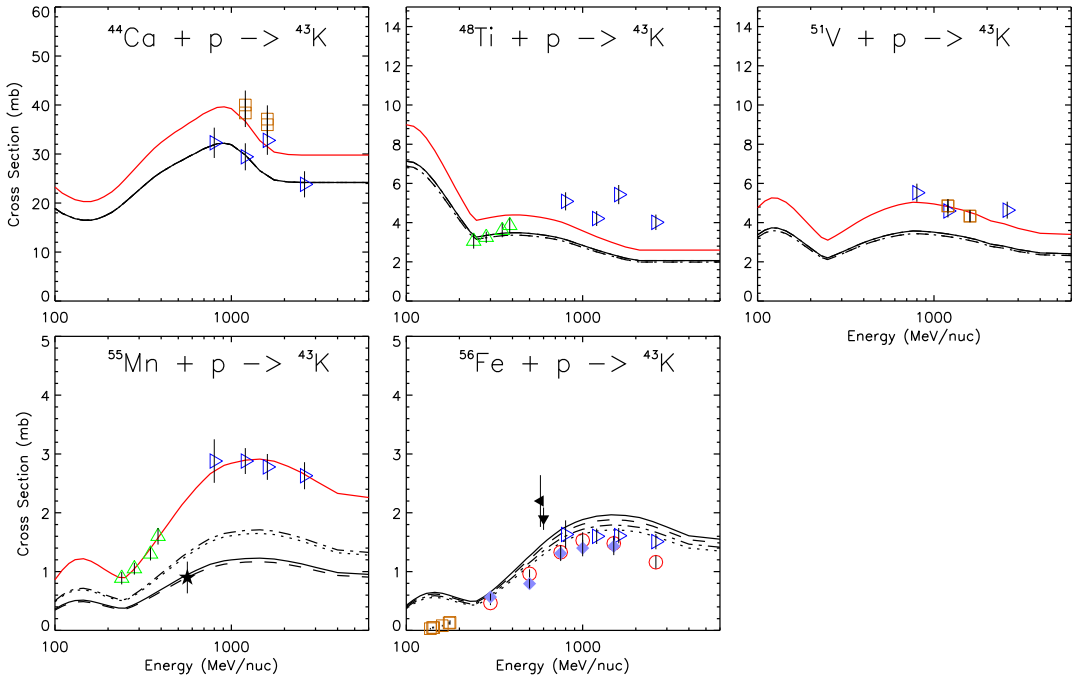

Figure C.10: Selected cross sections for the production of ^{43}K. For a definition of the data, please refer to the caption of Figure C.1.

^{44}Ca + p → ^{43}K: This reaction has no direct measurements, and the original cumulative S&T cross section is given by the black dot-dashed line (the black solid line is the cumulative S&T cross section after accounting for any rescaling in the indirect production routes). The cumulative data (open points) are higher than the cumulative S&T cross section, so S&T is rescaled (red solid line) according to these data.

^{48}Ti + p → ^{43}K: This reaction has the same features and problems as ^{44}Ca + p → ^{43}K. Therefore, the cumulative S&T (black solid line) is rescaled according to the cumulative data (open points). This is shown by the red solid line.

^{51}V + p → ^{43}K: This reaction has the same features and problems as ^{44}Ca + p → ^{43}K. Therefore, the cumulative S&T (black solid line) is rescaled according to the cumulative data (open points). This is shown by the red solid line.

^{55}Mn + p → ^{43}K: The original direct S&T cross section (black dotted line) is too high given the single direct Webber measurement (filled point), and so it can be rescaled (black dashed line). Neither the unscaled or rescaled cumulative S&T cross sections (black dot-dashed and solid lines, respectively) give a good fit to the cumulative data (open points). Therefore, the cumulative S&T cross section is rescaled (red solid line) to these data.

^{56}Fe + p → ^{43}K: The original direct S&T cross section (black dotted line) can be rescaled using the direct measurements. The Webber data (black filled points) are not in agreement with the rest of the direct data (other filled points), and so the rescaled S&T cross section (black dashed line) is a little high compared to the non-Webber data. The unscaled and rescaled cumulative S&T cross sections (black dot-dashed and solid lines, respectively) are nearly the same and a little high compared to the cumulative data (open points). However, this reaction is not very important to ^{43}K production, so we have decided that no further rescaling is necessary.

C.2.11 ^{47}Ca production

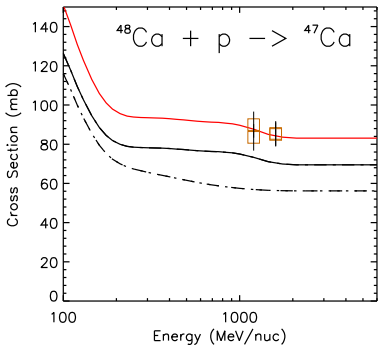

Figure C.11: Selected cross sections for the production of ^{47}Ca. For a definition of the data, please refer to the caption of Figure C.1.

^{48}Ca + p → ^{47}Ca: This reaction has no direct measurements, and the original cumulative S&T cross section is given by the black dot-dashed line (the black solid line is the cumulative S&T cross section after accounting for any rescaling in the indirect production routes). The cumulative data (open points) are higher than the cumulative S&T cross section, so S&T is rescaled (red solid line) according to these data.

C.2.12 ^{43}Sc production

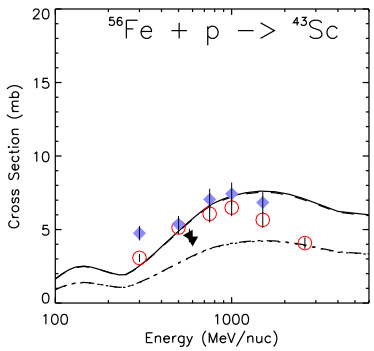

Figure C.12: Selected cross sections for the production of ^{43}Sc. For a definition of the data, please refer to the caption of Figure C.1.

^{56}Fe + p $\rightarrow$ ^{43}Sc: The original direct S&T cross section (black dotted line) is too low given the direct data (filled points). After rescaling (black dashed line), the data are mostly well fit by S&T. The unscaled cumulative S&T cross section (black dot-dashed line, overlaying the dotted line) is too low compare to the cumulative data (open points), though when it is rescaled (black solid line, overlaying the dashed line) the data are well fit below $\sim$1 GeV/nucleon. Since the higher energies are not very important for this work, the rescaled cumulative S&T cross section is good enough to be used here.

C.2.13 ^{47}Sc production

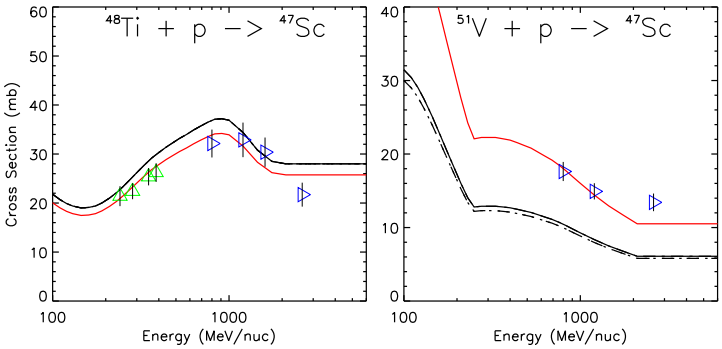

Figure C.13: Selected cross sections for the production of ^{47}Sc. For a definition of the data, please refer to the caption of Figure C.1.

^{48}Ti + p → ^{47}Sc: This reaction has no direct measurements, and the original cumulative S&T cross section is given by the black dot-dashed line (it is overlapped by the black solid line, which is the cumulative S&T cross section after accounting for any rescaling in the indirect production routes). The cumulative data (open points) are generally a little lower than the cumulative S&T cross section, so S&T is rescaled (red solid line) according to these data.

^{51}V + p → ^{47}Sc: This reaction has the same features and problems as ^{48}Ti + p → ^{47}Sc, only now the cumulative data (open points) are high compared to S&T. Therefore, the cumulative S&T cross section (black solid line) is rescaled according to the data. This is shown by the red solid line.

C.2.14 ^{48}V production

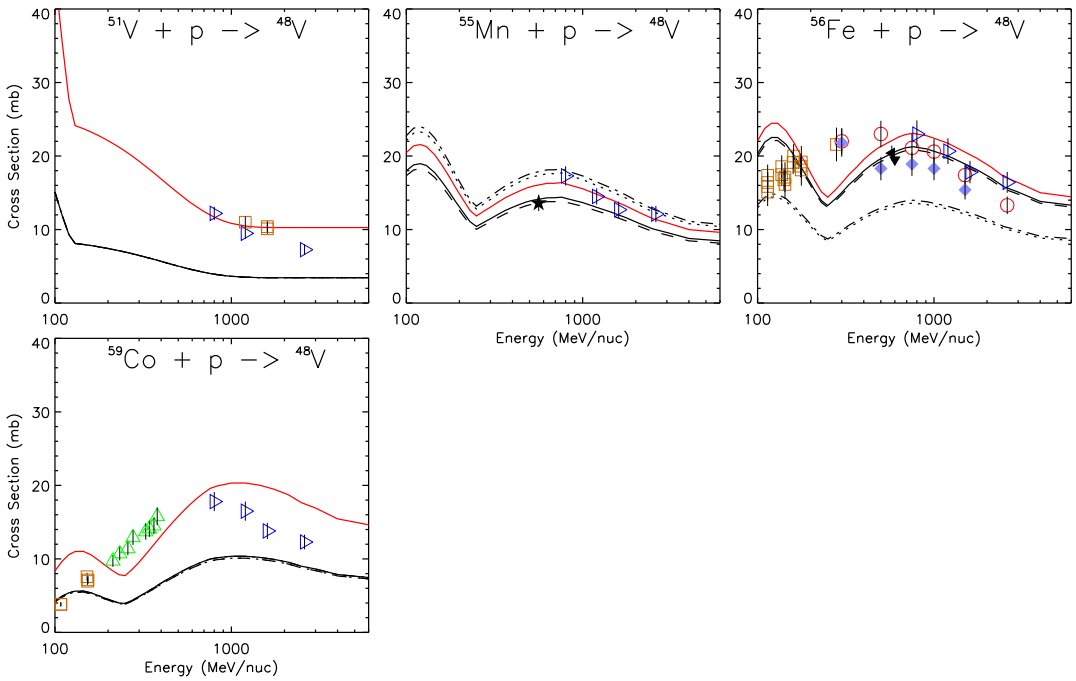

Figure C.14: Selected cross sections for the production of ^{48}V. For a definition of the data, please refer to the caption of Figure C.1.

^{51}V + p → ^{48}V: This reaction has no direct measurements, and the original cumulative S&T cross section is given by the black dot-dashed line (it is overlapped by the black solid line, which is the cumulative S&T cross section after accounting for any rescaling in the indirect production routes). The cumulative data (open points) are higher than the cumulative S&T cross section, so S&T is rescaled (red solid line) according to these data.

^{55}Mn + p → ^{48}V: The original direct S&T cross section (black dotted line) is too high given the single Webber measurement (filled point), and so it can be rescaled (black dashed line). The cumulative data (open points) fall between the unscaled and rescaled cumulative S&T cross sections (black dot-dashed and solid lines, respectively). Therefore, S&T is rescaled to the cumulative data (red solid line) to obtain a better fit.

^{56}Fe + p → ^{48}V: The original direct S&T cross section (black dotted line) is too low given the Webber data (filled points), and so it can be rescaled (black dashed line). However, the lowest energy direct measurement (∼300 MeV/nucleon) is higher than the rest of the data, so the rescaling pulls S&T up a bit from the rest of the data. The cumulative data (open points) are higher than the unscaled cumulative S&T cross section (black dot-dashed line), though above ∼700 MeV/nucleon the fit is much closer for the cumulative S&T that has been rescaled (black solid line) according to the direct measurements. Below ∼500 MeV/nucleon, the fit is poor because the data peak at a lower energy than S&T. The cross sections below a few hundred MeV/nucleon are not relevant for this work, so the discrepancy should not be a problem here. Since this reaction is the most important route for the production of ^{48}V, we have chosen to rescale the cumulative S&T cross section (solid red line) to the cumulative data.

^{59}Co + p → ^{48}V: This reaction has the same features and problems as ^{51}V + p → ^{48}V. Therefore, the cumulative S&T (black solid line) is rescaled according to the

cumulative data (open points), which is shown by the red solid line. Though S&T peaks at a higher energy than the data suggest, Co is much less abundant than Fe; therefore this reaction is not very important for ^{48}V production and no additional changes are adopted here.

C.2.15 ^{48}Cr production

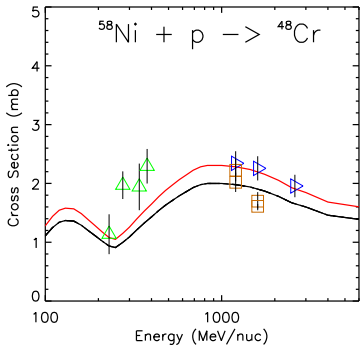

Figure C.15: Selected cross sections for the production of ^{48}Cr. For a definition of the data, please refer to the caption of Figure C.1.

^{58}Ni + p → ^{48}Cr: This reaction has no direct measurements, and the original cumulative S&T cross section is given by the black dot-dashed line (the black solid line is the cumulative S&T cross section after accounting for any rescaling in the indirect production routes). The cumulative data (open points) are a little higher than the cumulative S&T cross section, so S&T is rescaled (red solid line) according to these data.

C.2.16 ^{49}Cr production

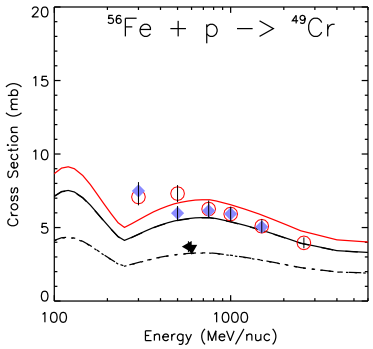

Figure C.16: Selected cross sections for the production of ^{49}Cr. For a definition of the data, please refer to the caption of Figure C.1.

^{56}Fe + p → ^{49}Cr: The original direct S&T cross section (black dotted line, overlapped by the black dot-dashed line) is low compared to all of the available direct measurements. The Webber data (black filled points) are not in agreement with the rest of the direct data (other filled points), and so when S&T is rescaled (black dashed line, overlapped by the black solid line) it is a little low compared to the non-Webber data. Compared to the cumulative data (open points), the unscaled cumulative S&T cross section (black dot-dashed line) is also too low. When rescaled according to the direct measurements (black solid line) it is also a little low compared to the cumulative data. Therefore, the cumulative S&T cross section is rescaled according to the cumulative data, as shown by the red solid line.

C.2.17 ^{51}Cr production

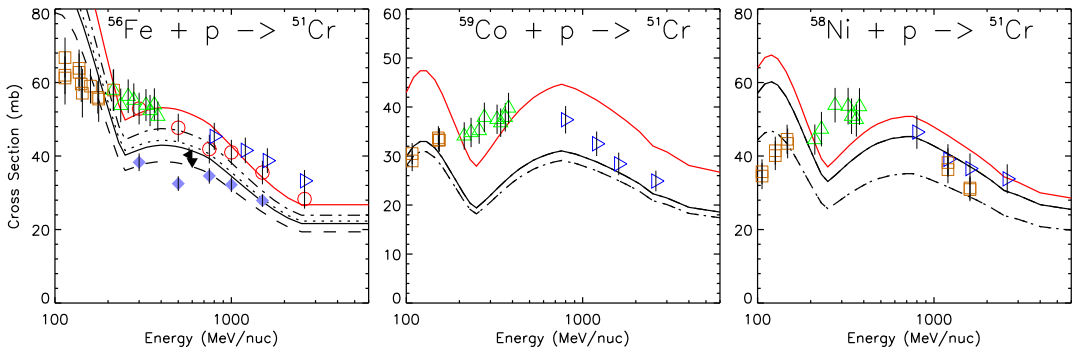

Figure C.17: Selected cross sections for the production of ^{51}Cr. For a definition of the data, please refer to the caption of Figure C.1.

^{56}Fe + p → ^{51}Cr: The original direct S&T cross section (black dotted line) is too high given the direct measurements (filled points), and therefore it can be rescaled (black dashed line). The cumulative data (open points) are high compared to the unscaled cumulative S&T cross section (black dot-dashed line). The rescaling according to the direct measurements also means that the rescaled cumulative S&T cross section (black solid line) is even lower than the cumulative data. These data also do not suggest the same energy dependence as S&T; therefore, we have chosen to rescale the cumulative S&T to the cumulative data (red solid line). This give a fairly good fit to the data, except at energies below ∼200 MeV/nucleon (though these energies are too low to be important for this work).

^{59}Co + p $\rightarrow$ ^{51}Cr: This reaction has no direct measurements, and the original cumulative S&T cross section is given by the black dot-dashed line (the black solid line is the cumulative S&T cross section after accounting for any rescaling in the indirect production routes). The cumulative data (open points) are higher than the cumulative S&T cross section, and they peak at a lower energy than S&T. We chose to rescale S&T (red solid line) according to these data. Though the fit is not great, Co is much less abundant than Fe so this reaction is not very important for ^{51}Cr production, and the discrepancy should not affect the results in this work.

^{58}Ni + p $\rightarrow$ ^{51}Cr: This reaction has the same features and problems as ^{59}Co + p $\rightarrow$ ^{51}Cr. Therefore, the cumulative S&T (black solid line) is rescaled according to the cumulative data (open points). This is shown by the red solid line. The fit isn't great below 500 MeV/nucleon, though the problems at the lowest energies are not an issue since they too low to be important for this work.

C.2.18 ^{52}Mn production

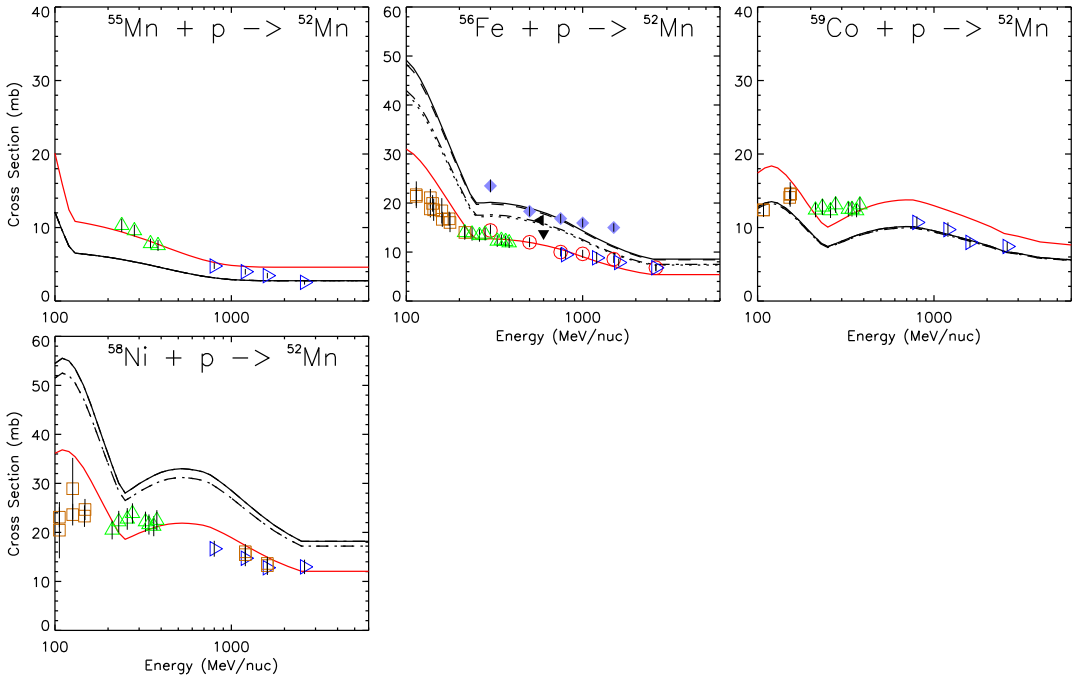

Figure C.18: Selected cross sections for the production of ^{52}Mn. For a definition of the data, please refer to the caption of Figure C.1.

^{55}Mn + p → ^{52}Mn: This reaction has no direct measurements, and the original cumulative S&T cross section is given by the black dot-dashed line (the black solid line, which overlays the dot-dashed line, is the cumulative S&T cross section after accounting for any rescaling in the indirect production routes). The cumulative data (open points) are higher than the cumulative S&T cross section, so S&T is rescaled (red solid line) according to these data.

^{56}Fe + p → ^{52}Mn: The original direct S&T cross section (black dotted line) is a little low given the direct measurements (filled points), and so it can be rescaled (black dashed line). The cumulative data (open points) aren't fit by the unscaled cumulative S&T cross section (black dot-dashed line), or when it is rescaled according to the direct and indirect measurements (black solid line). These data are significantly lower than the direct measurements, which is simply unphysical. Since there are several experiments whose cumulative cross section measurements agree with one another, this suggests that the direct measurements may have had corrections that gave cross sections that were too large. Therefore, we chose to rescale S&T to the cumulative data (red solid line).

^{59}Co + p → ^{52}Mn: This reaction has no direct measurements, and the original cumulative S&T cross section is given by the black dot-dashed line (the black solid line, which overlays the dot-dashed line, is the cumulative S&T cross section after accounting for any rescaling in the indirect production routes). The cumulative data (open points) are higher than the cumulative S&T cross section, and they peak at a lower energy than S&T. We chose to rescale S&T (red solid line) according to these data. Though the fit is not perfect, Co is much less abundant than Fe so this reaction is not very important for ^{52}Mn production, and the discrepancy should not affect the results in this work.

^{58}Ni + p → ^{52}Mn: This reaction has the same features and problems as ^{59}Co + p → ^{52}Mn, though the cumulative data (open points) are lower than the unscaled

(black dot-dashed line) and rescaled (black solid line) cumulative S&T. Therefore, we chose to rescale S&T according to the cumulative data, shown by the red solid line.

C.2.19 ^{55}Co production

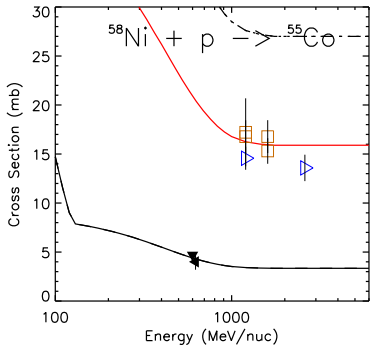

Figure C.19: Selected cross sections for the production of ^{55}Co. For a definition of the data, please refer to the caption of Figure C.1.

^{58}Ni + p → ^{55}Co: The original direct S&T cross section (black dotted line, overlapped by the black dot-dashed line) is much too high compared to the direct Webber measurements (filled points), and so it can be rescaled (black dashed line, overlapped by the black solid line). The cumulative data (open points) are not fit by the rescaled cumulative S&T cross section (black solid line), which is too low compared to the data. On the other hand, the unscaled cumulative S&T cross section (black dot-dashed line) is much too high for these data. Therefore, S&T is rescaled to the cumulative data, given by the red solid line.

C.2.20 ^{56}Co production

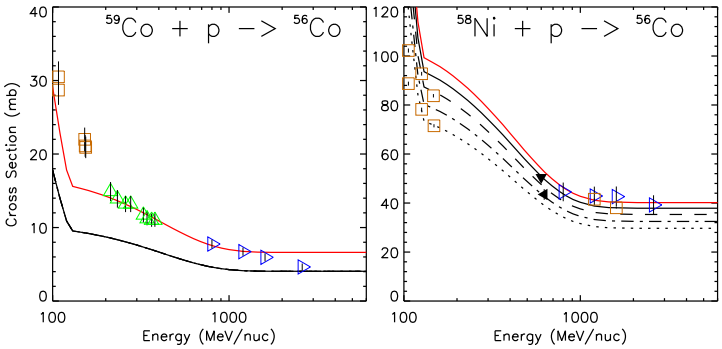

Figure C.20: Selected cross sections for the production of ^{56}Co. For a definition of the data, please refer to the caption of Figure C.1.

^{59}Co + p → ^{56}Co: This reaction has no direct measurements, and the original cumulative S&T cross section is given by the black dot-dashed line (the black solid line, which overlays the dot-dashed line, is the cumulative S&T cross section after accounting for any rescaling in the indirect production routes). The cumulative data (open points) are higher than S&T, so we chose to rescale S&T (red solid line) according to these data. The fit at the lowest energies is not perfect, however this should not be a problem since the discrepancy occurs at energies that are too low to be important for this work.

^{58}Ni + p → ^{56}Co: The original direct S&T cross section (black dotted line) is too low given the direct Webber measurements (filled points), and therefore it can be rescaled (black dashed line) to better fit those data. The unscaled cumulative S&T

cross section (black dot-dashed line) is also too low compared to the cumulative data (open points), though they are nearly fit by the cumulative S&T (black solid line) that is rescaled according to the Webber data. Since this is a large production cross section, we chose to rescale S&T to the cumulative data (red solid line) to get the best fit.

C.2.21 ^{57}Co production

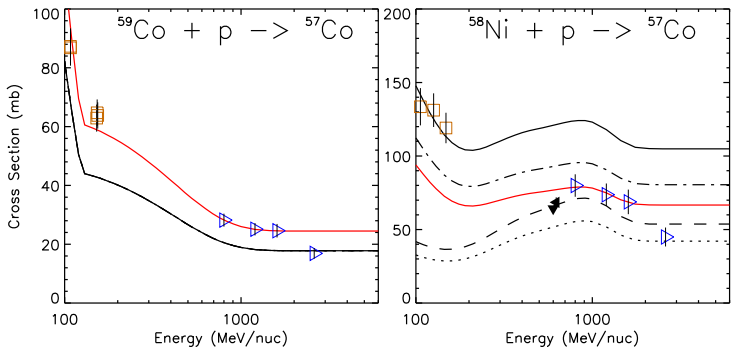

Figure C.21: Selected cross sections for the production of ^{57}Co. For a definition of the data, please refer to the caption of Figure C.1.

^{59}Co + p → ^{57}Co: This reaction has no direct measurements, and the original cumulative S&T cross section is given by the black dot-dashed line (the black solid line, which overlays the dot-dashed line, is the cumulative S&T cross section after accounting for any rescaling in the indirect production routes). The cumulative data (open points) are higher than S&T, so we chose to rescale S&T (red solid line) according to these data.

^{58}Ni + p → ^{57}Co: The original direct S&T cross section (black dotted line) is too low given the direct Webber measurements (filled points), and so it can be rescaled (black dashed line). The unscaled cumulative S&T cross section (black dot-dashed line) is high compared to the cumulative data (open points). Since we rescaled the direct cross section to the Webber data, the rescaled cumulative S&T cross section

(black solid line) gives a worse fit to the cumulative data. Therefore, we chose to rescale the cumulative S&T to the higher energy cumulative data only (red solid line), since the data suggest a different energy dependence than S&T and the low-energy measurements are outside our interest for this work.

C.2.22 ^{56}Ni production

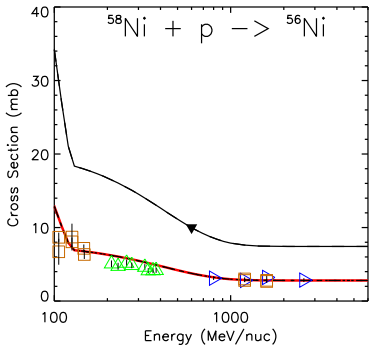

Figure C.22: Selected cross sections for the production of ^{56}Ni. For a definition of the data, please refer to the caption of Figure C.1.

^{58}Ni + p $\rightarrow$ ^{56}Ni: The original direct S&T cross section (black dotted line, overlapped by the black dot-dashed line) is too low given the single direct Webber measurement (filled point), and so it can be rescaled (black dashed line, overlapped by the black solid line). The cumulative data (open), which are lower than the direct measurement, are much lower than the rescaled cumulative S&T cross section (black solid line). In fact, the unscaled cumulative S&T (black dot-dashed line) gives a much better fit. Since it is unphysical for the cumulative cross sections to be lower than the direct measurement, we have chosen to use the unscaled cumulative S&T cross section (red solid line) since it fits the data well.

C.2.23 ^{57}Ni production

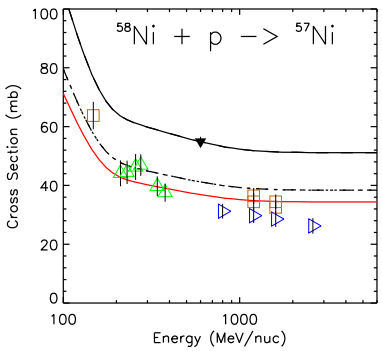

Figure C.23: Selected cross sections for the production of ^{57}Ni. For a definition of the data, please refer to the caption of Figure C.1.

^{58}Ni + p $\rightarrow$ ^{57}Ni: The original direct S&T cross section (black dotted line, overlapped by the black dot-dashed line) is too low given the single direct Webber measurement (filled point), and so it can be rescaled (black dashed line, overlapped by the black solid line). The cumulative data (open) are much lower than the rescaled cumulative S&T cross section (black solid line). The unscaled cumulative S&T (black dot-dashed line) gives a closer fit, though it is still high compared to the data. Therefore, we have chosen to rescale the cumulative S&T cross section (red solid line) to the cumulative data.

C.3 Electron-capture decay nuclides

The NNDC databases were also used to ensure that we had the most up-to-date decay half-lives and branching ratios (for those nuclides that decayed by multiple processes). Nuclides that decay only by electron capture require an adjusted decay half-life, which can be calculated using the following procedure (George 1999).

Nuclear decays are governed by a transition rate λ (probability/time) that is the sum of all the transition rates for all possible decay channels:

$$\lambda_{filled} = \lambda_{K_1} + \lambda_{K_2} + \lambda_{L_1} + \lambda_{L_2} + \lambda_{L_3} + \cdots \tag{C.1}$$

There is an equal probability the a nuclide will capture either the K_1 or K_2 electron. For the isotopes we are interested in, capture from the L_1 shell dominates over all higher shells. In the cosmic rays there is at most a single attached electron and therefore a single decay channel, and so we define $\lambda_{K_1} = \lambda_{K_2} = \lambda_K = \lambda_{CR}$. Therefore, the capture probability can be rewritten as:

$$\frac{\lambda_{filled}}{\lambda_{CR}} = 2 + \frac{\lambda_{L_1}}{\lambda_K} \, . \tag{C.2}$$

Radioactive decay half-lives are given by $0.5 = \exp(-\lambda T_{1/2})$, which may be substituted into Equation C.2:

$$\frac{T_{1/2,CR}}{T_{1/2,filled}} = \frac{\lambda_{filled}}{\lambda_{CR}} = 2 + \frac{\lambda_{L_1}}{\lambda_K} \, . \tag{C.3}$$

From this equation we see that the laboratory half-life $T_{1/2,filled}$ is related to the cosmic-ray half-life $T_{1/2,CR}$ by the L_1/K capture ratio. These ratios may be calculated with the following equation (Firestone and Shirley 1998):

$$\frac{\lambda_{L_1}}{\lambda_K} = c(Z)\left(\frac{E(EC) - E(L_1)}{E(EC) - E(K)}\right)^2 , \tag{C.4}$$

where $E(EC)$ is the electron capture decay energy, E_{L_1} and E_K are the binding energies for the L_1 and K shells, and $c(Z) = 9.5 \times 10^{-4}Z + 6.4 \times 10^{-2}$. For the species we consider in this work, the cosmic-ray half-lives are $\sim$2 times longer than the laboratory half-lives. For example, $T_{1/2,CR}/T_{1/2,filled}$ is 2.09 for ^{49}V and 2.08 for ^{51}Cr.

Appendix D

Simple and Nested Leaky-box Model Spectra

In this Appendix we provide the boron, carbon, scandium, titanium, vanadium, and iron energy spectra for each of the simple and nested leaky-box models presented in Chapters 4 and 5. Results are given for both solar minimum periods (Section 3.2) studied here. Though energy spectra are an important test of any model, we note that it is difficult to draw conclusions about interstellar transport models because the results are sensitive to shape of the injection spectrum as well as the solar modulation model, which substantially affects the spectra below a few GeV/nucleon. Tests of our solar modulation model (Chapter 1.4.3) are beyond the scope of this thesis, and so we recommend further studies of solar modulation before critiquing how well our interstellar models are able to reproduce the observed energy spectra.

D.1 Simple leaky-box model

For the simple leaky-box model we examined two interstellar models, each of which was defined by a different energy dependence for the escape mean free path from the

Galaxy (Section 4.1). For each model, we used our numerical solution discussed in Section 4.3 to calculate the isotopic interstellar equilibrium intensities. After summing the isotope spectra for a given element, we applied our solar modulation model (Chapter 1.4.3) to determine the elemental cosmic-ray intensities at Earth for each of the two solar minimum periods CRIS observed (Section 3.2). Here we present the calculated energy spectra for boron, carbon, scandium, titanium, vanadium, and iron. These six species are used to calculate the secondary-to-primary ratios B/C and $(Sc + Ti + V)/Fe$ for Models #1 (Section 4.4) and #2 (Section 4.5). We note that, of these species, boron and carbon will be most sensitive to the parameterization of escape from the Galaxy, while the sub-iron species and iron will be more sensitive to nuclear interactions. This may be seen in Figure 4.1, which compares the mean free paths for escape and interaction for ^{12}C and ^{56}Fe.

Using data from various spacecraft and balloon experiments that cover a large range in energy ($\sim 10 - 10^5$ MeV/nucleon), we can evaluate how well each model reproduces the observations. We have used data from the space missions IMP-8 (Garcia-Munoz et al. 1977) and HEAO-3 (Engelmann et al. 1990). Data from balloon experiments come from the University of Alabama (Huntsville) (Derrickson et al. 1992), the University of New Hampshire (Lezniak and Webber 1978), TRACER (Ave et al. 2008), and CRISIS (Young et al. 1981).

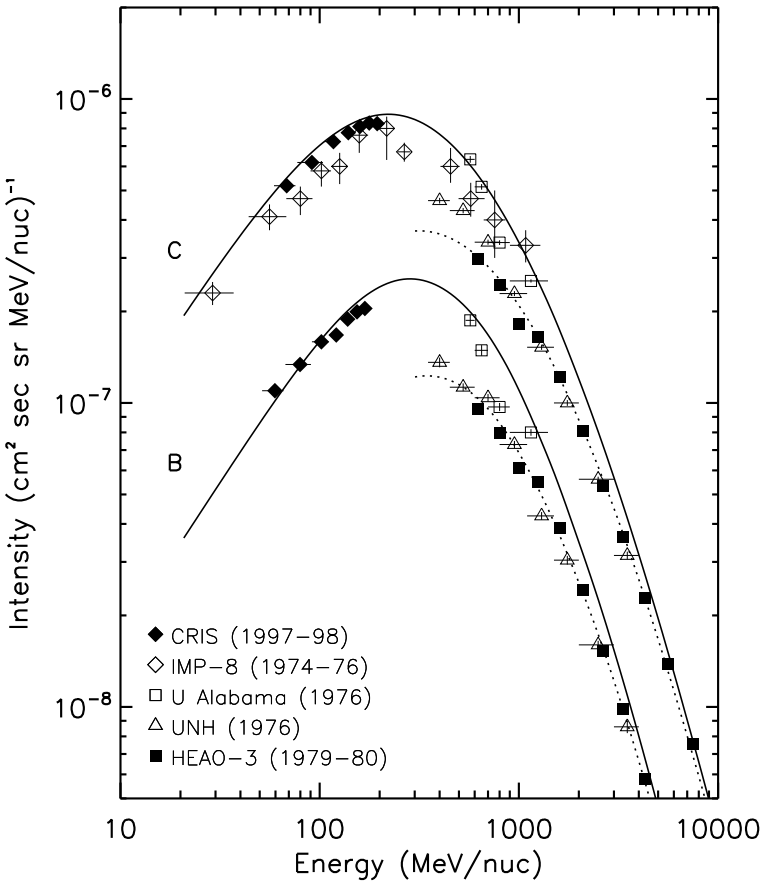

Figure D.1: Boron and carbon energy spectra for the 1997-98 solar minimum. CRIS observations discussed in this work are shown as filled diamonds; for references to all other data used here, refer to Appendix D.1. The solid curves are the result of an interstellar transport model using the Davis form of the escape mean free path (Equation 4.3), with a solar modulation level of $\phi = 325$ MV. The injection spectrum was taken to be a power law in momentum per nucleon, with a spectral index of -2.35. The dotted curves correspond to a modulation level of $\phi = 750$ MV, which is appropriate for the HEAO-3 mission.

D.1.1 Model #1: Davis escape mean free path

This first leaky-box transport model uses an injection spectrum was taken to be a power law in momentum per nucleon with a spectral index of -2.35, and the Davis form (Equation 4.3) for the escape mean free path in the Galaxy. The calculated

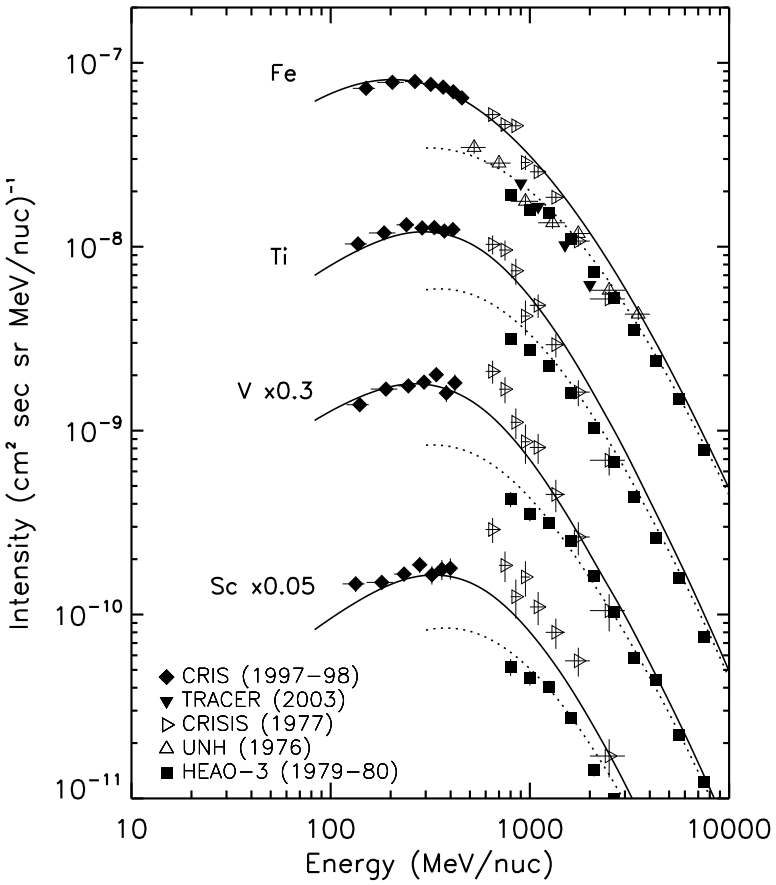

Figure D.2: Scandium, titanium, vanadium, and iron energy spectra for the 1997-98 solar minimum. For additional information concerning the data and interstellar transport models used here, refer to the caption of Figure D.1.

energy spectra for the 1997-98 solar minimum for each of the six chosen species are compared with experimental data in Figures D.1 and D.2. During this period of time, we estimate a solar modulation value of $\phi = 325$ MV; the model corresponding to this value is shown by the solid lines. For reference we also include our model for a modulation value of $\phi = 750$ MV, which is appropriate for the HEAO-3 mission, as shown by the dotted lines.

The CRIS boron and carbon measurements are nicely fit by the $\phi = 325$ MV

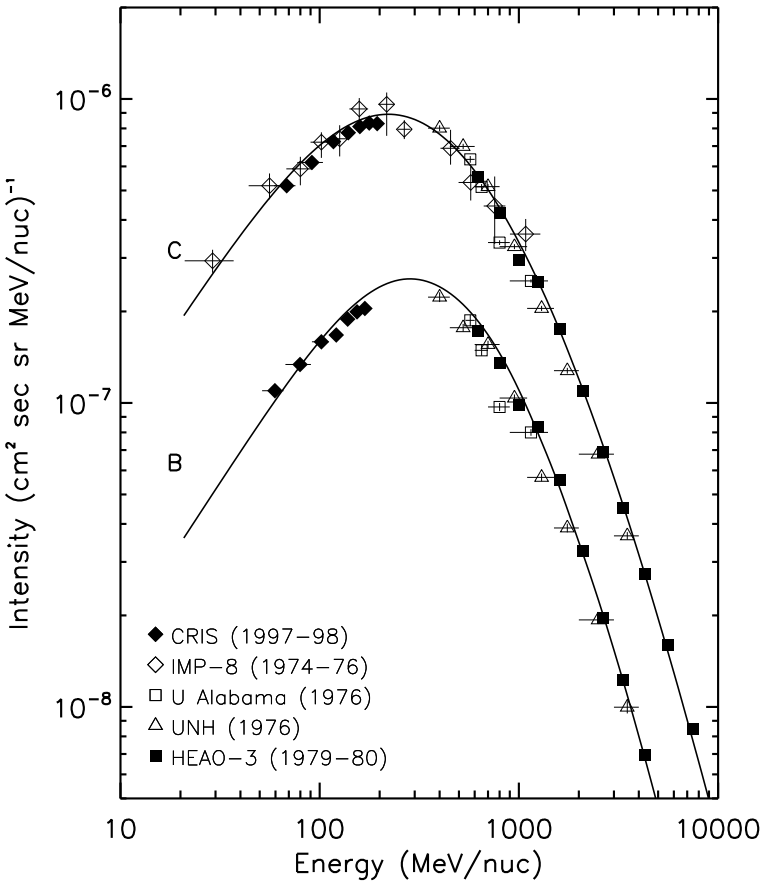

Figure D.3: Boron and carbon energy spectra for the 1997-98 solar minimum. CRIS observations discussed in this work are shown as filled diamonds; for references to all other data used here, refer to Appendix D.1. The solid curves are the result of an interstellar transport model using the Davis form of the escape mean free path (Equation 4.3), with a solar modulation level of $\phi = 325$ MV. The injection spectrum was taken to be a power law in momentum per nucleon, with a spectral index of -2.35. All data have been adjusted to this modulation level, as described in Appendix D.1.1.

model, though the carbon spectrum is slightly overestimated. The average differences between the model and the CRIS boron and carbon data are around 6%. The scandium, titanium, and vanadium spectra are also well fit by the model, with average differences of 7-9%. The best fit of the model to the CRIS data is for iron, where the data and the model differ on average by 3%. Out of these six species, the

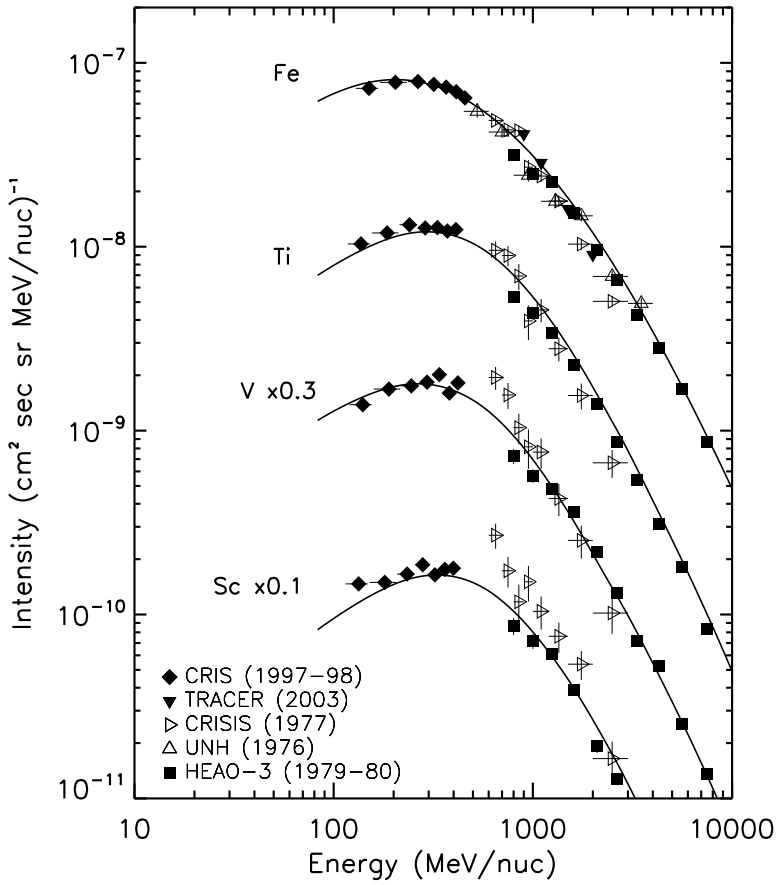

Figure D.4: Scandium, titanium, vanadium, and iron energy spectra for the 1997-98 solar minimum. For additional information concerning the data and interstellar transport models used here, refer to the caption of Figure D.3.

largest individual difference is at the lowest energy scandium measurement (21%). For most other CRIS measurements the differences are below 10%. We also note that the HEAO measurements for all six species are well fit by the $\phi = 750$ MV curve.

We can use other experimental data to test this model, as mentioned in Appendix D.1. These instruments operated at different periods of time in the solar cycle from CRIS, so we must first assign a solar modulation level for each dataset that is appropriate for the average conditions when the data were collected. As previously

indicated, we found that the CRIS and HEAO spectra were best fit using modulation levels of 325 MV and 750 MV, respectively. We obtained the values for other experiments by linearly interpolating the mean Climax neutron monitor rates for the various periods of time, as was done in our previous work (George et al. 2009). The following solar modulation levels are used here: 275 MV (CRISIS), 325 MV (UAH), 400 MV (IMP-8), 625 MV (UNH), and 900 MV (TRACER).

For each of the experiments we can adjust the data so that they are representative of a common modulation level. We do this by calculating the ratios of the intensities for each value of ϕ with respect to the intensities for $\phi = 325$ MV to determine the energy-dependent correction factors that should be applied to the data. Figures D.3 and D.4 plot all of the experimental data adjusted in this manner for the 1997-98 solar minimum. With the exception of the CRISIS data, which have large uncertainties for the rarer sub-iron species, we see that the other experimental data are well fit by this model and they are consistent with the CRIS energy spectra.

Similar plots for the 2009-10 solar minimum are shown in Figures D.5 through D.8. For this period of time, we estimate a solar modulation value of $\phi = 250$ MV (shown by the solid lines). For reference we again include our model for a modulation value of $\phi = 750$ MV that is appropriate for the HEAO-3 mission (shown by the dotted lines).

As with the previous solar minimum, the 2009-10 CRIS boron and carbon measurements are nicely fit by the $\phi = 250$ MV model, though again the carbon spectrum is systematically slightly overestimated. We note that this modulation level is

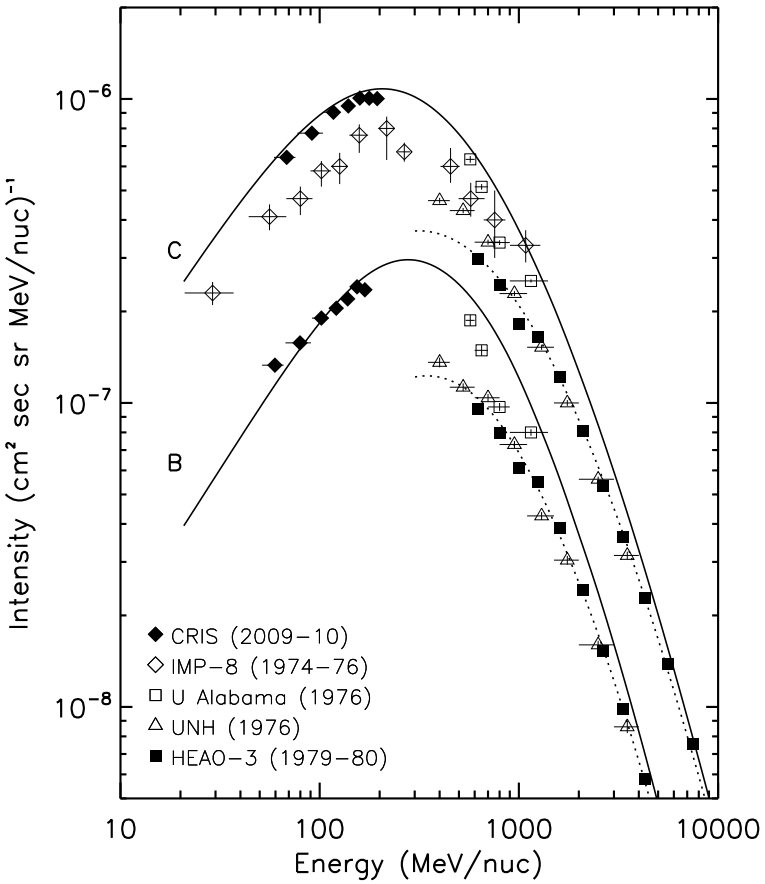

Figure D.5: Boron and carbon energy spectra for the 2009-10 solar minimum. CRIS observations discussed in this work are shown as filled diamonds; for references to all other data used here, refer to Appendix D.1. The solid curves are the result of an interstellar transport model using the Davis form of the escape mean free path (Equation 4.3), with a solar modulation level of $\phi = 250$ MV. The injection spectrum was taken to be a power law in momentum per nucleon, with a spectral index of -2.35. The dotted curves correspond to a modulation level of $\phi = 750$ MV, which is appropriate for the HEAO-3 mission.

the lowest of the space age (Usoskin et al. 2011), giving us the opportunity to study record-level cosmic-ray intensities at near-interstellar conditions. The average differences between the model and these CRIS data are around 7%. Scandium, titanium, and vanadium are also fairly well fit by the model, with average differences between

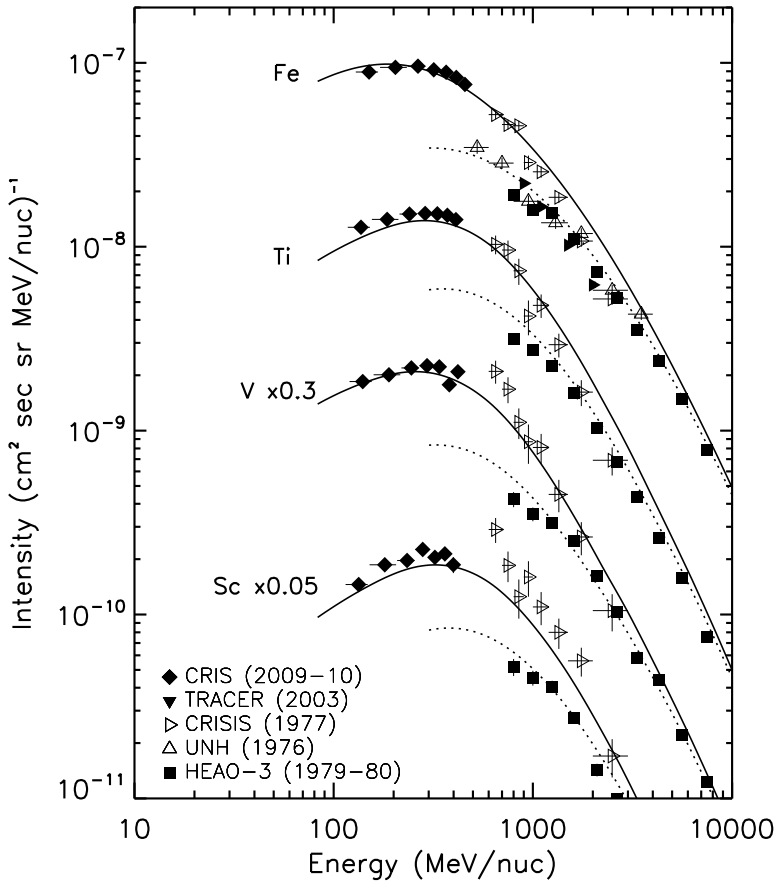

Figure D.6: Scandium, titanium, vanadium, and iron energy spectra for the 2009-10 solar minimum. For additional information concerning the data and interstellar transport models used here, refer to the caption of Figure D.5.

6-11%. Again, the iron energy spectrum is the best fit out of the six species, with an average difference of 5%. The largest individual difference is seen at the middle energy scandium measurement (19%), while most other CRIS measurements have differences below 10%.

We adjusted the other instrument data so that all observations were representative of the CRIS 2009-10 solar minimum modulation level, as shown in Figures D.7 and D.8. Again, with the exception of some of the CRISIS data, we see that the other

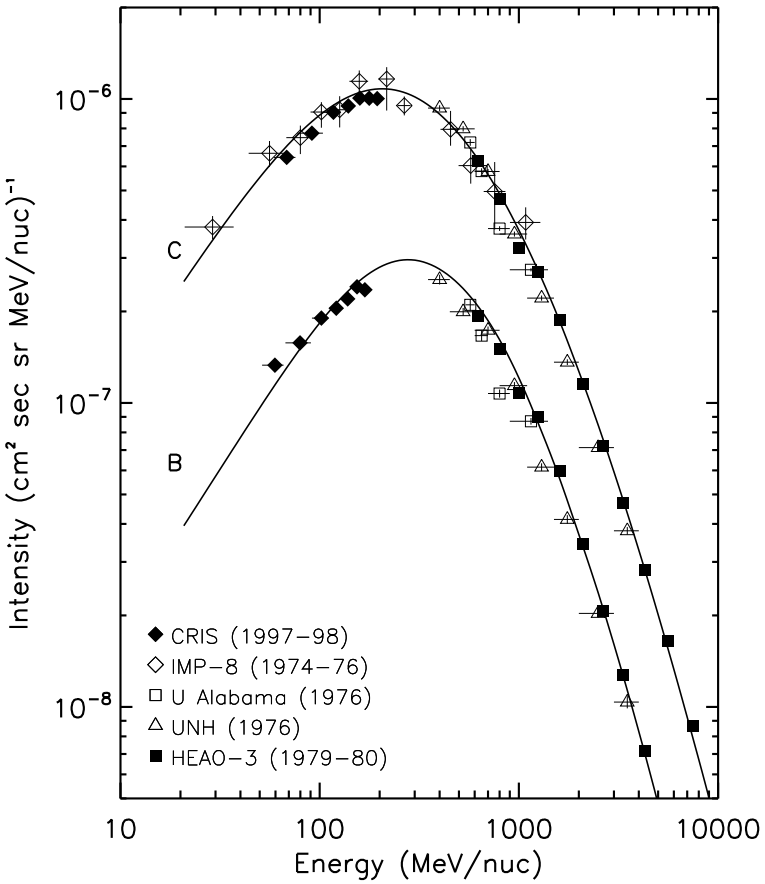

Figure D.7: Boron and carbon energy spectra for the 2009-10 solar minimum. CRIS observations discussed in this work are shown as filled diamonds; for references to all other data used here, refer to Appendix D.1. The solid curves are the result of an interstellar transport model using the Davis form of the escape mean free path (Equation 4.3), with a solar modulation level of $\phi = 250$ MV. The injection spectrum was taken to be a power law in momentum per nucleon, with a spectral index of -2.35. All data have been adjusted to this modulation level, as described in Appendix D.1.1.

experimental data are well fit by this model and they are consistent with the CRIS energy spectra.

The relatively small disagreements seen between the model and the CRIS solar minima observations are not surprising for two important reasons. First, the S&T semi-empirical production cross sections we use in the transport model (Appendix

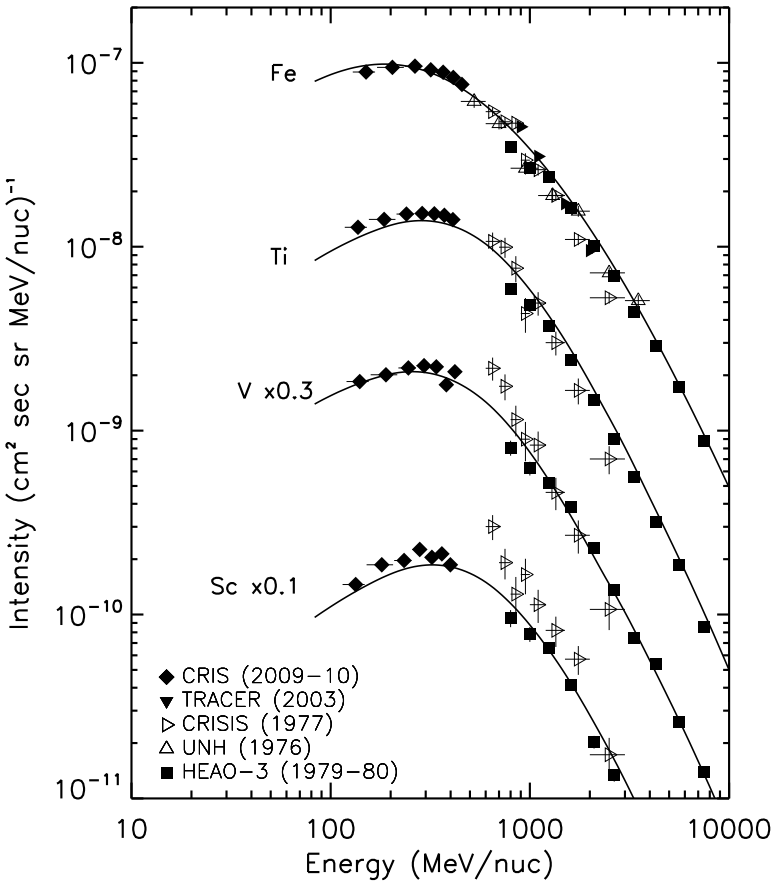

Figure D.8: Scandium, titanium, vanadium, and iron energy spectra for the 2009-10 solar minimum. For additional information concerning the data and interstellar transport models used here, refer to the caption of Figure D.7.

C) have estimated uncertainties ∼30% (Silberberg et al. 1985). Second, though the cosmic-ray energy spectra below ∼1 GeV/nucleon are quite sensitive to solar modulation model used here, we have chosen the value of ϕ that best fits the primary element spectra. We note that Wiedenbeck (2011) observed that different primaries seem to be better fit with slightly different ϕ, as seen in Figure D.9.

Though the various observations are fit quite well with this model, we have used a parameterization of the escape mean free path in the Galaxy (Equation 4.3) that

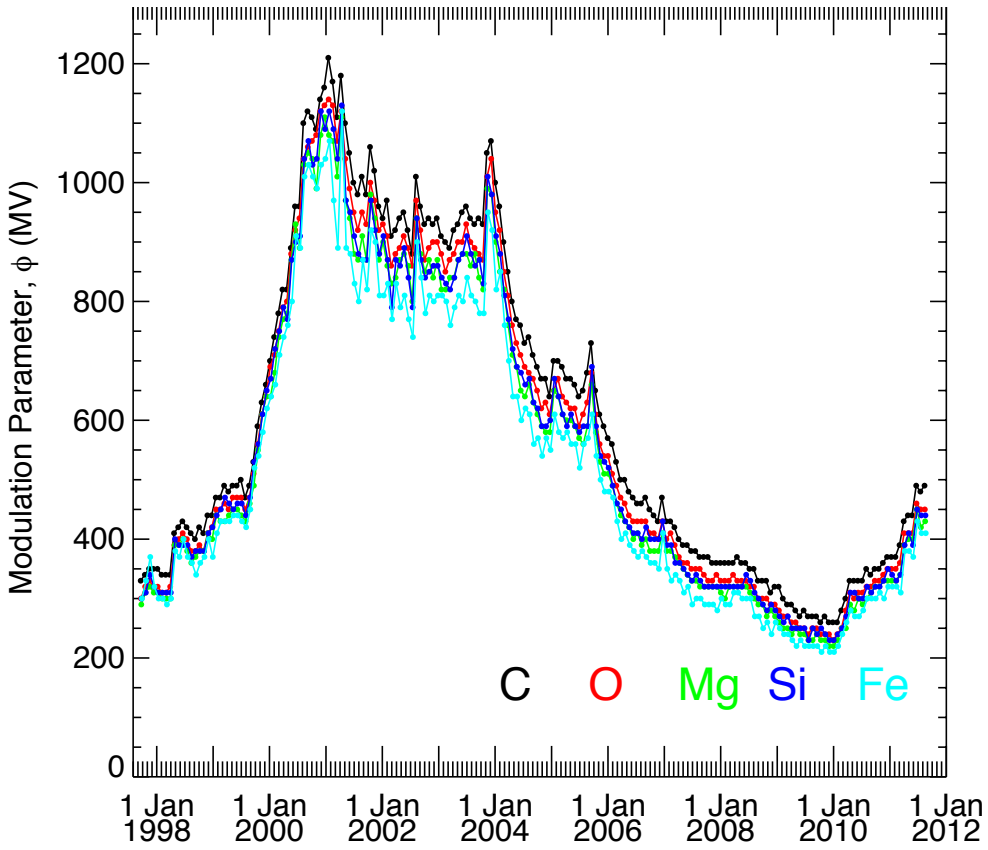

Figure D.9: The inferred solar modulation parameter ϕ versus time for the primary cosmic rays carbon, oxygen, magnesium, silicon, and iron. Values are based on fits of the low-energy roll-offs of the energy spectra (Wiedenbeck 2011).

artificially decreases at low energies the amount of material that cosmic rays traverse. This form is specifically tailored to better fit the CRIS data, even though there is no physical reason for such an energy dependence. Therefore, we must look for an alternative escape form that will still reproduce the observations at all energies without introducing unphysical elements to the parameterization.

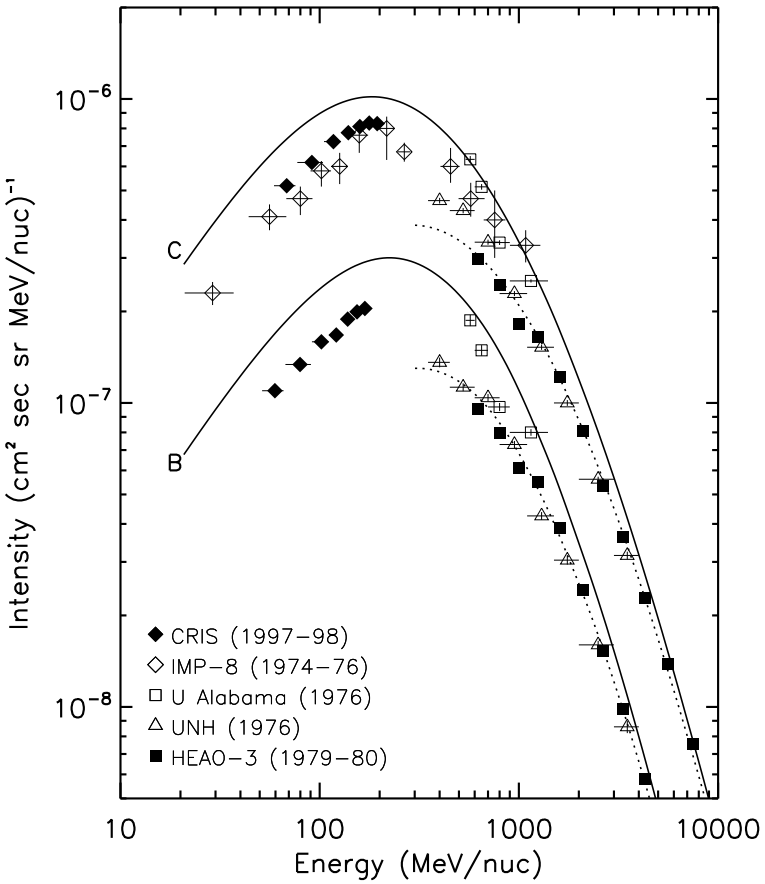

Figure D.10: Boron and carbon energy spectra for the 1997-98 solar minimum. CRIS observations discussed in this work are shown as filled diamonds; for references to all other data used here, refer to Appendix D.1. The solid curves are the result of an interstellar transport model using a simple rigidity-dependent form of the escape mean free path (given by Equation 4.6 with $\Lambda_o = 29.5$ g/cm^2 and $\gamma = -0.6$), with a solar modulation level of $\phi = 325$ MV. The injection spectrum was taken to be a power law in momentum per nucleon, with a spectral index of -2.35. The dotted curves correspond to a modulation level of $\phi = 750$ MV, which is appropriate for the HEAO-3 mission.

D.1.2 Model #2: simple R-dependent escape mean free path

For the second leaky-box transport model the injection spectrum was taken to be a power law in momentum per nucleon, with a spectral index of -2.35, and we used a simple rigidity-dependent escape mean free path in the Galaxy (Equation 4.6 with

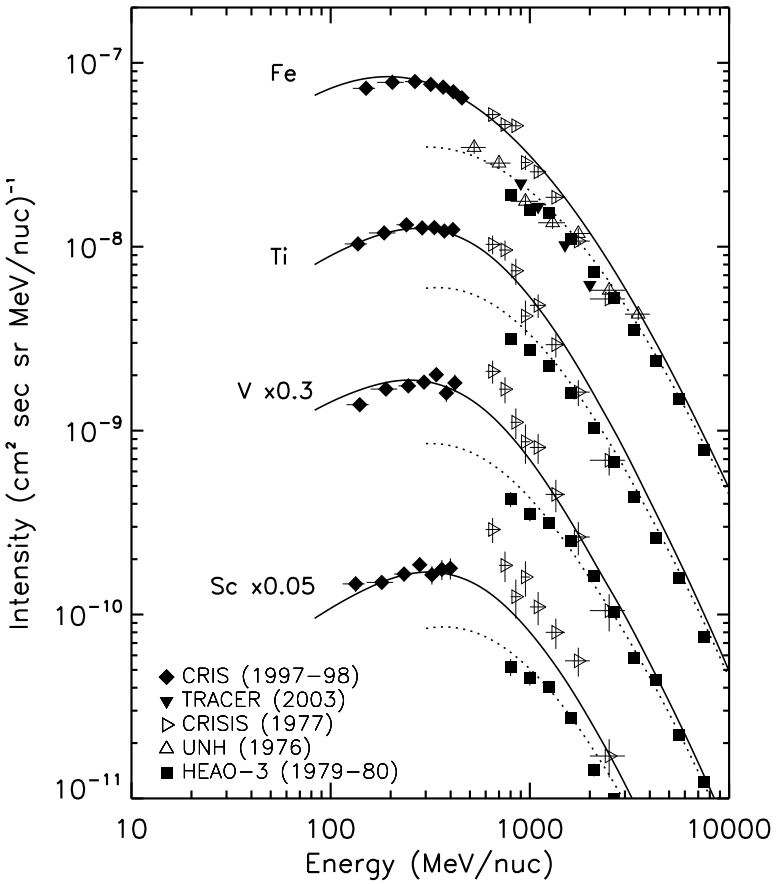

Figure D.11: Scandium, titanium, vanadium, and iron energy spectra for the 1997-98 solar minimum. For additional information concerning the data and interstellar transport models used here, refer to the caption of Figure D.10.

$\Lambda_o = 29.5$ g/cm^2 and $\gamma = -0.6$). This form is very similar to the parameterization used in Model #1 (Appendix D.1.1), though it does not artificially adjust the shape of the escape mean free path at low interstellar energies. Figures D.10 and D.11 show the calculated energy spectra for the 1997-98 solar minimum for the six chosen species and compare the model results with experimental data. We estimate a solar modulation value of $\phi = 325$ MV for this time period, shown by the solid lines. For reference we also include our model for a modulation value of $\phi = 750$ MV, which is

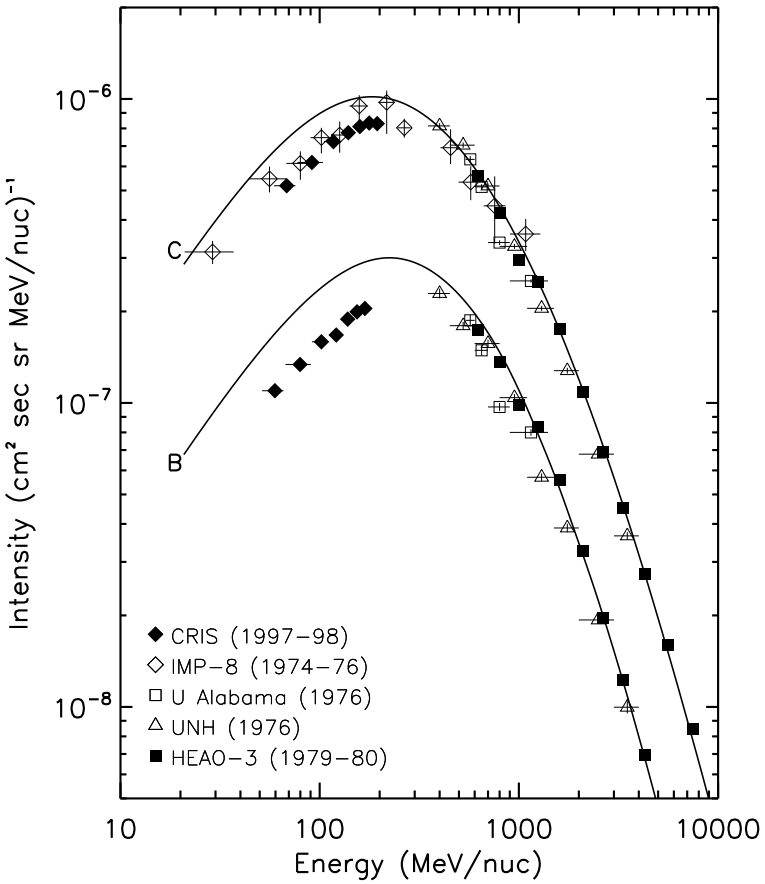

Figure D.12: Boron and carbon energy spectra for the 1997-98 solar minimum. CRIS observations discussed in this work are shown as filled diamonds; for references to all other data used here, refer to Appendix D.1. The solid curves are the result of an interstellar transport model using a simple rigidity-dependent form of the escape mean free path (Equation 4.6 with $\Lambda_o = 29.5$ g/cm^2 and $\gamma = -0.6$), with a solar modulation level of $\phi = 325$ MV. The injection spectrum was taken to be a power law in momentum per nucleon, with a spectral index of -2.35. All data have been adjusted to this modulation level, as described in Appendix D.1.1.

appropriate for the HEAO-3 mission (shown by the dotted lines).

Immediately we see that the $\phi = 325$ MV model does not fit the CRIS boron and carbon energy spectra. For boron the average difference between the model and the CRIS data is 50%, while for carbon it is 30%. Conversely, the scandium, titanium,

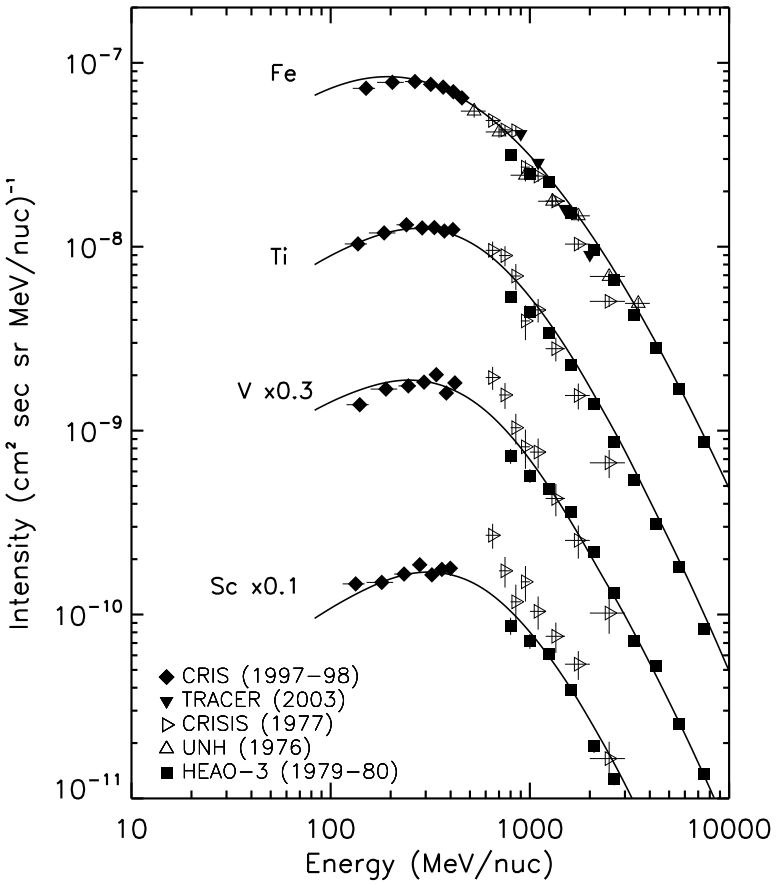

Figure D.13: Scandium, titanium, vanadium, and iron energy spectra for the 1997-98 solar minimum. For additional information concerning the data and interstellar transport models used here, refer to the caption of Figure D.12.

vanadium, and iron spectra are all well fit by the model, with average differences of 2-9%. We also note that even though not all of the CRIS data are fit by this model, the HEAO measurements for all six species are well fit by the $\phi = 750$ MV curve.

We note that these values of ϕ were determined by choosing the value that best fit Model #1 to the observations. Since boron and carbon are not well fit with these values while scandium through iron are, it suggests that very different values of ϕ are required for different charge regimes, or that a different modulation model is

required. Alternatively, these results may indicate that a different injection spectrum for carbon than for iron should be used. However, the energy spectra depend on the injection spectra, the interstellar transport model, and the modulation model while secondary-to-primary ratios mainly depend on the interstellar transport model. Investigations into the modulation and injection are beyond the scope of this thesis, which is primarily concerned with the interstellar transport model.

Observations from each of the experiments can be adjusted so that the data are representative of a common modulation level; we repeated the procedure described in Appendix D.1.1 using the spectra from Model #2. The results are shown in Figures D.12 and D.13, where all of the experimental data are adjusted to the CRIS 1997-98 modulation level. Though the data are consistent with one another (with the exception of some of the CRISIS observations) and they are well fit at energies above several hundred MeV/nucleon, there remains the large overestimation of the low-energy boron and carbon spectra.

Similar plots for the 2009-10 solar minimum are shown in Figures D.14 through D.17. A solar modulation value of $\phi = 250$ MV (shown by the solid lines) is estimated for this time period, as was used in Model #1. Again, we include for reference our model for a modulation value of $\phi = 750$ MV that is appropriate for the HEAO-3 mission (shown by the dotted lines).

As with the 1997-98 solar minimum we see the same problems in fitting the CRIS boron and carbon spectra with the $\phi = 250$ MV model. The disagreements here are slightly larger, where the average difference between the model and the CRIS boron

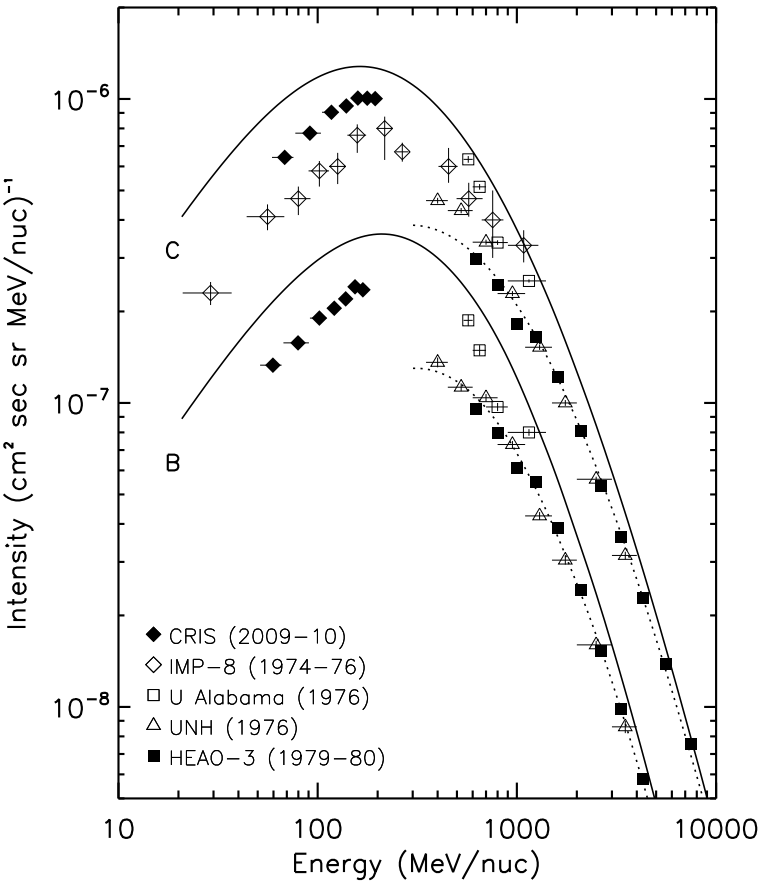

Figure D.14: Boron and carbon energy spectra for the 2009-10 solar minimum. CRIS observations discussed in this work are shown as filled diamonds; for references to all other data used here, refer to Appendix D.1. The solid curves are the result of an interstellar transport model using a simple rigidity-dependent form of the escape mean free path (given by Equation 4.6 with $\Lambda_o = 29.5$ g/cm^2 and $\gamma = -0.6$), with a solar modulation level of $\phi = 250$ MV. The injection spectrum was taken to be a power law in momentum per nucleon, with a spectral index of -2.35. The dotted curves correspond to a modulation level of $\phi = 750$ MV, which is appropriate for the HEAO-3 mission.

and carbon data is 55% and 36%, respectively. The scandium, titanium, vanadium, and iron spectra are all still well fit by the model, with average differences of 4-7%. Again, the HEAO measurements for all six species are well fit by the $\phi = 750$ MV curve even though there are problems fitting some of the CRIS data.

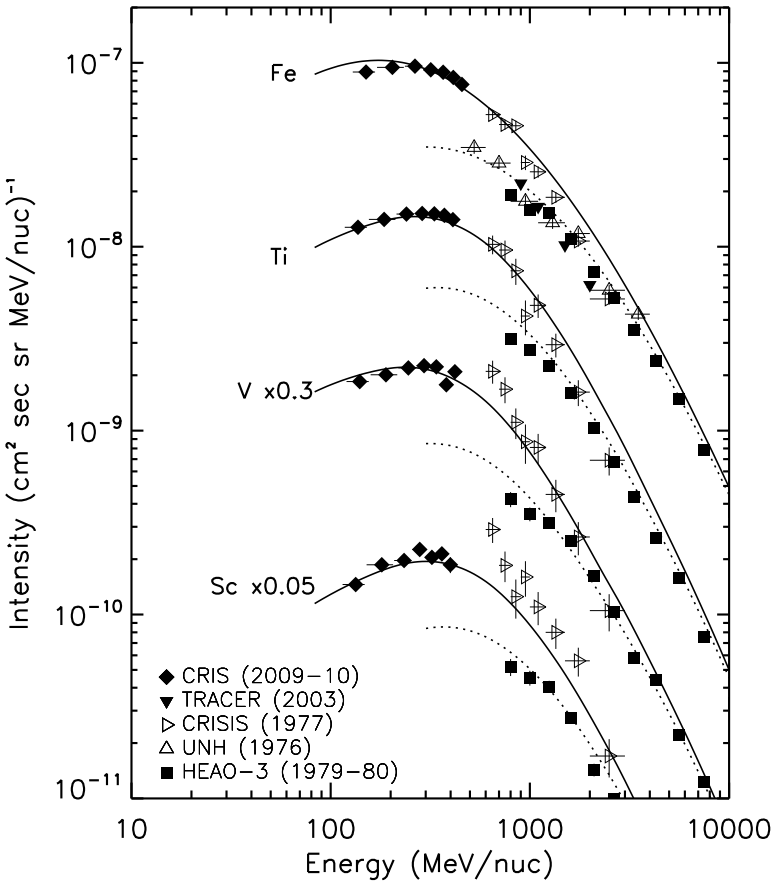

Figure D.15: Scandium, titanium, vanadium, and iron energy spectra for the 2009-10 solar minimum. For additional information concerning the data and interstellar transport models used here, refer to the caption of Figure D.14.

We adjusted the other instrument data so that all observations were representative of the CRIS 2009-10 solar minimum modulation level, as shown in Figures D.16 and D.17; again, we repeated the procedure described in Appendix D.1.1 using the spectra from Model #2. Though the other experimental data are generally consistent with one another and are well fit above several hundred MeV/nucleon, the model does not fit the low-energy boron and carbon energy spectra.

It is no surprise that the spectra for scandium, titanium, vanadium, and iron are

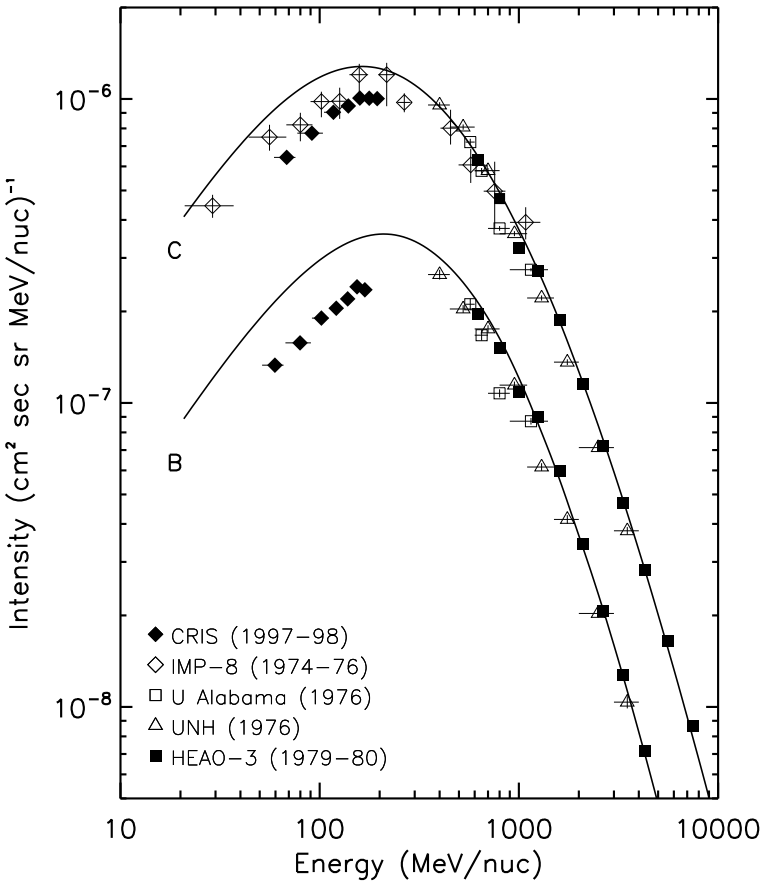

Figure D.16: Boron and carbon energy spectra for the 2009-10 solar minimum. CRIS observations discussed in this work are shown as filled diamonds; for references to all other data used here, refer to Appendix D.1. The solid curves are the result of an interstellar transport model using a simple rigidity-dependent form of the escape mean free path (Equation 4.6 with $\Lambda_o = 29.5$ g/cm^2 and $\gamma = -0.6$), with a solar modulation level of $\phi = 250$ MV. The injection spectrum was taken to be a power law in momentum per nucleon, with a spectral index of -2.35. All data have been adjusted to this modulation level, as described in Appendix D.1.1.

well-fit by both models at low energies, while there are large differences between the two models for boron and carbon. According to Figure 4.1, high-Z species like iron are much more sensitive to interaction than escape, so our choice for the parameterization won't significantly affect their low-energy spectra. For low-Z species like carbon the

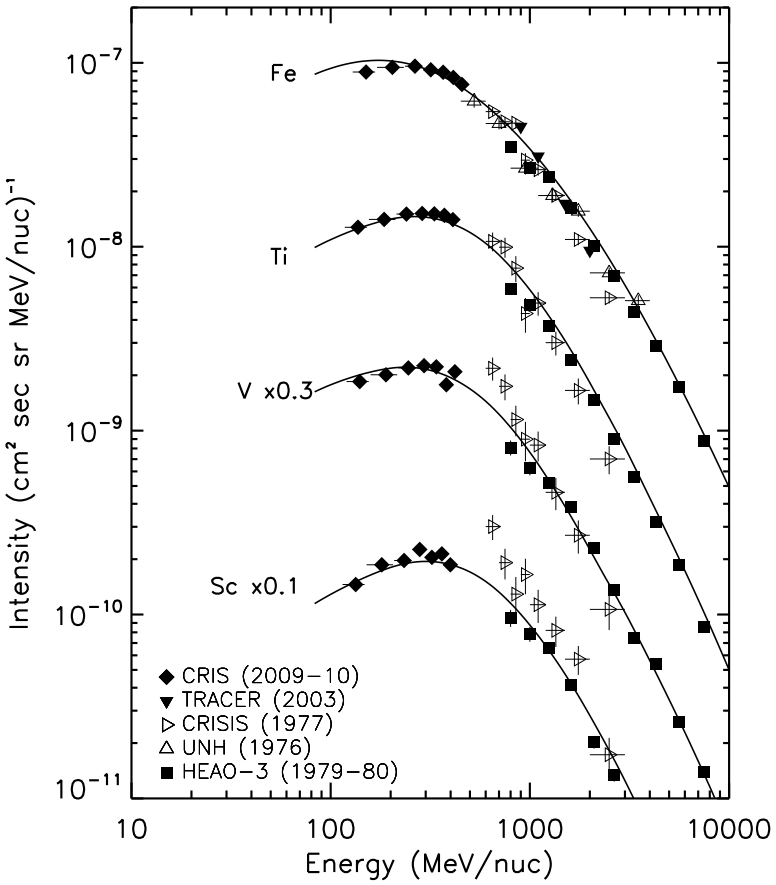

Figure D.17: Scandium, titanium, vanadium, and iron energy spectra for the 2009-10 solar minimum. For additional information concerning the data and interstellar transport models used here, refer to the caption of Figure D.16.

interaction mean free path is longer, and at low energies it is comparable to the escape path length used in Model #1. However, in Model #2 it is clear that escape is less important than interaction, and so we expect that the boron and carbon spectra in Model #2 should be higher at CRIS energies than those using Model #1.

Currently there is no accepted theoretical explanation for an escape mean free path form that strongly decreases with decreasing energy below ∼1 GeV/nucleon. This is therefore our impetus for testing a transport model with a simple rigidity-

dependent escape mean free path. However, the poor fit of the model to the boron and carbon energy spectra indicates that there is still some deficiency in this interstellar leaky-box model beyond any problems due to our production cross sections or our use of a simplified solar modulation model. Some studies found success by including reacceleration in the `GALPROP` numerical transport model (Strong and Moskalenko (1998); Moskalenko et al. (2003)). We use their results when discussing the B/C and $(Sc+Ti+V)/Fe$ ratios in Sections 4.4 (Model #1) and 4.5 (Model #2).

D.2 Nested leaky-box model

For the nested leaky-box model we chose to examine two interstellar models, each of which was defined by a different energy dependence for the escape mean free path from the cocoons (Section 5.1). We used our numerical solution discussed in Section 5.3 to calculate the isotopic interstellar equilibrium intensities, and after applying our solar modulation model (Chapter 1.4.3) we determined the elemental cosmic-ray intensities at Earth for each of the two solar minimum periods CRIS observed (Section 3.2). In this section, we will present the calculated energy spectra for boron, carbon, scandium, titanium, vanadium, and iron. In Sections 5.4 and we will use these six species to calculate the secondary-to-primary ratios B/C and $(Sc+Ti+V)/Fe$. We note that boron and carbon will be most sensitive to the escape form in the cocoon, while the sub-iron species and iron will be more sensitive to nuclear interactions, as is seen in Figure 4.1. Data from various spacecraft and balloon experiments listed in

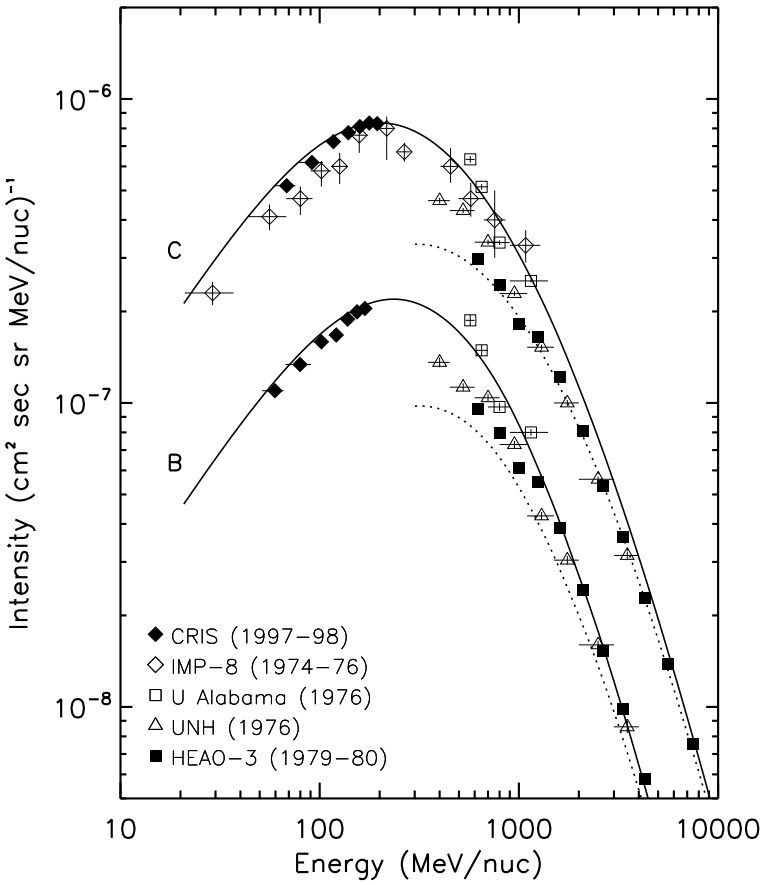

Figure D.18: Boron and carbon energy spectra for the 1997-98 solar minimum. CRIS observations discussed in this work are shown as filled diamonds; for references to all other data used here, refer to Section D.2. The solid curves are the result of an interstellar transport model using a simple rigidity-dependent form of the escape mean free path in the cocoon (given by Equation 4.6, where $\Lambda_o = 16.5$ g/cm^2 and $\gamma = -0.6$) and an energy-independent form in the Galaxy ($\Lambda_G = 0.5$ g/cm^2), with a solar modulation level of $\phi = 325$ MV. The injection spectrum was taken to be a power law in momentum per nucleon, with a spectral index of -2.8. The dotted curves correspond to a modulation level of $\phi = 750$ MV, which is appropriate for the HEAO-3 mission.

Section D.1 are again used to evaluate the nested leaky-box models.

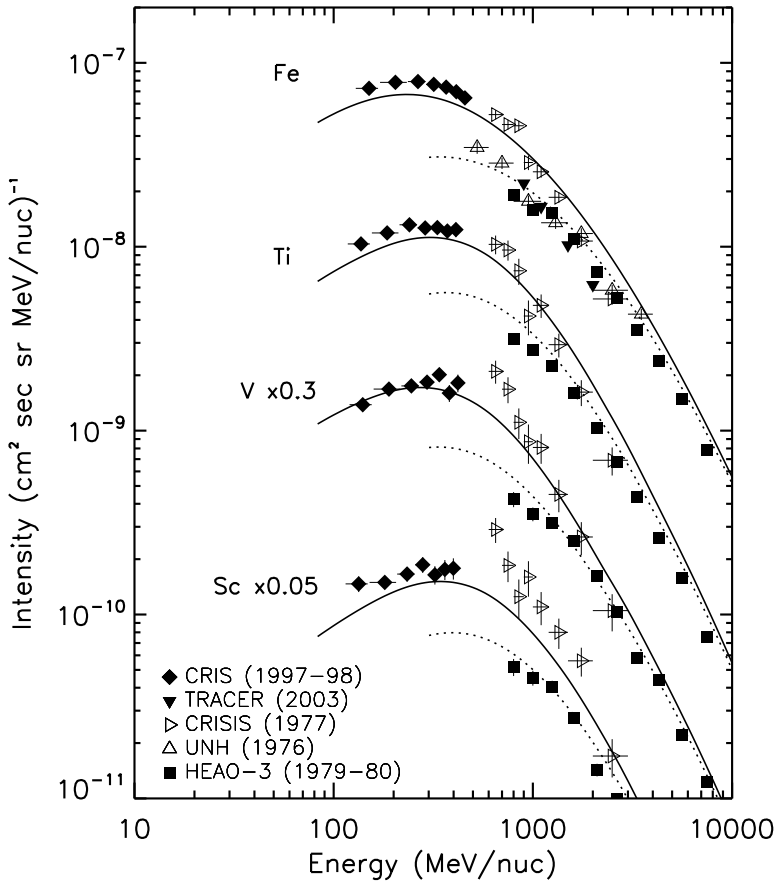

Figure D.19: Scandium, titanium, vanadium, and iron energy spectra for the 1997-98 solar minimum. For additional information concerning the data and interstellar transport models used here, refer to the caption of Figure D.18.

D.2.1 Model #1

For the first nested leaky-box transport model the injection spectrum was taken to be a power law in momentum per nucleon, with a spectral index of -2.8, and we use a simple rigidity-dependent form of the escape mean free path in the cocoon (Equation 4.6, with $\Lambda_o = 16.5$ g/cm^2 and $\gamma = -0.6$ (Equation 4.6). The escape mean free path in the Galaxy is taken to be $\Lambda_G = 0.5$ g/cm^2. Figures D.18 and D.19 show the calculated energy spectra for the 1997-98 solar minimum for the six species. We

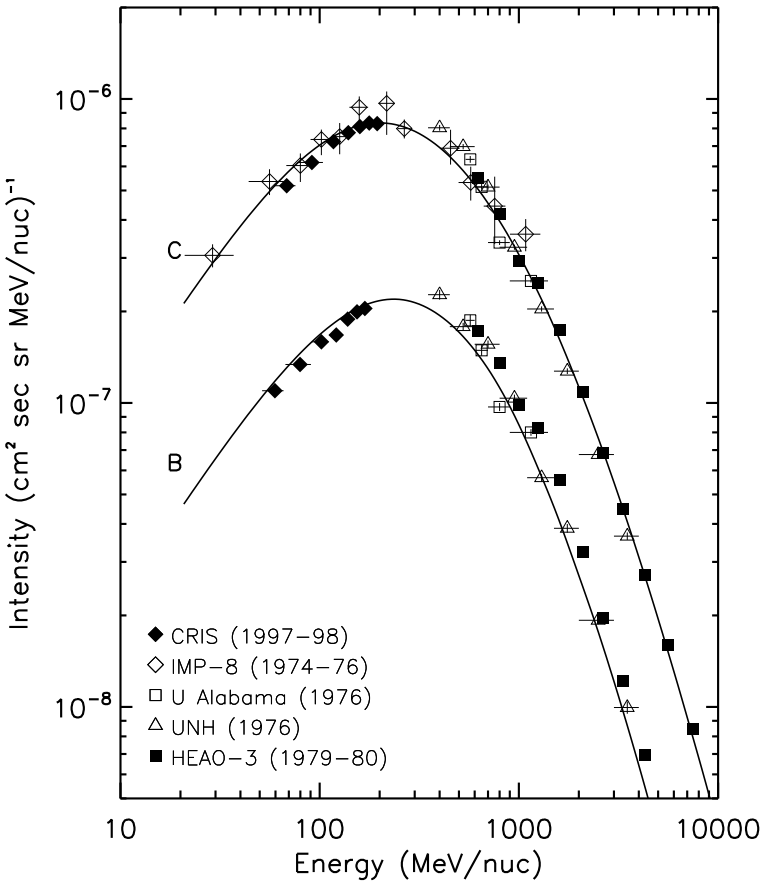

Figure D.20: Boron and carbon energy spectra for the 1997-98 solar minimum. CRIS observations discussed in this work are shown as filled diamonds; for references to all other data used here, refer to Section D.2. The solid curves are the result of an interstellar transport model using a simple rigidity-dependent form of the escape mean free path in the cocoon (given by Equation 4.6, where $\Lambda_o = 16.5$ g/cm^2 and $\gamma = -0.6$) and an energy-independent form in the Galaxy ($\Lambda_G = 0.5$ g/cm^2), with a solar modulation level of $\phi = 325$ MV. The injection spectrum was taken to be a power law in momentum per nucleon, with a spectral index of -2.8. All data have been adjusted to this modulation level, as described in Section D.1.1.

estimate a solar modulation value of $\phi = 325$ MV for this time period, which is the same value used in our analysis of the leaky-box models in Section D.1, shown by the solid lines. Our model for a modulation value of $\phi = 750$ MV is also given for reference (shown by the dotted lines).

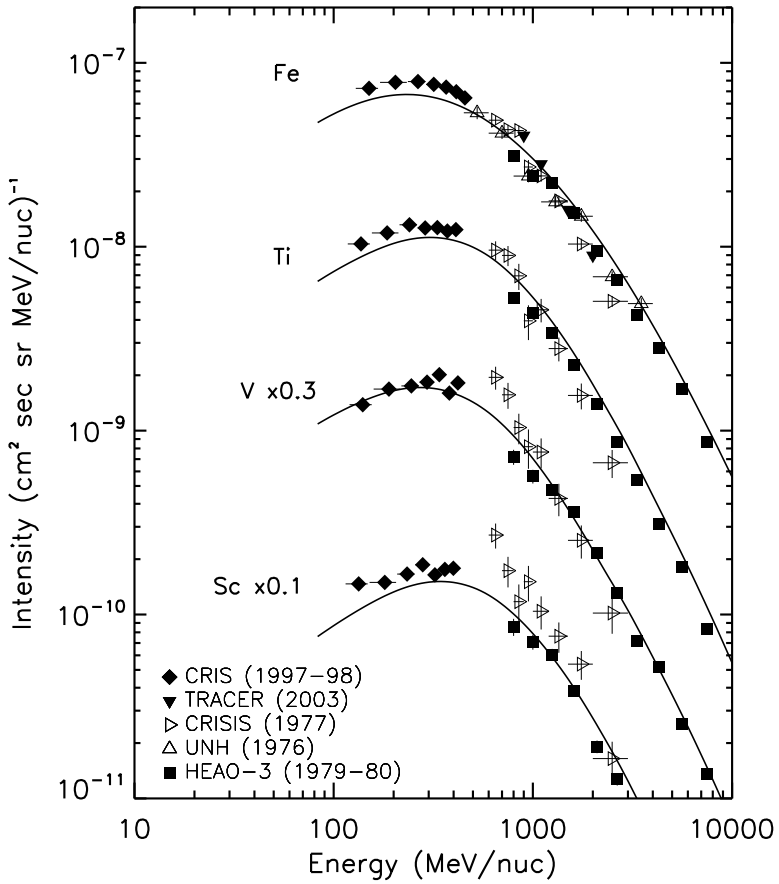

Figure D.21: Scandium, titanium, vanadium, and iron energy spectra for the 1997-98 solar minimum. For additional information concerning the data and interstellar transport models used here, refer to the caption of Figure D.20.

The CRIS boron and carbon measurements are well fit by the $\phi = 325$ MV curve, with an average difference of 6% and 4%, respectively, between this model and the data. Though the model underestimates the scandium, titanium, and iron spectra (with average differences of 13-17%), the vanadium spectrum is the best fit of the high-Z species (with a 7% average difference). We also note that the HEAO measurements, with the exception of boron, are fairly well fit by the $\phi = 750$ MV curve. With this model, the boron spectrum at high energies is underestimated by about 20%.

Other experimental data were used to test this model at higher energies, and we adjusted the observations from each experiment so that the data are representative of a common modulation level, $\phi = 325$ MV. To do this we repeated the procedure described in Appendix D.1.1 using the spectra from this nested leaky-box model. Figures D.20 and D.21 show the adjusted experimental data for the 1997-98 solar minimum. For carbon we see that the other experimental data are well fit by this model and they are consistent with the CRIS energy spectra. The boron data are consistent with one another, though this is due to the large energy bands for the UAH and UNH data (which are indicated by the horizontal bars on the points). However the HEAO observations are clearly underestimated by the model. With the exception of some of the CRISIS data, the scandium, titanium, vanadium, and iron observations are all consistent with one another. Below ∼500 MeV/nucleon the data are underestimated by the model, though above this energy the fit is quite good.

Similar plots for the 2009-10 solar minimum are shown in Figures D.22 through D.25. The estimated value of the solar modulation parameter is $\phi = 250$ MV for this time period (shown by the solid lines). We include for reference our model for a modulation value of $\phi = 750$ MV (shown by the dotted lines).

Here the CRIS boron and carbon spectra are fairly well fit by the $\phi = 250$ MV model, though the model tends to slightly overestimate the spectra below ∼100 MeV/nucleon. Compared to the 1997-98 solar minimum, the disagreements here are slightly larger for boron and carbon; the average difference between the model and the CRIS data is 7-9%. The scandium, titanium, and iron spectra are all still

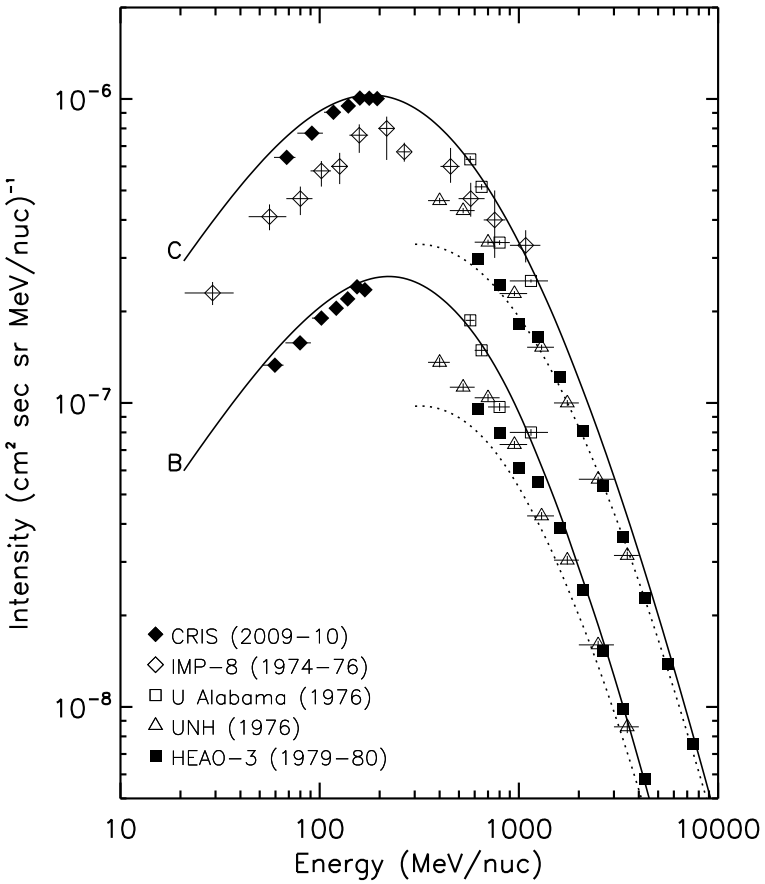

Figure D.22: Boron and carbon energy spectra for the 2009-10 solar minimum. CRIS observations discussed in this work are shown as filled diamonds; for references to all other data used here, refer to Section D.2. The solid curves are the result of an interstellar transport model using a simple rigidity-dependent form of the escape mean free path in the cocoon (given by Equation 4.6, where $\Lambda_o = 16.5$ g/cm^2 and $\gamma = -0.6$) and an energy-independent form in the Galaxy ($\Lambda_G = 0.5$ g/cm^2), with a solar modulation level of $\phi = 250$ MV. The injection spectrum was taken to be a power law in momentum per nucleon, with a spectral index of -2.8. The dotted curves correspond to a modulation level of $\phi = 750$ MV, which is appropriate for the HEAO-3 mission.

underestimated by the model, with average differences of 16-19%, while the vanadium spectrum is underestimated by 10%.

The other instrument data were adjusted (using the procedure described in Ap-

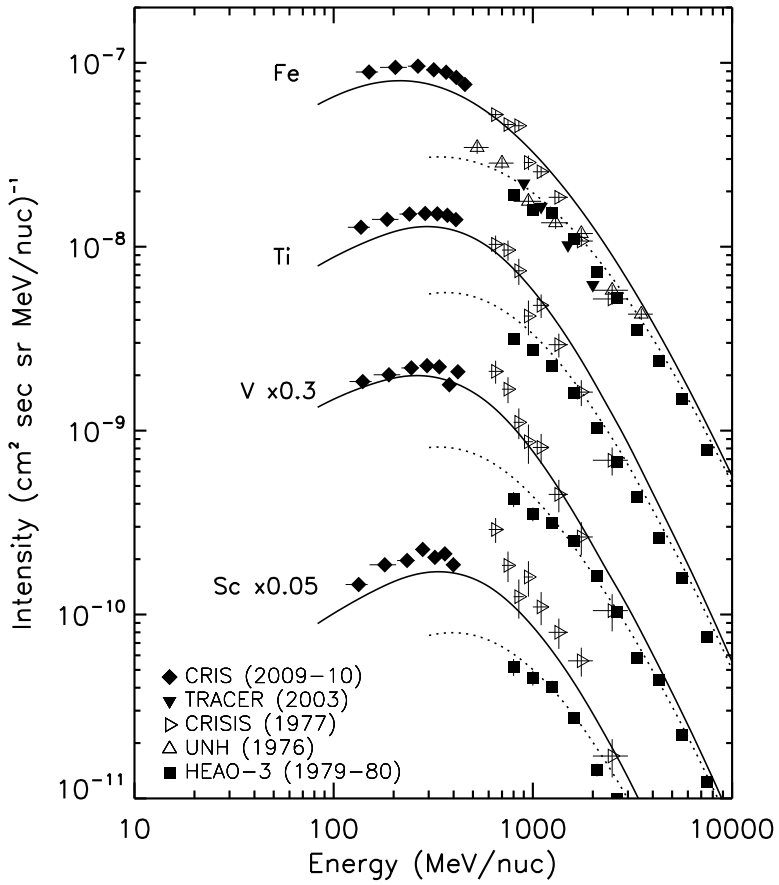

Figure D.23: Scandium, titanium, vanadium, and iron energy spectra for the 2009-10 solar minimum. For additional information concerning the data and interstellar transport models used here, refer to the caption of Figure D.22.

pendix D.1.1 and the spectra from this nested leaky-box model) so that all observations were representative of the CRIS 2009-10 solar minimum modulation level, as shown in Figures D.24 and D.25. Again, though the other experimental data are generally consistent with one another, the model does not fit HEAO's high-energy boron spectrum. Carbon is well fit across the entire energy range, and for the remaining four species the model fits the data at high energies and underestimates the spectra at CRIS energies.

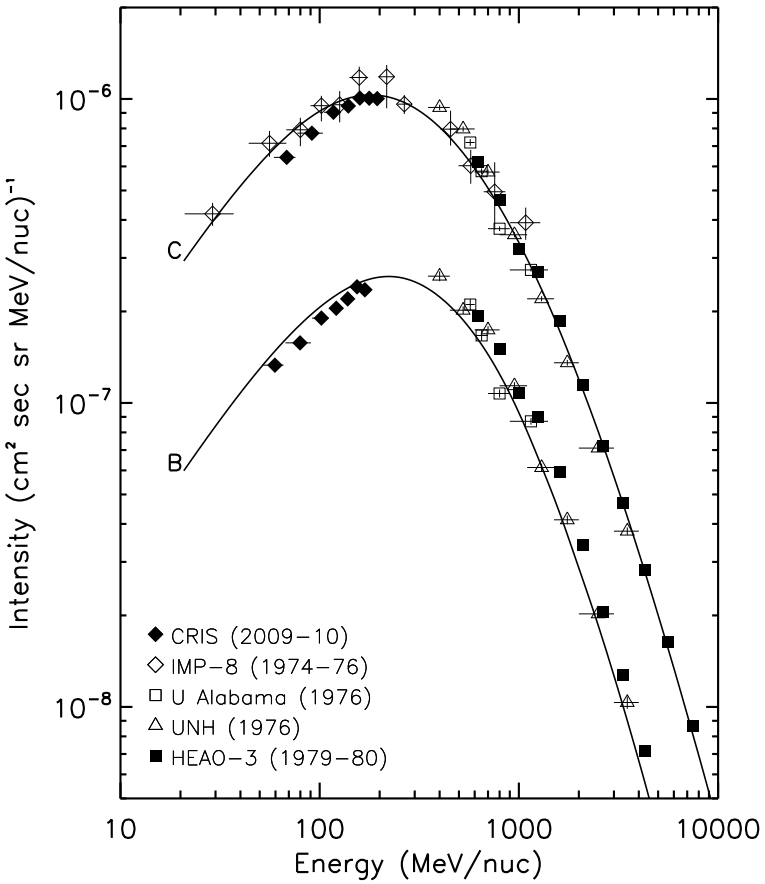

Figure D.24: Boron and carbon energy spectra for the 2009-10 solar minimum. CRIS observations discussed in this work are shown as filled diamonds; for references to all other data used here, refer to Section D.2. The solid curves are the result of an interstellar transport model using a simple rigidity-dependent form of the escape mean free path in the cocoon (given by Equation 4.6, where $\Lambda_o = 16.5$ g/cm^2 and $\gamma = -0.6$) and an energy-independent form in the Galaxy ($\Lambda_G = 0.5$ g/cm^2), with a solar modulation level of $\phi = 250$ MV. The injection spectrum was taken to be a power law in momentum per nucleon, with a spectral index of -2.8. All data have been adjusted to this modulation level, as described in Section D.1.1.

For the low-energy boron and carbon energy spectra, the disagreements seen between the model and the CRIS data are most likely due to uncertainties in the production cross sections and the simplified modulation model (as discussed at the end of Section D.1.1). The same reasoning can not explain the larger disagreements seen

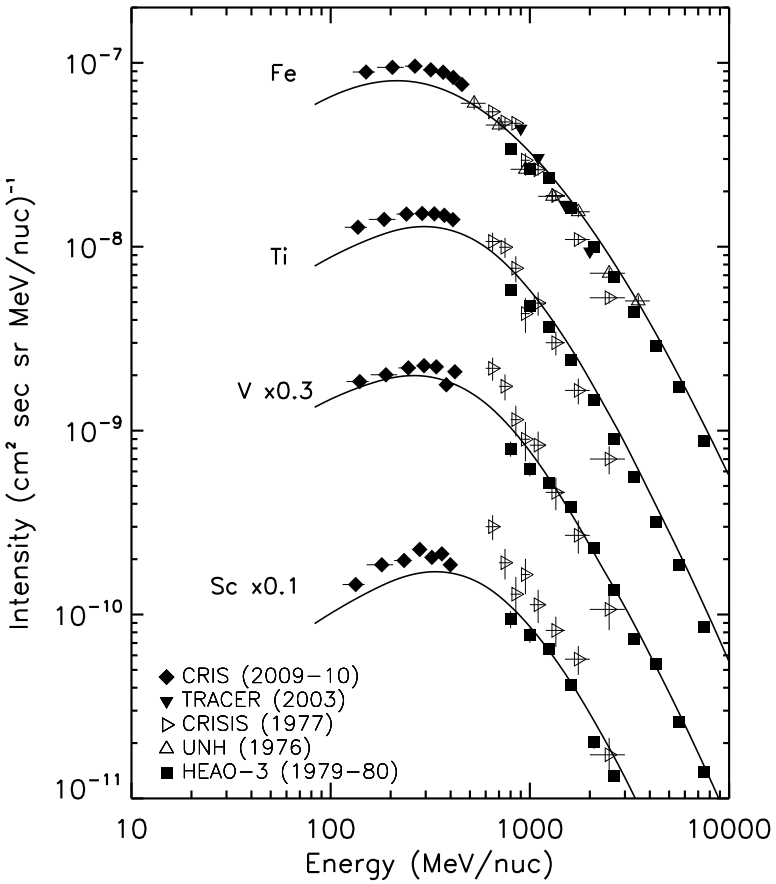

Figure D.25: Scandium, titanium, vanadium, and iron energy spectra for the 2009-10 solar minimum. For additional information concerning the data and interstellar transport models used here, refer to the caption of Figure D.24.

in the high-energy boron spectrum and the scandium, titanium, vanadium, and iron energy spectra. Most likely the problems with the secondary species are due to the modeling of the cocoon, where the majority of the secondary cosmic rays are produced; it is unclear why we see poor agreement with the iron spectrum.

Looking at Equation 5.6 we see that an increase in the cocoon residence time (τ_C), and therefore an increase in the cocoon escape mean free path (Λ_C), would lead to an increase in the number density of secondary species produced in the cocoon. However,

this increase in τ_C will actually decrease the number density of primary species in the cocoon (according to Equation 5.4. Therefore, it is not immediately clear whether a longer residence time will resolve the discrepancies we see between the model and the data. We will test this theory is in Section D.2.2 by using a longer mean free path in the cocoon.

D.2.2 Model #2

This second nested leaky-box transport model uses an injection spectrum taken to be a power law in momentum per nucleon, with a spectral index of -2.8, and a similar escape mean free path in the cocoon as in Model #1. However, now we use $\Lambda_o = 23.0$ g/cm^2 (with $\gamma = -0.6$) in Equation 4.6; as in Model #1, we use an energy-independent escape form in the Galaxy ($\Lambda_G = 0.5$ g/cm^2). The calculated energy spectra for the 1997-98 solar minimum for each of the six chosen species are compared with experimental data in Figures D.26 and D.27. We estimate a solar modulation value of $\phi = 325$ MV (shown by the solid lines). For reference we also include our model for a modulation value of $\phi = 750$ MV, which is appropriate for the HEAO-3 mission (shown by the dotted lines).

With this model the CRIS boron and carbon measurements are nicely fit by the $\phi = 325$ MV model, though the carbon spectrum is slightly underestimated at the highest CRIS energies. The average differences between the model and the CRIS boron and carbon data are around 6-8%, and the largest individual difference is 11%. The scandium, titanium, and vanadium spectra are all underestimated by the model,

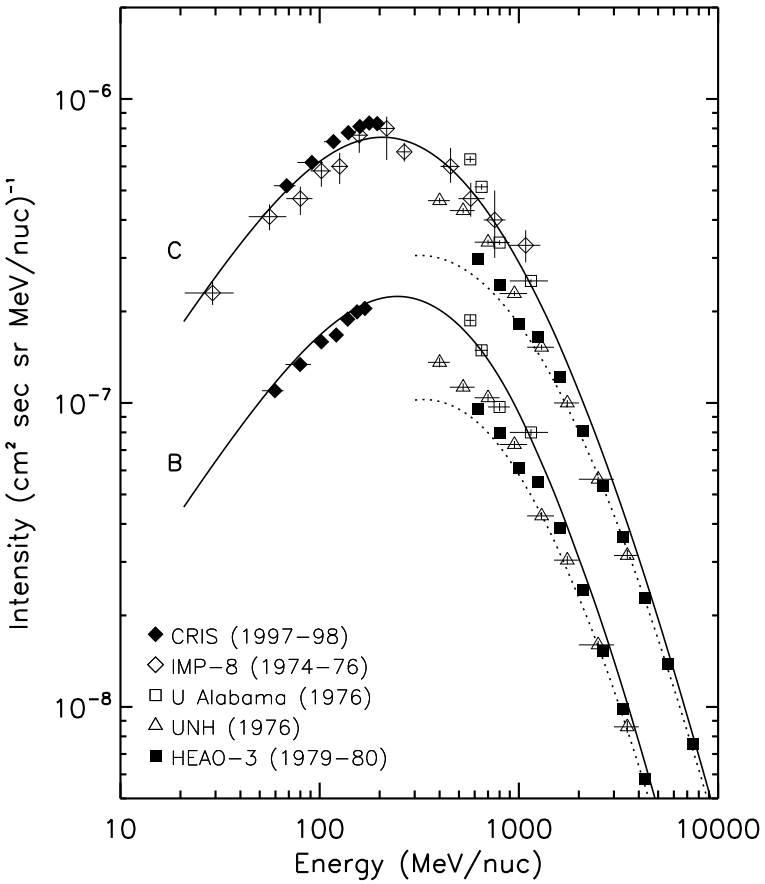

Figure D.26: Boron and carbon energy spectra for the 1997-98 solar minimum. CRIS observations discussed in this work are shown as filled diamonds; for references to all other data used here, refer to Section D.2. The solid curves are the result of an interstellar transport model using a simple rigidity-dependent form of the escape mean free path in the cocoon (given by Equation 4.6, where $\Lambda_o = 23.0$ g/cm^2 and $\gamma = -0.6$) and an energy-independent form in the Galaxy ($\Lambda_G = 0.5$ g/cm^2), with a solar modulation level of $\phi = 325$ MV. The injection spectrum was taken to be a power law in momentum per nucleon, with a spectral index of -2.8. The dotted curves correspond to a modulation level of $\phi = 750$ MV, which is appropriate for the HEAO-3 mission.

with average differences of 16-24%. The worst fit of the model to the CRIS data is for iron, which is underestimated on average by 29%. The HEAO measurements for all six species are fairly well fit by the $\phi = 750$ MV curve.

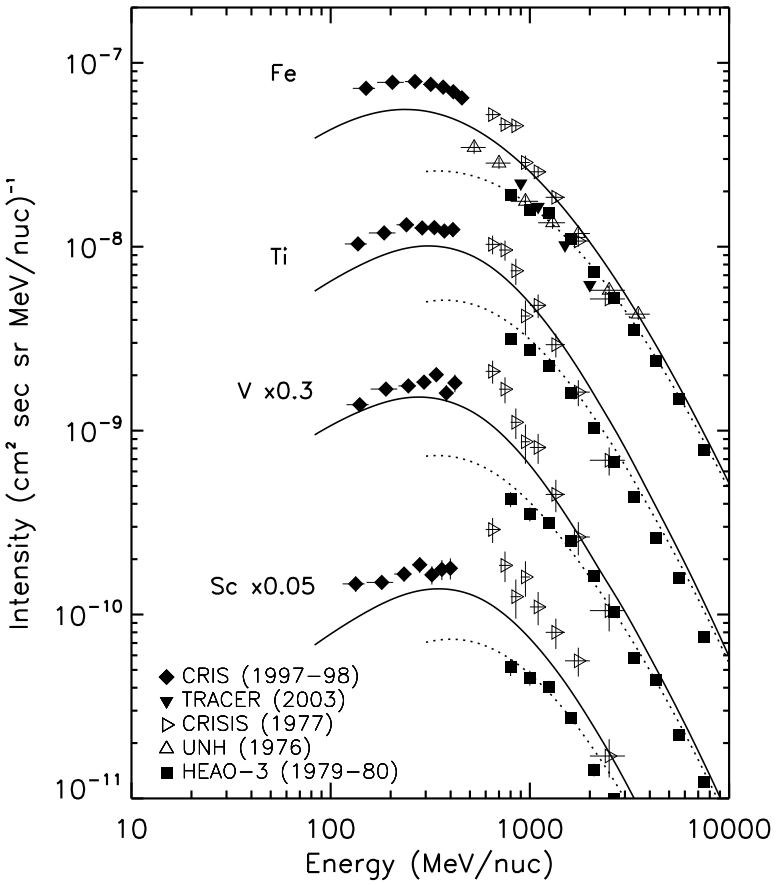

Figure D.27: Scandium, titanium, vanadium, and iron energy spectra for the 1997-98 solar minimum. For additional information concerning the data and interstellar transport models used here, refer to the caption of Figure D.26.

We can use other experimental data to test this model at higher energies, and observations from each experiment were adjusted (using the procedure described in Appendix D.1.1 and the spectra from this nested leaky-box model) so that the data are representative of a common modulation level, $\phi = 325$ MV. Figures D.28 and D.29 plot all of the experimental data adjusted in this manner for the 1997-98 solar minimum. For boron and carbon, we see that the other experimental data are well fit by this model and they are consistent with the CRIS energy spectra. With the

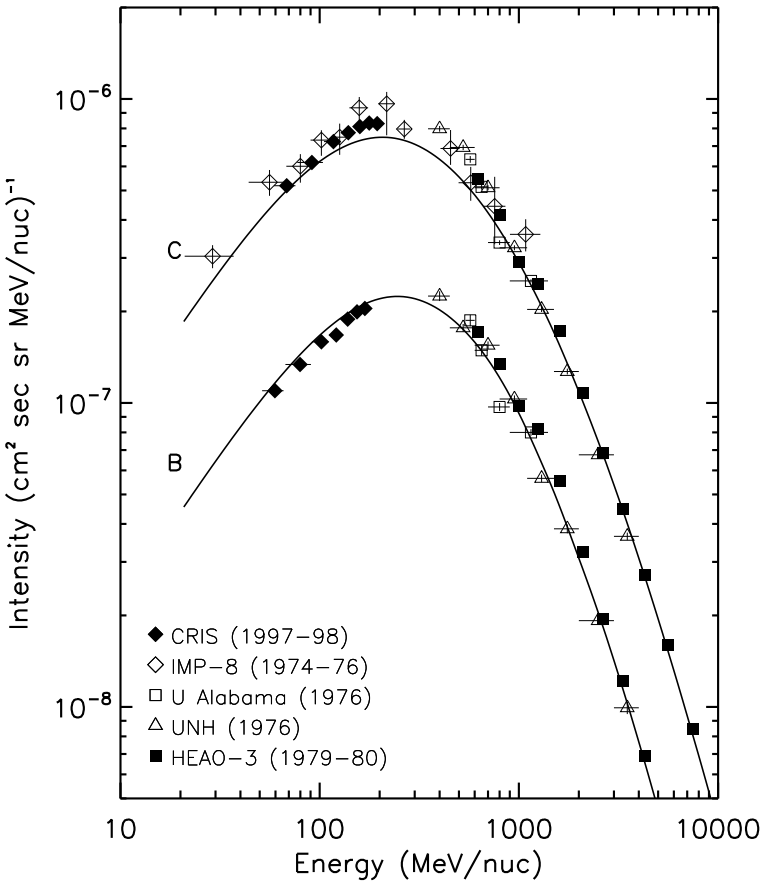

Figure D.28: Boron and carbon energy spectra for the 1997-98 solar minimum. CRIS observations discussed in this work are shown as filled diamonds; for references to all other data used here, refer to Section D.2. The solid curves are the result of an interstellar transport model using a simple rigidity-dependent form of the escape mean free path in the cocoon (given by Equation 4.6, where $\Lambda_o = 23.0$ g/cm^2 and $\gamma = -0.6$) and an energy-independent form in the Galaxy ($\Lambda_G = 0.5$ g/cm^2), with a solar modulation level of $\phi = 325$ MV. The injection spectrum was taken to be a power law in momentum per nucleon, with a spectral index of -2.8. All data have been adjusted to this modulation level, as described in Section D.1.1.

exception of some of the CRISIS data, we also see that the scandium, titanium, vanadium, and iron observations are consistent with one another. However, it is clear that this model underestimates those spectra below ∼1 GeV/nucleon.

Similar plots for the 2009-10 solar minimum are shown in Figures D.30 through

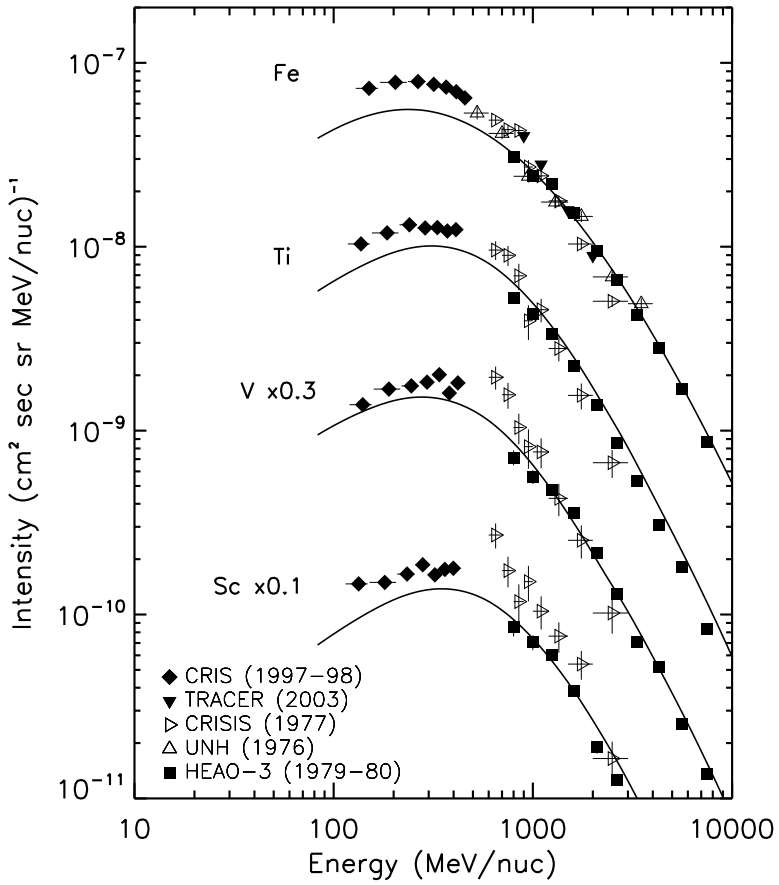

Figure D.29: Scandium, titanium, vanadium, and iron energy spectra for the 1997-98 solar minimum. For additional information concerning the data and interstellar transport models used here, refer to the caption of Figure D.28.

D.33. We estimate a solar modulation value of $\phi = 250$ MV (shown by the solid lines) for this time period, as was used in Model #1. We again show for reference our model for a modulation value of $\phi = 750$ MV (shown by the dotted lines).

We see that the 2009-10 CRIS boron and carbon measurements are nicely fit by the $\phi = 250$ MV model, with the average differences between the model and these CRIS data around 6-8%. This model underestimates the scandium, titanium, and vanadium spectra by an average of 19-26%. The iron spectrum is again the worst fit

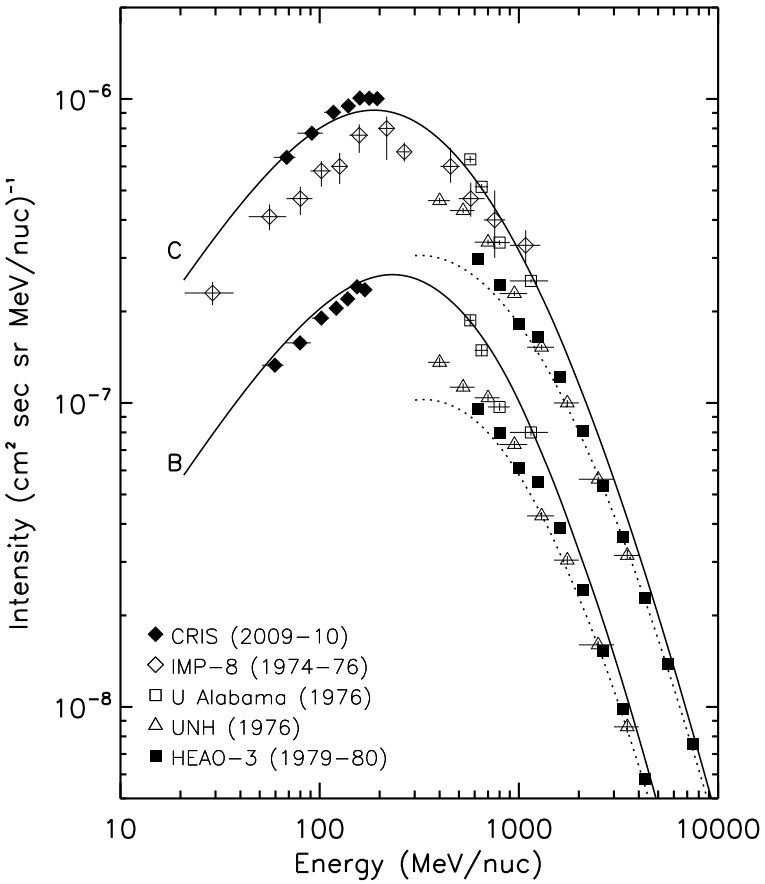

Figure D.30: Boron and carbon energy spectra for the 2009-10 solar minimum. CRIS observations discussed in this work are shown as filled diamonds; for references to all other data used here, refer to Section D.2. The solid curves are the result of an interstellar transport model using a simple rigidity-dependent form of the escape mean free path in the cocoon (given by Equation 4.6, where $\Lambda_o = 23.0$ g/cm^2 and $\gamma = -0.6$) and an energy-independent form in the Galaxy ($\Lambda_G = 0.5$ g/cm^2), with a solar modulation level of $\phi = 250$ MV. The injection spectrum was taken to be a power law in momentum per nucleon, with a spectral index of -2.8. The dotted curves correspond to a modulation level of $\phi = 750$ MV, which is appropriate for the HEAO-3 mission.

out of the six species, with an average difference of 31%.

When the other instrument data are adjusted (using the procedure described in Appendix D.1.1 and the spectra from this nested leaky-box model) so that all

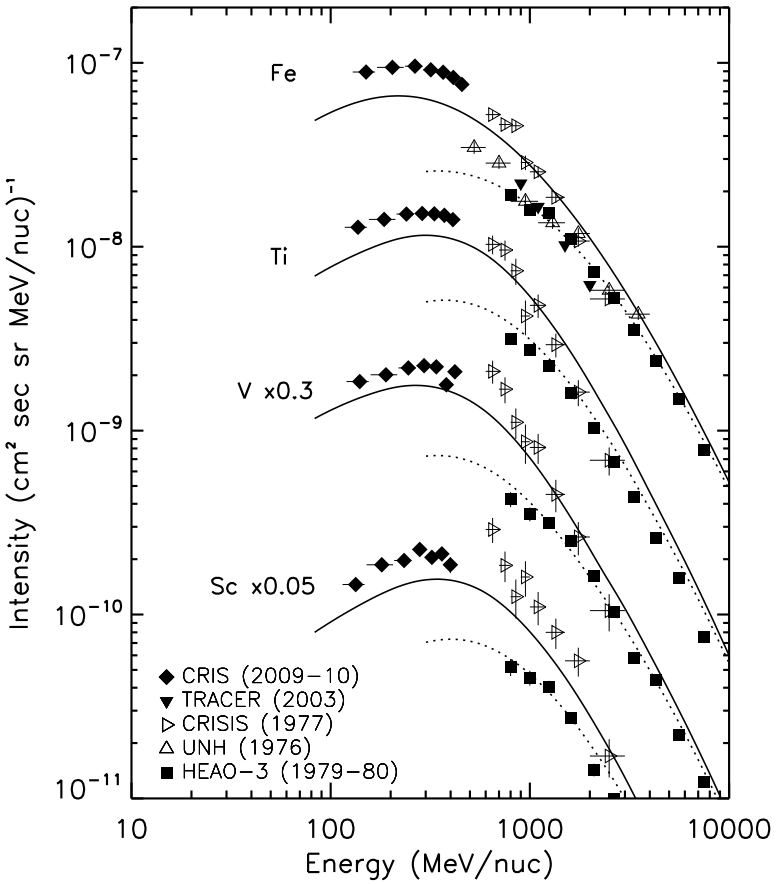

Figure D.31: Scandium, titanium, vanadium, and iron energy spectra for the 2009-10 solar minimum. For additional information concerning the data and interstellar transport models used here, refer to the caption of Figure D.30.

observations are representative of the CRIS 2009-10 solar minimum modulation level (Figures D.32 and D.33), we still see that the data are consistent with one another. As in the prior solar minimum, the observations are well fit by the model above ∼1 GeV/nucleon (excluding some of the CRISIS data), but below this energy the model still underestimates the spectra.

As we saw in Model #1, the disagreements seen between this model and the CRIS data for the boron and carbon energy spectra are most likely due to uncertainties in

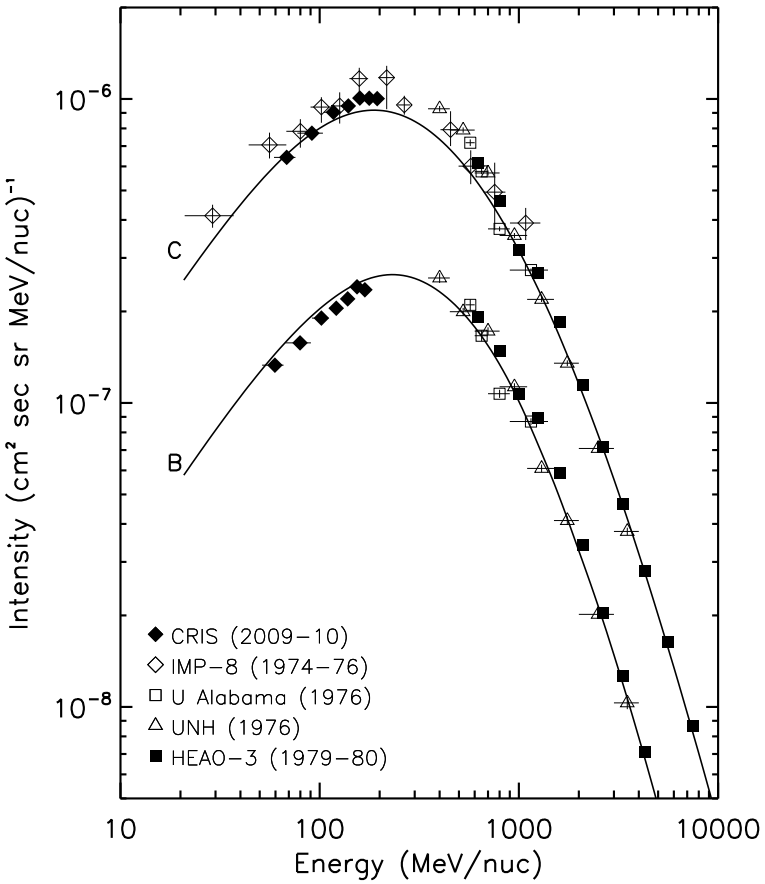

Figure D.32: Boron and carbon energy spectra for the 2009-10 solar minimum. CRIS observations discussed in this work are shown as filled diamonds; for references to all other data used here, refer to Section D.2. The solid curves are the result of an interstellar transport model using a simple rigidity-dependent form of the escape mean free path in the cocoon (given by Equation 4.6, where $\Lambda_o = 23.0$ g/cm^2 and $\gamma = -0.6$) and an energy-independent form in the Galaxy ($\Lambda_G = 0.5$ g/cm^2), with a solar modulation level of $\phi = 250$ MV. The injection spectrum was taken to be a power law in momentum per nucleon, with a spectral index of -2.8. All data have been adjusted to this modulation level, as described in Section D.1.1.

the production cross sections and the simplified modulation model (as discussed at the end of Section D.1.1). This can not explain the large disagreements seen in the scandium, titanium, vanadium, and iron energy spectra. We also note that the high-energy boron spectrum is now better fit with Model #2, so the longer escape path

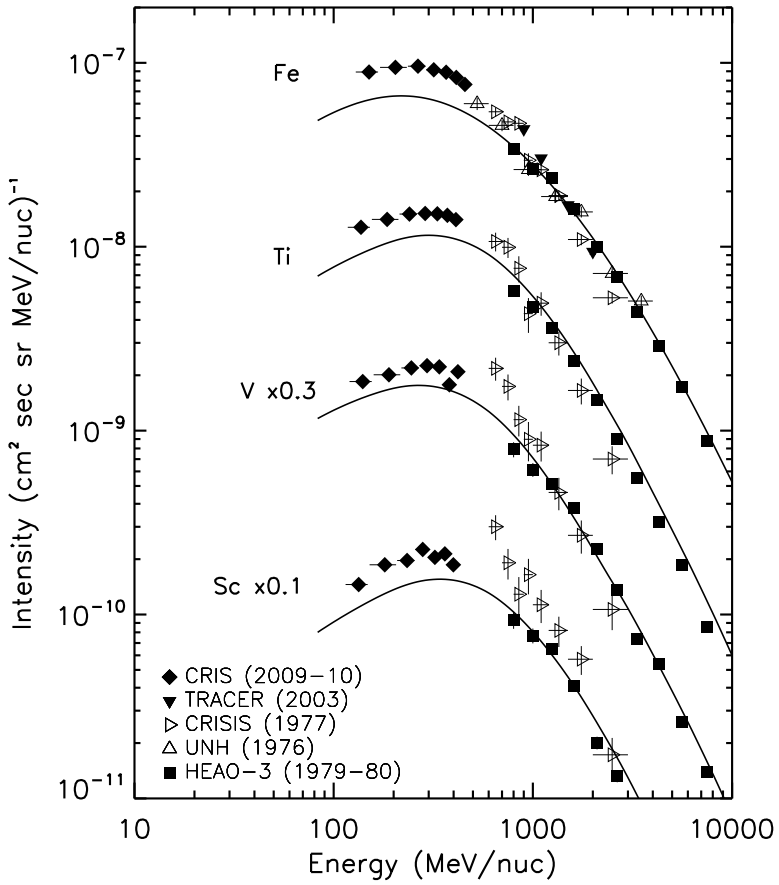

Figure D.33: Scandium, titanium, vanadium, and iron energy spectra for the 2009-10 solar minimum. For additional information concerning the data and interstellar transport models used here, refer to the caption of Figure D.32.

length in the cocoon did have the effect of creating more boron.

With the longer escape mean free path in the cocoon we see that the ∼20% disagreement for boron at high energies using Model #1 dropped to ∼12% with Model #2. However, the longer path length also translated to a larger underestimation of the sub-iron and iron spectra at CRIS energies. These observations are likely due to the competition between escape and total interaction for the different charge regimes, which can be seen in Figure 5.1. For Model #2, only the low-Z species at the highest

energies are more likely to escape the cocoon before being lost by interactions; in Model #1 escape of low-Z species is more likely at almost all energies, though the two loss processes begin to compete below a few GeV/nucleon. Conversely, in either model the high-Z species will almost always interact before they escape the cocoon, though with the longer path length it is even more likely that fewer of these cosmic rays will escape before interacting. Unfortunately, this seems to indicate that for these two escape models there is no parameterization that will produce enough high-energy boron and low-energy sub-iron and iron, while maintaining the same production of low-energy boron and carbon and high-energy sub-iron and iron.